Image Analysis as Measuring Technique in Flows[1]

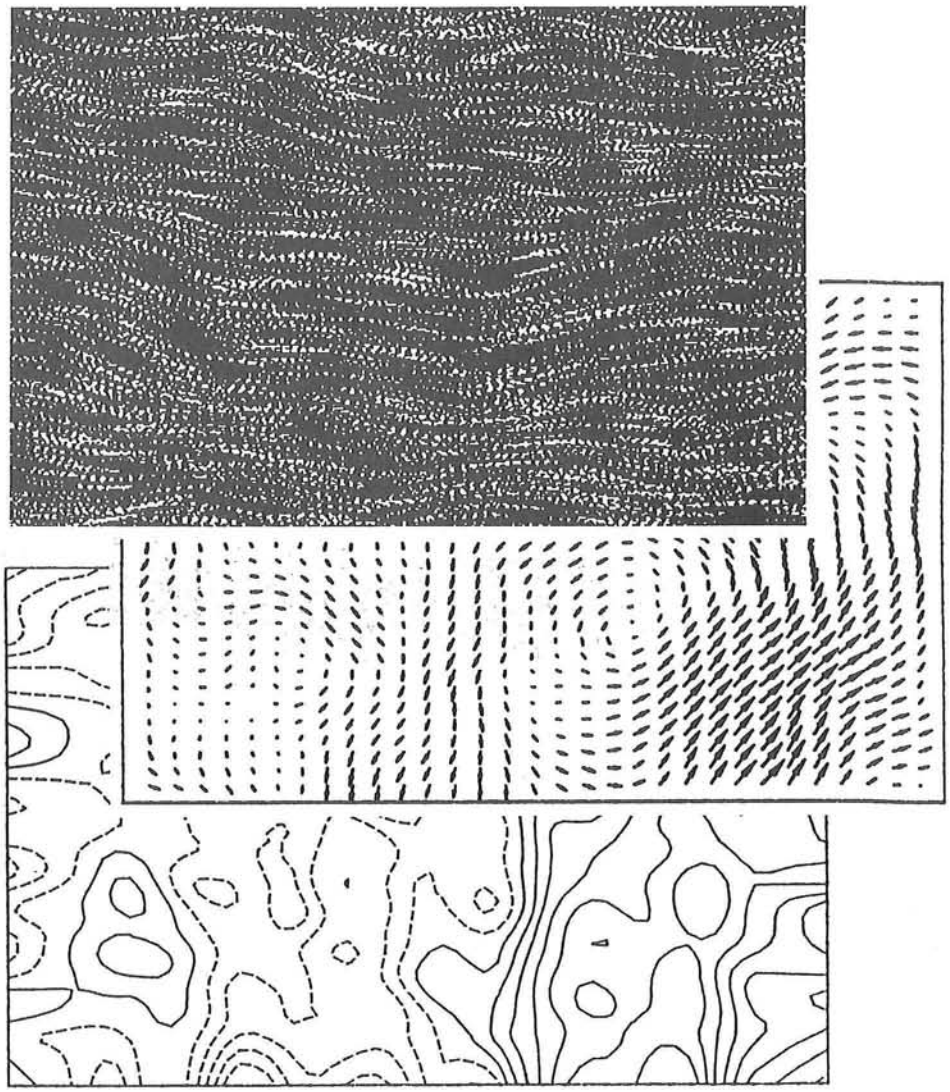

TU Delft

Delft University of Technology

[1] Articles and extended abstracts of the Euromech Colloquium 279, 2-5 July 1991, J.M. Burgers Centre, Delft University of Technology, Delft, the Netherlands

Image Analysis
as
Measuring Technique in Flows

Invited Lectures and Extended Abstracts
of the Euromech Colloquium 279

2-5 July 1991
J.M. Burgers Centre
Lab. Aero and Hydrodynamics
Delft University of Technology
Rotterdamseweg 145
2628 AL Delft

Sponsors

Akzo
Delft Hydraulics
D.S.M. Research
Min. of Transport and Public Works
Shell Nederland B.V
Dantec
Deltalab
Kluwer Academic Publishers
Philips Research
T.S.I.

Colloquium chairmen
prof.dr.ir. F.T.M. Nieuwstadt and prof.dr. M.L. Riethmuller

Local Organizing Committee

ir. J.M. Bessem	H.J. van der Brugge-Peeters	C.J.A. van Leeuwen
M. Oemar-Gemerts	P. Baan Hofman	ir. J. Westerweel

Program
EuroMech Colloquium 279
Image analysis as measuring technique in flows

Tuesday 2 July. PIV – methods : techniques and applications

Chairman: **F.T.M. Nieuwstadt**

08.30-09.30 registration and opening

09.30-10.00 Invited lecture: Past and Future of PIV
R. Meynart
European Space Agency, the Netherlands

10.00-10.50 Invited Lecture: Recent advances in the application of PIV (Particle Image Velocimetry), LSV (Laser Speckle Velocimetry) and PTV (Particle Tracking Velocimetry)
L. Lourenço
Florida State University, USA

10.50-11.10 Coffee

11.10-11.35 Stochastic optimization of processing techniques for PIV
C.S. Moraitis and M.L. Riethmuller
Von Karman Institute for Fluid Dynamics, Belgium

11.35-12.00 Development of particle image velocimetry: a new computation method with directional resolution
P. Guibert, M. Murat, Q.C. Dudan and J. Julien
Université de Paris, France

12.00-12.25 An automatic evaluation system for PIV record and specklegrams based on transputers
H. Wintrich and W. Merzkirch.
University of Essen, Germany

12.00-14.00 Lunch

Chairman: **R. Meynart**

14.00-14.25 A PIV system for application in transsonic wind tunnels
J. Kompenhans and R. Höcker
DLR Götingen, Germany

14.25-14.50 An experimental comparison between optical and digital particle velocimetry
J.M. Cornelisse, H.W.H.E. Godefroy, F. Koopmans, R.E. Uittenbogaard and J. Westerweel
Delft Hydraulics, the Netherlands

14.50-15.15 Particle image velocimetry at T.U. Denmark
P. Buchhave and M.L. Jakobsen
Technical University of Denmark, Denmark

15.15-15.40 A 3D PIV system and its aplication to the measurement of acoustic streaming
P. Arroyo, C. Greated and D. Hahn
Stanford University, USA

15.40-16.00 Tea

16.00-16.25 Investigation of turbulence structure using imaging methods
R.J. Adrian, P.W. Offutt and C.E. Wark
University of Illinois, USA

16.25-16.50 Application of digital particle image velocimetry to turbulent flows
J. Westerweel, C. Elgaard and F.T.M. Nieuwstadt
Delft Universty of Technology, the Netherlands

16.50-17.15 Application of particle image displacement velocimetry to industrial flows
S. Arefi, M. Chanconne, B. Broussouloux and M. Moine
Centre Technique des Industries Aerauliques et Thermiques, France

17.30-18.30 Cocktail party

Wednesday 3 July. PIV and Particle Tracking : techniques and applications

Chairman: **H. Royer**

09.00-09.50 Invited Lecture: Theory and priciple of PIV (Particle Image Velocimetry) methods
R.J. Adrian
University of Illinois, USA

09.50-10.15 Development and potential of a photogrammetric 3-D particle tracking velocimeter
H.G. Maas and Th. Dracos
Swiss Federal Institute of Technology, Switzerland

10.15-10.40 PIV technique in the turbulent intensity and space derivative evaluation
A. Cedenese and G.P. Romano
Università degli Studi di Roma, Italy

10.40-11.00 Coffee

11.00-11.25 A colored method for PIV technique
J. Stefanini, G. Cognet, J.C. Vila, B. Merite
CEA-Cadarache, France

11.25-11.50 A camera for measuring density, size and velocity of rising air bubbles and water velocity in a bubble plume
A. Müller and C. Hugi
Swiss Federal Institute of Technology, Switzerland

11.50-12.15 Time varying turbulence: some particle tracking experiments
S. Dalziel
University of Cambridge, Engeland

12.15-12.40 Stereometry in studies of friction wakes
A.A. Borisov, B.G. Novikov and V.D. Fedosenko
Institute of Thermophysiks, Novosibirsk, USSR

12.40-14.00 Lunch

Chairman: **R.J. Adrian**

14.00-14.25 Coherent structures in two-dimensional flow: measurement and results
J.B. Flōr and C.W.M. Williams
Eindhoven University of Technology, the Netherlands

14.25-14.50 Particle image velocimetry measurements of the aerodynamics of a wind turbine
I. Grant, G.H. Smith, A. Liu, D. Infield, T. Eich
Heriot-Watt University, Scotland

14.50-15.15 A critical analysis of particle image velocimetry technique as applied to waves on beaches
P.A. Quinn, C. Gray, D.J. Skyner, C.A. Greated and W.J. Easson
Edinburg University, Scotland

15.15-15.30 Tea

15.30-17.00 Excursion

Thursday 4 July. Scalar fields and data analysis

Chairman: **L. Lourenço**

09.00-09.50 Invited Lecture: Visualization methods for fluid flow data sets
L. Hesselink
Stanford University, USA

09.50-10.15 Digital Image processing for Schlieren optics
G.H. Schnerr, R.R. Huber and H.A. Jantzen
University of Karlsruhe, Germany

10.15-10.40 A study of pressurized gas release by laser induced fluorescence and image analysis techniques
S.G. Bryce and R.J. Fryer-Taylor
Shell Research Thornton, England

10.40-11.00 Coffee

11.00-11.25 Applications of an automated PIV and post-processing techniques system
T. Bruce, C. Elgaard and D.R. McCluskey
University of Edinburgh, Scotland

11.25-11.50 Determination of velocity - concentration correlations by Particle image velocimetry and laser induced fluorence imaging
S. Simoens and M. Ayrault
Ecole Centrale de Lyon, France

11.50-12.15 An application of image processing methods to determine the critical shear stress in sewer systems
W. Bechteler, V. Baier and S. Hartmann
University of the Armed Forces Munich, Germany

12.15-12.40 Study of vortex multiples in a stratified fluid by particle displacement analysis
S.I. Voropayev and Ya.D. Afanasyev
Institute of Oceanology, Acad. of Sci., USSR

12.40-14.00 Lunch

Chairman: **L. Hesselink**

14.00-14.25 Laser tomography of a buoyant turbulent diffusion flame
G. Wheater and K.N. Bray
Cambridge University, England

14.25-14.50 Measurement of product concentration fluctuations of two parallel reactive jets using digital image processing
H. Stapountzis, J.M. Bessem, F.T.M. Nieuwstadt and J. Westerweel
University of Thesssaloniki, Greece

14.50-15.15 New processing techniques for fluid velocity measurements by laser tomography
T. Fournel, M.J. Laboure, M.C. Hoyez, J.C. Monnier, J. Pigeon and J.P. Schon
Université de St Etienne, France

15.15-15.35 Tea

15.35-17.00 **Poster session**

19.30-21.30 Conference Dinner

Friday 5 July. Holographic Techniques

Chairman: **M.L. Riethmuller**

09.00-09.50 Invited Lecture: Contribution of microholography to 3-D flow measurements
H. Royer
Institut Saint-Louis, France

09.50-10.15 Optical processing of in-line and off-line holograms for 3D instantaneous velocity measurements
C.S. Moraitis and M.L. Riethmuller
von Karman Institute for Fluid Dynamics, Belgium

10.15-10.40 Digital processing of multipass holograms
R. Deron
Office National d'Etudes et de Recherches Aerospatiales, France

10.40-11.05 Extension of particle image Velocimetry (PIV) to a 3-D measuring method
H. Hinrichs, K. Hinsch, G. Kuhfal and P. Meinlschmidt
Carl-von-Ossietzky University, Germany

11.05-11.30 Coffee

11.30-11.55 Particle detection criteria for automatic data reduction from micro-holograms
M. Stanislas, C. Geiler, H. Royer, M. Courbon, J. Azema and J. Danieres
Institut de Mecaniques de fluides, Lille, France

11.55-12.20 Algorithms for automatic meaurement of size and velocity of spray droplets from holographic reconstructions
A. Chavez and F. Mayinger
Technische Universtät München, Germany

12.20-12.45 Digital holographic interferometry in the investigation of unsteady flows
T.A.W.M. Lanen
Delft University of Technology, the Netherlands

12.45-13.45 Lunch

POSTERS

Characterizition of Savonius rotor wake using image processing techniques
J. Massons, Jna. Gavaldà, J. Escoda, X. Ruiz and F. Diaz
University of Barcelona, Spain

Flow experiments and visualization in a hydrostatic journal bearing
M.J. Braun and R.C. Hendricks
University of Akron, USA

LSV applied to the flow in a rotating channel
S. Uellner
Technische Hochschule Darmstadt, Germany

An automatic image analysis method for determining each sense of velocity vectors using a path line picture
K. Hojo
Osaka Institute of Technology, Japan

Unsteady flows velocity field restoration by a specific digital image processing
P. de Ramefort, A. Texier and M. Coutanceau
Université de Poitiers, France

Use of fractal analysis in turbulent flows
J.M. Redondo
Universitad Politechnica de Catalunya, Spain

Investigation of the free edge of an unsteady axisymmetric turbulent jet
F.Z. Lahbabi, J. Boree, H.J. Nuglisch and G. Charnay
Institut Mecaniques des Fluides Toulouse, France

Study of horizontal jet in a stratified fluid using thymol blue velocimetry and weak disturbance propagation method
S.I. Voropayev and Y.D. Afanasyev
Institute of Oceanology, Acad. of Sci., USSR

A comparative study of optical autocorrelators for PIV
C.S. Moraitis and M.L. Riethmuller
von Karman Institute for Fluid Dynamics, Belgium

Detection of low speed streaks over a drag reducing surface
A.D. Schwarz-van Manen, H.P. Sparidans, K. Krishna Prasad, F.T.M. Nieuwstadt
Eindhoven University of Technology, the Netherlands

Digital image processing for the analysis of hydrogen-bubble time-line visualizations in a turbulent boundary layer
A.J. Brand and F.T.M. Nieuwstadt
Delft University of Technology, the Netherlands

Analysis of a bubbling 2D-gas-fluidized bed using Image Processing
H.B.M. Schulte, R.F. Mudde, H.E.A. van de Akker
Delft University of Technology, the Netherlands

Determination of flow profiles in the die-region of an extruder
F. Buitendijk
Koninklijke/Shell Laboratory Amsterdam, the Netherlands

Collision of two dipolar vortices in a stratified fluid studied by digital PIV
J.B. Flōr, J. Westerweel and C.W.M. Williams
Eindhoven University of Technology/Delft University of Technology, the Netherlands

Oil film interferometry; An optical method of measuring wall shear stress
H.A. Siller, R.J. Perkins and G. Janke
DAMPT, University of Cambridge, England

Invited lectures

Past and Future of PIV

Roland Meynart

European Space Agency - European Space Research and Technology Centre
Instrument Technology Division
2200 AG Noordwijk - The Netherlands

The historical development of the technique known under the names Laser Speckle Velocimetry or, more recently, Particle Image Velocimetry will be described and illustrated by examples and results dating back to the early times when only a few "pioneers" were believing in the potential capabilities of this technique.

It will be shown how the technique inherited from the so-called speckle techniques of stress analysis in solid mechanics and why the analysis of optical fringes for data reduction in place of direct inspection of the recorded images was considered as a major advance.

Various types of flows (Poiseuille and convection flows, gas jets) were used in the first years to validate the technique and show how it can provide whole-field velocity information difficult or sometimes impossible to obtain by other techniques.

The inherent limitations of the technique due to basic physical principles will be covered as well as the rapidly improving hardware limitations. The importance of optimum recording of the particle field images will be emphasized.

Finally, the prospects of improvement of the technique will be outlined, with particular attention drawn to the applications of the technique. Two examples of experiments considered by the European Space Agency for possible implementation in the International Space Station will be shortly described: a multi-purpose facility for the study of the structure of liquid flows and a combustion flow diagnostics facility.

Title: Recent Advances in LSV, PIV and PTV
Author : L. Lourenco

Paper to be presented at the EuroMech Colloquium 279
Delft 2-5, July, 1991

1. Introduction

Whole field velocimetry techniques such as Laser Speckle (LSV) Particle Image (PIV) and Particle Tracking Velocimetry (PTV) are different implementations of the same basic principles measuring instantaneous fluid velocities by recording the position of images by small tracers suspended in the fluid at successive time instants. The common underlying assumption is that these tracers follow closely, and with minimal lag, the fluid motion. This assumption holds true for a wide variety of flows of interest provided that the tracers are small enough and/or that their density approaches that of the fluid.

Besides their common goal LSV and PIV, on one hand, and PTV on the other hand do not share the same historical development and practice. An important difference is that in LSV and PIV, which have been established as two operating modes of the same method (Meynart and Lourenco, 1984) and (Adrian, 1984), the concentration of tracers is rather high and the measurement of a "local" fluid velocity results from an average over many tracers contained in a interrogation cell. The cell is regularly spaced and its size determines the spatial resolution. This is in contrast with PTV were the velocity is determined at random locations using the images produced by a single tracer.

Particle Tracking Velocimetry has evolved as a means of extracting quantitative information from conventional flow visualization data, such as streak photography or multiple exposure photography (Elkins et al, 1977), (Kobayashi et al, 1983), (Utami and Ueno, 1984) and (Gharib et al, 1985). While these methods excel as a means for fast and easy mapping of the flow basic structures, they fail in providing an accurate velocity field map with high spatial density. Typically the evaluation of the particulate displacements directly from their images, such as evaluating streak length or spacing between successive images of the same tracer, requires processing large amounts of data and rather sophisticated software. These techniques tend to be quite laborious and usually not very accurate, as the measurement errors become large when the mean distance between tracers is of the same order of magnitude of the streak length, or the spacing between successive particle images, and/or these become small. As a consequence the tracer density is kept small, resulting in velocity measurements with poor spatial resolution. The problem of having sparse velocity information at random locations has been addressed with the introduction of rather sophisticated interpolating schemes, but the validity of this approach is questionable considering that is most cases the spacing between data points is larger than the flow

scales, and the velocity may be interpolated at best with first order accuracy.

LSV and PIV offer a valid alternative to the more conventional PTV methods because of their ability to provide higher temporal and spatial resolution of the instantaneous flow field. These two techniques are based on essentially the same principles and method of operation with exception to the amount of seeding employed. Meynart and Lourenco (1984) argued that best results are obtained when the particle concentration is kept as high as possible as to ensure a maximum number of particle images in an interrogation cell but not so high to overlap and generate speckle. Generation of speckle patterns is not desirable in most applications due to dependence of the speckle formation with the fluid motion. Other reasons to limit the concentration are related to the degradation of the light sheet propagation and possible interference with the mechanics of the fluid motion.

In this article the application of the PIV technique to the study of practical flow fields is used as a means to illustrate both the techniques ability to map spatially and temporally developing flows, as well as the most recent features incorporated in the technique.

2. Application of PIV to the measurement of an unsteady flow:
Pitching NACA airfoil.

The unsteady flow past a NACA 0012 airfoil in pitching up motion is experimentally investigated in a water towing tank using the Particle Image Velocimetry technique. The Reynolds number, based on the airfoils chord and the freestream velocity, is 5000. The airfoil pitching motion is from 0 to 30 degrees angle of attack at a dimensionless pitching rate of 0.131.

The water towing tank facility is 180 cm long and 43x55 cm in cross sectional area. The towing carriage is driven by a D.C. and has a speed which varies from 0.3 to 30 cm/sec. A motor speed control system controls the towing speed via a digital-to-analog converter. To ensure a smooth traverse of the towing carriage, an acceleration ramp at the beginning of the travel and a deceleration ramp at the end of travel are implemented on the controller. The NACA 0012 airfoil has a chord length of 6 cm and an aspect ratio of 6.67. A recording camera with a scanning mirror system are mounted on a reinforced, vibration free platform that extends from the airfoil carriage. The airfoil pitching motion is provided by a stepping motor with a programmable controller, which is pre-programmed with the test profile and activated by the host computer. The airfoil changes linearly from 0 to 30 degrees after the airfoil is towed more than one chord length. A DEC Vaxstation II computer monitors all motions (figure 1).

A dual pulsed laser system, consisting of two frequency doubled Spectra-Physics DCR 11 Nd-Yag pulsed laser systems is used to provide the double illumination pulses. A system of prisms and polarizing cube beam combiners make the light beams emitted from the two lasers collinear (figure 2). Time separation between the laser light pulses can be varied from a fraction of one microsecond to a few seconds by adjusting a pulse generator used as a trigger. A cylindrical lens is used to form the combined beam into a sheet that illuminates the mid-span section of the airfoil. Metallic coated particles (TSI model 10087), with an average diameter of 4 microns, are used as the flow tracers. A phase-triggered 35 mm camera (Nikon F-3) with a 105mm Macro lens is used in the recording of the flow field. Synchronization between components is accomplished using a Tektronix modular electronics system. This system also provides the phase-reference between the motion of the airfoil and the PIV photographic timing sequence.

Once the photographic film is processed contact prints are made. It has been shown by Meynart and Lourenco (1984) and Pickering and Halliwell (1984) that when using the Young's fringe approach to retrieve the displacement data this process increases the SNR and fringe visibility. These prints are used to obtain the velocity data by point wise scanning following a Cartesian grid. The step size of the scanning operation was chosen to be 0.5 mm in both directions; this corresponds to a step size of 1.25 mm in the physical plane. The interrogation beam diameter corresponds to an equivalent physical probe size of 0.625 mm, which is approximately half of the mesh size. The Young's fringes produced by the beam were digitally processed to produce the velocity at the interrogated point on the negative, and the vorticity was found by numerical differentiation.

As mentioned earlier, the airfoil is started with a ramp type motion at zero angle of attack and is allowed to move one chord length, after which the flow field is fully established with minimal effects of the starting process. Next the airfoil is impulsively given its pitching motion and allowed to pitch to 30 degrees angle of attack. During the pitch up motion the airfoil travels approximately four chord lengths. Once the pitch up motion stops the airfoil is allowed to travel for an additional four chord lengths before it comes to a complete stop. In the present experiments the airfoil pitches about its quarter chord point.

Figures 3 and 4 show the time development of the flow around the pitching airfoil using the PIV technique. Figure 3 presents the velocity field at different times as uniformly scaled velocity vectors. The corresponding

vorticity fields are presented as iso-vorticity contour plots in figure 4.

The essential component of the technique that makes it possible to measure complex flow fields, such as the one presented above is the velocity bias method. Due to limited range in the fluid velocity, about 20 cm/sec, the velocity bias method was successfully implemented in this experiment using a scanning mirror. However, the scanning mirror approach suffers from some restrictions. Firstly, it requires the motion of mechanical components and precise synchronization with the camera shutter and the laser illumination pulses. This makes the use of the mirror very unpractical, if not impossible, in cases when asynchronous recording of flow events is necessary, e.g. turbulent events, and when the required bias velocity magnitude exceeds the mirror's mechanical capabilities. Therefore the implementation of a passive velocity bias method which does not require the movement of mechanical components is very desirable.

A new method introduced by Landreth and Adrian (1988) uses the polarization of light scattered from seeding particles by switching the polarization of the illumination beam and placing a birefringent crystal, e.g. calcite, in front of the photographic lens to displace the particle image between illumination pulses. In the arrangement proposed by Landreth and Adrian a Pockels cell is used to rotate by 90 degrees the polarization of the laser output providing the illumination pulses. The method is quite effective provided that the most of the light scattered by the tracers retains its original state of polarization. This happens to be the case for the particles and recording optics geometries used in most current PIV applications.

There are, however, some inconveniences when using this method. The magnitude and orientation of the shift changes in the film plane, due to the fact that the light is collected from a large, finite view angle. Also, the shift amount for a given camera magnification cannot be changed unless the crystal thickness is varied or more than one crystal is used in series. In order to resolve these problems another shifting method using the light polarization effect was proposed by Lourenco (1989). The birefringent crystal is replaced by a polarizing beam splitter cube and two isolators (1/4 wave plate) arrangement (figure 5 a,b,c). The light paths for the light scattered by a particle having both the s and p polarization states are also illustrated. The principle of operation of the apparatus is as follows. Consider a stationary particle that is first illuminated by p-polarized light. The scattered beam travels through the cube undisturbed in its path and changes its state of polarization from p to s when it propagates through the 1/4 wave undergoes a total reflection and reverses it sense. Now having its state of polarization rotated by 90 degrees, the light beam is totally reflected

at the cube's interface and directed towards the camera objective. In contrast, if the light beam is s-polarized then it undergoes first a total reflection at the interface, followed by a change in its state of polarization while interacting with the 1/4 wave plate (figure 5b). It then proceeds through the cube and into the camera lens. Providing that the light paths have similar distances and that the 1/4 wave plates are parallel to the cube's surfaces, the image of the scattering seed will appear in the film plane at the same location. A uniform displacement (shift) can be generated by slightly tilting one of the 1/4 wave plates with respect to the cuber's surface. The amount of displacement is proportional to the angle of tilt (figure 5c).

This method is currently being used to examine both high and low speed flows. An example of its application while studying the transition region of a rectangular jet is given below.

3. Vortex interactions in the transition region of a rectangular jet

The transition region of a rectangular jet of aspect ratio 4 at a Reynolds number, based on the equivalent diameter, of 4500 was investigated. A low speed air supply system is used to flow air in a settling chamber 25 cm in length and 7.5 cm in diameter. A honeycomb and a series of screens at the inlet of the settling chamber were used to reduce the flow disturbances. The cross-section area of the nozzle contraction changes gradually from a circular cross-section, 7.5 cm in diameter, to a rectangular nozzle. The long (L) and short (W) dimensions of the nozzle are 3 cm and 0.75 cm respectively and streamwise contours of the contraction are fifth order polynomials. The contoured nozzle has a contraction ratio of 19.6:1 over a length of 1.6 times the inlet diameter. In order to obtain appropriate jet seeding, smoke particles in the micron range are produced. The smoke and the ambient air are mixed in a large mixing and settling chamber. The air smoke mixture is then supplied to the settling chamber of the jet using a small axial fan. A second smoke generator of the same type is used to seed the outside air surrounding the jet.

The laser sheet illuminates the central plane of the jet through the small dimension of the nozzle. Two laser pulses with a duration of 10 nsec and separation of 50 microseconds are used for the double exposure recording. The particle image doublets are recorded using the 35 mm camera with the 105 mm Macro lens. The camera is installed in an assembly containing the polarizing cube and 1/4 wave plates to obtain a shift during the recording. Photographs of the flow field were taken at random times. After development the photographs were analyzed using the Young's fringe method, and the velocity vectors were obtained on a Cartesian grid

(60x80). Using a central difference scheme, the instantaneous vorticity was obtained, with an estimated accuracy of 5%.

Typical double exposure photographs of the jet, for two different times, are shown in figure 6. The pictures display the flow field from the nozzle exit to a downstream location of 8 widths. From a number (about 500) of similar photographs the near field (X/W<20, where X is the downstream coordinate) of the jet can be characterized by three distinctive regions. The first region in which the initial shear layer is unstable and rolls up into discrete vortices; an interaction region in which two or more vortices interact with each other, and a region in which vortices break-up into three-dimensional motion.

Figure 7 shows a typical instantaneous velocity field corresponding to one of the double exposure photographs in figure 6. The results are shown after removal of the velocity bias. Using a central finite difference scheme the instantaneous vorticity and strain rates are calculated and shown in figure 7. Also included are the instantaneous Reynolds stresses. The results represent, with great fidelity, the aforementioned regions of the flow field.

4. Digital or "On-line" PIV

As demonstrated by the previous examples PIV is a superior tool for the diagnostics of flows that evolve both in space and time, as it is the only method capable of providing the researcher with flow field strain and vorticity information. However, the current bottleneck and difficulty in the utilization of the technique still remains the photographic step. This difficulty stems from the fact that before the double exposure frames can be analyzed there is one or two wet photographic processes involved, depending on whether or not contact prints of the original negatives are required to improve the data quality. This does not account for the fact that for proper and optimal operational use of the technique, quite a few photographic parameters (e.g. time between exposures, velocity bias amount) and seeding rates must be adjusted by trial and error. It is, therefore, desirable to develop an alternative approach that facilitates this set-up stage by making the image acquisition step less laborious and time consuming.

Several investigators, having recognized the above mentioned shortcomings, have proposed various methods of solution. Okada et al (1990) proposed the replacement of the photographic film by a liquid crystal televison (LC-TV). The double exposed photographs are recorded using a video camera and stored in a frame buffer for later display on the LC-TV. The velocity information is then retrieved using a point by point analysis method based on the Young's fringes approach. The current limitation if this approach is the limited

resolution of about 320x220 pixels of the LC-TV. An obvious variation of this method is the digital processing of the double images stored in memory. In 1989 Cho first formulated the theory associated with the digital counterpart of the Young's fringe analysis method. In his approach the double exposed digital image frames were obtained by digitizing single exposed video images and then adding successive frames. This method has also been implemented by Westerwell and Nieuwstadt (1990) who used such a technique to study the flow behind a circular cylinder. The major shortcoming of these methods is that they can only be applied to the measurement of slow moving flows and lack the resolution and accuracy of their analog counterparts. The limitation in velocity range is due to the fact that the image acquisition is tied to the timing of the video cameras (25 or 30 Hz); an additional timing problem is that not all the pixel elements are acquired at the same time, due to the video image scanning. Another implementation of the same idea was put in practice by Willert and Gharib (1991). The merit of their approach is that instead of adding togheter the individual frames to generate a double exposure image for processing using autocorrelation algorithms, the cross-correlation of successive images is carried out to obtain the displacement. As such, because the frames phase information is not lost, the technique provides displacements without directional ambiguity without the need to implement any other method like the velocity bias method.

The emphasis on the current PIV research at the Fluid Mechanics Research Laboratory at the Florida State University is mainly in the are of so-called "on-line" systems. These systems use non-standard video cameras togheter with high capacity frame digitizers and buffers for the acquisition and storage multiple exposed frames. Present capability allows the digitization of images in various levels of spatial resolution and area coverage. Available systems are the standard resolution (512x512 pixels), the high resolution (1280x1024 pixels) and the very high resolution (2048x2048 pixels). Processing of the digital frames is carried out using auto- and cross-correlation algorithms. Results are very encouraging and seen to indicate that at the present time some applications can be fully met using these easier to use systems. A brief presentation of one of such systems based on the standard resolution format (512x512 pixel) CID camera follows.

5.1 Hardware configuration

The multiple exposed frames are acquired by a CID video camera with a 512x512 pixel sensor. The square pixels are 15 microns on each side. Unlike commonly available RS-170 format commercial cameras which "scan" the images at a rate of 30 Hz this camera has the capability of grabbing extremely fast (strobed) scenes due to the fact that all the

pixels are illuminated and charged at the same time. The image read-out is performed in a sequential, non-interlaced fashion, at at rate of about 10 MHz, after which a new image can be acquired. The timing for image acquisition and read-out corresponds, approximately, a maximum image refresh rate of 30 Hz.

The non-interlaced CID camera output can be viewed directly by inputing this analog signal into a monitor equipped to handle the non-standard progressive scan format, or as shown in figure 8, as the input for a frame grabber/buffer combination board resident on a PC-AT type microcomputer. The frame grabber which allows for the input and digitzation of non-standard video formats, digitizes the image retaining its 512x512 resolution, square aspect ratio, and with 8 bits resolution of gray scale. The frame grabber board also has the capability to convert the digital frame information on one of its memory buffers into an analog video signal (RS-170 format) which is displayed in a conventional RGB video monitor. The system synchronization is acheived by means of an especially developed interface which ensures that the camera stays in the acquisition mode during the time the laser illumination pulses are fired, and in the read-out mode during the image acquisition phase by the frame grabber. Again with this arrangement a maximum number of 30 frames per second can be digitized and stored. The present on-board memory of the frame buffer allows for the storage of a maximum of 16 images. However, images can be transferred to the PC-AT hard disk for permanent storage and/or later processing. Another method available to acheive long record lengths of flow events is to record on a high quality super VHS type tape the analog video output of the frame grabber, for later playback and re-digitization. The incovinience of this approach is that some image degradation will occur.

Using this arrangement a variety of laser sources can be used without restriction. In the application described herein a CW laser with a Bragg cell as the shutter is used.

The processing of the multiple exposed frames is performed using the PC-AT microcomputer and an array processor in order to acheive computational efficiency and speed.

5.2 Processing of the digital frames and typical results

Using the hardware described in the previous section a whole field velocity measurement of the flow past a circular cylinder towed in a water tank has been carried out. The cylinder is 25.4 mm in diameter and is towed with a velocity of 2.5 cm/sec corresponding to a flow Reynolds number of approximatelly 600. The flow is seeded with 4 micron in diameter metallic coated particles and the F# number for the recording is 16. Consequently the particle image size is mostly dominated by diffraction effects and is evaluted to

be around 20 microns, i.e. just slightly above the pixel size. The magnification computed as the size of the sensor divided by the size of the scene being recorded is equal to .07. In order to resolve the ambiguity of the velocity vector a scanning mirror method was implemented in the recording of the frames.

Figure 9 is a typical example of a velocity field obtained after processing of the triply exposed frames, and removal of the velocity bias. This velocity map corresponds to the flow after the cylinder has been impulsiveley started from rest and moved 3 diameters. Analysis of this figure reveals that with this technique it is possible to map the velocity field with reasonable detail and accuracy.

Point by point processing of the multiple exposed frames is accomplished using an autocorrelation algorithm. The frames are divided into interrogation cells 16, or multiples of 16, interrogation cells in both the vertical and horizontal axis. The aspect ratio of this pixels need not be square and may be changed to accomodate flows with a dominant velocity component. The digital autocorrelation in two dimensions of the particle image doublets is performed using a FFT algorithm. The algorithm is implemented using the array processor and allows for the entire processing of a full frame image containing about 1000 vectors in just 4 minutes. Figure 10 is autocorrelation map from one of such interrogation cell. The off-center peek location of this autocorreltion array corresponds to the average displacement of the tracer images contained in the interrogation cell. An interpolation algorithm is implemented in order to acheive sub-pixel resolution for the evaluation of the peek location. Discrimination between a valid measurement and spurious data (e.g.,cylinder wall, drop-out regions without seeding) is performed by comparing the amplitudes of the three most important peeks in the correlation array, including the zero order peek.

The accuracy of the technique was evaluated first by means of a simple experiment. A uniform flow was generated towing the carriage of the towing tank with constant velocity. This flow was recorded using the "On-line" PIV arrangement, while changing the time between exposures and the number of exposures according to the schedule presented in table 1. Also included in the table are the results of the average displacement measured in pixels and the corresponding rms. The average displacement and rms were determined averaging the results of about 1000 interrogations per frame. A measure of the techniques' accuracy is obtained comparing the variation of carriage velocity measured as the ratio of pixel displacement divided by the time between exposures. This measurements are within 1% to 1.5% of each other. Another measure of the technique's

accuracy is given by the scatter of the measurement in terms of its rms. The scatter does not exceed .1 pixels. The reasons for this surprisingly high accuracy will be discussed in a forthcoming publication.

6. Conclusions

Whole field measurement techniques, in particular PIV, have demonstrated the ability to record the instantaneous velocity field with accuracy comparable to that of LDV while retaining its non-invasive nature. The development of special recording techniques, such as the velocity bias make it possible to measure complex flows and within wide ranges in velocity. The most noteworthy development is, in the authors' opinion, the introduction of video techniques as means of not only eliminating the wet photographic processing stage, but also to provide the operator with an almost real-time capability of data access. Due to the introduction of higher resolution cameras, e.g. 2048x2048 pixel format, these systems are undergoing rapid development, and at the present stage can replace in quite a few applications the 35 mm format camera without loss of accuracy and spatial resolution.

References

Adrian, R.J.
Applied Optics, vol 23, 1984

Cho, Y. C.
Applied Optics , vol 28, 1989

Elkins, R.E. et al
Rev. Sci. Instr., vol 48, 1977

Gharib, M et al
AIAA paper 85-0172

Kobayashi, T. et al
Proc. Int. Symp. Flow Vis., Ann Harbor, Michigan, 1983

Landreth, C. C. and Adrian R.J.
Applied Optics, vol 27, 1988

Lourenco, L.
Bulletin of APS, 1989

Meynart, R. and Lourenco, L.
VKI Lecture Series, 1984

Okada, E. et al
Proc. App. Laser Vel. Fluid Mech., Lisbon, Portugal, 1990

Pickering, C. J. and Halliwell, N. A.
Applied Optics, vol 23, 1984

Utami, T. and Ueno, T.
Exp. in Fluids, vol 2, 1984

Westerwell, J. and Nieuwstadt, F.T.
Proc. App. Laser Vel. Fluid Mech,, Lisbon, Portugal, 1990

Willert, C. E. and Gharib, M.
Exp. in Fluids, vol 10, 1991

Yao, C. S. and Adrian R. J.
Applied Optics, vol 23, 1984

Table 1 : Time between exposures vs displacement

Time (msec)	Number of exposures	Average displ(pixels)	Rms displ(pixels)
10	2	3.21	.089
	3	3.36	.078
	4	3.24	.075
15	2	5.02	.095
	3	5.06	.074
	4	5.07	.064
20	2	6.99	.120
	3	7.01	.061
	4	7.05	.079
30	2	10.77	.139
	3	10.87	.133
	4	10.76	.170
40	2	12.32	.146
	3	12.56	.127
	4	12.29	.137

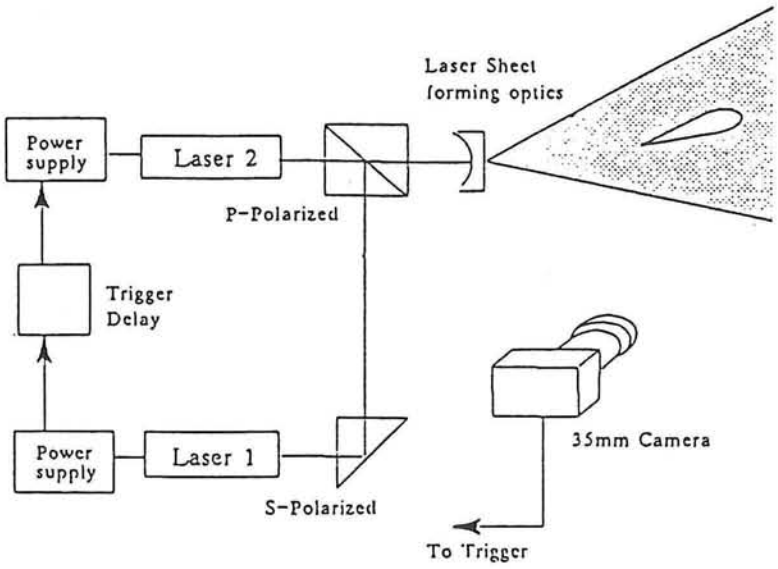

Figure 1: Schematic arrangement for the dual pulse laser system

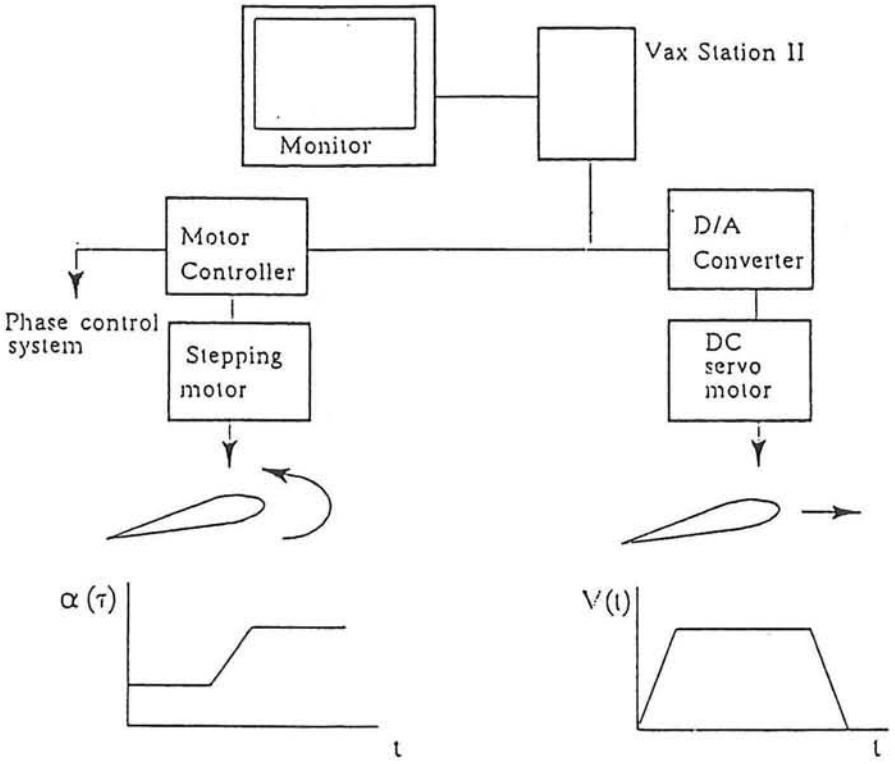

Figure 2: Schematic of the airfoil's motion control system

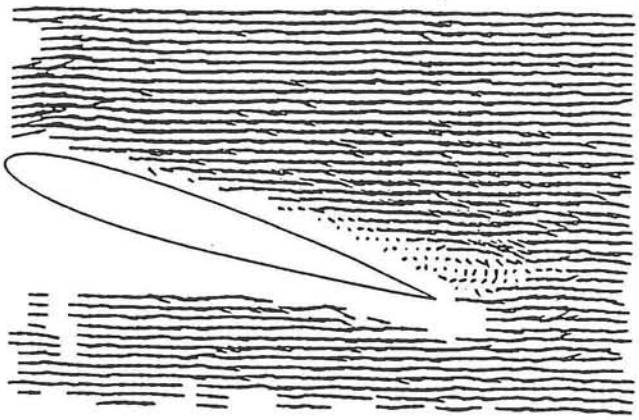

(a) $t\ U_\infty/C=2.56,\quad \alpha=19.2$ deg.

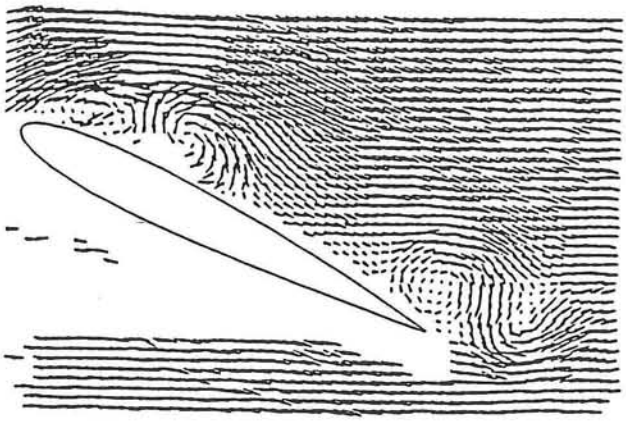

(b) $t\ U_\infty/C=3.84,\quad \alpha=28.8$ deg.

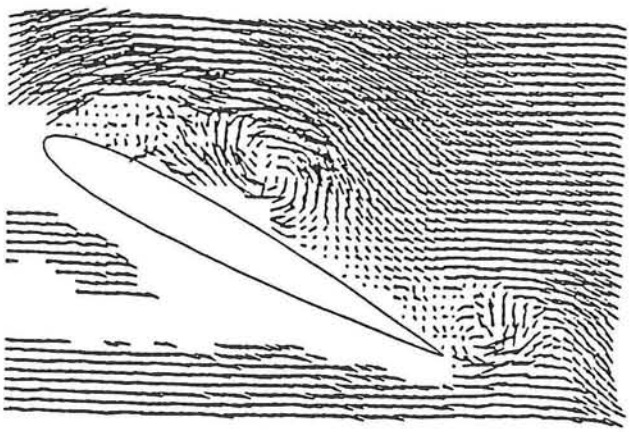

(c) $t\ U_\infty/C=4.70,\quad \alpha=30.0$ deg.

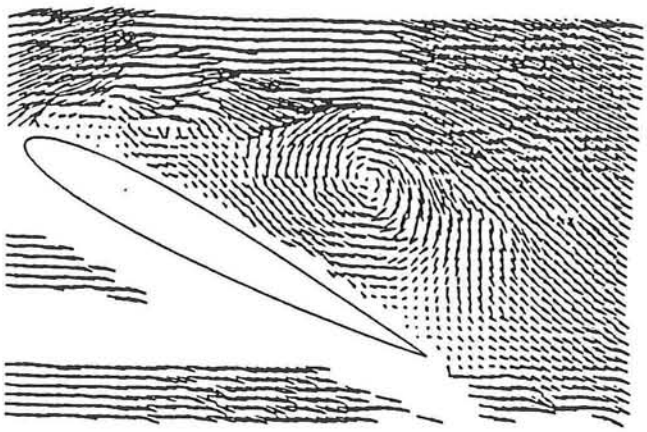

(d) $t\ U_\infty/C=5.13,\quad \alpha=30.0$ deg.

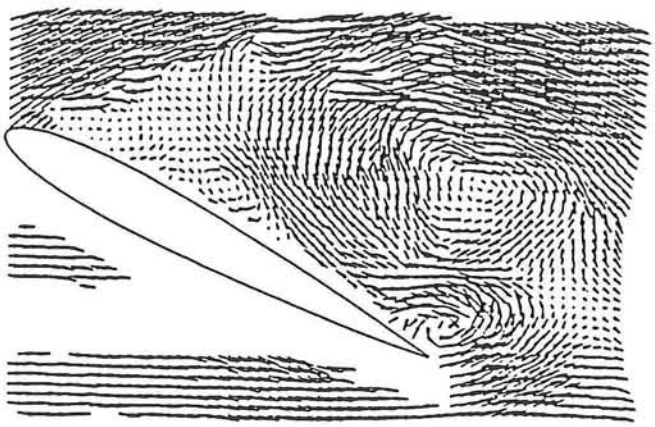

(e) $t\ U_\infty/C=5.99,\quad \alpha=30.0$ deg.

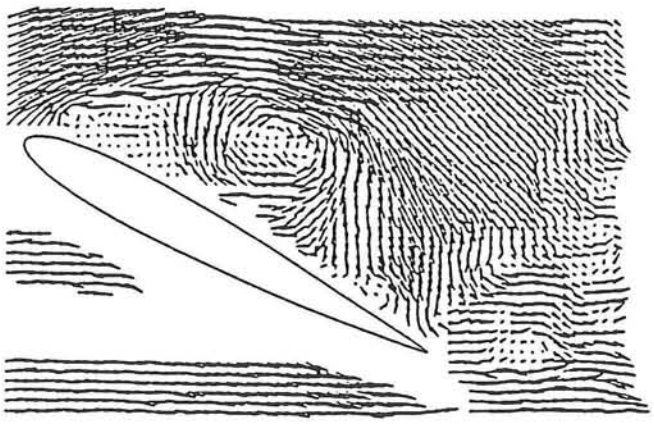

(f) $t\ U_\infty/C=8.56,\quad \alpha=30.0$ deg.

Figure 3: Velocity map of flow past NACA 0012

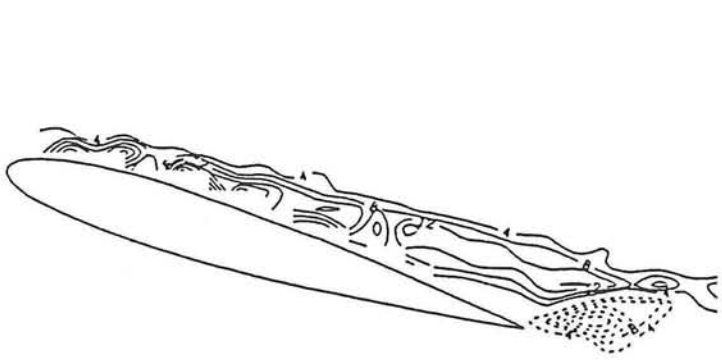

(a) $tU_\infty/C = 2.56$

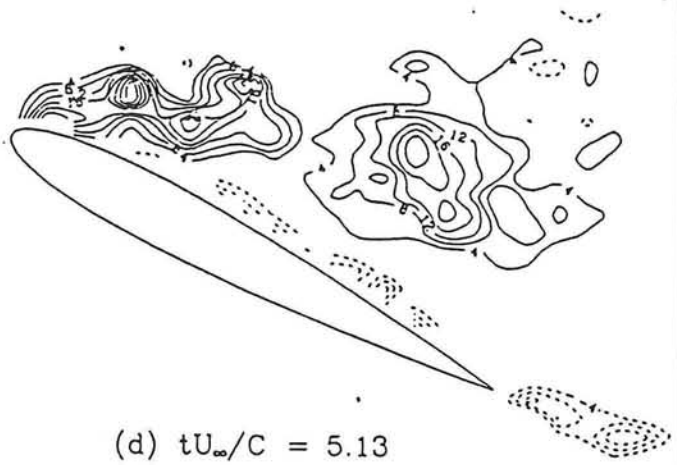

(d) $tU_\infty/C = 5.13$

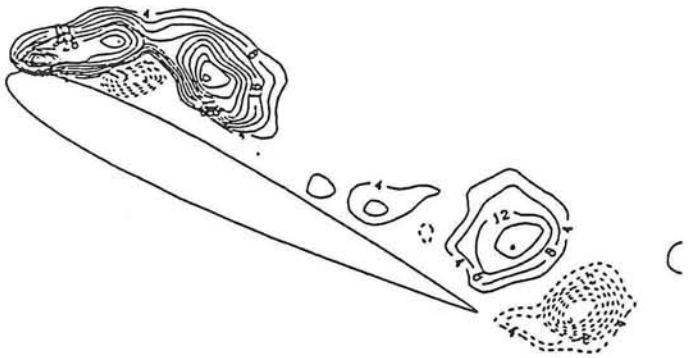

(b) $tU_\infty/C = 3.84$

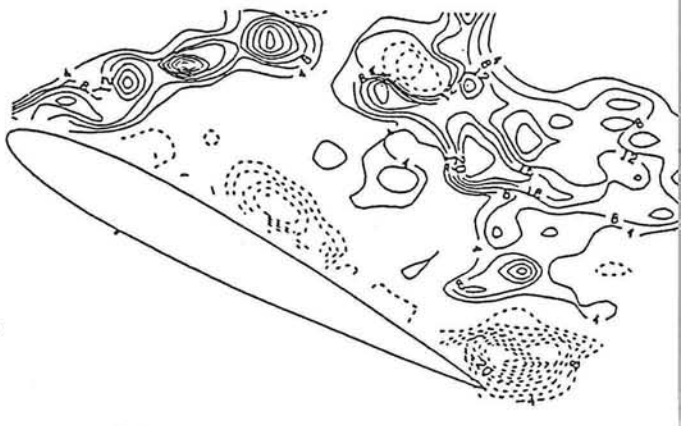

(e) $tU_\infty/C = 5.99$

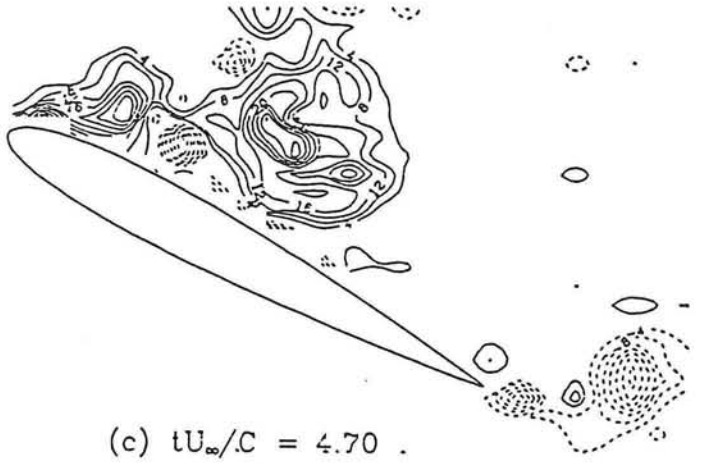

(c) $tU_\infty/C = 4.70$

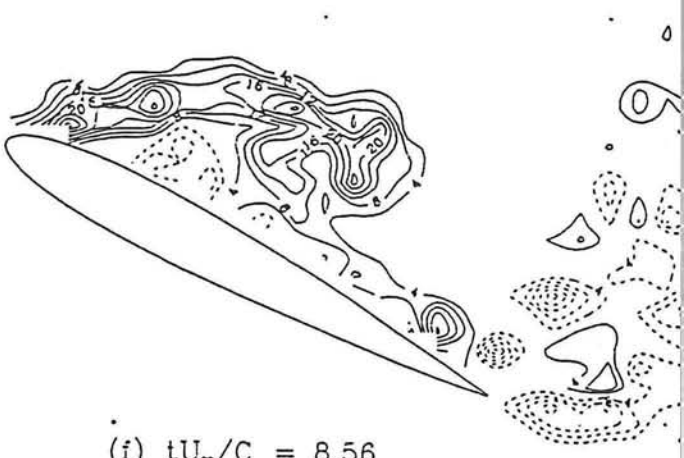

(f) $tU_\infty/C = 8.56$

Figure 4: Vorticity map of flow past NACA 0012

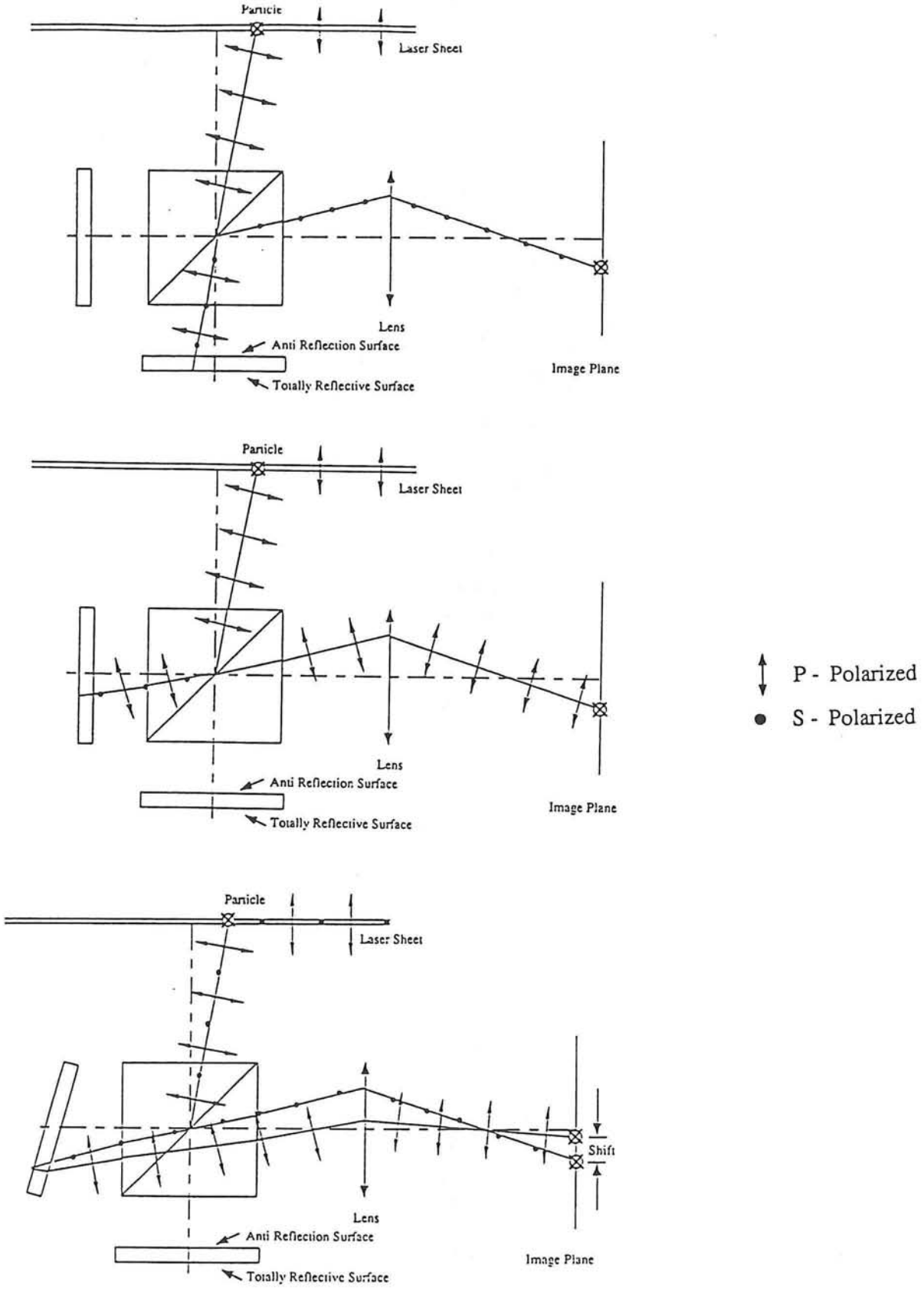

Figure 5: Velocity Bias: beam splitter/isolators arrangement
a) p-polarized light path
b) s-polarized light path
c) operation for velocity bias

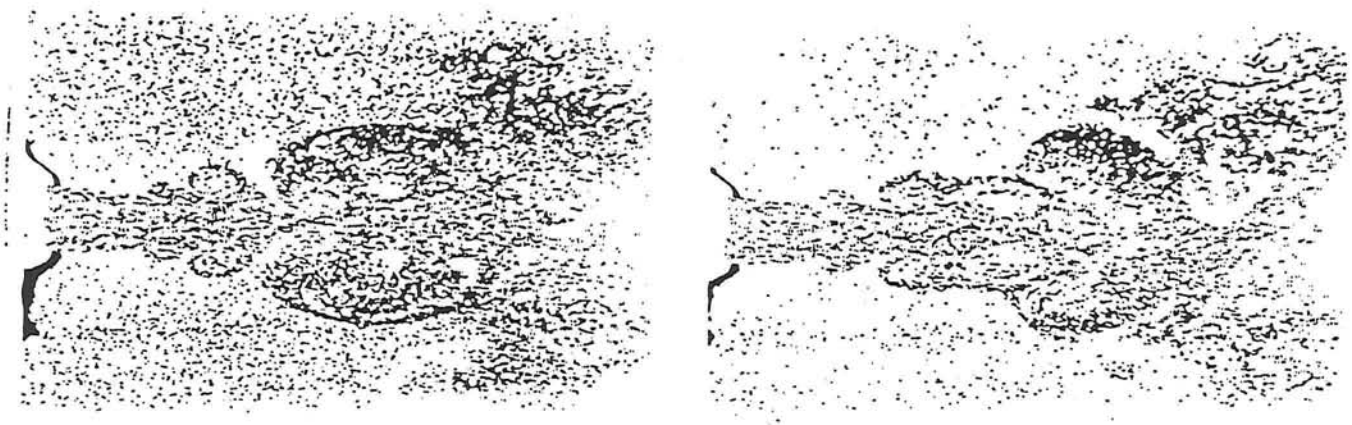

Figure 6: Instantaneous double exposure photographs of the central plane containing the small dimension of the nozzle

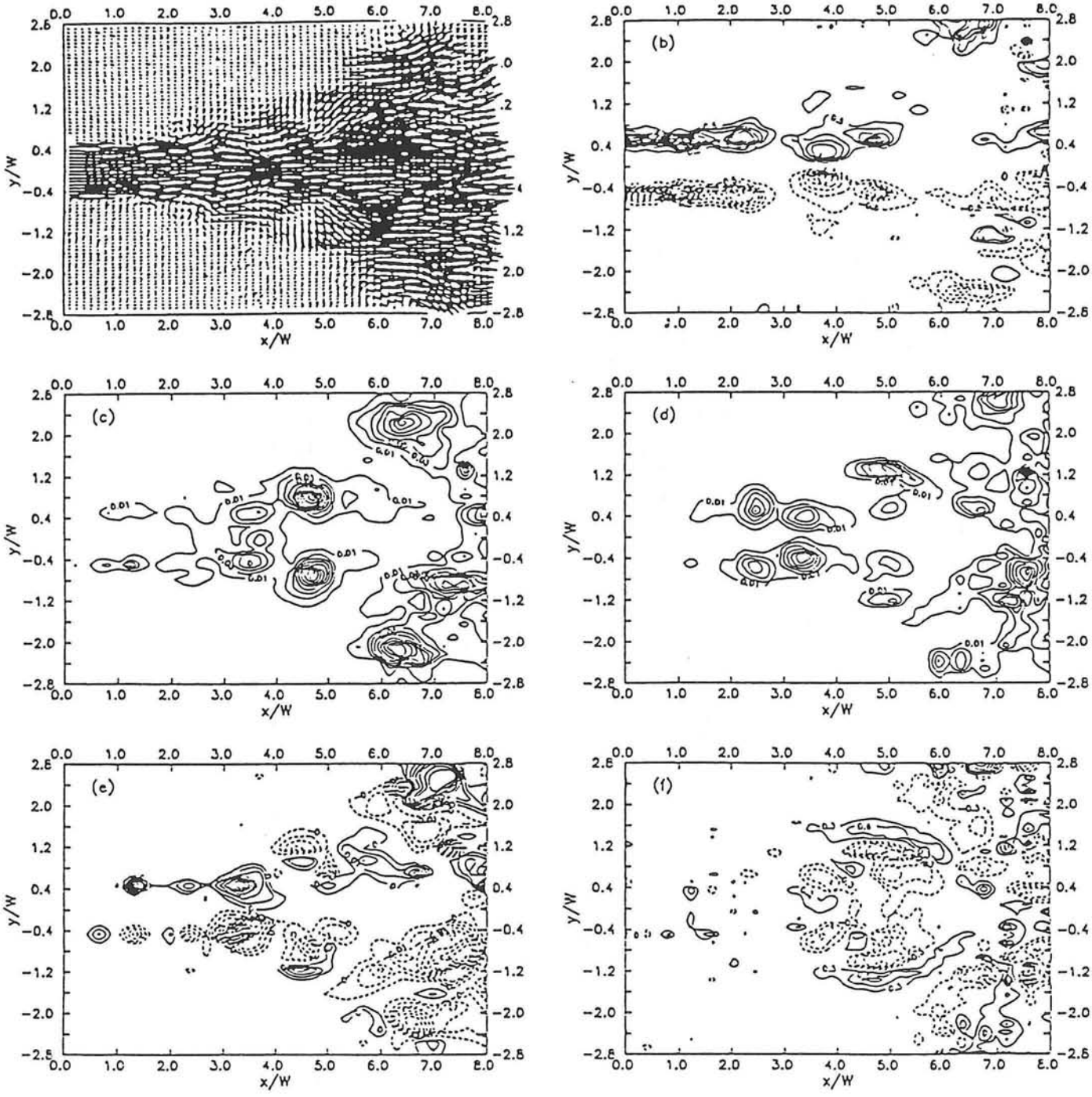

Figure 7: Instantaneous quantities corresponding to the photograph in figure 6a.
a)Two-dimensional velocity field, b)Normalized velocity field, c)$\frac{u'^2}{U_e^2}$, d)$\frac{v'^2}{U_e^2}$, e)$\frac{u'v'}{U_e^2}$, f)$\frac{\partial W}{\partial z}$

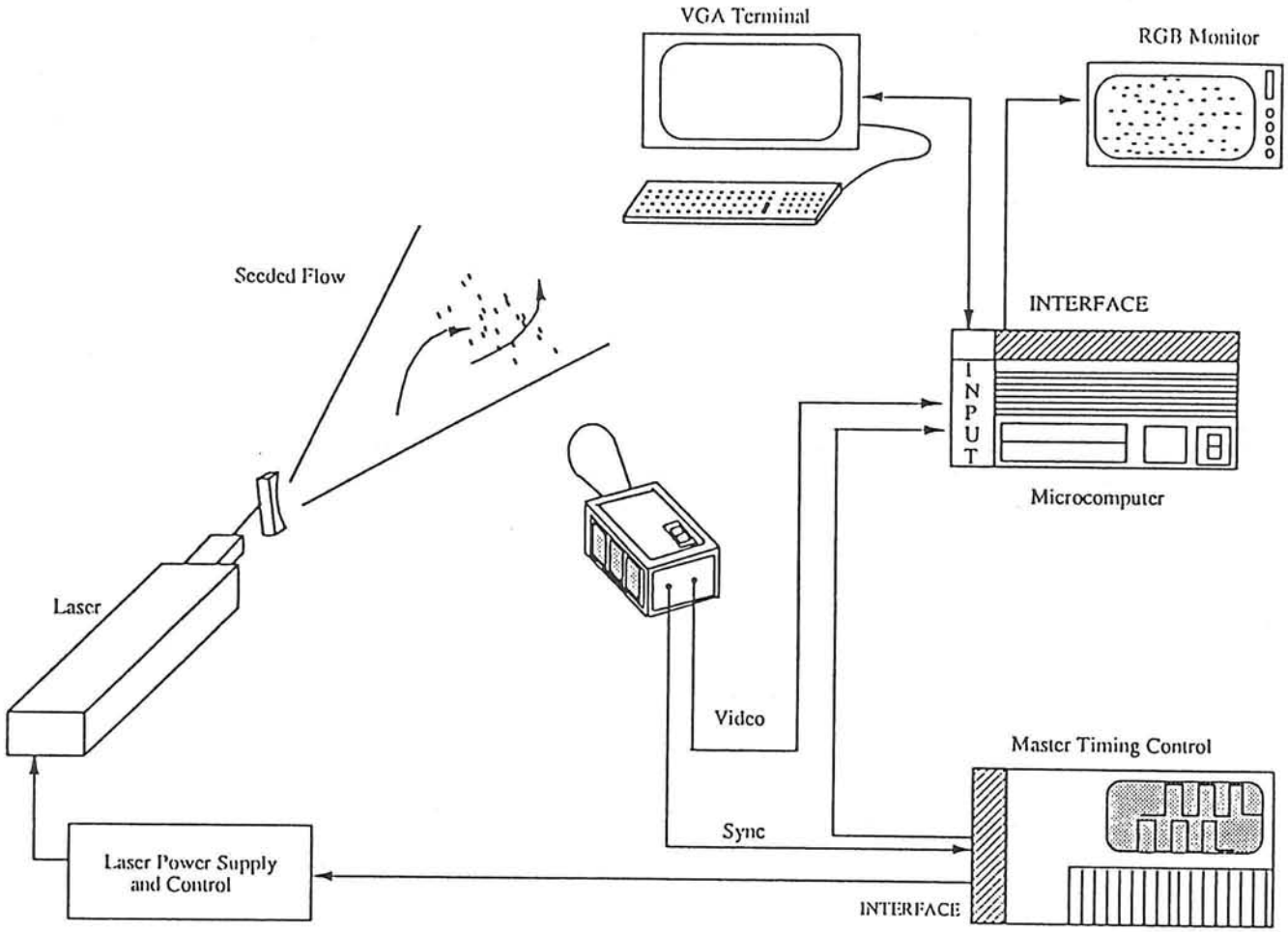

Figure 8: Schematic for "On-line" PIV

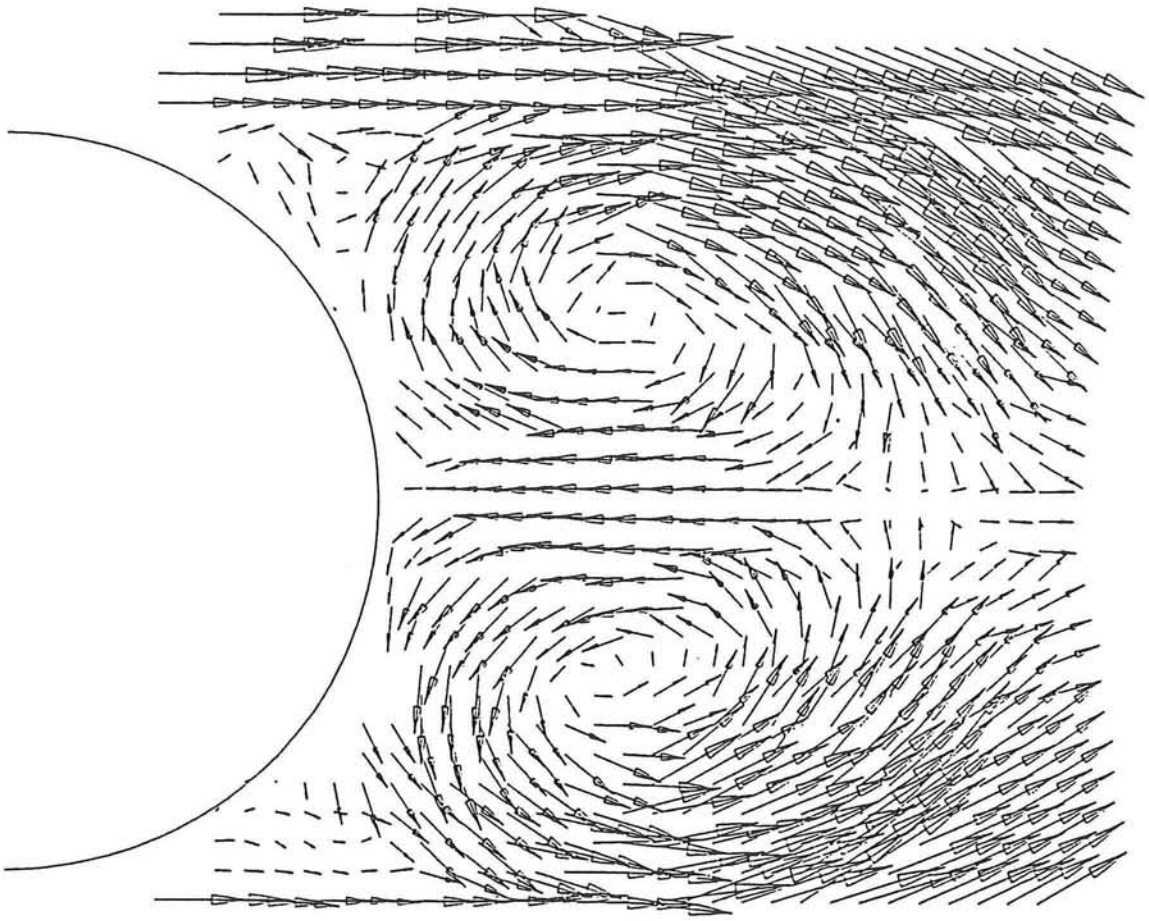

Figure 9: Velocity field for flow past impulsively started circular cylinder

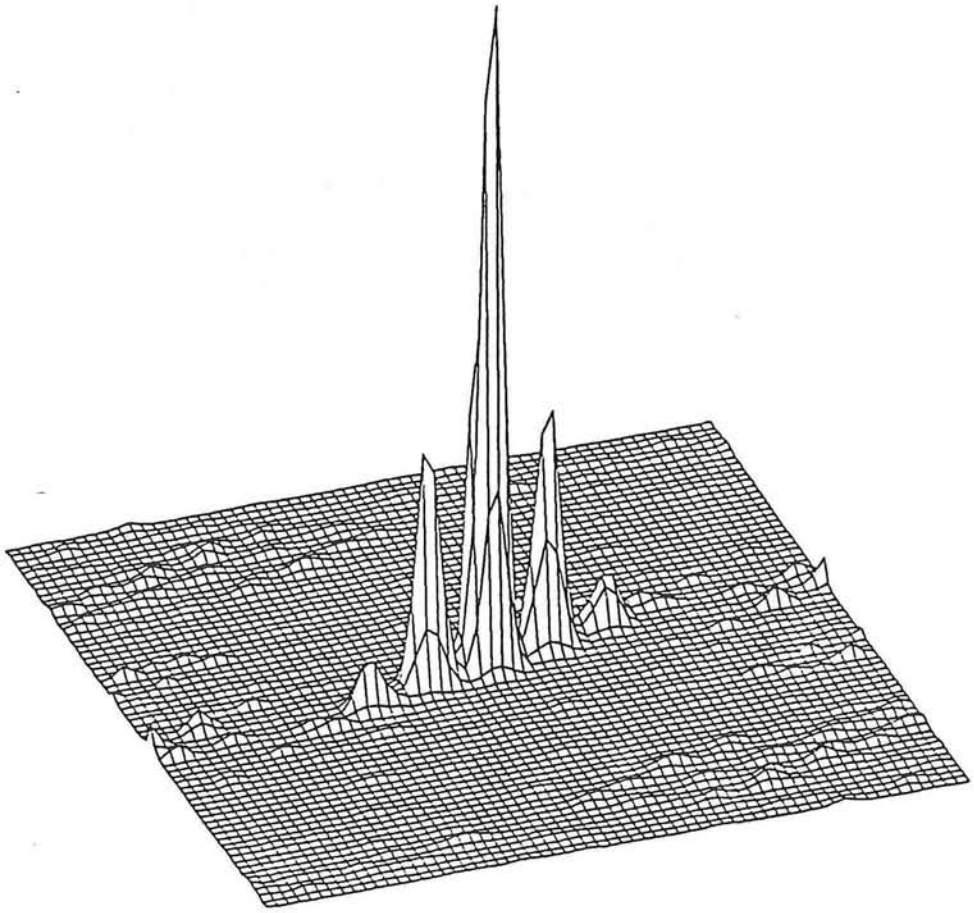

Figure 10: Two-dimensional autocorrelation map

Meas. Sci. Technol. 1 (1990) 1202–1215. Printed in the UK

Optimization of particle image velocimeters. Part I: Double pulsed systems

Richard D Keane and Ronald J Adrian

Department of Theoretical and Applied Mechanics, University of Illinois at Urbana-Champaign, 104 South Wright Street, Urbana, IL 61801, USA

Received 13 February 1990, in final form 1 June 1990, accepted for publication 26 June 1990

Abstract. The spatial resolution, detection rate, accuracy and reliability of a particle image velocimeter depend critically upon the careful selection of a number of parameters of the PIV system and the fluid motion. An analytical model and a Monte Carlo computer simulation have been developed to analyse the effects of experimental parameters and to optimize the system parameters. A set of six non-dimensional parameters that are the most significant in optimizing PIV performance are identified. They are the data validation criterion, the particle image density, the relative in-plane image displacement, the relative out-of-plane displacement, a velocity gradient parameter and the ratio of the mean image diameter to the interrogation spot diamater.

These parameters are studied for the case of interrogation by autocorrelation analysis. By a single transformation, these results can be applied to interrogation by two-dimensional Fourier transform analysis of the Young's fringes.

It is shown that double pulsed systems operate best when the image density exceeds 10–20 and the maximum relative in-plane and out-of-plane displacements do not exceed 30%. Velocity gradients reduce the valid data rate, and they introduce a small statistical bias. Corrections for the statistical bias are developed, with recommendations for minimizing bias effects and loss of signal strength.

1. Introduction

Particle image velocimetry (PIV) is a quantitative method of measuring velocity fields instantaneously in experimental fluid mechanics (Simpkins and Dudderar 1978, Barker and Fourney 1977, Adrian 1986, Meynart 1983, Grousson and Mallick 1977, Dudderar *et al* 1988, Hesselink 1988, Lauterborn and Vogel 1984). In a double pulsed planar PIV system, two light pulses of intensity $I_{01}(x)$ and $I_{02}(x)$ separated by a time interval Δt, illuminate a light sheet of thickness Δz_0 (as shown in figure 1) to produce a double exposed single photographic frame having pairs of particle images from which simultaneous in-plane velocity measurements result.

The position in the image plane $X=(X, Y)$ for erected images is related to the position in the fluid $x=(x, y, z)$ by

$$X=\frac{d_i}{d_0-z}(x\hat{x}+y\hat{y}). \tag{1}$$

Thus, the local in-plane image displacement between pulses, dX, is related to the velocity $u=(u, v, w)$ by

$$dX=(dX, dY)=M(u\hat{x}+v\hat{y})\Delta t+M\frac{x}{d_0-z}(w\Delta t). \tag{2}$$

In paraxial recording this reduces to

$$dX=M(dx\hat{x}+dy\hat{y}) \qquad \text{where} \qquad |X|/d_0 \ll 1. \tag{3}$$

The interrogation procedure for measuring the displacement, dX, is carried out by illuminating a small interrogation spot, centred on X_I and with diameter d_I, with an interrogation beam of intensity $I_I(X)$. The displacement of particle image pairs, $\Delta X(X_I)$, is determined and scanning X_I over the entire photograph produces displacements over the entire image plane. The measured in-plane velocity is determined by

$$u_m(x_I)=\Delta X(X_I)/M\Delta t \tag{4}$$

where x_I is the location in the fluid corresponding to the interrogation spot location on the photograph X_I.

The Young's fringe method and the direct imaging method are utilized to obtain the mean displacement of particle images for each interrogation spot. In the direct imaging method, the physical image plane is digitized and analysed completely within the computer. When the image density, N_I, defined to be the mean number of particles per interrogation spot, is too high to allow individual image pairs to be identified, a statistical method of analysis such as correlation is used (Adrian 1986). The

0957-0233/90/111202+14 $03.50

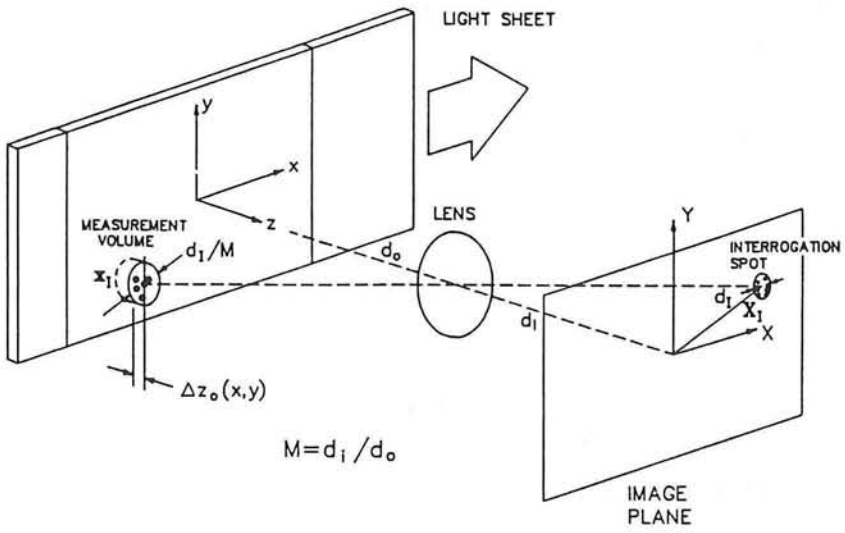

Figure 1. Light sheet and image recording system for planar pulsed laser velocimetry.

autocorrelation of particle image intensities over the interrogation spot is analysed to determine mean image displacements from peak values in the autocorrelation function.

In the Young's fringe method of interrogation, the image field of the interrogation spot is Fourier transformed by a lens so that each pair of particle images produces a system of interference fringes whose spacing is inversely proportional to the image spacing and whose orientation is perpendicular to the image displacement vector (Burch and Tokarski 1968, Meynart 1983). The displacement and orientation of the Young's fringe pattern are found by taking a two-dimensional (2-D) Fourier transform of the digitized Young's fringe data.

The full 2-D correlation and the full 2-D Fourier transform of Young's fringe methods each use all of the digitized data and concentrate the signal energy into peaks that are almost optimally narrow, so it is reasonable to expect that the results obtained from them constitute upper bounds on the performance of less complete methods of analysis, which involve multiple one-dimensional Fourier transforms of the digitized data and are reviewed elsewhere (cf Yao and Adrian 1984, for example). In general, all of these methods achieve enhanced computational rates by sacrificing some of the image information, either through using only a subset of the image data or through reducing the number of image data by averaging or spatial filtering. Likewise, photographic parameters and marker particle characteristics are not expected to affect the details of the interrogation method. Hence, conclusions derived from PIV performance based on full 2-D correlation or on full 2-D Fourier transformation of the fringes will be useful and relatively universal guidelines to the optimization of PIV performance when other types of analysis are used.

The performance of PIV is determined by the spatial resolution, the detection rate and the accuracy of the velocity measurements. The spatial resolution is defined by the size of the measurement volume relative to the length scales of the flow field. The detection rate is defined as the number of interrogation spots per unit area of image plane that produce velocity measurements which satisfy certain interrogation criteria. The accuracy of the velocity data is determined by the interrogation method, the optics and the nature of the velocity field. The accuracy of all detections that satisfy the interrogation criteria, whether they are valid or not, measures the ability of the interrogation criteria to produce valid measurements which agree with a known velocity field. These three parameters are affected by the experimental configuration, the interrogation procedure and its criteria and in turn depend upon: the mean concentration of seeding particles, C, the character of the flow field, $u(x)$ as determined by the local velocity at the centre of the measurement volume and the velocity variations within the measurement volume, the thickness of the light sheet, Δz_0, the time interval between exposures, Δt, and the size, d_1, and shape of the interrogation spot. The foregoing variables depend upon the lens magnification, M, the wavelength of the pulsed light, λ, and the f-number of the camera lens, $f^{\#}$, which determine the particle image diameters, d_τ, from known particle diameters, d_p. To optimize the performance of PIV it is necessary to understand the influence of all of these parameters.

In the present paper, an analytical model is developed and used with a Monte Carlo simulation of a double pulsed planar PIV system to optimize the performance of PIV for a full 2-D interrogation by either spatial correlation or Young's fringes. Paraxial image recording is assumed for simplicity. The marker particles have a constant diameter so that the particle images have equal diameters. The recording film properties are linear and there is assumed to be no noise background in the image field and the N_1 is sufficiently low to discount the probability of images overlapping. Locally linear, three-dimensional velocity fields are considered.

The experimental and interrogation parameters can be reduced to a smaller set of dimensionless parameters.

The particle image density, N_I, is defined for a circular interrogation spot to be

$$N_I = C\frac{\pi d_I^2}{4M^2}\Delta z_0. \tag{5}$$

The dimensionless mean displacement of particle images in an interrogation spot relative to the spot diameter is $|\Delta X|/d_I$. The appropriate dimensionless out-of-plane motion of the particles in the light sheet is $\Delta z/\Delta z_0$ where $\Delta z = w\Delta t$ is the out-of-plane displacement. The extent of image displacement variation within an interrogation spot caused by velocity gradients can be expressed in terms of d_τ and d_I. The optimal value and acceptable range for N_I, $|\Delta X|/d_I, w\Delta t/\Delta z_0$, velocity variations and a non-dimensional detectability criterion D_0, to be defined later, will be determined in terms of given experimental parameters.

The above non-dimensional parameters are important for both methods of interrogation whose similarity is demonstrated in the next section, while differences between the optimal parameters for each method are explained where appropriate.

2. Interrogation methods

2.1. Spatial correlation

When a photograph is interrogated by a light beam of intensity $I_I(X - X_I)$ centred at X_I, the transmitted light intensity immediately after the photograph is

$$I(X) = I_I(X - X_I)\tau(X) \tag{6}$$

where $\tau(X)$, the intensity transmissivity of the photograph is

$$\tau(X) = \sum_i [I_{01}(x_i)\tau_0(X - Mx_i(t)) + I_{02}(x_i)\tau_0(X - Mx_i(t + \Delta t))] \tag{7}$$

given the model assumptions stated above and where $x_i(t)$ is the location of the ith particle at time t. The value $\tau_0(X - Mx)$ represents the transmissivity of an individual particle image per unit of illuminating intensity in the light sheet and is the same for every particle.

The spatial autocorrelation of $I(X)$ with separation s is approximated by the following spatial average estimator over an interrogation spot

$$R(s) = \int I(X)I(X + s)\,dX. \tag{8}$$

Using notation of Adrian (1988a), it can be shown that the estimator consists of five components

$$R(s) = R_C(s) + R_P(s) + R_{D^+}(s) + R_{D^-}(s) + R_F(s) \tag{9}$$

Figure 2(*a*) illustrates the components of the correlation function for a single interrogation spot in which a velocity field across the spot is constant and it contains $N_I = 15$ randomly located particles. $I_I(X)$ is a constant intensity over the interrogation spot and the particle image transmissivity, τ_0 is modelled as a Gaussian function with diameter d_τ. The light sheets are identical with constant intensity $I_{01} = I_{02} = I_0$ inside the sheet and zero intensity outside. Then

$$\tau(X) = I_0 \sum_i [\tau_0(X - X_i(t)) + \tau_0(X - X_i(t + \Delta t))] \tag{10}$$

where i is summed over all particles within the sheet, and $X_i(t)$ is the location of the ith particle image at time t.

The mean image displacement across the interrogation spot is determined by locating the centroid of R_{D^+}

$$\bar{\mu}_{D^+} = \frac{\int sR_{D^+}(s)\,ds}{\int R_{D^+}(s)\,ds} \tag{11}$$

where $\bar{\mu}_{D^+}$ is an estimate of the mean translation ΔX that appears in equation (5).

The mean velocity is then estimated by $\bar{\mu}_{D^+}/M\Delta t$. With no *a priori* knowledge of $R_{D^+}(s)$, $\bar{\mu}_{D^+}$ can be estimated by locating s_{D^+}, the position of the peak value of $R_{D^+}(s)$, by a search over the s-plane, taking into account the self-correlation peak R_P at the origin. This assumes that the tallest peak is the R_{D^+} peak although the random noise peaks from $(R_C + R_F)$ can sometimes exceed the peak of R_{D^+}. The centroid of R_{D^+} is then approximated by integration over a region around the peak value s_{D^+}, the details of which will be discussed later in section 4, where algorithms are described.

2.2. Young's fringe method

The amplitude transmissivity of the image recorded on the film, $t(X)$, is related to the intensity transmissivity, $\tau(X)$, by

$$t(X) = \tau(X)^{1/2}e^{i\theta(X)} \tag{12}$$

where $\theta(X)$ is the phase of the amplitude transmissivity.

The scalar light field from the interrogation spot is given by

$$E(X) = I_I(X - X_I)^{1/2}t(X). \tag{13}$$

The Young's fringes are obtained by taking the Fourier transform of the scalar light field. The scalar field at x_f in the Young's fringe plane can then be written as

$$\hat{E}(x_f) = \int \exp\left(-\frac{2\pi i}{\lambda f}X\cdot x_f\right)E(X)\,dX \tag{14}$$

where f is the focal length of the Fourier transform lens and λ is the wavelength of the interrogation beam. The intensity of the fringe pattern is

$$I_f(x_f) = |\hat{E}(x_f)|^2 = \hat{E}(x_f)\hat{E}^*(x_f). \tag{15}$$

It can be digitized by an electronic camera and analysed by two-dimensional Fourier transformation, e.g.

$$G(s) = \frac{1}{4\pi^2}\int \exp\left(\frac{2\pi i}{\lambda f}s\cdot x_f\right)I_f(x_f)\,dx_f \tag{16}$$

where s is the variable in the numerically computed Fourier transform plane. By the convolution theorem, $G(s)$ is equal to the convolution of the Fourier

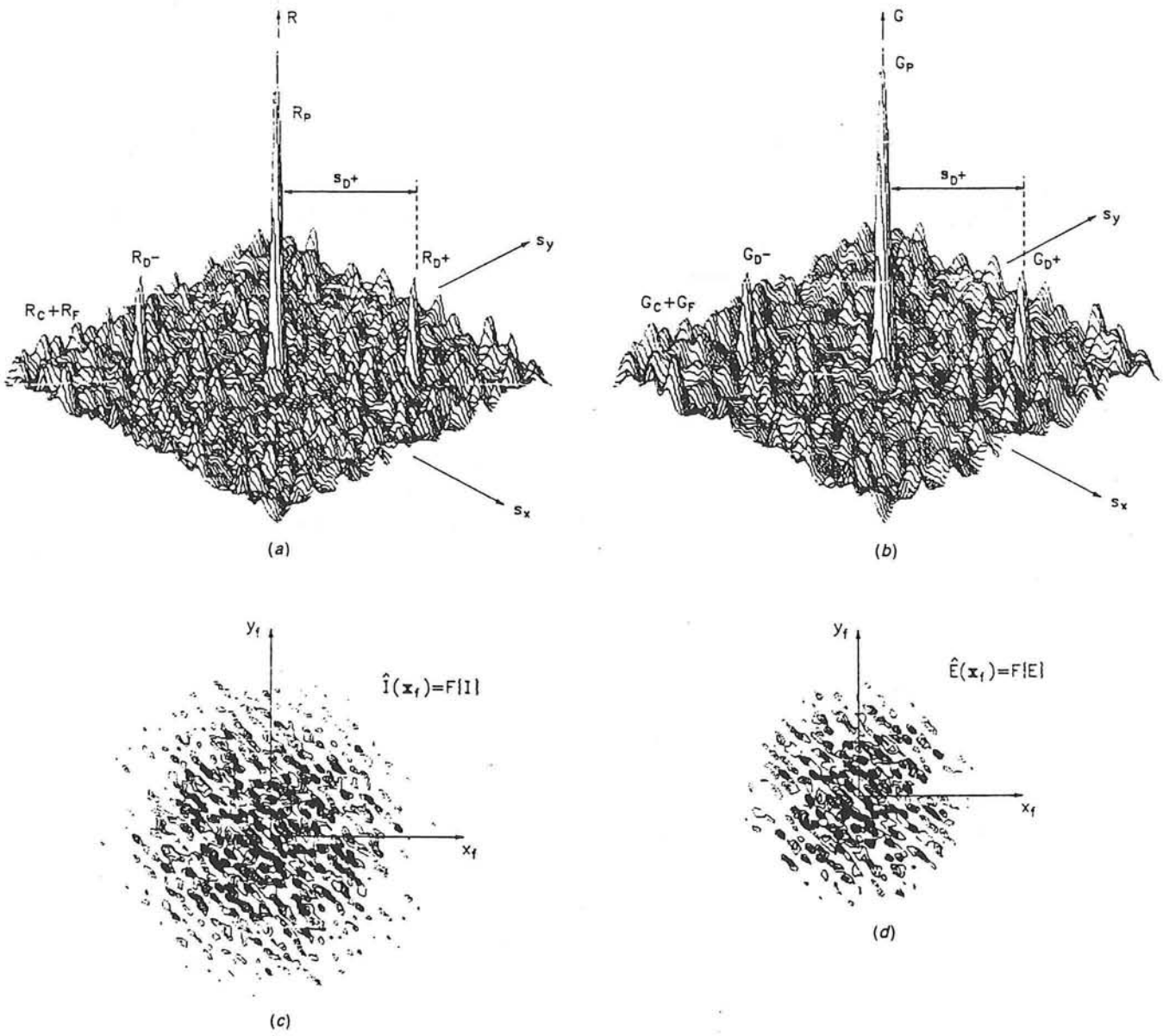

Figure 2. (*a*) Correlation function R for constant velocity within the measurement volume. $N_I = 15$ and mean image displacement, $\Delta X/d_\tau = (0.25, 0.25)$. (*b*) Correlation function G for image transmissivity amplitude $E(X)$. (*c*) |FFT of particle image intensity $I(X)|^2$. (*d*) |FFT of particle image amplitude $E(X)|^2$.

transforms:

$$G(s) = \frac{f^2\lambda^2}{4\pi^2}\int E(X)E^*(X-s)\,\mathrm{d}X. \tag{17}$$

This convolution is very similar to the direct imaging correlation function defined in equation (8), with the transmitted light amplitude, $E(X)$, replacing the transmitted light intensity, $I(X)$. While the direct imaging method uses the erected image, the Fourier transform of the Young's fringe pattern does not, having no effect on $G(s)$ due to its reflectional symmetry.

The Fourier transform of the Young's fringe pattern can be decomposed into five components in a manner similar to equation (9), namely

$$G(s) = G_C(s) + G_P(s) + G_{D^+}(s) + G_{D^-}(s) + G_F(s). \tag{18}$$

Once again, the mean image displacement across the interrogation spot is determined by locating the centroid of G_{D^+} in a manner similar to equation (11).

To illustrate the relationship between the two methods of calculating displacement, consider the example of figure 2 wherein the particle image transmissivities were modelled as Gaussian functions of constant diameter d_τ, in equation (24) and the interrogation intensity, $I_1(x)$, was constant over the interrogation spot. As no images overlap, the particle image amplitude transmissivities are additive, giving

$$t(X) = \sum t_0(X - X_i) \tag{19}$$

where

$$t_0(X - X_i) = \sqrt{\tau_0(X - X_i)}\exp\left[i\theta(X - X_i)\right]. \tag{20}$$

As the diameter of t_0 is $\sqrt{2}d_\tau$, the diameter of G_{D^+} is wider than that of R_{D^+} by a factor of $\sqrt{2}$. However, the

location of the peak in $G_{D+}(s)$ is identical to the location of R_{D+}, in the mean (figure 2(*b*)). Figure 2(*d*) illustrates the Young's fringe pattern obtained for the parameters cited above, and figure 2(*b*) illustrates the full two-dimensional Fourier transform of the fringes.

3. Mean autocorrelation and mean Fourier transform of Young's fringes

3.1. General velocity fields

To determine the statistical properties of R, we consider an ensemble of photographs of identical velocity fields in which each realization contains different sets of randomly located particles. For a known velocity field, $\boldsymbol{u}(\boldsymbol{x})$, the conditional average $\langle R(s)|\boldsymbol{u}\rangle$ calculated over random particle locations measures the mean behaviour of R given the flow field, $\boldsymbol{u}$.

The conditional average of R is determined by conditionally averaging equation (9):

$$\langle R(s)|\boldsymbol{u}\rangle = \langle R_C(s)|\boldsymbol{u}\rangle + \langle R_P(s)|\boldsymbol{u}\rangle + \langle R_{D+}(s)|\boldsymbol{u}\rangle + \langle R_{D-}(s)|\boldsymbol{u}\rangle \tag{21}$$

where it can be shown that $\langle R_F(s)|\boldsymbol{u}\rangle = 0$.

To study the behaviour of $\langle R(s)|\boldsymbol{u}\rangle$ parametrically for a variety of velocity fields, specific models of the transmissivity functions and light intensities are employed. The intensities of the light pulses, I_{01} and I_{02}, are assumed to be top hat functions equal to I_0 within the light sheet and zero outside of it, while the interrogation beam intensity is modelled for computational simplicity as a Gaussian function centred at X_I with diameter d_I measured at the e^{-2} points. The particle images are assumed to be identical with the image transmissivity being a Gaussian curve centred at the image centre with diameter, d_τ where d_τ is, again an e^{-2} diameter. This is a good approximation to a real particle image less its diffraction rings which are normally weak. Thus we have

$$I_{01}(x) = I_{02}(x) = \begin{cases} I_0 & |z| < \Delta z_0/2 \\ 0 & \text{otherwise} \end{cases} \tag{22}$$

$$I_I(X - X_I) = I_{I0} \exp(-8|X - X_I|^2/d_I^2) \tag{23}$$

and

$$\tau_0(X) = \frac{8\tau_{00}}{\pi d_\tau^2} \exp(-8|X|^2/d_\tau^2). \tag{24}$$

Here, $\tau_{00} = \int \tau_0 \mathrm{d}X$, is determined by the photographic process and the development process.

The components of equation (21) for a general displacement field $\Delta\boldsymbol{x}(\boldsymbol{x}, t)$ become

$$\langle R_C(s)\rangle = \frac{4}{\pi} I_0^2 I_{I0}^2 \tau_{00}^2 \frac{N_I^2}{d_I^2} \exp\left(-\frac{4|s|^2}{d_I^2}\right) \tag{25}$$

$$\langle R_P(s)\rangle = \frac{2}{\pi} I_0^2 I_{I0}^2 \tau_{00}^2 \frac{N_I}{d_\tau^2} \exp\left[-\frac{4|s|^2}{d_\tau^2}\left(1 + \frac{d_\tau^2}{d_I^2}\right)\right] \tag{26}$$

$$\langle R_{D+}(s)|\boldsymbol{u}\rangle = C \int \mathrm{d}x I_0(z) I_0(z + \Delta z) \times \int \mathrm{d}X I_{I0}^2 \exp(-8|X|^2/d_I^2) \exp(-8|X + s|^2/d_I^2) \times \left(\frac{8\tau_{00}}{\pi d_\tau^2}\right)^2 \exp(-8|X - Mx|^2/d_\tau^2) \times \exp(-8|X - Mx + s - M\Delta x|^2/d_\tau^2). \tag{27}$$

These results are valid for arbitrary $\boldsymbol{u}$ through the displacement $\Delta\boldsymbol{x}$. If the velocity field does not evolve significantly between pulses, the simple relationship is

$$\Delta\boldsymbol{x}(\boldsymbol{x}, t) = \boldsymbol{u}(\boldsymbol{x}, t)\Delta t. \tag{28}$$

Both $\langle R_C(s)|\boldsymbol{u}\rangle$ and $\langle R_P(s)|\boldsymbol{u}\rangle$ are independent of the velocity field in the interrogation volume. $\langle R_C(s)\rangle$, approximately the convolution of the mean interrogation intensity with itself, is a broad function of s with diameter $\sqrt{2}\,d_I$ and an amplitude proportional to N_I^2. $\langle R_P(s)\rangle$, the mean of the correlation of each particle image with itself, is a narrow function of s with diameter $\sim\sqrt{2}\,d_\tau$. Its amplitude is proportional to the number of image pairs present, N_I. $\langle R_{D+}(s)|\boldsymbol{u}\rangle$, the 'displacement' component of the correlation, depends upon the velocity field in the interrogation volume and it can be determined analytically for special cases of $\boldsymbol{u}(\boldsymbol{x}, t)$.

The statistical properties of $G(s)$, the Fourier transform of the Young's fringes are determined similarly by taking the conditional average of each term in equation (18). To compare the behaviour of $\langle G(s)|\boldsymbol{u}\rangle$ with that of $\langle R(s)|\boldsymbol{u}\rangle$, the specific model above is used.

Assuming that the image intensity transmissivity is given in equation (24), equation (20) gives the image amplitude transmissivity as

$$t_0(X - X_I) = \frac{2\sqrt{2}\sqrt{\tau_{00}}}{\sqrt{\pi}\,d_\tau} \times \exp(-4|X - X_I|^2/d_\tau^2) \exp[i\theta(X - X_I)]. \tag{29}$$

All image transmissivity phases are assumed to be equal to zero.

With the interrogation beam intensity, I_I, modelled as before in equation (23), equation (13) becomes

$$E_I(X - X_I) = \sqrt{I_{I0}} \exp(-4|X - X_I^2|/d_I^2) \tag{30}$$

Thus, the components of $\langle G(s)|\boldsymbol{u}\rangle$ are

$$\langle G_C(s)\rangle = \frac{f^2\lambda^2}{\pi^2} I_0^2 I_{I0} \tau_{00} N_I^2 \frac{d_\tau^2}{d_I^2} \exp\left(-\frac{2|s|^2}{d_I^2}\right) \tag{31}$$

$$\langle G_P(s)\rangle = \frac{f^2\lambda^2}{4\pi^2} I_0^2 I_{I0} \tau_{00} N_I \exp\left[-\frac{2|s|^2}{d_\tau^2}\left(1 + \frac{d_\tau^2}{d_I^2}\right)\right] \tag{32}$$

$$\langle G_{D+}(s)|\boldsymbol{u}\rangle = \frac{f^2\lambda^2}{4\pi^2} C \int \mathrm{d}x I_0(z) I_0(z + \Delta z) \times \int \mathrm{d}X I_{I0} \exp(-4|X|^2/d_I^2) \times \exp(-4|X - s|^2/d_I^2) \frac{8\tau_{00}}{\pi d_\tau^2} \exp(-4|X - Mx|^2/d_\tau^2) \times \exp(-4|X - Mx - M\Delta x - s|^2/d_\tau^2). \tag{33}$$

$G_C(s)$ is a broad Gaussian function of s with diameter $2d_I$ while $G_P(s)$ is a narrow function of s with diameter $\sim 2d_\tau$ when it is assumed $d_\tau \ll d_I$.

3.2. Weak velocity gradients

When the velocity field varies slowly within the interrogation spot, it can be approximated by a locally constant velocity field evaluated at the centre of the measurement volume.

$$u(x) = u_I = u(x_I). \tag{34}$$

Criteria to determine the validity of this approximation will be developed in the next section on strongly varying velocity fields. The present constant velocity analysis contains most of the important phenomena that affect the autocorrelation so that flow non-uniformity can often be neglected with good accuracy.

Given a constant velocity, the equations for the mean background component R_C and the mean pedestal component R_P remain as in equations (25) and (26). The mean displacement component simplifies to

$$\langle R_{D+}(s)|u\rangle = \frac{1}{\pi} I_0^2 I_{I0}^2 \tau_{00}^2 \frac{N_I}{d_\tau^2} F_0(w_I \Delta t) F_I(s) \times \exp(-4|s - Mu_I \Delta t|^2/d_\tau^2) \tag{35}$$

where

$$F_0(\Delta z) \equiv \int dz I_{01}(z) I_{02}(z + \Delta z) \Big/ \int dz I_{01}(z) I_{02}(z) \tag{36}$$

$$F_I(s) \equiv \int dX I_I(X) I_I(X + s) \Big/ \int dX I_I^2(X) \tag{37a}$$

$$= \exp(-4|s|^2/d_I^2). \tag{37b}$$

Equations (36) and (37*a*) are identical to those in Adrian (1988a). Equation (37*b*) follows from the assumed Gaussian form for $I_I(x)$ in equation (23). If $I_{01}(z)$ were assumed to be a Gaussian function with an e^{-2} width, Δz_0, then F_0 would be a Gaussian function with width $\sqrt{2}\,\Delta z_0$. In the present case, where we take I_0 to be a top hat function of width Δz_0, F_0 is a triangle function whose base is $2\Delta z_0$ wide. F_I is the normalized correlation of the interrogation intensity across the interrogation spot while $F_0(\Delta z)$ is the normalized correlation of the intensities of the two light pulses in terms of the particle displacements, $\Delta z_I = w_I \Delta t$ in the out-of-plane direction.

If the interrogation volume contains a random number N of randomly located particles at the instant of the first exposure, the maximum possible number of pairs of images that could contribute to R_{D+} would be N. However, particle motion between exposures causes certain particles to leave the interrogation volume, so that the maximum number of true image pairs is less than N, and the amplitude of R_{D+} is thereby reduced. We call this the *loss of pairs effect*. It is a consequence of out-of-plane motion, represented by F_0, and in-plane motion, represented by F_I. If I_I, I_{01} and I_{02} were uniform within the interrogation volume and zero outside it, then $F_0(w_I \Delta t) F_I(Mu_I \Delta t) N_I$ would represent the mean number of particles whose second images remained in the interrogation volume to produce a pair of images, where N_I is the mean value of N.

The effect of loss of pairs is seen most clearly by evaluating the displacement autocorrelation at $s = Mu_I \Delta t$, where u_I in this context is the vector formed by the two in-plane components of velocity. From equation (35) the maximum value of R_{D+} occurs very near this location when the image diameter is small. The mean value is

$$\langle R_{D+}|u\rangle = I_0^2 I_{I0}^2 \tau_{00}^2 F_0(w_I \Delta t) F_I(Mu_I \Delta t) N_I/\pi d_\tau^2. \tag{38}$$

The strength of R_{D+} is proportional to the mean number of displacement pairs times the square of the interrogation intensity for one image times the area of an image. The amplitude of R_{D+} decreases in direct proportion to the number of displaced image pairs left in the interrogation volume. If I_I, I_{01} and I_{02} are not top-hat distributions, then $F_0 F_I N_I$ should be interpreted as the mean number of pairs weighted by the light intensity distribution.

Two important operating criteria are derived from the simple requirement that the loss of pairs effect should not be too large. Since F_0 decreases in proportion to the relative out-of-plane motion, this dimensionless parameter $w_I \Delta t/\Delta z_0$ must be limited to a maximum value. Likewise, since F_I decreases in proportion to $M|u_I|\Delta t/d_I$, (cf equation (37*b*)), the maximum in-plane displacement must be limited to a small fraction of d_I. The values recommended previously in Adrian (1988a), max $(w_I \Delta t/z_0) = 0.5$ and max $(M|u_I|\Delta t/d_I) = 0.5$, yield min $(F_I) = e^{-1}$ and min $(F_0) = 0.5$. Recently, more conservative values, max $(w_I \Delta t/\Delta z_0) = 0.25$ and max $(M|u_I|\Delta t/d_I) = 0.25$, have been recommended on the basis of practical experience with PIV interrogation (Adrian (1988b)).

Ideally, the maximum of $\langle R_{D+}|u\rangle$ is located at $Mu_I \Delta t$, but according to equation (35) the maximum is pulled toward $s = 0$ by the factor $F_I(s)$ and located at

$$s_{D+} = Mu_I \Delta t/(1 + d_\tau^2/d_I^2) \tag{39}$$

Hence, simple detection of the peak of R_{D+} (or its centroid) leads to an error of order d_τ^2/d_I^2. In experiments where care has been taken to minimize the image diameter, the error is negligible. For example, if $d_\tau = 20\ \mu$m and $d_I = 1$ mm, the error is 0.04%, which is negligible compared with the 0.5–1% error typically achieved in PIV measurements (Landreth *et al* 1988). If d_τ/d_I is allowed to exceed 0.1, the error exceeds 1%, and explicit correction should be made, assuming that adequate information about d_τ is available experimentally.

The ratio of the amplitude of the displacement correlation to the amplitude of the self-correlation provides a useful dimensionless measure of the signal quality. It is

$$\langle R_{D+}(s_{D+})|u\rangle/R_P(\mathbf{0}) = \tfrac{1}{2} F_0(w_I \Delta t) \times \exp[-4|Mu_I \Delta t|^2/(d_I^2 + d_\tau^2)]. \tag{40}$$

The ratio approaches one-half as the displacement approaches zero because the signal energy is split equally between R_{D+} and R_{D-}. It is always less than or equal to

one-half by virtue of the pair loss effect. The visibility of the fringe system obtained by Fourier transforming the autocorrelation function is equal to this ratio.

The analysis of the mean Fourier transform of the Young's fringes proceeds similarly, so that equation (33) becomes

$$\langle G_{D^+}(s)|u\rangle = \frac{f^2\lambda^2}{8\pi^2} I_0^2 I_{10}\tau_{00} N_1 F_0(w_1\Delta t)H_1(s) \times \exp(-2|s + Mu_1\Delta t|^2/d_\tau^2) \quad (41)$$

where

$$H_1(s) \equiv \int dX I_1^{1/2}(X) I_1^{1/2}(X+s) \Big/ \int dX I_1(X) \quad (42a)$$

$$= \exp(-2|s|^2/d_1^2). \quad (42b)$$

The peak of $\langle G_{D^+}|u\rangle$ lies at that same point given for the autocorrelation in equation (39), although the Gaussian diameters are all broadened by a factor of $\sqrt{2}$. H_1 measures the loss of pairs effect caused by in-plane motion, in a similar manner to F_1.

The ratios of amplitudes of $\langle G_{D^+}(s)|u\rangle$ and $\langle G_{D^-}(s)|u\rangle$ to that of $G_P(s)$ are identical to those of R after allowing for peak broadening, namely

$$\langle G_{D^+}(s_{D^+})|u\rangle / G_P(\mathbf{0}) = \tfrac{1}{2}F_0(w_1\Delta t)\exp\left(\frac{-2|Mu_1\Delta t|^2}{d_1^2 + d_\tau^2}\right). \quad (43)$$

3.3. Strong velocity gradients

In many experimental applications the effects of pair loss due to translation are small. However, the interrogation spot diameter, d_1, and the light sheet thickness, Δz_0, are frequently not small enough to warrant neglect of the velocity variations in the interrogation volume due to strong gradients, as in turbulent flow. Gradients distribute the image displacements over finite regions in the correlation plane which affects measurement in two ways.

The first effect is to necessitate careful interpretation of the relationship between the location of the displacement correlation and the mean fluid motion. It has been shown (Adrian 1988a) that the centroid of the expected value of R_{D^+} corresponds to a volume averaged velocity

$$\bar{\mu}_{D^+} = \int s\langle R_{D^+}|u\rangle\, ds \Big/ \int \langle R_{D^+}|u\rangle\, ds \quad (44a)$$

$$= \int W(x, X, u)u(x, t)\,dx \Big/ \int W(x, X, u)\,dx \quad (44b)$$

wherein the weight function is given by

$$W = I_{01}(x)I_{02}(x + u\Delta t)I_1(Mx - X_1)I_1(Mx + Mu\Delta t - X_1) \quad (45)$$

(The centroid of $\langle R_{D^+}|u\rangle$ is not necessarily equal to the conditional mean of the centroid defined in equation (11) by virtue of random fluctuations in $\int R_{D^+}\,ds$. We shall, however ignore this difference on the grounds that fluctuations in the denominator of (11) are larger than fluctuations in the numerator). Since W decreases with increasing $|u|$, the measurement is statistically biased toward the lower speed particles. This bias can be made negligible. Firstly, its magnitude is bounded by the total variation of the velocity within the interrogation volume, so it is small if the gradients are weak. Secondly, limiting the displacements to constrain the loss of pairs effect on the amplitude of R_{D^+}, as recommended in section 3.2, also limits the variation of W with u. To a first approximation,

$$W \simeq I_{01}(x)I_{02}(x)I_1^2(Mx - X_1) \quad (46)$$

and the weight function depends only upon the light intensity distribution in the intersection of the interrogation spot with the illuminating beams.

The second, often more important, effect is that gradients diminish the amplitude of the correlation peak and broaden its width. When the amplitude becomes too small, the peak of the correlation function may not be detectable, resulting in failed measurements for regions of high velocity gradient.

Equation (46) provides a useful working definition of the measurement volume of a PIV. We shall refer to it as the small displacement measurement volume. Its e^{-2} diameter in the X–Y plane is $d_1/\sqrt{2}$ if the interrogation spot is a Gaussian with e^{-2} diameter d_1. Its thickness in the z-direction is Δz_0 if the light sheet has a top-hat intensity profile.

The behaviour of $\langle R_{D^+}|u\rangle$ is analysed by expanding the velocity field within the measurement volume in a Taylor series about x_1 and truncating at the first-order linear term:

$$u_i(x) = u_i(x_1) + (\partial u_i/\partial x_j)_{x_1}(x_j - x_{1j}). \quad (47)$$

The results depend in general upon the deformation tensor $d_{ij} = \partial u_i/\partial x_j$, but for simplicity we shall consider two special cases: simply shear and pure rotation.

In the case of simple shear with $\partial u/\partial y \neq 0$, v, w constant it can be shown by direct calculation that

$$\langle R_{D^+}(s)|u\rangle = \frac{1}{\pi} I_0^2 I_{10}^2 \tau_{00}^2 \frac{N_1}{d_\tau^2} F_0(w_1\Delta t) \times [1 + (M\Delta u\Delta t/d_\tau)^2]^{1/2} \times \exp(-4|Mu_1\Delta t|^2/d_1^2)\exp[-4(s_y - Mv_1\Delta t)^2/d_\tau^2] \times \exp\{-4[1 + (M\Delta u\Delta t/d_\tau)^2]^{-1} \times \{s_x - [Mu_1\Delta t - Mu_1\Delta t(M\Delta u\Delta t/d_1)]\}^2/d_\tau^2\}. \quad (48)$$

Here Δu is the maximum variation in u across d_1

$$\Delta u = \left(\frac{\partial u}{\partial y}\right)_{x_1}\frac{d_1}{2M}. \quad (49)$$

Furthermore it is assumed that $d_\tau \ll d_1$ and second order effects of velocity variation are ignored.

The amplitude of R_{D^+} is diminished by the factor $[1 + (M\Delta u\Delta t/d_\tau)^2]^{1/2}$ in the presence of this velocity variation, decreasing the likelihood of detecting the dis-

placement peak. In addition, the diameter of the peak is broadened by the same factor in the direction of shear. The peak of R_{D^+} and its centroid are both located at

$$s_{D^+} = \left[Mu_1\Delta t - Mv_1\Delta t\left(\frac{M\Delta u\Delta t}{d_1}\right), Mv_1\Delta t \right]. \quad (50)$$

The second case we consider is a local rotational motion about the z-axis at x_1 defined by $(\partial u/\partial y)_{x_1} = -(\partial y/\partial x)_{x_1}$ and all other components of the deformation tensor are equal to zero. We obtain

$$\begin{aligned}\langle R_{D^+}(s)|u\rangle = {} & \frac{1}{\pi} I_0^2 I_{10}^2 \tau_{00}^2 \frac{N_1}{d_\tau^2} F_0(w_1\Delta t) \\ & \times [1 + (M\Delta u\Delta t/d_\tau)^2]^{-1} \exp(-4|Mu_1\Delta t|^2/d_1^2) \\ & \times \exp[-4(1 + (M\Delta u\Delta t/d_\tau)^2)^{-1} \\ & \times \{[s_x - (Mu_1\Delta t - Mv_1\Delta t(M\Delta u\Delta t/d_1)]^2 \\ & + [s_y - (Mv_1\Delta t - Mu_1\Delta t(M\Delta v\Delta t/d_1))]^2\}/d_\tau^2]. \end{aligned} \quad (51)$$

The amplitude of R_{D^+} has been reduced by the factor $(1 + (M\Delta u\Delta t/d_\tau)^2)$ due to velocity variations in the u- and v-components of velocity and the Gaussian peak is broadened in each direction by the same factor as before. The peak and the centroid are now located at

$$\begin{aligned} s_{D^+} = \bar{\mu}_{D^+} = ((Mu_1\Delta t - Mv_1\Delta t(M\Delta u\Delta t/d_1)), \\ (Mv_1\Delta t - Mu_1\Delta t(M\,\Delta v\Delta t/d_1))) \end{aligned} \quad (52)$$

where $\Delta v = -\Delta u$ for a local rotation in the velocity field.

In each case above, the peak and the centroid of the mean of R_{D^+} are statistically biased towards velocities lower than u_1. We call this *gradient bias*. It occurs because the correlation is biased against the faster moving particle within the measurement volume. The extent of this gradient bias cannot exceed the maximum variation of velocity within the measurement volume and is determined by the dimensionless parameter $(M\Delta u\Delta t/d_1, M\Delta v\Delta t/d_1)$.

A second type of bias occurs because the peak amplitude of R_{D^+} is diminished, in the presence of a velocity gradient, by a factor which depends upon $M\Delta u\Delta t/d_\tau$. This consequence of the variation of particle image displacements from randomly located particles in the velocity field within the interrogation volume, lowers the probability of detecting the correlation peak among the noise peaks. We call this *detection bias*. When $M|\Delta u|\Delta t = d_\tau$ the reduction factors in equations (48) and (51) are $\sqrt{2}$ and 2 respectively, illustrating the need to minimize the variation in velocity within an interrogation volume by a judicious selection of Δt. In addition to biasing the estimate of the mean, the broadening of the displacement component, R_{D^+}, leads to increased uncertainty in estimating velocity from individual realizations.

In analysing the mean Fourier transform of the Young's fringes, $\langle G_{D^+}(s)|u\rangle$ the peak location s_{D^+}, and the extent of gradient bias are not affected by peak broadening factors and are identical to those in $\langle R_{D^+}(s)|u\rangle$. However, peak broadening and peak splintering increase the likelihood of detection bias in this method of analysis.

The close similarity between the spatial correlation and the 2-D Fourier transform of the Young's fringes is evident and the results for one form of analysis can be transferred directly into results for the other form. Consequently, the following sections will consider only the autocorrelation method, that being the most simply understood approach.

4. Autocorrelation fluctuations and performance

4.1. Validation

Interrogation performance is gauged in terms of the *spatial resolution*, the *data yield*, the *valid data yield*, and the *accuracy* of the measurements of data that are deemed to be valid. The data yield, or *detection* probability, is the probability that a single interrogation spot produces a velocity measurement that is acceptable according to certain validation criteria. The valid data yield, or valid detection probability, is the probability that a measurement judged to be valid is actually valid. All aspects of the performance are affected by random fluctuations of the autocorrelation function, and these in turn, are affected by the dimensionless parameters presented in the introduction, and by the specific details of the interrogation procedure.

The interrogation procedure locates the highest peak in $R(s)$, excluding the self-correlation peak R_P, and assumes that this peak corresponds to R_{D^+}. However, there is a non-negligible probability that the tallest peak is a noise peak, if the peak of the displacement correlation is comparable to the noise correlation level. To discriminate against this possibility, the tallest peak is required to be significantly stronger than the second tallest peak. This detectability criterion eliminates interrogations in which the displacement correlation is barely distinguishable from the noise, but it is not guaranteed to eliminate interrogations in which there is a very strong noise correlation peak.

The detectability is defined to be the ratio of the first tallest peak to the second tallest peak, located at s_1 and s_2, respectively (Adrian 1985):

$$D(X_1) = R(s_1)/R(s_2). \quad (53)$$

Because of the symmetry of $R(s)$, only one half of the plane needs to be searched. To validate the assumption that the tallest peak does indeed correspond to the displacement peak R_{D^+}, the detectability is compared to a threshold level D_0 which is a preset constant. The interrogation is accepted if $D \geqslant D_0$; the interrogation is rejected if $D < D_0$, i.e. if the correlation peak fails to exceed a certain signal-to-noise ratio.

The location s_1 estimates the mean displacement, namely $s_1 = \Delta X_1$. Then, the centroid of the correlation peak can be calculated by defining a small area A_1 around the peak, and integrating according to

$$\bar{\mu}_1 = \int_{A_1} sR\,ds \Big/ \int_{A_1} R\,ds. \quad (54)$$

The centroidal calculation offers accuracy greater than the resolution of the computational grid used in the s-plane. Since the grid spacing is defined by the pixel spacing of the device used to record the interrogation spot image field, this implies the possibility of locating the particle displacement to within an accuracy of a fraction of a pixel. The area A_1 should be defined in such a way that it contains only the displacement correlation peak, R_{D^+} and A_1 is defined here to be the area around s_1 in which $R(s)$ is greater than 1% of $R(s_1)$. Since R is the sum of R_{D^+}, R_C, and the random fluctuations R_F, the centroidal estimate is always contaminated, and it randomly fluctuates around a mean value that approximates to the mean displacement. The centroidal location becomes less accurate as velocity gradients broaden R_{D^+} and diminish its peak value, as discussed in section 3.

Invalid data are allowed by this criterion when the correlation of randomly located particle images, given by $R_C(s) + R_F(s)$, has a maximum larger than $R_{D^+}(s)$. The probability of such invalid data decreases as the detectability criterion, D_0, increases, as, however, does the probability of a successful interrogation. In order to determine an optimum value for D_0, which minimizes the occurrence of invalid data while maintaining a satisfactory probability of successful interrogations, a range of values for D_0 has been considered.

4.2. Monte Carlo simulation

The analysis of the mean correlation function, offers some insights into the performance of this interrogation procedure, but it cannot directly address questions concerning the probabilities of measurement and validation. Hence, a numerical simulation of the PIV image field and interrogation analysis has been constructed so that statistics of the detection probabilities can be found by Monte Carlo simulation.

An ensemble of 1200 realizations is generated for each velocity field in which particles are scattered randomly with an average N_I, governed by Poisson statistics. The seeded volume is sufficiently large to ensure no loss of particle images by restrictive boundaries from each interrogation volume. Both light sheet pulses have intensity as in equation (22) and the interrogation intensity, I_I is also constant across the square interrogation spots following experimental procedure unlike the analytical model in section 3, where I_I was defined as a Gaussian curve. The image transmissivity of the monodisperse particles image is given above in equation (24). The recording film properties are linear, the images interfere incoherently, i.e. N_I is sufficiently low to avoid image overlap and there is no background light noise level in the recording. Velocity gradients are assumed to be linear across the interrogation spot centred at x_I, as in equation (47).

Figure 3 shows a simulated region of the interrogation plane in which a constant in-plane velocity causes the image displacement, $\Delta X/d_I = (0.25, 0.25)$. Although $N_I = 15$, random fluctuations for individual interrogation spots are obvious.

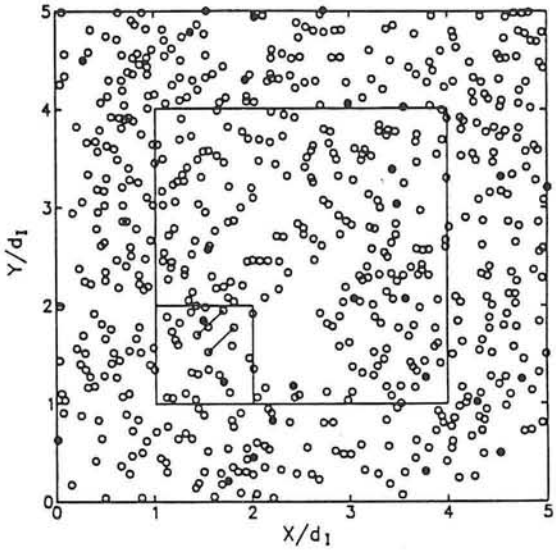

Figure 3. Simulated region of the interrogation plane. The velocity is constant within the measurement volume, $N_I = 15$ and the mean image displacement, $\Delta X/d_I = (0.25, 0.25)$. The smaller square denotes an interrogation spot.

The autocorrelation is computed using 2-D fast Fourier transforms of $I(X)$ digitized on a 256 × 256 array from each interrogation spot. Without padding the region around each spot with zeroes, the intensity I is effectively periodically extended, and a convolution of the periodic extension results. Figure 4 illustrates the mean correlation for 1200 realizations in which no zero padding of the intensity array was performed, resulting in a constant value for $\langle R_C(s) \rangle$ when I_{10}, I_{01} and I_{02} were constant intensities. Zero padding of the intensity array could be achieved by embedding the 128 × 128 intensity array within a 256 × 256 array containing zeroes otherwise. As I would no longer be periodically extended, this would

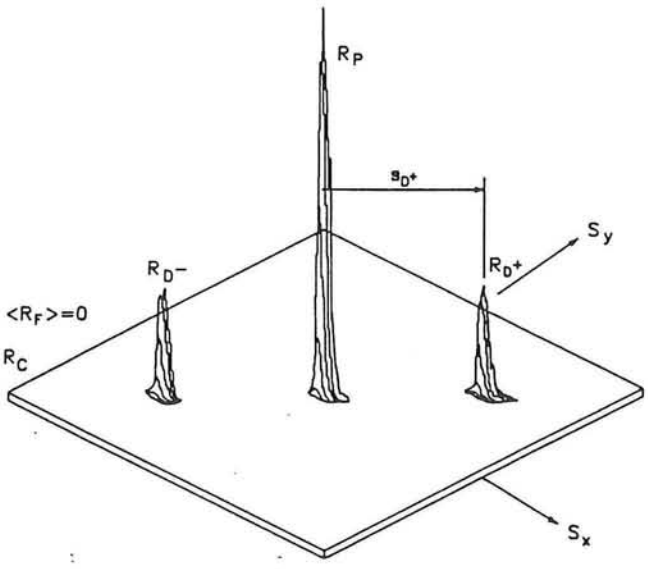

Figure 4. Expected value of correlation function R for constant velocity within the measurement volume. (Conditions as in figure 2.)

result in fewer noise peaks and a pyramidal form of $\langle R_C(s)\rangle$, thus improving the signal-to-noise ratio. However, as the spatial resolution is reduced and the valid detection probability is not significantly improved for the optimum parameters considered below, the use of no padding improves spatial resolution. The maximum image displacement is limited to $|\Delta X|/d_I \leqslant 0.5$ since it will be shown that larger displacements are undesirable. After determining D and u_m, a comparison is made between u_m and u_I to ascertain whether the measurement is valid or invalid, yielding both the detection probability and valid detection probability.

4.3. Performance: weak velocity gradients

The effect of variation of N_I is illustrated in figure 5 for a range of image displacements, $|\Delta X|/d_I$ using a detectability criterion of $D_0 = 1.5$ and constant in-plane velocities. Increasing N_I generally increases the detection probability and the valid detection probability because, from equation (35), the amplitude of R_{D+} is proportional to N_I. The minimum detection probability occurs when $N_I \approx 2$–3 because this low density does not give enough pairs to unambiguously define the correct pairing of images nor satisfy the detectability criterion, $D_0 = 1.5$. For lower values of N_I, the correct pairing of images does occur, but the total detection probability is low. This is

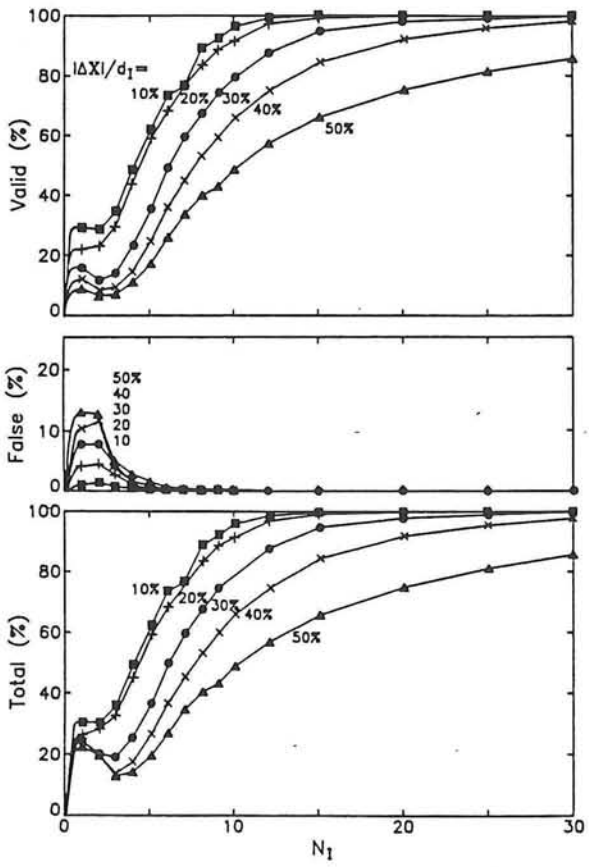

Figure 5. Total, false and valid detection probabilities as a function of relative image displacement $|\Delta X|/d_I$ and image density, N_I for $D_0 = 1.5$. The velocity within the interrogation spot is constant.

the operating range studied by Landreth *et al* (1988). The estimate of $N_I \geqslant 4$ given by Lourenco and Krothapalli (1987) applies to a multiple pulsed PIV system and lies significantly below the optimal range for a double pulsed system. Recent analysis of multiple systems shows it is applicable when five or more pulses are employed.

As $|\Delta X|/d_I$ increases, fewer particle pairs remain in the interrogation spot as the first or second images move out of the spot. Because I_I is constant in the interrogation spot and zero elsewhere, F_I as defined in equation (37a) measures the ratio of the area that is common to both shifted and unshifted images to the total spot area. Thus, $N_I F_I$ is the mean number of image pairs in this region and is the effective number of image pairs in the spot.

To achieve a valid detection probability of at least 90%, the image density, N_I must be greater than 15 with $|\Delta X|/d_I < 0.3$. The valid detection rate is a decreasing function of relative displacement which declines sharply when $|\Delta X|/d_I$ exceeds 20–30% (figure 6). To achieve a high detection rate, the maximum value for $|\Delta X|/d_I$ is suggested to be 0.25. The choice of the time interval between light pulses, Δt, must then satisfy (cf Adrian 1988b).

$$\Delta t < 0.25 d_I / M \text{ Max } |u|. \tag{55}$$

The detectability threshold, D_0, is designed to minimize the false detection probability while ensuring an acceptable detection rate. There is an abrupt decrease in both the detection probability and the valid detection probability when $D_0 > 1.3$–1.5 for a wide range of N_I when a relative image displacement is $|\Delta X|/d_I = 0.30$ (figure 7). Relatively few peaks in R are stronger than $1.5\,R(s_2)$. Thus, a reasonable value for D_0 is in the range 1.2–1.5.

In the limit of small N_I, the probability of detection is equal to the probability of finding precisely one pair of images belonging to the same particle within the interrogation spot. This probability is given by the prob-

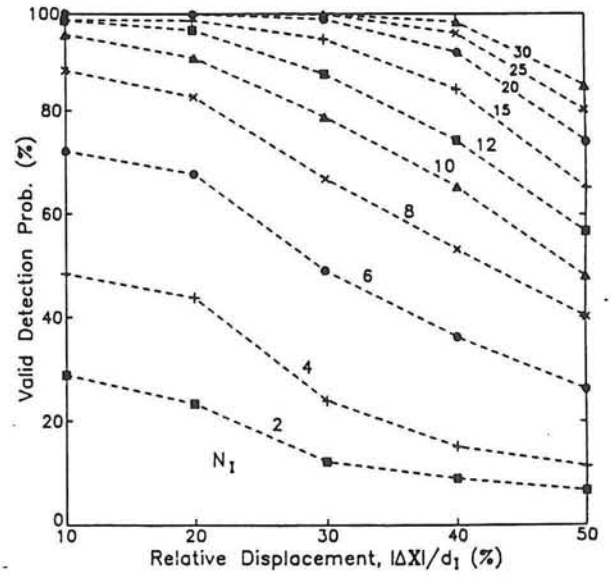

Figure 6. Valid detection probability versus relative image displacement $|\Delta X|/d_I$ for $D_0 = 1.5$ and variable particle image density, N_I.

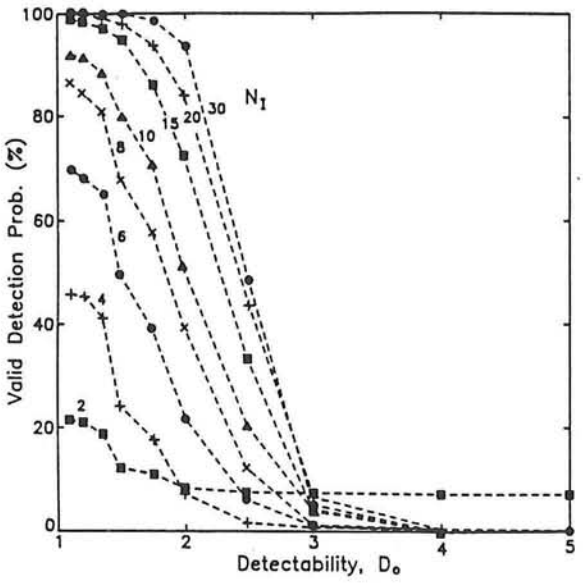

Figure 7. Valid detection probability as a function of detectability for variable particle image density N_I and $|\Delta X|/d_I = 0.3$.

ability of finding one particle in that portion of the interrogation volume from which the particle could be displaced and still remain within the interrogation volume at the time of the second exposure. The average number of particles within this region is $N_I F_0 F_I$, and therefore from the Poisson distribution it follows that

Prob {exactly one pair of images}

$$= N_I F_0 F_I \exp(-N_I F_0 F_I) \exp[-2N_I F_0(1-F_I)]. \quad (56)$$

This result shows that the effects of in-plane displacement, out-of-plane displacement and particle concentration can be correlated in terms of the single parameter $N_I F_0 F_I$ when the image density is small. Figure 8 confirms this correlation, and shows that equation (56) is valid for $N_I F_I$ less than about 0.3. These results are independent of D_0 due to the lack of noise peaks in $R(s)$. In low image density cases, the correlation procedure can be replaced by simpler methods such as orthogonal image compression (Yao and Adrian 1984), and the detection probability depends principally upon the probability of finding a true pair of images.

When the velocity includes a component perpendicular to the light sheet, the number of image pairs per interrogation spot is reduced, decreasing the peak amplitude of R_{D+} and increasing the contribution of $R_C + R_F$. Thus the valid detection probability decreases as the relative out-of-plane motion, $w\Delta t/\Delta z_0$ increases (figure 9). In the extreme case, where $w\Delta t/\Delta z_0 \geqslant 1$, the detection rate becomes zero, as no image pairs remain in the interrogation spot.

The detection probability for various values of N_I can be correlated in terms of $N_I F_0(\Delta z)$, which represents the mean number of particles that reside in the light sheet for both light pulses. Figure 10 correlates this probability

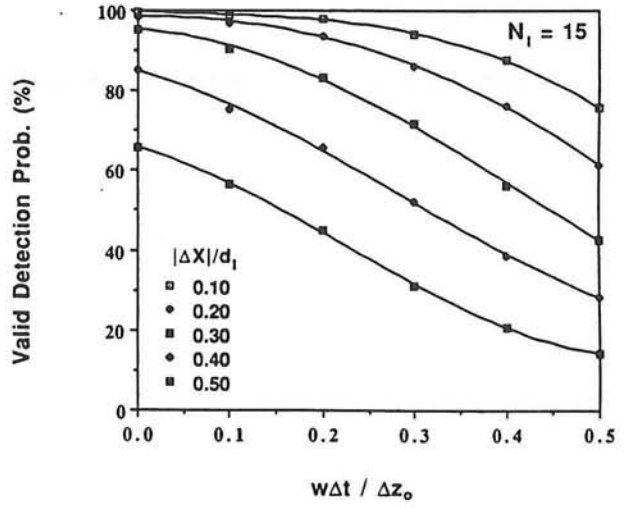

Figure 9. Valid detection probability as a function of the relative out-of-plane motion for $N_I = 15$ and $D_0 = 1.5$.

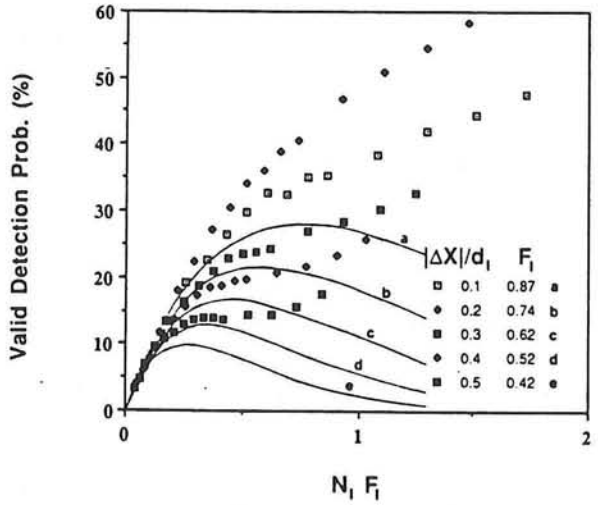

Figure 8. Valid detection probability for low image density; N_I in terms of the effective image density, $N_I F_I$, for detectability $D_0 = 1.5$. Full curves illustrate equation (56) with $F_0 = 1$ and F_I as tabulated.

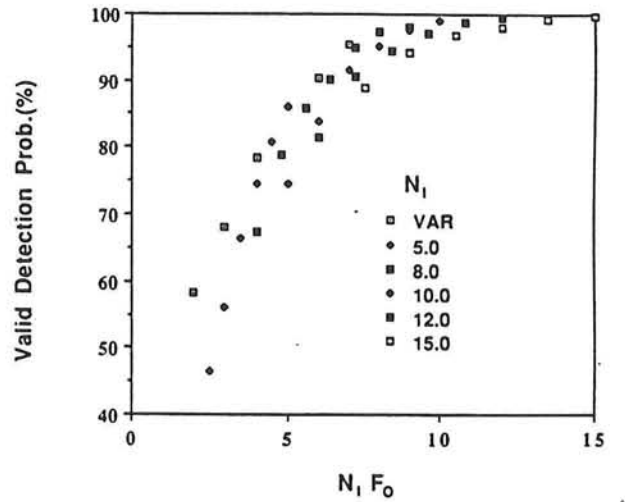

Figure 10. Correlation of the valid detection probability for out-of-plane displacements in terms of the effective image density, $N_I F_0$. Detectability $D_0 = 1.0$ and $|\Delta X|/d_I = 0.2$.

with $N_I F_0$ for a range of N_I using $D_0 = 1.0$ and $|\Delta X|/d_I = 0.2$. Both figures 9 and 10 illustrate the need to select Δz_0 to minimize loss of detection rate without losing spatial resolution in the out-of-plane direction.

4.4. Performance: strong velocity gradients

As outlined in section 3, the effects of velocity gradients are to diminish the mean correlation peak while broadening its diameter, and to statistically bias the centroid of $\langle R_{D^+} | u \rangle$ against high velocities. Figure 11 shows the correlation function of a single interrogation spot for conditions identical to those in figure 2, except that a simple shear, $\partial u/\partial y = 0.24 u_I/d_I$ has been added to the uniform translation. The decreased amplitude of R_{D^+} is apparent.

Figure 12 shows the detection probability as a function of the dimensionless velocity variation $M\Delta u\Delta t/d_\tau$ for various displacements $|\Delta X|/d_I$. The parameter $M\Delta u\Delta t/d_\tau$ is suggested by the theory for $\langle R_{D^+} | u \rangle$ in which the amplitude is proportional to $[1 + (M\Delta u\Delta t/d_\tau)^2]^{-1/2}$. The detection probability is proportional to this amplitude with only a weak dependence upon $|\Delta X|/d_I$. Figure 12 indicates that high detection probabilities can be achieved if the velocity variation is such that $M\Delta u\Delta t/d_\tau < 1$, and $|\Delta X|/d_I < 0.25$, as indicated by the shaded area. The worst-case detection probability for operation within this area is 92%, and over much of the region the detection probability exceeds 98%. These values are consistent with experience derived from interrogation of experimental PIV photographs of turbulent flows (Reuss *et al* 1989, Landreth and Adrian 1989).

The constraints $M\Delta u\Delta t/d_\tau < 1$ and $|\Delta X|/d_I < 0.25$ imply that

$$\Delta u/u_I < 4d_\tau/d_I \tag{57}$$

which can be used to estimate the maximum velocity

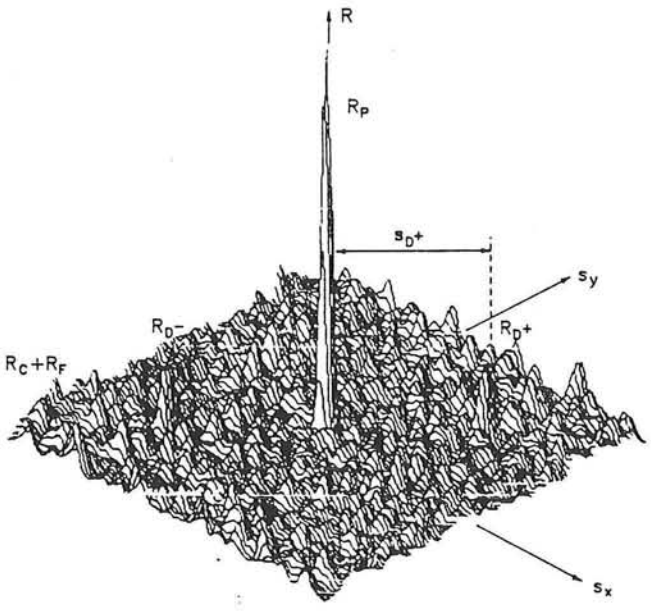

Figure 11. Correlation function R for a plane shearing velocity within the measurement volume. $N_I = 15$, $\Delta X/d_I = (0.25, 0.25)$, $(\partial u/\partial y)_{x_i} = 0.24 M u_I/d_I$.

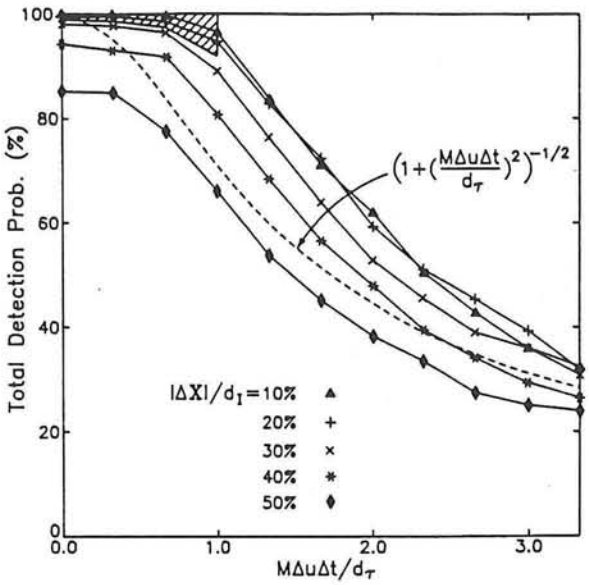

Figure 12. Total detection probability for a simple shear in terms of the relative image displacement variation, $M\Delta u\Delta t/d_\tau$, for variable image displacements, $|\Delta X|/d_I$, $N_I = 15$, $D_0 = 1.2$. -----, amplitude of $\langle R_{D^+} | u \rangle$ from theory.

difference that can be comfortably treated by the correlation technique for a given interrogation spot diameter, or to define the diameter needed for a given maximum velocity variation. For example, if the total velocity variation across d_I is 40% ($\Delta u/u_I = 0.2$), and if the image diameter is 25 μm then the maximum interrogation spot size should be less than 0.5 mm. The requirement that N_I should exceed 15–20 places a lower bound on the size of the interrogation spot. Hence, velocity gradients ultimately place a fundamental limit on the measurements that can be made with double pulsed autocorrelation PIV. While other techniques such as multiple pulse recording or individual particle tracking may (or may not) offer some alleviation of these limits, it is clear that the smallest scales of motion that can be measured will also ultimately be limited by the diameter of the images. Thus, an inequality like equation (57) is expected to pertain to any type of PIV system, with the constant depending upon the system operation.

Velocity variation affects the accuracy of valid data measurements by statistically biasing measurements based on the centroid $R_{D^+}(s)$. For the simple shear velocity field, figures 13 and 14 relate the relative bias in the velocity component, u, to the variation of u. In figure 13, the bias is measured in terms of $M\Delta u\Delta t/d_I$ for a range of mean image displacements with $N_I = 15$ and $D_0 = 1.2$. The relative bias is independent of the mean image displacement, $|\Delta X|/d_I$, and varies linearly with $M\Delta u\Delta t/d_I$, in agreement with equation (50), which is based on analytical models with parameters similar to the parameters of the simulation.

The only way to reduce this bias is to reduce the time interval between pulses, but these measures also decrease the accuracy as $|\Delta X|$ decreases. In principle, the bias can be eliminated by using measurements of the velocity field to estimate gradients and then using a simple formula

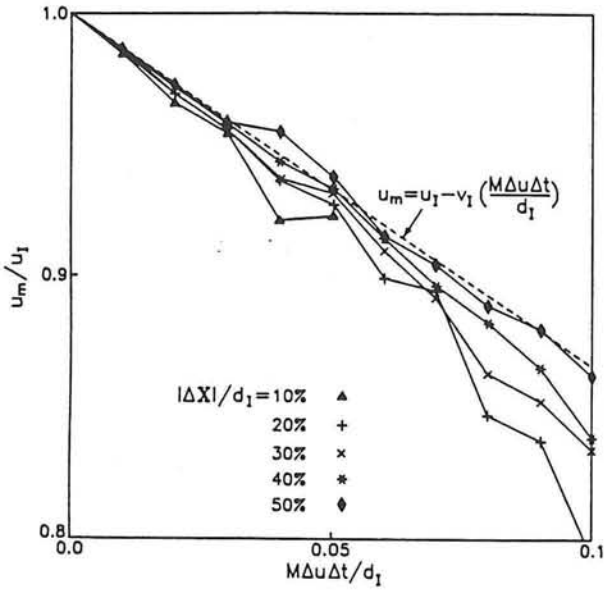

Figure 13. Relative measured mean velocity for a plane shearing velocity in terms of $M\Delta u\Delta t/d_I$. Conditions as in figure 12.

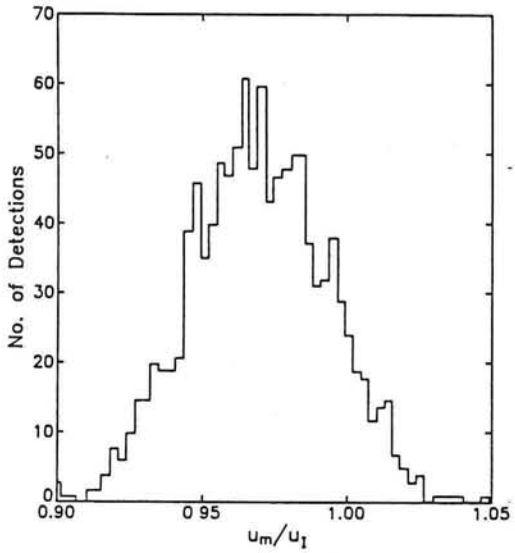

Figure 14. Variation in measured velocity for 1200 realizations where $N_I = 15$, $|\Delta X|/d_I = 0.30$, $M\Delta u\Delta t/d_I = 0.02$ for detectability $D_0 = 1.2$.

like that in figure 13 to correct the measurements. Further work is needed to develop the equation for arbitrary gradients.

Finally, velocity variation causes random errors in valid measurements because the random particle locations within the varying velocity field cause R_{D+} to spread out over a discrete range of displacements which vary for each realization. A typical distribution of sample displacements from 1200 realizations is illustrated in figure 14 with $N_I = 15$, $D_0 = 1.2$, $|\Delta X|/d_I = 0.3$. The mean and standard deviation of the distribution are $\langle u_m \rangle/u_I = 0.97$ and $\sigma_{u_m}/u_I = 0.024$. The 2.4% standard deviation compares with results by Landreth *et al* (1988). Figure 15 relates the rms of the random variation in u_m to the

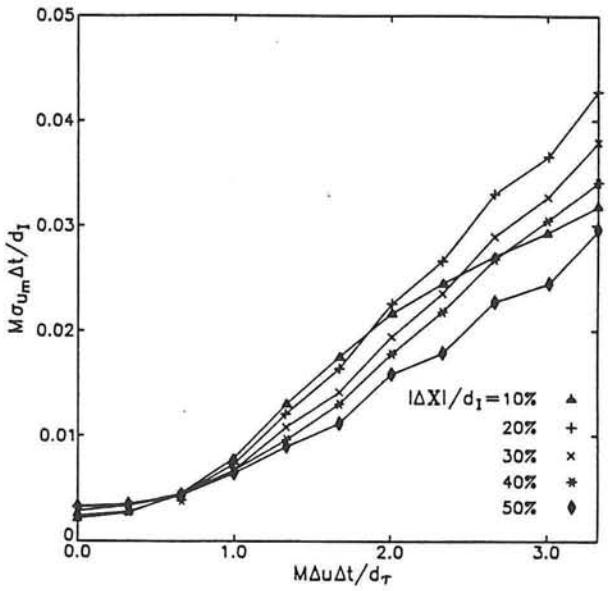

Figure 15. Variation in measured velocity in terms of the relative image displacement variation $M\Delta u\Delta t/d_\tau$ for variable image displacements $|\Delta X|/d_I$, $N_I = 15$, $D_0 = 1.2$.

velocity variation due to gradients for $N_I = 15$ and $D_0 = 1.2$. To restrict the variation in u_m about its mean, which is already biased (equation (50)), the previous criterion for acceptable detection probability applies, ensuring $M\Delta u\Delta t/d_\tau \leqslant 1$. This produces an RMS variation in image displacement less than 0.8% of the spot size, d_I. The selection of Δt ensures an acceptable detection probability, degree of bias and variation in individual measured velocities about the measured mean.

5. Summary and conclusions

The two-pulse PIV method has been studied to optimize its performance for a range of velocity fields. Analyses by full 2-D spatial correlation of direct images and by 2-D Fourier transform of Young's fringes are shown to be equivalent with minor differences when analytical models based on experimental results are used for each approach. Theoretical analyses of both methods and a Monte Carlo simulation of the correlation method reveal the critical parameters of the mean autocorrelation and its fluctuations. The important dimensionless parameters, have been defined and investigated in the Monte Carlo simulation to determine their effect upon the performance of PIV. They are

$$N_I,\ D_0,\ |\Delta X|/d_I,\ |\Delta u|/|u_I|,\ M|\Delta u|\Delta t/d_\tau,\ d_\tau/d_I \text{ and } w\Delta t/\Delta z_0.$$

To optimize this performance, the following broad criteria are recommended; (*a*) $N_I \geqslant 15$, (*b*) $|\Delta X|/d_I \leqslant 0.25$, (*c*) $|w|\Delta t/\Delta z_0 < 0.25$, (*d*) $M|\Delta u|\Delta t/d_I < 0.05$, (*e*) $1.2 < D_0 < 1.5$. While these optimal criteria are a good general combination, modified values can be used for particular flow fields by reference to the appropriate figures.

In order to achieve these optimal parameters the following PIV experimental design procedure can be adopted. To maintain spatial resolution and restrict

effects of out-of-plane motion, choose d_I and Δz_0, based on *a priori* knowledge of the flow field. The seeding density C should be determined such that $N_I \geq 15$, although this can be reduced if other parametric restrictions are small, so that $N_I \sim 10$–20. Then, choose Δt to minimize bias due to velocity gradients, minimize pair losses due to out-of-plane motion and give adequate image displacements as in criteria (b), (c) and (d) above.

The above recommendations and conclusions pertain to two pulse, planar PIV with analysis by full 2-D spatial correlation or equivalently by 2-D Fourier transform of Young's fringes. Analysis of a multipulse system with three or more pulses is continuing and will be considered separately.

Acknowledgment

This material is based on work supported by the National Science Foundation under Grant Nos ATM 86–00509 and ATM 90–20605.

References

Adrian R J 1984 Scattering particle characteristics and their effect on pulsed laser measurements of fluid flow: speckle velocimetry vs. particle image velocimetry *Applied Optics* **23** 1690

—— 1985 Multi-point vector measurement by pulsed laser velocimetry with image compression *Proc. Int. Symp. on Fluid Control and Measurement* (Oxford: Pergamon) p 1087

—— 1986 Multipoint optical measurements of simultaneous vectors in unsteady flow—a review *Int. J. Heat and Fluid Flow* **7** 127

—— 1988a Statistical properties of particle image velocimetry measurements in turbulent flow *Laser Anemometry in Fluid Mechanics* Vol. III (LADOAN Institute Superior Tecnico, Lisbon, Portugal) 115

—— 1988b Double exposure, multiple field particle image velocimetry for turbulent probability density *Opt. Lasers Eng.* **9** 211

Adrian R J and Yao C S 1983 Development of pulsed laser velocimetry for measurement of fluid flow *Proc. 8th Symp. on Turbulence* (*University of Missouri Rolla*) p 170

Barker D B and Fourney M E 1977 Measuring fluid velocities with speckle patterns *Opt. Lett.* **1** 135

Burch J M and Tokarski J M J 1968 Production of multiple beam fringes from photographic scatters *Opt. Acta* **15** 101

Dudderar T D, Meynart R and Simpkins P G 1988 Full field laser metrology for fluid velocity measurement *Opt. Lasers Eng.* **9** 163

Grousson R and Malleck S 1977 Study of flow pattern in a fluid by scattered laser light *Appl. Opt.* **16** 2334

Hesselink L 1988 Digital image processing in flow visualization *Ann. Rev. Fluid Mech.* **20** 421

Landreth C C and Adrian R J 1989 Measurement and refinement of velocity data using high image density analysis in particle image velocimetry *Applications of Laser Anemometry to Fluid Mechanics* ed R J Adrian *et al* (Berlin: Springer) p 484

Landreth C C, Adrian R J and Yao C S 1988 Double pulsed particle image velocimeter with directional resolution for complex flows *Exp. Fluids* **6** 119

Lauterborn W and Vogel A 1984 Modern optical techniques in fluid mechanics *Ann. Rev. Fluid Mech.* **16** 223

Lourenco L and Krothapalli A 1987 The role of photographic parameters in laser speckle or particle image displacement velocimetry *Exp. Fluids* **5** 29

Meynart R 1983 Instantaneous velocity field measurements in unsteady gas flow by speckle velocimetry *Appl. Opt.* **22** 535

Reuss D L, Adrian R J, Landreth C C, French D T and Fansler T D 1989 Instantaneous planar measurements of velocity and large-scale vorticity and strain rate in an engine using particle image velocimetry *Society of Automotive Engineers paper 890616*

Simpkins P G and Dudderar T D 1978 Laser speckle measurement of transient Bénard convection *J. Fluid Mech.* **89** 665

Yao C S and Adrian R J 1984 Orthogonal compression and 1-D analysis technique for measurement of particle displacements in pulsed laser velocimetry *Appl. Opt.* **23** 1687

Revised 2/18/91

Figures unchanged

OPTIMIZATION OF PARTICLE IMAGE VELOCIMETERS

PART II: MULTIPLE PULSED SYSTEMS

Richard D. Keane and Ronald J. Adrian
Department of Theoretical and Applied Mechanics
University of Illinois at Urbana-Champaign
Urbana, Illinois 61801
Classification Number: 47.80

To appear in *Measurement Science and Technology (1991)*

ABSTRACT

The spatial resolution, detection rate and reliability of a particle image velocimeter depend critically upon careful selection of a number of parameters of the PIV system and the fluid motion. From earlier work, an analytic model and a Monte Carlo computer simulation have been generalized to analyze the effects of experimental parameters and to optimize system parameters in a multiple pulsed PIV system. The set of six nondimensional parameters that were most significant in optimizing double pulsed PIV performance are generalized for a multiple pulsed system and shown to be similarly significant.

They are the data validation criterion, the particle image density, the relative in-plane image displacement, the relative out-of-plane displacement, the velocity gradient and the ratio of the mean image displacement to the interrogation spot diameter.

It is shown that a single transformation can be applied to the method of interrogation by autocorrelation analysis to extend these results to interrogation by two dimensional Fourier transform analysis of the Young's fringes. Thus, the non-dimensional parameters are studied for the case of interrogation by autocorrelation analysis.

It is shown that optimal parameters for a multiple pulsed system can be generalized from earlier results for a double pulsed system. A multiple pulsed system performs optimally when the density of image pairs exceeds 10-20 and the maximum relative in plane and out of plane displacements are limited to 25%. Velocity gradients reduce the signal strength causing a loss of valid data and produce statistical bias. Expressions for the statistical bias of three dimensional velocity fields are developed and corrections for this bias are presented. Furthermore, recommendations for experimental procedures to minimize the bias effects and reduction of signal strength are outlined.

1. INTRODUCTION

Particle Image Velocimetry (PIV) is a quantitative method of measuring velocity fields instantaneously in experimental fluid mechanics (Simpkins and Dudderar (1978), Adrian (1986), Meynart (1983), Dudderar, Simpkins and Meynart (1988), Lauterborn and Vogel (1984)). While earlier PIV systems used double pulsed photographs, many recent experimental investigations have used multiply exposed photographs. An investigation using triple exposed photographic film has been carried out by Lourenco and Krothapalli (1987) to study the flow field behind an impulsively started circular cylinder. Meynart, Simpkins and Dudderar (1987) studied an unsteady descending plume in a water filled rectangular convection cell by taking ten equally spaced exposures on a photographic plate and digitally processing the Young's fringe pattern to produce velocity vector fields. In addition, Cenedese and Paglialurga (1990) have developed digital techniques to analyze images of ten successive exposures in studying vertical structures in a mixer. Arroyo, Yonte, Quintanilla and Savirón (1988) have studied Rayleigh-Bénard convection using a very high number of exposures ranging from 13 to 40. The velocity field is obtained by 1-D integration method on optically produced Young's fringes in a point-by-point technique. In these multiple pulsed planar PIV systems, light pulses of intensity $I_{0i}(\mathbf{x}), i = 1, \cdots, n$ each separated by possibly different time intervals Δt_i, $i = 1, \cdots, n-1$ illuminate a light sheet of thickness Δz_0 as shown in figure 1 to produce a multiply exposed single photographic frame having n-tuples of particle images from which simultaneous in-plane velocity measurements can be made.

The interrogation procedure for measuring displacements, $\Delta \mathbf{X}$ in the image plane for a multiple pulsed system, is carried out in identical manner to a double pulsed system. A small interrogation spot centred on $\mathbf{X}_I$ with diameter d_I is illuminated by an interrogation beam of intensity $I_I(\mathbf{X})$. The displacement of successive particle images $\Delta \mathbf{X}(\mathbf{X}_I)$ is determined for each location $\mathbf{X}_I$ to produce image displacements over the entire image plane. Assuming the successive pulse intervals are equal to Δt, the measured in-plane velocity is calculated as

$$\mathbf{u}_m(\mathbf{x}_I) = \Delta \mathbf{X}(\mathbf{X}_I)/M\Delta t \quad (1)$$

where $\mathbf{x}_I$ is the location in the fluid corresponding to the interrogation spot location on the photograph, $\mathbf{X}_I$.

Either the direct imaging method or the Young's fringe method can be employed in calculating mean particle image displacements at each interrogation spot. In the direct imaging method, the full 2-D autocorrelation of digitized particle image intensities within the interrogation spot yields mean image displacements from peak values in the autocorrelation function. Likewise, the Young's fringe method determines mean image displacements by taking a two-dimensional Fourier transform of digitized Young's fringe data. The use of multiple pulses separated by equal pulse intervals, Δt, improves the strength of the displacement correlation in both the Fourier transform of the Young's fringes and autocorrelation function, by increasing the number of correlated pairs of images. Henceforth, we shall assume equal pulse intervals, Δt, unless otherwise indicated.

The performance of a multiple pulsed PIV system is determined by the spatial resolution, the detection rate and the accuracy or reliability of the velocity measurements, as defined for a double pulsed system (Keane and Adrian (1990)). These three parameters are affected by the interrogation criteria and the experimental configuration and to optimize the performance of PIV, it is necessary to understand the influence of all interrogation and experimental parameters.

In earlier work, an analytical model and a Monte Carlo simulation were developed to determine the most significant non-dimensional parameters in optimizing double pulsed systems. This work has now been extended and generalized by analyzing multiple pulsed systems similarly to optimize the performance of PIV for a full 2-D interrogation by either spatial autocorrelation or Young's fringes.

As for a double pulsed system, paraxial image recording is assumed for simplicity. The marker particles have constant diameter so that the particle images have equal diameters. There is

assumed to be no noise background in the image field and the particle density is sufficiently low to discount the probability of images overlapping, during any one exposure. Locally linear, three-dimensional velocity fields are considered.

The experimental and interrogation parameters can be reduced to a small set of dimensionless parameters which are generalized from the double pulsed system parameters by considering displacements between successive pulses and the time interval separating successive pulses. In a multiple pulsed system, the particle image pair density, N_P, measures the number of particle image pairs separated by the pulse interval, Δt, in an n-pulse system for a given mean concentration of seeded particles, C. It is defined for a circular interrogation spot of diameter, d_I to be

$$N_P = (n-1)C\frac{\pi d_I^2}{4M^2}\Delta z_0 = (n-1)N_I \qquad (2)$$

where N_I is the equivalent particle image density for a double pulsed system. The dimensionless mean displacement of particle images between successive pulses, relative to the spot diameter is $|\Delta \mathbf{X}|/d_I$. The appropriate dimensionless out-of-plane motion of the particles in the light sheet is $\Delta z/\Delta z_0$ as for a double pulsed system, where $\Delta z = w\Delta t$ is the out-of-plane displacement between successive pulses. The extent of image displacement variation between successive pulses caused by velocity gradients can be expressed in terms of d_τ and d_I. The optimal values and acceptable ranges for these parameters and the non-dimensional detectability criterion D_0, defined as for a double pulsed system, will be expressed in terms of given experimental parameters.

As for a double pulsed system, these non-dimensional parameters are important for both methods of interrogation.

2. INTERROGATION METHODS

2.1 Spatial Correlation

When a photograph is interrogated by a light beam of intensity $I_I(\mathbf{X}-\mathbf{X}_I)$, centred at $\mathbf{X}_I$, the transmitted light intensity immediately after the photograph is

$$I(\mathbf{X}) = I_I(\mathbf{X}-\mathbf{X}_I)\tau(\mathbf{X}) \tag{3}$$

where $\tau(\mathbf{X})$, the intensity transmissivity of the photograph is

$$\tau(\mathbf{X}) = \sum_i \sum_{j=1}^{n} I_{0j}(\mathbf{x}_i)\tau_0(\mathbf{X}-M\mathbf{x}_i(t_j)) \tag{4}$$

where I_{0j} is the intensity of the j-th illuminating beam pulse and $\mathbf{x}_i(t_j)$ is the location of the ith particle at time t_j, the time of the j-th pulse. $\tau_0(\mathbf{X}-M\mathbf{x})$ represents the transmissivity of an individual particle image per unit of illuminating intensity. It is taken to be identical for all particles. For multiple pulses being equally spaced in time, equation (4) becomes

$$\tau(\mathbf{X}) = \sum_i \sum_{j=1}^{n} I_{0j}(\mathbf{x}_i)\tau_0(\mathbf{X}-M\mathbf{x}_i(t+(j-1)\Delta t)) \tag{5}$$

The spatial autocorrelation of $I(\mathbf{X})$ with separation $\mathbf{s}$ is approximated by the spatial average over the interrogation spot

$$R(\mathbf{s}) = \int I(\mathbf{X})I(\mathbf{X}+\mathbf{s})d\mathbf{X} \tag{6}$$

It consists of five components, (Adrian (1988a))

$$R(\mathbf{s}) = R_C(\mathbf{s})+R_P(\mathbf{s})+R_{D^+}(\mathbf{s})+R_{D^-}(\mathbf{s})+R_F(\mathbf{s}) \tag{7}$$

$R_{D^+}(\mathbf{s})$ is the correlation of all earlier images shifted by $\mathbf{s}$ with subsequent unshifted images, while $R_{D^-}(\mathbf{s})$ is the correlation of all later images shifted by $\mathbf{s}$ with prior unshifted images. Both $R_{D^+}(\mathbf{s})$ and $R_{D^-}(\mathbf{s})$ can be decomposed further when the pulse separation is constant:

$$R_{D^+} = R^{(1)}_{D^+}(\mathbf{s})+R^{(2)}_{D^+}(\mathbf{s})+\cdots+R^{(n-1)}_{D^+}(\mathbf{s}) \tag{8}$$

where $R_{D^+}^{(k)}(\mathbf{s})$ is the correlation of all earlier images shifted by $\mathbf{s}$ with subsequent unshifted images at later time separation, $k\Delta t$, (Keane 1990). A similar decomposition exists for $R_{D^-}(\mathbf{s})$. Figure 2a illustrates the components of $R(\mathbf{s})$ for a quadruple pulsed system for a single interrogation spot in which the velocity field is constant and which contains, on average, five randomly located particles. $I_I(\mathbf{X})$ is constant across the interrogation spot, and the particle image transmissivity, τ_0, is modelled as a Gaussian function with diameter, d_τ. The four light sheets are identical with constant intensity I_0 inside the light sheet and zero outside.

To determine the mean image displacement across the interrogation spot between successive pulses, the centroid of $R_{D^+}^{(1)}(\mathbf{s})$ is located by

$$\overline{\mu}_{D^+}^{(1)} = \frac{\int \mathbf{s} R_{D^+}^{(1)}(\mathbf{s}) d\mathbf{s}}{\int R_{D^+}^{(1)}(\mathbf{s}) d\mathbf{s}}. \tag{9}$$

in an identical manner to locating $\overline{\mu}_{D^+}$ for a double pulsed system with the mean velocity estimated as $\overline{\mu}_D^{(1)}/M\Delta t$. Similarly, $\overline{\mu}_{D^+}^{(1)}$ can be estimated by locating $\mathbf{s}_{D^+}$, the position of the peak value of $R_{D^+}(\mathbf{s})$, by a search over the s-plane, taking into account the self correlation peak at the origin. The centroid of $R_{D^+}^{(1)}$ is approximated by integration over a region around the peak value, as for double pulsed systems.

2.2 Young's fringe method

The two-dimensional Fourier transform of the intensity of a Young's fringe pattern, $G(\mathbf{s})$, can be shown by the convolution theorem to be equal to the convolution of the Fourier transforms

$$G(\mathbf{s}) = \frac{f^2\lambda^2}{4\pi^2} \int E(\mathbf{X}) E^*(\mathbf{X}-\mathbf{s}) d\mathbf{X} \tag{10}$$

This convolution is very similar to the direct imaging correlation function of equation (6) and can be decomposed into five components in a manner similar to (7), viz.

$$G(\mathbf{s}) = G_C(\mathbf{s}) + G_P(\mathbf{s}) + G_{D^+}(\mathbf{s}) + G_{D^-}(\mathbf{s}) + G_F(\mathbf{s}) \tag{11}$$

Likewise, $G_{D^+}(\mathbf{s})$ and $G_{D^-}(\mathbf{s})$ can be decomposed into further components similarly to equation (9), Keane (1990).

$$G_{D^+}(\mathbf{s}) = G_{D^+}^{(1)}(\mathbf{s}) + G_{D^+}^{(2)}(\mathbf{s}) + \cdots + G_{D^+}^{(n-1)}(\mathbf{s}) \tag{12}$$

The mean image displacement across the interrogation spot is calculated by locating the centroid of $G_{D^+}^{(1)}(\mathbf{s})$ and similar approximations are made by using peak detection searches and centroidal calculations around these peaks.

Figure 2 illustrates the relationship between the two methods of calculating image displacements. As for double pulsed systems, the particle image intensity transmissivities were modelled as Gaussian functions of diameter d_τ so that the particle image amplitude transmissivities have diameters $\sqrt{2}\,d_\tau$ and are additive. Hence, the diameter of $G_{D^+}^{(j)}$ is wider than that of $R_{D^+}^{(j)}$ by a factor of $\sqrt{2}$, while the peak location of $G_{D^+}^{(j)}(\mathbf{s})$ is identical to that of $R_{D^+}^{(j)}(\mathbf{s})$, as in Figure 2b.

3. MEAN AUTOCORRELATION AND MEAN FOURIER TRANSFORM OF YOUNG'S FRINGES

3.1 General velocity fields

For a given velocity field, $\mathbf{u}(\mathbf{x})$, the conditional average $< R(\mathbf{s}) \mid \mathbf{u} >$ calculated over an ensemble of realizations containing velocity field $\mathbf{u}(\mathbf{x})$ and different sets of randomly located particles, measures the mean behaviour of R given the flow field $\mathbf{u}$.

Taking conditional averages of equations (7) and (8) yields

$$< R(\mathbf{s}) \mid \mathbf{u} > = < R_C(\mathbf{s}) \mid \mathbf{u} > + < R_P(\mathbf{s}) \mid \mathbf{u} > + < R_{D^+}(\mathbf{s}) \mid \mathbf{u} > + < R_{D^-}(\mathbf{s}) \mid \mathbf{u} > ; \tag{13}$$

where $< R_F(\mathbf{s}) \mid \mathbf{u} > \;=\; 0$; and

$$< R_{D^*}(\mathbf{s}) \mid \mathbf{u} > = < R_{D^*}^{(1)}(\mathbf{s}) \mid \mathbf{u} > + < R_{D^*}^{(2)}(\mathbf{s}) \mid \mathbf{u} > + \cdots + < R_{D^*}^{(n-1)}(\mathbf{s}) \mid \mathbf{u} > \tag{14}$$

In order to study the important parameters of $< R(\mathbf{s}) \mid \mathbf{u} >$ for a variety of velocity fields, earlier specific models of the transmissivity functions and light intensities are used: The intensities of the light sheet pulses I_{0i} are modelled as either top hat functions equal to I_0 within the light sheet and zero outside of it, or as Gaussian functions centred on the light sheet with width Δz_0 measured at the e^{-2} points. The interrogation beam intensity is modelled for computational simplicity as a Gaussian function centred at $\mathbf{X}_I$ with diameter, d_I, while all particle image transmissivities are Gaussian functions centred at the image centre with diameter, d_τ. Thus, we have

$$I_{0i}(\mathbf{x}) = I_0, \quad |z| < \Delta z_0/2 \qquad \text{or} \qquad I_0 e^{-8z^2/\Delta z_0^2}$$

$$0, \quad \text{otherwise} \tag{15}$$

$$I_I(\mathbf{X}-\mathbf{X}_I) = I_{I0} e^{-8|\mathbf{X}-\mathbf{X}_I|^2/d_I^2} \tag{16}$$

and

$$\tau_0(\mathbf{X}) = \frac{8\tau_{00}}{\pi d_\tau^2} e^{-8|\mathbf{X}|^2/d_\tau^2} \tag{17}$$

where $\tau_{00} = \int \tau_0 d\mathbf{X}$ is determined by the photographic process and the development process.

The components of equations (13) and (14) for general particle displacement $\Delta \mathbf{x}_{j,j+i}$ between pulses j and $j+i$, become

$$< R_C(\mathbf{s}) > = \frac{n^2}{\pi} I_0^2 I_{I0}^2 \tau_{00}^2 \frac{N_I^2}{d_I^2} \exp\left(-\frac{4 \mid \mathbf{s} \mid^2}{d_I^2} \right) \tag{18}$$

$$< R_P(\mathbf{s}) > = \frac{n}{\pi} I_0^2 I_{I0}^2 \tau_{00}^2 \frac{N_I}{d_\tau^2} \exp\left(-\frac{4 \mid \mathbf{s} \mid^2}{d_\tau^2} \left(1 + \frac{d_\tau^2}{d_I^2} \right) \right) \tag{19}$$

$$< R_{D^*}^{(i)}(\mathbf{s}) \mid \mathbf{u} > = C \int d\mathbf{x} \sum_j I_0(z) I_0(z + \Delta z_{j,j+i}) \int d\mathbf{X} I_{I0}^2) \exp(-8 \mid \mathbf{X} \mid^2 / d_I^2)$$

$$\times \exp(-8 \mid \mathbf{X} + \mathbf{s} \mid^2 / d_I^2) \cdot \left(\frac{8\tau_{00}}{\pi d_\tau^2} \right)^2 \exp(-8 \mid \mathbf{X} - M\mathbf{x} \mid^2 / d_\tau^2)$$

$$\times \exp(-8 \mid \mathbf{X} - M\mathbf{x} + \mathbf{s} - M\Delta\mathbf{x}_{j,j+i} \mid^2 / d_\tau^2) \tag{20}$$

These results generalize equations (25), (26) and (27) of Keane and Adrian (1990) for double pulsed systems and are valid for arbitrary **u** through the displacements $\Delta\mathbf{x}_{j,j+i}$.

As expected, $< R_C(\mathbf{s}) >$, which is approximately the convolution of the mean interrogation intensity with itself, is a broad Gaussian function of **s** with diameter $\sqrt{2}\, d_I$ and an amplitude proportional to the square of the mean number of particle images, $(nN_I)^2$. Likewise, $< R_P(\mathbf{s}) >$, the mean of the self correlation is a narrow Gaussian function of diameter $\sim\sqrt{2}\, d_\tau$ with amplitude proportional to the mean number of particle images, nN_I. $< R_{D^*}^{(i)}(\mathbf{s}) \mid \mathbf{u} >$ depends upon the velocity field **u** and can be determined explicitly for special cases of $\mathbf{u}(\mathbf{x},t)$ as for double pulsed systems.

The statistical properties of $G(\mathbf{s})$, the Fourier transform of the Young's fringes are determined similarly by taking conditional averages of each term in equations (11) and (12). The specific model above is used to compare the behaviour of $< G(\mathbf{s}) \mid \mathbf{u} >$ with that of $< R(\mathbf{s}) \mid \mathbf{u} >$ and to generalize the double pulsed system analysis.

Using the appropriate Gaussian functions for image amplitude transmissivity and interrogation beam amplitude and assuming all image transmissivity phases are equal to zero, the components of $< G(\mathbf{s}) \mid \mathbf{u} >$ become

$$< G_C(\mathbf{s}) > \;=\; \frac{f^2\lambda^2}{\pi^2} I_0^2 I_{I0} \tau_{00} n^2 N_I^2 \frac{d_\tau^2}{d_I^2} \exp\left(-\frac{2\,|\mathbf{s}|^2}{d_I^2}\right) \tag{21}$$

$$< G_P(\mathbf{s}) > \;=\; \frac{f^2\lambda^2}{4\pi^2} I_0^2 I_{I0} \tau_{00} n N_I \exp\left(-\frac{2\,|\mathbf{s}|^2}{d_\tau^2}\left(1+\frac{d_\tau^2}{d_I^2}\right)\right) \tag{22}$$

$$< G_{D^*}^{(i)}(\mathbf{s}) \mid \mathbf{u} > = \frac{f^2\lambda^2}{4\pi^2} C \int d\mathbf{x} \sum_j I_0(z) I_0(z + \Delta z_{j,j+i})$$

$$\times \int d\mathbf{X} I_{I0} \exp(-4\,|\,\mathbf{X}\,|^2/d_I^2) \exp(-4\,|\,\mathbf{X}-\mathbf{s}\,|^2/d_I^2)$$

$$\times \frac{8\tau_{00}}{\pi d_\tau^2} \exp(-4\,|\,\mathbf{X}-M\mathbf{x}\,|^2/d_\tau^2) \exp(-4\,|\,\mathbf{X}-M\mathbf{x}-\mathbf{s}-M\Delta\mathbf{x}_{j,j+i}\,|^2/d_\tau^2)$$

(23)

Hence, as for $< R_C(\mathbf{s}) >$, $< G_C(\mathbf{s}) >$ is a broad Gaussian function of $\mathbf{s}$ with amplitude proportional to $(nN_I)^2$ and with diameter $2d_I$, i.e. $\sqrt{2}$ times larger than the diameter of $< R_C(\mathbf{s}) >$. $< G_P(\mathbf{s}) >$ is a narrow pedestal function of $\mathbf{s}$ with amplitude proportional to nN_I and with diameter $\sim 2d_\tau$ when $d_\tau/d_I \ll 1$, again $\sqrt{2}$ times larger than the diameter of $< R_P(\mathbf{s}) >$.

3.2 Weak velocity gradients

If the velocity field varies slowly within the interrogation spot, it is approximated by the locally constant velocity field evaluated at the centre of the interrogation volume so that for equally spaced pulses

$$\mathbf{u}(\mathbf{x}) \;=\; \mathbf{u}_I \;=\; \mathbf{u}(\mathbf{x}_I). \tag{24}$$

and

$$\Delta\mathbf{x}_{j,j+i}(\mathbf{x},t) \;=\; i\mathbf{u}_I\Delta t \tag{25}$$

The criteria for this approximation will be developed in the next section on strongly varying velocity fields, as a generalization of double pulsed systems, by analyzing equation (35).

For constant velocity, the mean displacement components of equation (20) simplify to

$$< R_{D^*}^{(i)}(\mathbf{s}) \mid \mathbf{u} > \;=\; \frac{1}{\pi} I_0^2 I_{I0}^2 \tau_{00}^2 \frac{(n-i)N_I}{d_\tau^2} F_0(i w_I \Delta t) F_I(\mathbf{s})$$

$$\times \exp(-4 \mid \mathbf{s} - M \mathbf{u}_I i \Delta t \mid^2 / d_\tau^2) \qquad (26)$$

and, in particular, when $i = 1$

$$< R_{D^*}^{(1)}(\mathbf{s}) \mid \mathbf{u} > = \frac{1}{\pi} I_0^2 I_{I0}^2 \tau_{00}^2 \frac{N_P}{d_\tau^2} F_0(w_I \Delta t) F_I(\mathbf{s}) \exp(-4 \mid \mathbf{s} - M \mathbf{u}_I \Delta t \mid^2 / d_\tau^2)$$

(27)

where F_I is the normalized correlation of the interrogation intensity across the interrogation spot as defined by Adrian (1988a). $F_0(\Delta z)$ is the normalized correlation of the intensities of two successive light pulses in terms of the out of plane displacement Δz between the pulses. In general, it depends upon individual light pulse intensities which are identical in this model, viz

$$F_0(\Delta z)_{ij} \;=\; \int dz I_{0i}(z) I_{0j}(z + \Delta z) / \int dz I_{0i}(z) I_{0j}(z) \qquad (28)$$

As for double pulsed systems, the signal strength of $< R_{D^*}^{(1)}(\mathbf{s}) \mid \mathbf{u} >$ is proportional to the mean number of particle image pairs, N_p, in the interrogation volume. It is decreased by the fraction of incomplete image pairs that result from particles leaving the interrogation volume due to both out-of-plane and in-plane motion.

These reductions in the number of complete image pairs can be represented quantitatively by F_I and F_0 for in-plane and out-of-plane motion respectively and reduce the mean number of particle image pairs in the window to the lower weighted mean $F_0 F_I N_p$, as expressed in equation (27). As the above reduction in signal strength is caused physically by loss of complete image pairs, it is known as the loss-of-pairs effect. This loss-of-pairs effect increases as higher order displacement

components of $< R_{D^+}(\mathbf{s}) \mid \mathbf{u} >$ are considered because image displacements increase. By evaluating the successive components at $\mathbf{s}_i = M\mathbf{u}_I i\Delta t$, which approximate the location of the maximum value of $R_{D^+}^{(i)}$, equation (26) yields

$$< R_{D^+}^{(i)}(\mathbf{s}_i) \mid \mathbf{u} > = I_0^2 I_{I0}^2 \tau_{00}^2 F_0(w_I i\Delta t) F_I(M\mathbf{u}_I i\Delta t)\,(n-i) N_I/\pi d_\tau^2 \tag{29}$$

illustrating increasing loss-of-pairs effect as F_0, F_I decrease as $i\Delta t$ increases.

The loss-of-pairs effect is minimized by considering $R_{D^+}^{(1)}$ rather than higher order components and limiting the dimensionless parameters $w_I\Delta t/\Delta z_0$ and $M \mid \mathbf{u}_I \mid \Delta t/d_I$ as for double pulsed systems. Increased spatial resolution is achieved by locating peak positions of $< R_{D^+}^{(i)} >$ for increasing i, but the signal strength diminishes, because F_0, F_I decrease with increasing displacements.

The location of the maximum value of $< R_{D^+}^{(i)} >$ is diminished by the factor $F_I(\mathbf{s})$ in equation (29) by a constant factor to yield

$$\mathbf{s}_{D^+}^{(i)} \;=\; M\mathbf{u}_I i\Delta t/(1 + d_\tau^2/d_I^2) \tag{30}$$

Thus, care must be taken in multiple pulsed systems to minimize the error of order d_τ^2/d_I^2 by minimizing image diameters or to provide explicit corrections for it.

The signal quality of a multiple pulsed system increases as the number of pulses increases as can be seen by examining the ratio of the amplitude of the first displacement correlation to that of the self correlation

$$< R_{D^+}^{(1)}\left(\mathbf{s}_{D^+}^{(1)}\right) \mid \mathbf{u} > / R_P(\mathbf{0}) = \left(\frac{n-1}{n}\right) F_0(w_I\Delta t) \exp(-4 \mid M\mathbf{u}_I\Delta t \mid^2 /(d_I^2 + d_\tau^2)) \tag{31}$$

The amplitude of the first displacement correlation peak approaches that of the self-correlation peak with increasing number of pulses. In addition, a comparison of the amplitude of $< R_{D^+}^{(1)} >$ with the

expected noise peak amplitude of $R_C + R_F$ reveals that this signal-to-noise ratio increases with order $2(n-1)/n$ as an n-pulsed system is used instead of a double pulsed system. For a triple pulsed system, the mean signal-to-noise ratio is increased by 33% over that of a double pulsed system.

The analysis of the mean Fourier transform of the Young's fringes proceeds similarly with the peak locations of $< G_{D^+}^{(i)}(\mathbf{s}) \mid \mathbf{u} >$ being identical to those of $< R_{D^+}^{(i)}(\mathbf{s}) \mid \mathbf{u} >$ while all Gaussian diameters are broadened by a factor of $\sqrt{2}$. The loss-of-pairs effect generalizes likewise from the double pulsed system and the signal strength amplitude of $< G_{D^+}^{(1)}\left(\mathbf{s}_{D^+}^{(1)}\right) \mid \mathbf{u} >$ compared to $G_P(\mathbf{0})$ is modified only by peak broadening, viz,

$$< G_{D^+}^{(1)}\left(\mathbf{s}_{D^+}^{(1)}\right) \mid \mathbf{u} > / G_P(\mathbf{0}) = \left(\frac{n-1}{n}\right) F_0(w_I \Delta t) \exp\left(\frac{-2 \mid M\mathbf{u}_I \Delta t \mid^2}{d_I^2 + d_\tau^2}\right) \tag{32}$$

3.3 Strong velocity gradients

As discussed in Keane and Adrian (1990), velocity variations in the interrogation volume due to strong gradients, as in turbulent flow, cause a distribution of image displacements over finite regions in the correlation plane which affects measurements in two ways.

Finally, the location of the centroid of $R_{D^+}^{(1)}$ corresponds to a weighted average of image displacements which is statistically biased towards the displacement of lower speed particles. This is known as gradient bias. In addition, the distribution of image displacements diminishes the amplitude of each displacement correlation component peak and broadens its width. The signal strength decreases until the correlation peaks are undetectable, leading to failed measurements for regions of large velocity gradient. This is known as detection bias.

To quantify these two effects upon the behaviour of $< R_{D^+}^{(i)} \mid \mathbf{u} >$ the local velocity field within the interrogation volume is expanded in a first order Taylor series about $\mathbf{x}_i$

$$u_i(\mathbf{x}) = u_i(\mathbf{x}_I) + (\partial u_i / \partial x_j)_{\mathbf{x}_I} (x_j - x_{Ij}). \tag{33}$$

As the results depend upon the deformation tensor $d_{ij} = (\partial u_i/\partial x_j)_{x_1}$, two special cases considered in Keane and Adrian (1990), namely simple shear and pure rotation, will be generalized for the n pulse system, and a general three dimensional velocity gradient will be analyzed.

For a given particle density, N_I, and time interval, Δt, between successive pulses, the relationship between the displacement correlation $< R_{D^*}^{(1)}(\mathbf{s}) \mid \mathbf{u} >$ for an n pulsed system and $< R_{D^*}(\mathbf{s}) \mid \mathbf{u} >$ for a double pulsed system can be seen from equation (20) above and equation (27) of Keane and Adrian (1990) to be

$$< R_{D^*}^{(1)}(\mathbf{s}) \mid \mathbf{u} > \;=\; (n-1) < R_{D^*}(\mathbf{s}) \mid \mathbf{u} >_{2\ \text{pulses}} \tag{34}$$

Thus, the signal strength is improved and, consequently, detection bias is reduced for an n pulse system. The effect of velocity variation upon gradient bias is identical, however, for both systems. The peak and centroid of $< R_{D^*}^{(1)}(\mathbf{s}) >$ are located at the same position as the peak and centroid of $< R_{D^*}(\mathbf{s}) >$ in a double pulse system and in the two cases cited above, the amplitude reduction factor and peak broadening factors for $< R_{D^*}^{(1)}(\mathbf{s}) >$ are identical with those given earlier for $< R_{D^*}(\mathbf{s}) >$ in a double pulse system.

In general, for a three-dimensional velocity gradient, in which $(\partial u_i/\partial x_j)_{x_1}$ are nonzero, the peak and centroid of $< R_{D^*}^{(1)} >$ are located at

$$\mathbf{s}_{D^*}^{(1)} = \left(M u_I \Delta t - M u_I \Delta t \left(\frac{M \Delta u_x \Delta t}{d_I}\right) - M v_I \Delta t \left(\frac{M \Delta u_y \Delta t}{d_I}\right) - M w_I \Delta t \left(\frac{M \Delta u_z \Delta t}{\Delta z_0}\right),\right.$$
$$\left. M v_I \Delta t - M u_I \Delta t \left(\frac{M \Delta v_x \Delta t}{d_I}\right) - M v_I \Delta t \left(\frac{M \Delta v_y \Delta t}{d_I}\right) - M w_I \Delta t \left(\frac{M \Delta v_z \Delta t}{\Delta z_0}\right)\right) \tag{35}$$

where

$$(\Delta u_x, \Delta u_y, \Delta u_z) \;=\; \left(\frac{\partial u}{\partial x} \cdot \frac{d_I}{2M}, \frac{\partial u}{\partial y} \cdot \frac{d_I}{2M}, \frac{\partial u}{\partial z} \cdot \frac{\Delta z_0}{2M}\right)_{x_1}$$

and

$$(\Delta v_x, \Delta v_y, \Delta v_z) = \left(\frac{\partial v}{\partial x} \cdot \frac{d_I}{2M}, \frac{\partial v}{\partial y} \cdot \frac{d_I}{2M}, \frac{\partial v}{\partial z} \cdot \frac{\Delta z_0}{2M} \right)_{x_I}$$

where it is assumed that $d_\tau \ll d_I$ and second order effects of velocity variation are ignored. This location is biased against faster moving particles but is independent of velocity variation in the out-of-plane component, w, the particle image density or the number of pulses. The dimensionless parameters determining the extent of gradient bias are of the form $d_{ij}\Delta t/2$ measuring the variation of each in-plane velocity component caused by both in-plane and out-of-plane velocity variations.

The approximation of a locally constant velocity field in the previous section can be made provided that the extent of the gradient bias in $s_{D^*}^{(1)}$ expressed in equation (35) is sufficiently low. This is determined by the dimensionless parameters, $d_{ij}\Delta t/2$, and the mean image displacement, $M\mathbf{u}_I\Delta t$. In order to achieve a gradient bias less than α of the mean image displacement, equation (35) shows that we need $\| d_{ij}\Delta t/2\| < \alpha$. Further examples of this restriction will be given in section 4.4.

The amplitude of $< R_{D^*}^{(1)}(\mathbf{s}) \mid \mathbf{u} >$ is dependent upon dimensionless parameters of the form, $M\Delta u_z \Delta t/d_\tau$, which measure the variation in peak location as a function of particle image diameter. These parameters can also be rewritten in the form $(d_{ij}\Delta t/2)(d_I/d_\tau)$ and $(d_{ij}\Delta t/2)(\Delta z_0/d_\tau)$ illustrating the need for judicious selections of $d_I, \Delta z_0$ and Δt to minimize the variation in velocity across an interrogation volume and consequently both gradient and detection bias.

As in Keane and Adrian (1990), the analysis of the mean Fourier transform of the Young's fringes, $< G_{D^*}^{(1)}(\mathbf{s}) \mid \mathbf{u} >$, illustrates that the peak location $s_{D^*}^{(1)}$ and the extent of gradient bias are identical to those above for $< R_{D^*}^{(1)}(\mathbf{s}) \mid \mathbf{u} >$ and are not affected by peak broadening. Thus the results for one form of analysis can be transferred directly into results for the other form with due allowance for peak broadening effects. The following section will consider only the autocorrelation method to determine statistical fluctuations of the autocorrelation function.

4. AUTOCORRELATION FLUCTUATIONS AND PERFORMANCE

4.1 Validation

The performance of an interrogation method as a means of measuring image displacements for a multiple pulse PIV system is evaluated in an identical manner to the interrogation method for a double pulse system. This performance is measured in terms of the spatial resolution, the data yield, the valid data yield and the accuracy of the data measurements that are considered to be valid. The interrogation method's performance is affected by random fluctuations of the autocorrelation function, and these can be related to the dimensionless parameters presented in the Introduction and discussed in section 3 and specific details of the interrogation procedure.

We consider an interrogation procedure for a multiple pulse system that is identical to that of a double pulse system. It locates the highest peak in $R(\mathbf{s})$, excluding the self-correlation peak R_P and, in assuming this peak corresponds to $R_{D^+}^{(1)}$, compares it to the second tallest peak. To improve computational speed, the procedure does not distinguish noise peaks from the peaks corresponding to $R_{D^+}^{(2)}, \cdots, R_{D^+}^{(n)}$ in determining the second tallest peak and calculating the detectability, D, as the ratio of the tallest peak to the second tallest peak.

The centroid of the correlation peak is determined by integrating a small area around the peak, as described in Keane and Adrian (1990), in order to calculate $\mathbf{u}_n$ from equation (1).

4.2 Monte Carlo simulation

As the analysis of the mean correlation function does not directly address questions concerning probabilities of measurement and the fluctuation in the statistics of individual velocity measurements the numerical simulation of the PIV image field and interrogation analysis used in double pulse system analysis has been extended to multiple pulse systems. The details of the simulation can be found in section 4.2 of Keane and Adrian (1990). The simulation has been performed with 2,3,4 and 6 pulse systems for three dimensional velocity fields over a range of velocity gradients. Figure 3 shows a simulated region of the interrogation plane for a four pulse system in which a constant velocity causes a mean particle displacement with $M\Delta\mathbf{x}/d_I = (0.1, 0.1, 0.1)$ where $N_I = 5$.

The detection probability for a given ensemble of realizations of experimental parameters is defined to be the probability, calculated over all realizations, of a single realization yielding a velocity measurement for which the detectability is larger than the pre-set threshold level, D_0. The valid detection probability is the probability that such a measurement is valid by making a comparison between $\mathbf{u}_m$ and $\mathbf{u}_I$, the known velocity field.

4.3 Performance: Weak velocity gradients

The effect of varying the particle density N_I for a four pulse systems is illustrated in figure 4 for a range of image displacements, $|\Delta \mathbf{X}|/d_I$ using a detectability criterion of $D_0 = 1.2$ and constant in-plane velocities. Unlike the double pulse analysis, detection probability and valid detection probability increase monotonically with increasing N_I. To achieve a valid detection probability of at least 90%, the particle density N_I must be greater than 8, 5 and 3 with $|\Delta \mathbf{X}|/d_I < 0.3$ for three, four and six pulse systems respectively. The latter bound of $N_I \geq 4$ for a multiple pulsed PIV system where $n \geq 5$ agrees with the estimate given by Lourenco and Krothapalli (1987).

The analytical model of the correlation function reveals that a more significant parameter than N_I in comparing systems with different numbers of pulses is N_P, the mean number of particle image pairs in an interrogation spot. In figure 5, the effect of variation of N_P is shown for a range of image displacements, $|\Delta \mathbf{X}|/d_I$, with $D_0 = 1.2$ and constant in-plane velocities, as in figure 4 for 2,3,4 and 6 pulse systems. The valid detection rate is independent of the number of pulses provided N_P remains fixed as is shown by the curves for mean detection rate for variable N_P. The valid detection rate is a decreasing function of $|\Delta \mathbf{X}|/d_I$ for variable numbers of pulses declining below 90% when $|\Delta \mathbf{X}|/d_I$ exceeds 30%, figure 6. Hence to achieve a high detection rate, optimal parameter values are $D_0 = 1.2$, $|\Delta \mathbf{X}|/d_I < 0.25$, $N_P \geq 15$. The detectability threshold, D_0 is restrained in multiple pulse systems by bounds estimated from the relative magnitude of the first two displacement correlation components, $< R_{D^+}^{(1)}\left(\mathbf{s}_{D^+}^{(1)}\right) > / < R_{D^+}^{(2)}\left(\mathbf{s}_{D^+}^{(2)}\right) >$. However, when n=3, $\mathbf{s}_{D^+}^{(2)}$ is generally large in comparison to d_I, and the second tallest peak is almost always a noise peak.

When the constant velocity includes a component perpendicular to the light sheets, the effective number of image pairs is reduced, decreasing the peak amplitude of $< R_{D^*}^{(1)} >$. The valid detection probability decreases as the relative out-of-plane motion, $w\Delta t/\Delta z_0$ increases and is independent of the number of pulses, illustrated in Figure 7 for 2, 3 and 4 pulse systems where $N_P = 15$. The mean valid detection probability is shown for each group of in-plane displacements.

The detection probability for various values of N_P can be related to the effective mean number of image pairs within the light sheet, $N_P F_0(\Delta z)$ for general n. Figure 8 illustrates the dependence upon $N_P F_0$ for a range of n and N_I when $|\Delta \mathbf{X}|/d_I = 0.2$. The valid detection probability can be modelled by the expression $(1 - \exp(-0.35 N_P F_0))$ independently of n.

As the parameter, $N_P F_0 F_I$, is a measure of the mean effective number of particle image pairs in the interrogation spot, the valid detection probability can be related to $N_P F_0 F_I$ for a range of particle image densities and both in-plane and out-of-plane motions. Figure 9 shows the dependence of the valid detection probability upon the mean effective particle image pair density for both in-plane and out-of-plane particle displacements for variable number of pulses n and $D_0 = 1.2$. It can be seen that a valid detection probability of at least 98% can be achieved when the single parameter $N_P F_0 F_I$ is larger than 10.

When the particle image density is sufficiently low, N_P is no longer an appropriate parameter due to the sparse nature of the particle locations. The valid detection probability, in such cases, is independent of the detectability criterion D_0 due to sparse data density and improves as the number of pulses increases. Figure 10 illustrates the improvement in valid detections for 2, 3, and 4 pulsed systems as a function of the effective image density, $N_I F_I$.

4.4 Performance: Strong velocity gradients

The analysis of section 3 concludes that the effects of velocity gradients for multiple pulse systems are identical to those for double pulse systems as the gradients diminish and broaden the mean correlation peak $< R_{D^*}^{(1)} | \mathbf{u} >$ while producing a statistical bias in the centroid as expressed in

equation (35). Furthermore, it has been shown for a double pulse system and in section 3 that the effect of the gradient bias upon detection probability has only a weak dependence upon $|\Delta \mathbf{X}|/d_I$ and N_P.

The dimensionless velocity variations such as $M\Delta u_y \Delta t/d_\tau$ in the case of simple shear reduce the amplitude of $< R_{D^+}^{(1)} | \mathbf{u} >$ and lower the detection probability. The previous case was a simple shear, where $\partial u/\partial y = 0.24 u_I/d_I$ has been added to a uniform translation. It has been considered for three and four pulse systems to illustrate the dependence upon $M\Delta u_y \Delta t/d_\tau$ for various $|\Delta \mathbf{X}|/d_I$ and N_P and to relate the detection probability to the amplitude of $< R_{D^+}^{(1)} | \mathbf{u} >$. Figure 11 confirms that conclusions for a double pulse system can be extended to multiple pulse systems, namely that high detection probabilities result when the velocity variation is restricted to $M\Delta u_y \Delta t/d_\tau < 1$ and $|\Delta \mathbf{X}|/d_I < 0.25$. From these restrictions, the maximum velocity difference that can be tolerated for successful interrogation can be extended to multiple pulse systems, namely

$$\Delta u/u_I < 4 d_\tau/d_I, \tag{36}$$

and can be used as a guideline for all PIV systems. Figure 11 shows that the valid detection probability is higher than expected from an analysis of the amplitude of $< R_{D^+}^{(1)} >$ in equation (48) of Keane and Adrian (1990) and it is higher in both 3 and 4 pulse systems than in a double pulse system.

The statistical bias of measurements based on the centroid of $R_{D^+}^{(1)}(\mathbf{s})$ can be related to the dimensionless parameters causing gradient bias in the location of $\mathbf{s}_{D^+}^{(1)}$ in equation (35). For the simple shear velocity field, this relative bias in the velocity component u is measured in terms of $M\Delta u_y \Delta t/d_I$ for multiple pulse systems over a range of mean image displacements with $N_P = 15$ and $D_0 = 1.2$ (Figure 12). The relative bias agrees with the relative bias in the centroid of $< R_{D^+}^{(1)} | \mathbf{u} >$ from equation (35) and is independent of the number of pulses n and the mean image displacement $|\Delta \mathbf{X}|/d_I$. This relative bias can be limited to 6% provided that $M\Delta u_y \Delta t/d_I$ is less than 0.05.

By considering the dimensionless parameters determining the extent of gradient bias in equation (35), namely $d_{ij}\Delta t/2$, and the restriction that $M \mid \mathbf{u}_{max} \mid \Delta t/d_I < 0.25$, which ensures an acceptable valid detection probability, it can be seen that the gradient bias can be reduced in two ways. A reduction in Δt, the time interval between pulses, reduces gradient bias while decreasing the accuracy of $\mid \Delta \mathbf{X} \mid = M \mid \mathbf{u}_{max} \mid \Delta t$ simultaneously. Alternatively, for a given Δt, the size of the interrogation spot, d_I, can be reduced subject to the condition that max $\mid \Delta \mathbf{X} \mid /d_I < 0.25$ limiting the gradient bias as $d_{ij}\Delta t/2 < 0.25 d_{ij}/ \mid \mathbf{u}_{max} \mid (d_I/2)$. In addition, equation (35) can be used to correct measurements of the velocity field by estimating in-plane gradients but the out-of-plane gradients, $\partial u/\partial z$ and $\partial v/\partial z$ remain unknown. As the relative bias is independent of the number of pulses in the system (figure 12), no reduction of bias is achieved by increasing the number of pulses.

Finally, the random particle locations in individual realizations of a varying velocity field cause the centroid of $R_D^{(1)}(\mathbf{s})$ to be located over a finite range of displacements and thus cause random variations in valid measurements. Figure 13 generalizes earlier results for the simple shear velocity field to multiple pulse systems and relates the rms of the random variation in $\mathbf{u}_m$ to the dimensionless velocity variation. The variation in $\mathbf{u}_m$ about its mean is independent of the number of pulses and the mean image displacement, when the acceptable criterion for high detection probability ensures that $M\Delta u_y \Delta t/d_\tau \leq 1$. Thus in multiple pulse systems, the choices of Δt and d_I are determined by criteria for adequate spatial resolution, acceptably high detection probability, degree of gradient bias and variation in velocity measurements about the measured mean, as for double pulse systems.

5. SUMMARY AND CONCLUSIONS

Multiple pulse PIV systems have been studied for a range of velocity fields. Theoretical analysis of full 2-D spatial correlation of direct images and 2-D Fourier transform of Young's fringes demonstrates the similarity of the two approaches for multiple pulse systems. The analysis of both methods and a Monte Carlo simulation of the correlation method for two, three, four and six pulse systems reveal the critical parameters of the mean autocorrelation function and its fluctuations for

a range of velocity fields. They are $N_P, D_0, |\Delta \mathbf{X}|/d_I, |\Delta \mathbf{u}|/|\mathbf{u}_I|, M|\Delta \mathbf{u}|\Delta t/d_\tau, d_z/d_I$ and $w\Delta t/\Delta z_0$ where N_P generalizes N_I from the double pulse system and all other parameters are unaltered. To optimize the performance, the following broad criteria are recommended. (a) $N_p \geq 15$, (b) $|\Delta \mathbf{X}|/d_I \leq 0.25$, (c) $|w|\Delta t/\Delta z_0 \leq 0.25$, (d) $M|\Delta \mathbf{u}|\Delta t/d_I < 0.05$ (e) $D_0 = 1.2$. Thus, both relative in-plane and out-of-plane displacements should be less than one quarter. While these criteria are a good general combination, more precise values can be used for a given number of pulses and particular flow fields by reference to the appropriate figures and equations.

To achieve these optimum parameters for a given number of pulses, PIV design procedure can be adopted which differs only slightly from that for a double pulse system in its choice of seeding density C needed to achieve adequate particle image pairing density N_P. Based on experimental knowledge of the flow field, choose d_I and Δz_0 to ensure adequate spatial resolution and yet restrict effects of out-of-plane motion. The seeding density C should be determined so that $N_P \geq 15$ which is less restrictive as the number of pulses increases. Then choose Δt, and possibly modify d_I, to minimize bias due to velocity gradients, to minimize pair loss due to out-of-plane motion and to give adequate image displacements.

Although the above recommendations depend upon n, the number of pulses for a given PIV system, only indirectly through N_P, the advantages of increasing the number of pulses are twofold. For a given adequate particle seeding density C, the number of effective image pairs increases and the signal quality improves as the number of pulses increases (equations (2), (31)), hence improving valid detection probabilities. This is particularly true in the case of lower particle image densities when $N_I < 1$. Furthermore, the valid detection probability increases in the presence of a velocity gradient for increased number of pulses, figure 9. The valid detection probability improves most significantly when a triple pulsed system is employed in preference to a double pulsed system, with lesser improvements as the number of pulses increases further.

ACKNOWLEDGEMENT

This material is based on work supported by the National Science Foundation under Grant Nos. ATM 86-00509 and ATM 90-20605 and TSI, Inc.

REFERENCES

Adrian R J 1984 Scattering particle characteristics and their effect on pulsed laser measurements of fluid flow: speckle velocimetry vs. particle image velocimetry
Applied Optics **23** 1690

Adrian R J 1985 Multi-point vector measurement by pulsed laser velocimetry with image compression
Proc. Int. Symp. on Fluid Control and Measurement (Oxford: Pergamon) 1087

Adrian R J 1986 Multipoint optical measurements of simultaneous vectors in unsteady flow—a review
Int. J. Heat and Fluid Flow **7** 127

Adrian R J 1988a Statistical properties of particle image velocimetry measurements in turbulent flow
Laser Anemometry in Fluid Mechanics Vol. III LADOAN Institute Superior Tecnico Lisbon Portugal 115

Adrian R J 1988b Double exposure, multiple field particle image velocimetry for turbulent probability density
Optics and Lasers in Engineering **9** 211

Arroyo M P Yonte T Quintanilla M and Savirón J M 1988 Particle image velocimetry in Rayleigh-Bénard convection: Photographs with high number of exposures
Optics and Lasers in Engineering **9** 295

Cenedese A and Paglialunga A 1990 Digital direct analysis of a multiexposed photograph in PIV
Experiments in Fluids **8** 273

Dudderar T D Meynart R and Simpkins P G 1988 Full field laser metrology for fluid velocity measurement
Optics and Lasers in Engineering **9** 163

Keane R D and Adrian R J 1990 Optimization of particle image velocimeters. Part I: Double pulsed systems
Measurement Science and Technology **1** 1202

Keane R D Optimization of particle image velocimeters
Ph.D. Thesis University of Illinois To appear

Lauterborn W and Vogel A 1984 Modern optical techniques in fluid mechanics
Ann Rev Fluid Mech **16** 223

Lourenco L and Krothapalli A 1987 The role of photographic parameters in laser speckle or particle image displacement velocimetry
Exp in Fluids **5** 29

Meynart R 1983 Instantaneous velocity field measurements in unsteady gas flow by speckle velocimetry
Appl Optics **22** 535

Meynart R Simpkins P G and Dudderaar T D 1987 Speckle measurements of convection in a liquid cooled from above
Journal of Fluid Mechanics **182** 235

Simpkins P G and Dudderar T D 1978 Laser speckle measurement of transient Bénard convection
J Fluid Mech **89** 665

LIST OF FIGURE CAPTIONS

Figure

1 Light sheet and image recording system for planar pulsed laser velocimetry.

2(a) Correlation function R for constant velocity within the interrogation volume for a quadruple pulse system. $N_P = 15$ and the mean image displacement, $\Delta \mathbf{X}/d_I = (0.10, 0.10)$.

2(b) Correlation function G for image transmissivity amplitude $E(\mathbf{X})$.

3 Simulated region of the interrogation plane for a quadruple pulse system. The velocity is constant within the measurement volume for a mean particle displacement with $M\Delta \mathbf{X}/d_I = (0.1, 0.1, 0.1)$ $N_P = 15$. The smaller square denotes an interrogation spot.

4 Total, false and valid detection probabilities for a four pulse system as a function of $|\Delta \mathbf{X}|/d_I$ and N_I for $D_0 = 1.2$ and constant velocity.

5 Valid detection probability as a function of image pair density, N_P for variable image displacements $|\Delta \mathbf{X}|/d_I$ and for $D_0 = 1.2$.

6 Valid detection probability vs relative image displacement $|\Delta \mathbf{X}|/d_I$ for $D_0 = 1.2$ and variable particle image pair density N_P.

7 Valid detection probability vs relative out-of-plane motion for $N_P = 15$, $D_0 = 1.2$ and variable number of pulses n.

8 Correlation of the valid detection probability for out-of-plane displacements in terms of the effective pair density, $N_P F_0$. Detectability $D_0 = 1.0$ and $|\Delta \mathbf{X}|/d_I = 0.2$.

9 Valid detection probability in terms of the effective particle image pair density, $N_P F_0 F_I$, for both in-plane and out-of-plane particle displacements for variable number of pulses, n, and $D_0 = 1.2$.

10 Valid detection probability for low image density, N_I, in terms of the effective image density, $N_I F_I$, for detectability $D_0 = 1.0$ where (a) $n = 2$, (b) $n = 3$, and (c) $n = 4$.

11 Valid detection probability for a simple shear in terms of relative image displacement variation, $M\Delta u_y \Delta t/d_\tau$ for variable image displacements $|\Delta \mathbf{X}|/d_I, N_p = 15, D_0 = 1.2$. Amplitude of $< R_{D^+}^{(1)} | \mathbf{u} >$ from theory and mean detection probabilities are indicated.

12 Relative measured mean velocity for a plane shearing velocity in terms of $M\Delta u_y \Delta t/d_I$. Conditions as in Fig. 11.

13 Variation in measured velocity in terms of relative image displacement variation $M\Delta u_y \Delta t/d_\tau$ for variable image displacements $|\Delta \mathbf{X}|/d_I, N_p = 15, D_0 = 1.2$.

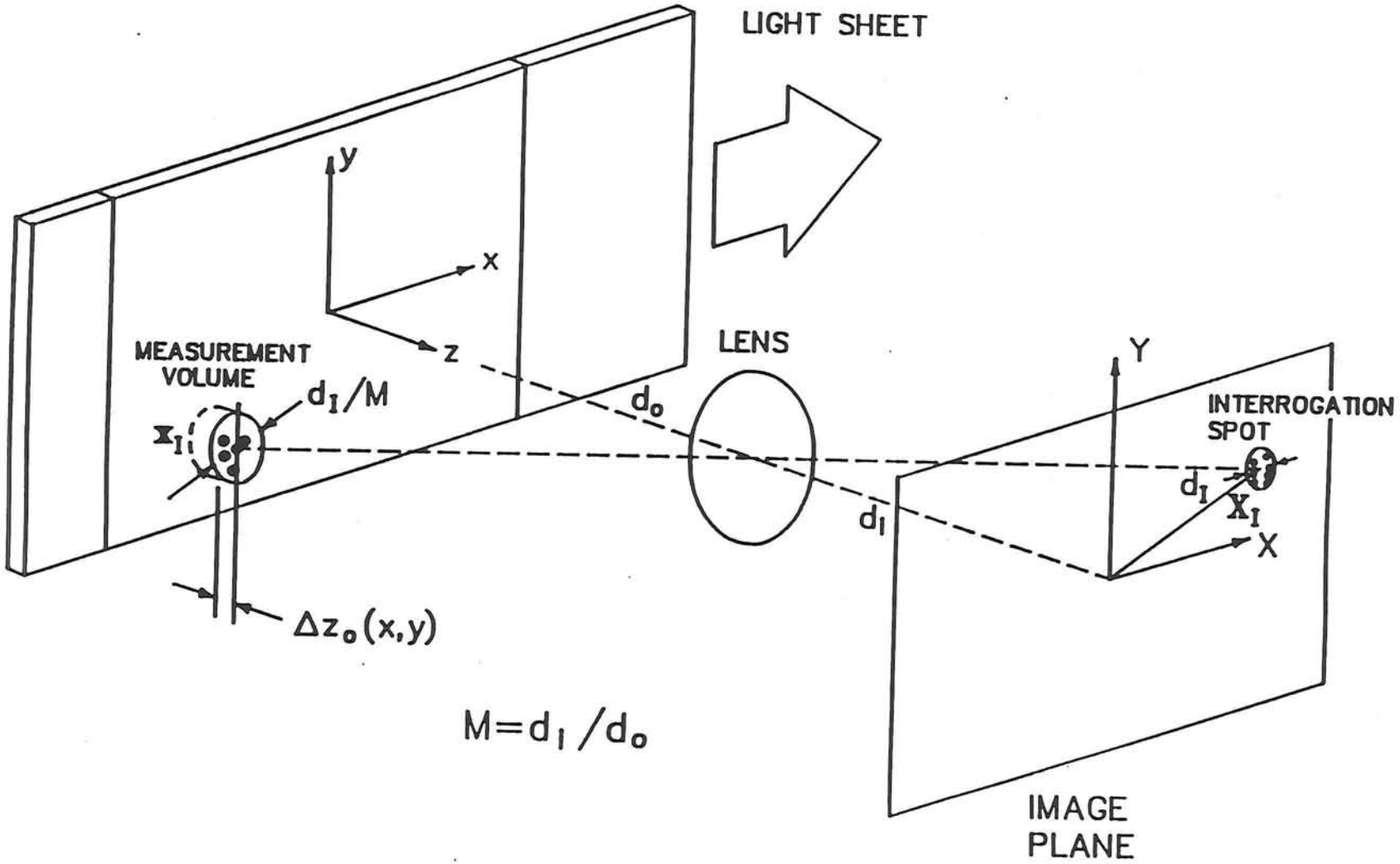

Fig. 1 Light sheet and image recording system for planar pulsed laser velocimetry.

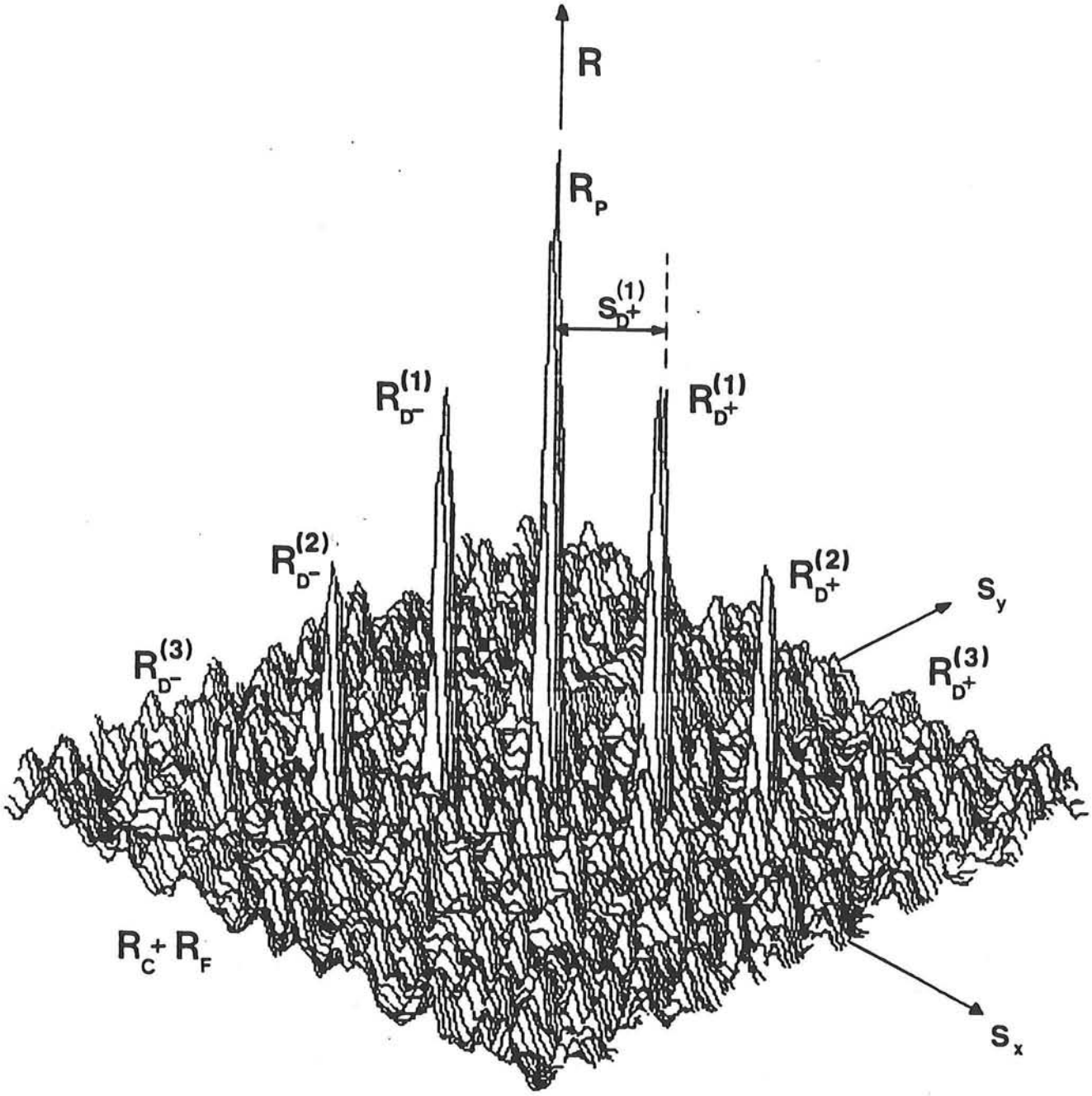

Fig. 2(a) Correlation function R for constant velocity within the interrogation volume for a quadruple pulse system. $N_P = 15$ and the mean image displacement, $\Delta X/d_I = (0.10, 0.10)$.

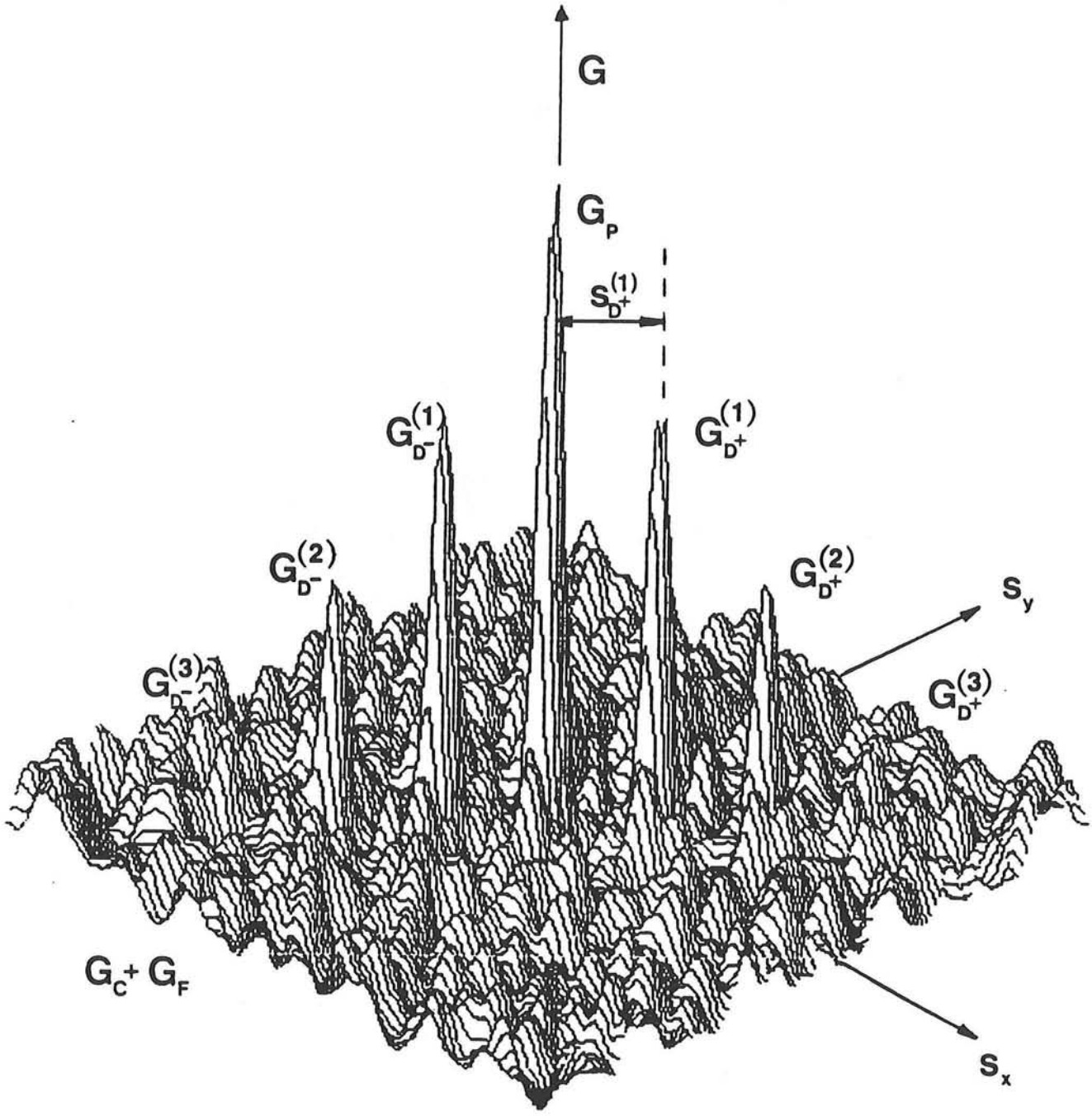

Fig. 2(b) Correlation function G for image transmissivity amplitude $E(X)$.

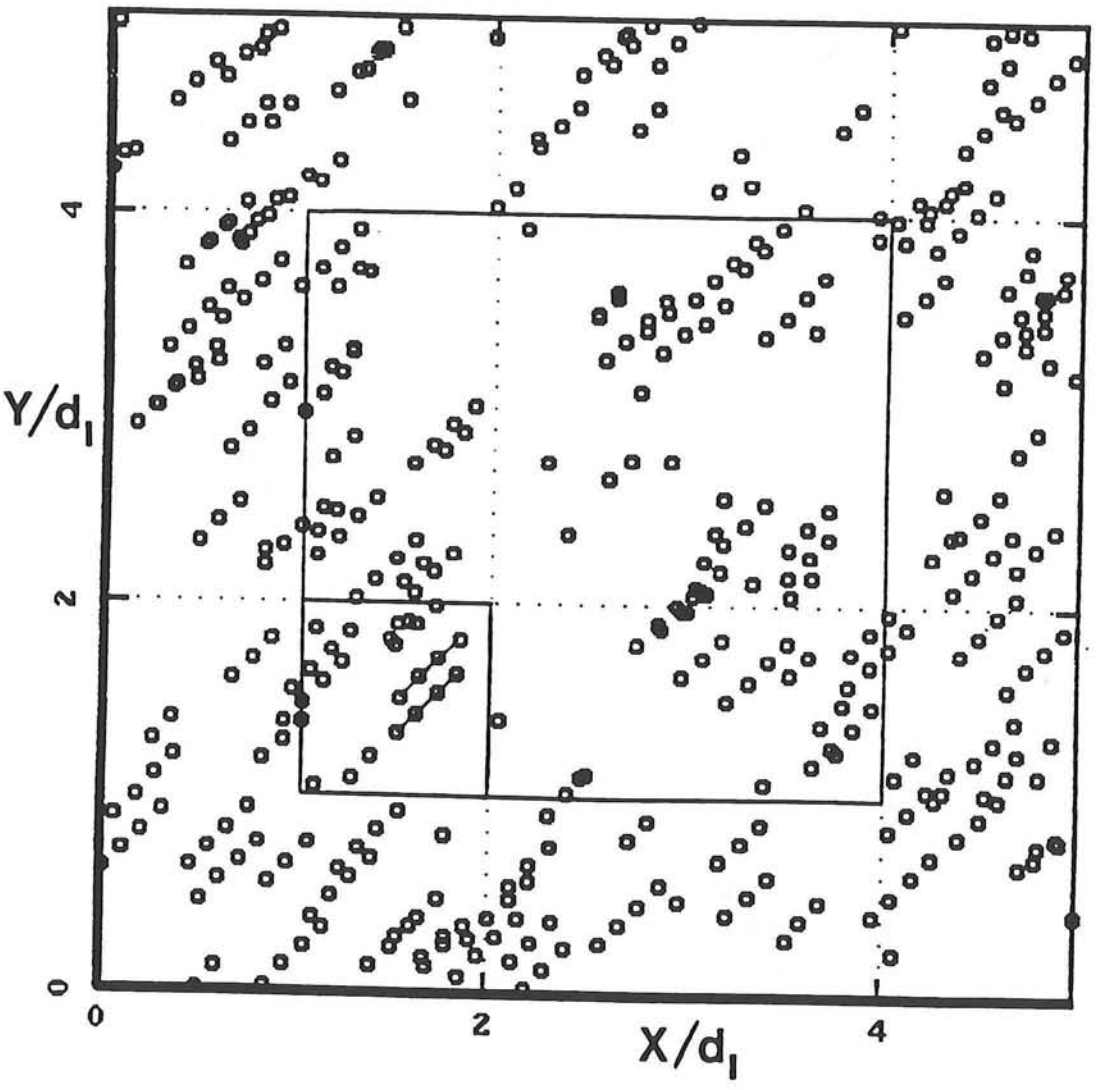

Fig. 3 Simulated region of the interrogation plane for a quadruple pulse system. The velocity is constant within the measurement volume for a mean particle displacement with $M\Delta X/d_I = (0.1, 0.1, 0.1)\, N_P = 15$. The smaller square denotes an interrogation spot.

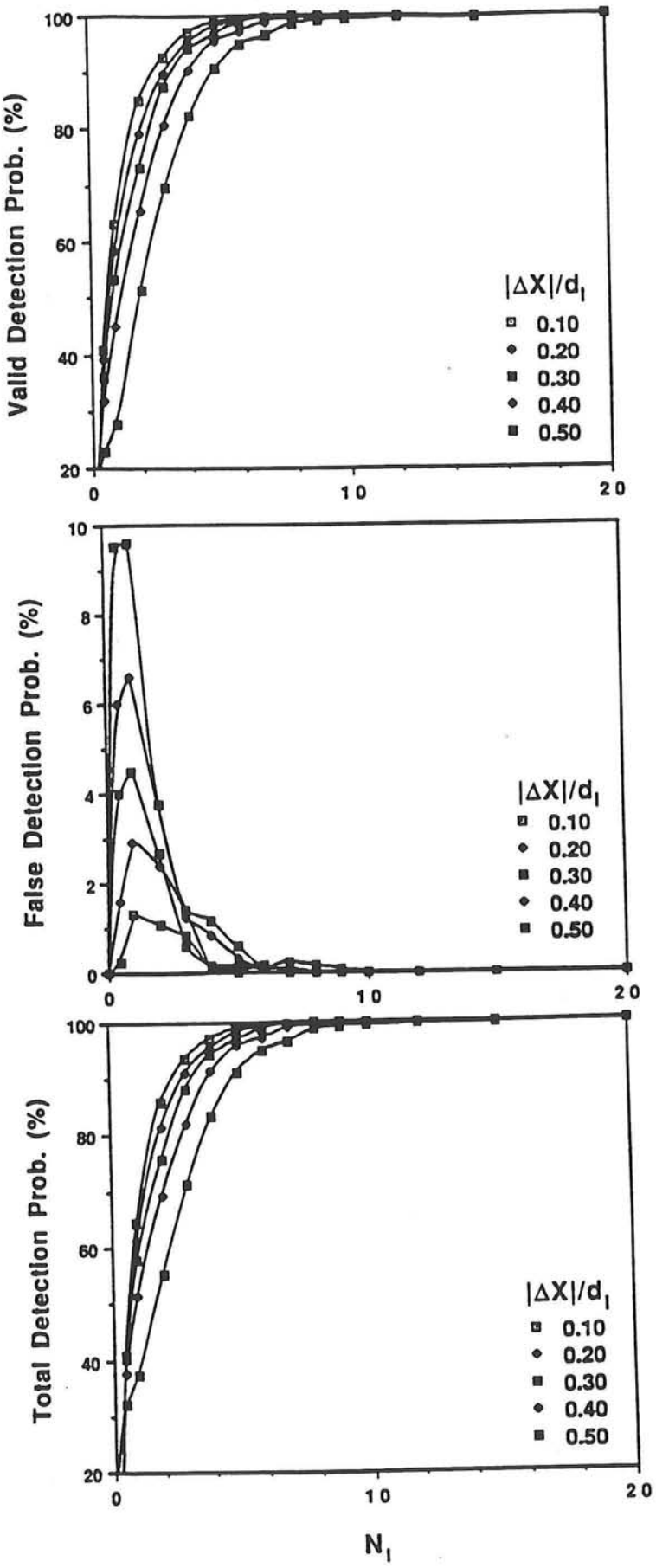

Fig. 4 Total, false and valid detection probabilities for a four pulse system as a function of $|\Delta X|/d_l$ and N_l for $D_0 = 1.2$ and constant velocity.

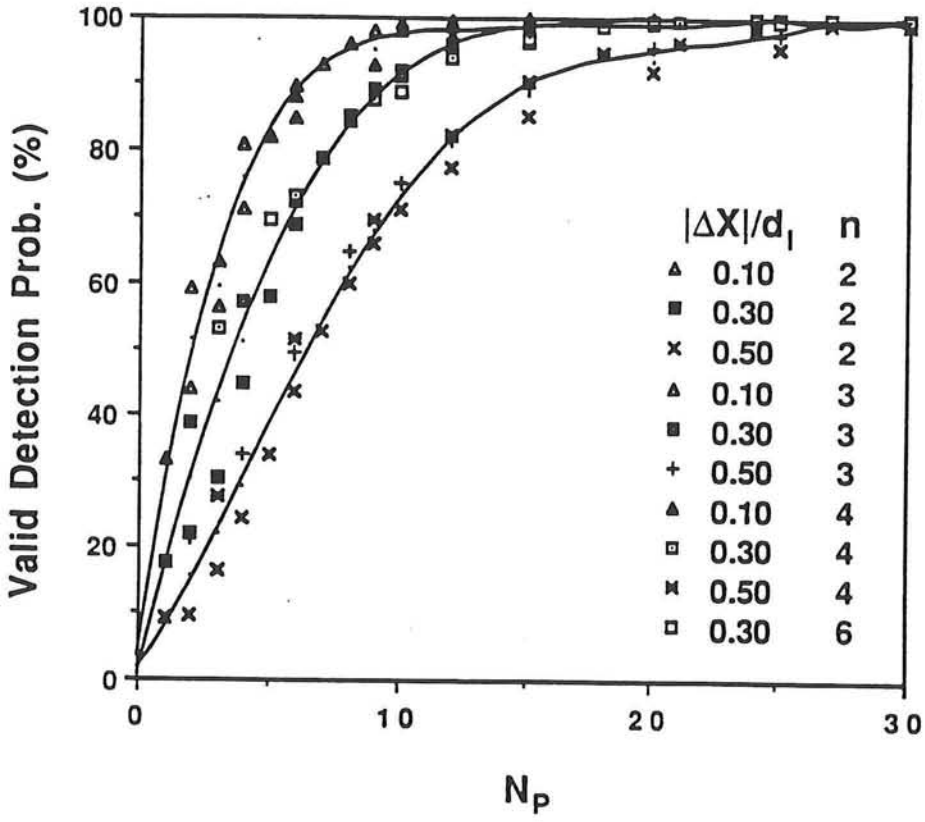

Fig. 5 Valid detection probability as a function of image pair density, N_P for variable image displacements $|\Delta X| / d_I$ and for $D_0 = 1.2$.

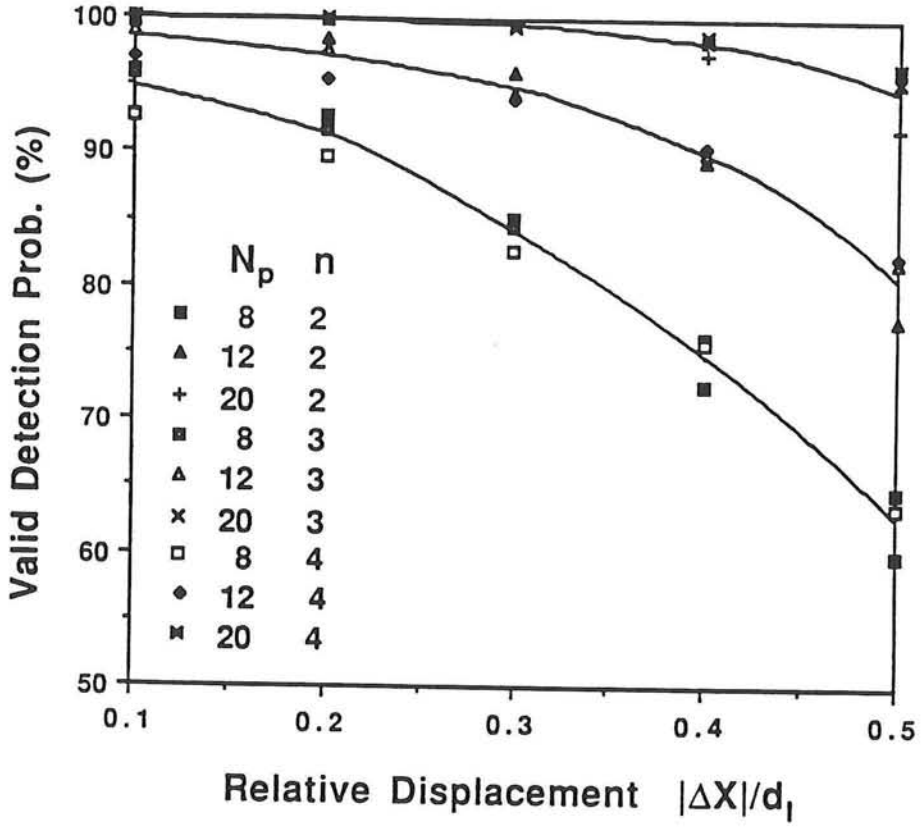

Fig. 6 Valid detection probability vs relative image displacement $|\Delta X| / d_I$ for $D_0 = 1.2$ and variable particle image pair density N_P.

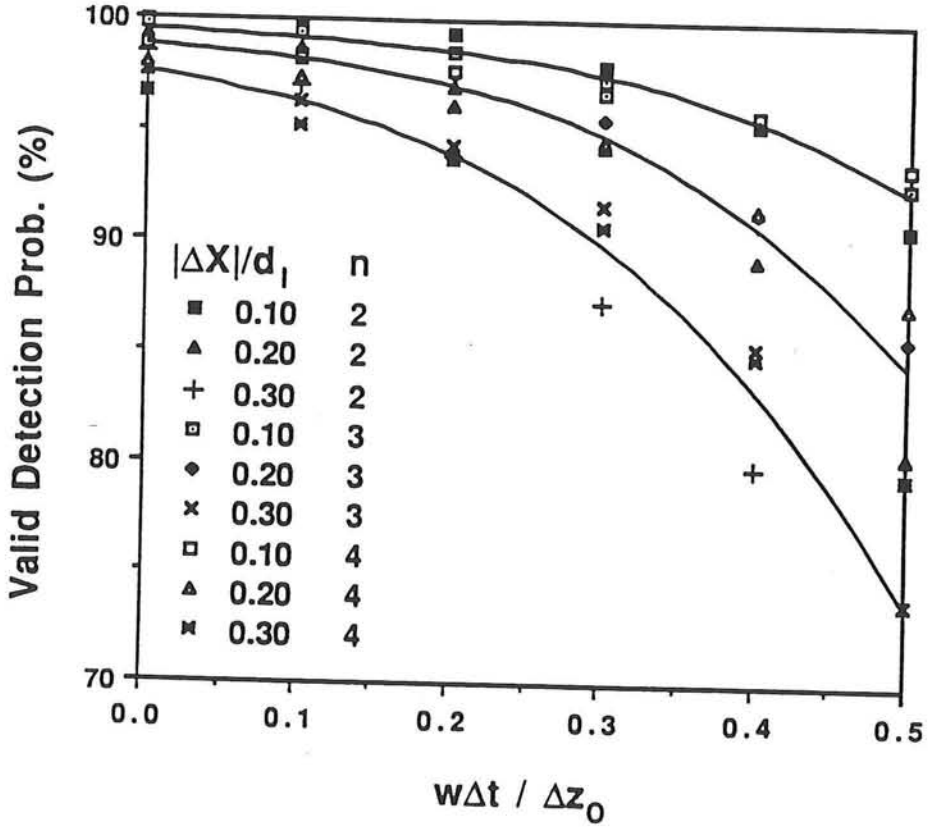

Fig. 7 Valid detection probability vs relative out-of-plane motion for $N_P = 15$, $D_0 = 1.2$ and variable number of pulses n.

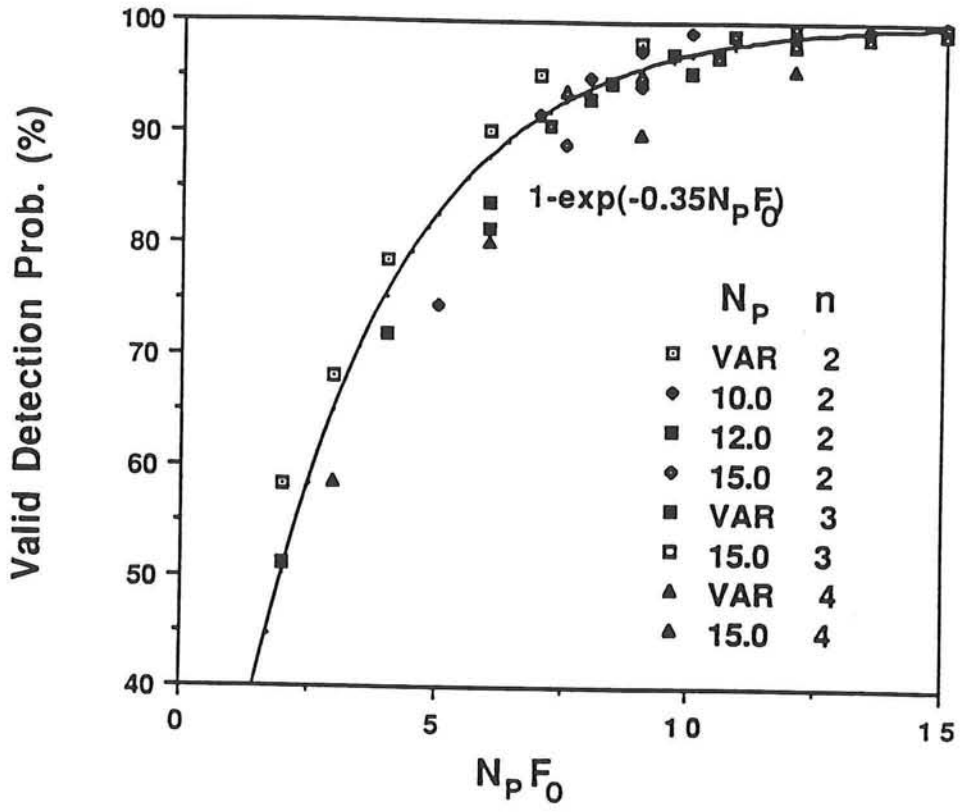

Fig. 8 Correlation of the valid detection probability for out-of-plane displacements in terms of the effective pair density, $N_P F_0$. Detectability $D_0 = 1.0$ and $| \Delta X | / d_I = 0.2$.

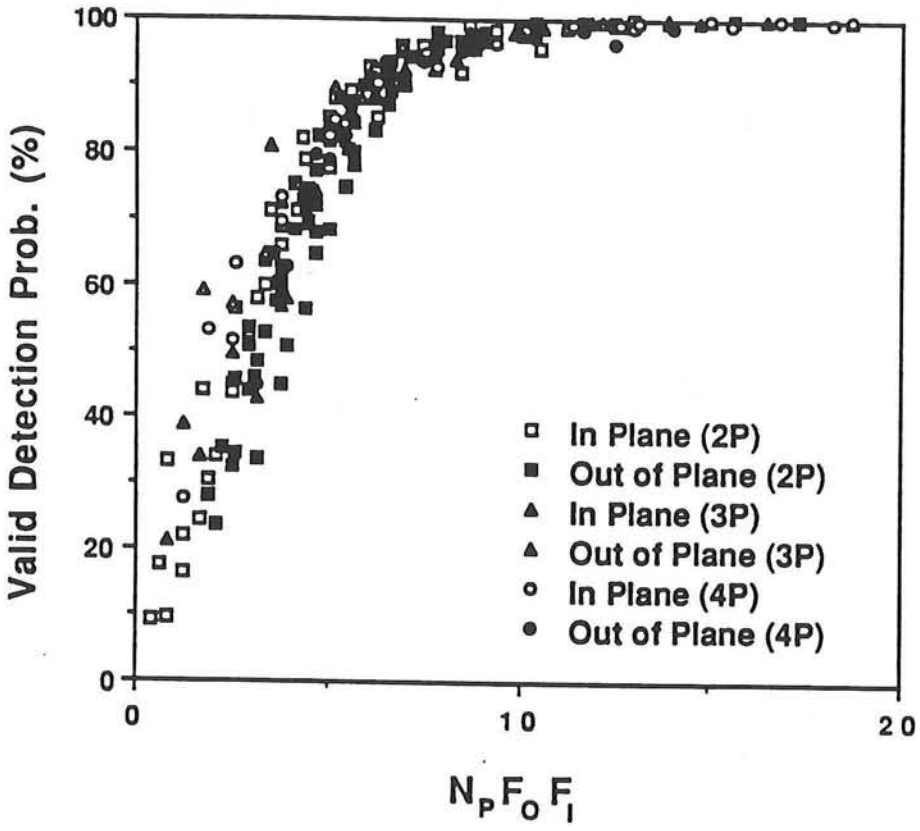

Fig. 9 Valid detection probability in terms of the effective particle image pair density, $N_P F_0 F_I$, for both in-plane and out-of-plane particle displacements for variable number of pulses, n, and $D_0 = 1.2$.

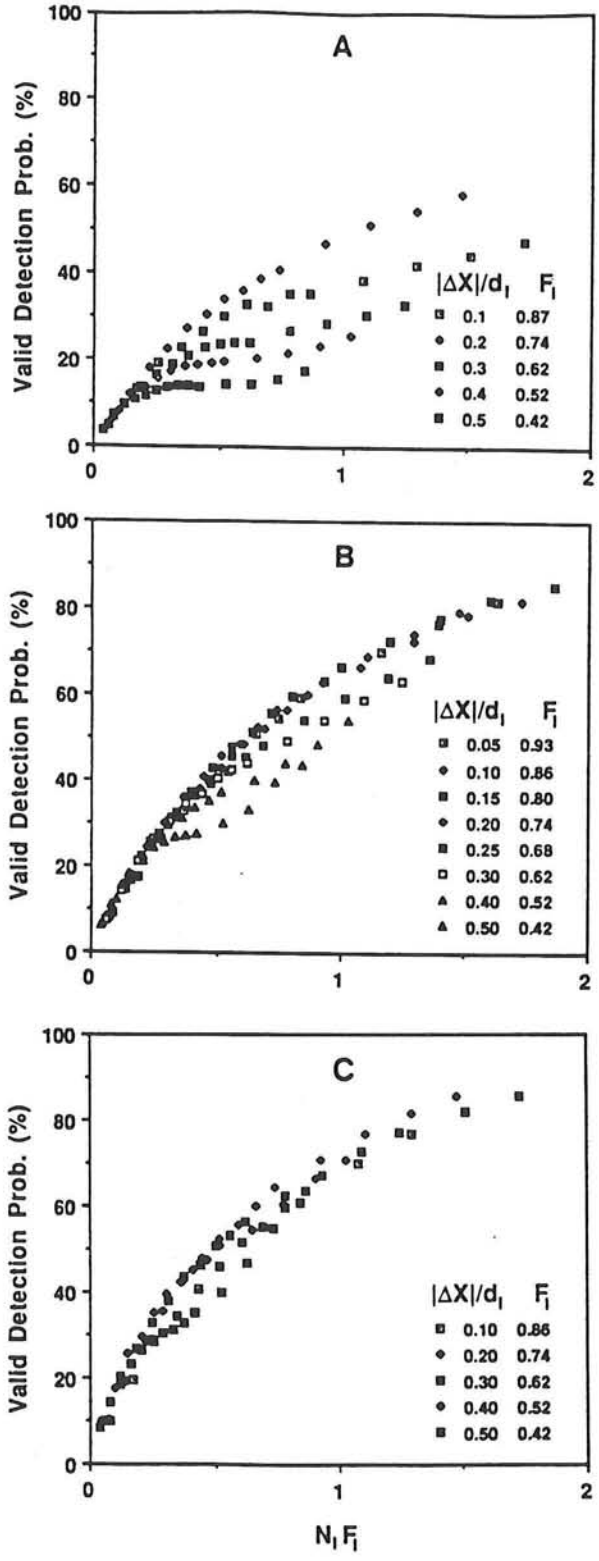

Fig. 10 Valid detection probability for low image density, N_I, in terms of the effective image density, $N_I F_I$, for detectability $D_0 = 1.0$ where (a) $n = 2$, (b) $n = 3$, and (c) $n = 4$.

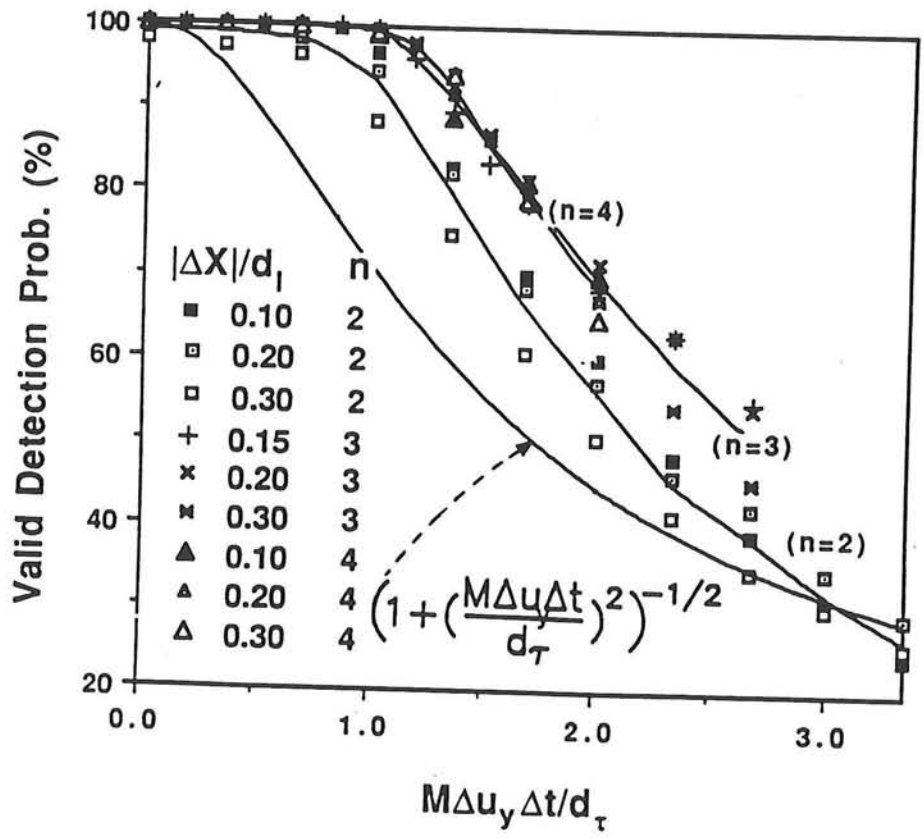

Fig. 11 Valid detection probability for a simple shear in terms of relative image displacement variation, $M\Delta u_y \Delta t/d_\tau$ for variable image displacements $|\Delta X|/d_I, N_p = 15, D_0 = 1.2$. Amplitude of $< R_{D^+}^{(1)} | \mathbf{u} >$ from theory and mean detection probabilities are indicated.

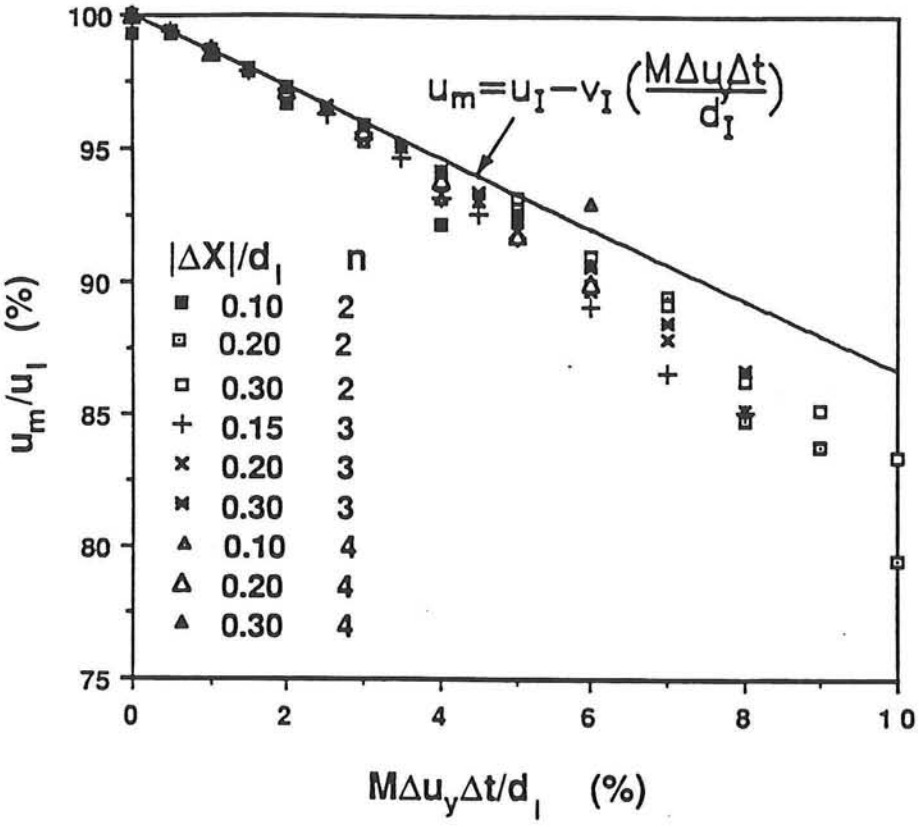

Fig. 12 Relative measured mean velocity for a plane shearing velocity in terms of $M\Delta u_y\Delta t/d_I$. Conditions as in Fig. 11.

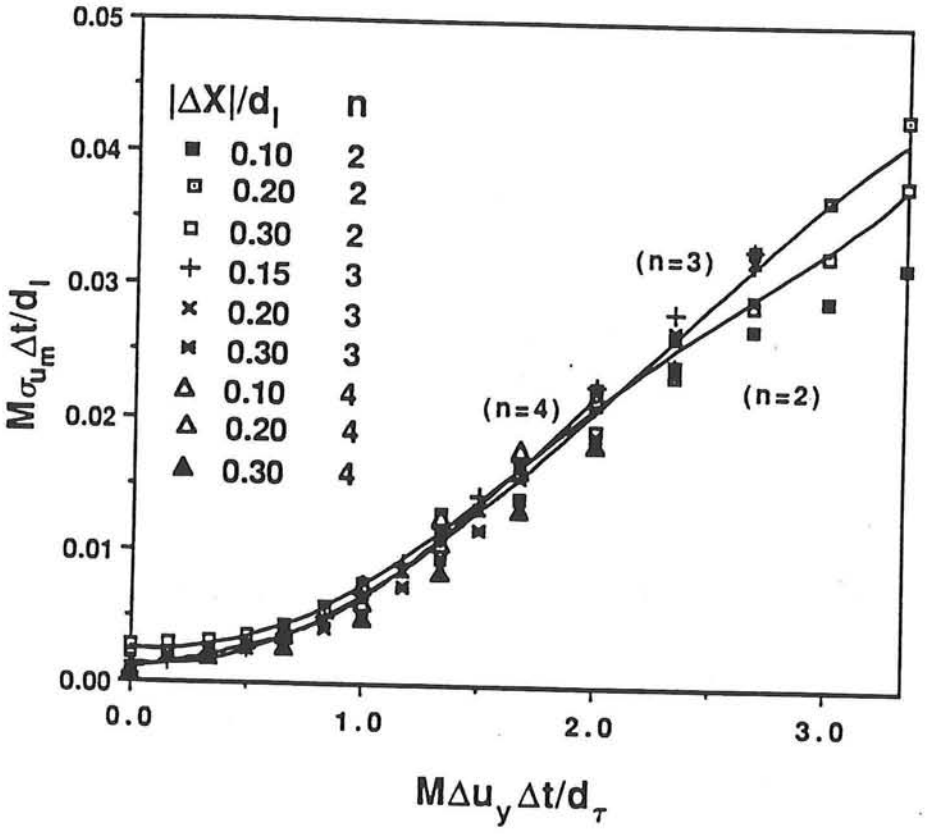

Fig. 13 Variation in measured velocity in terms of relative image displacement variation $M\Delta u_y \Delta t/d_\tau$ for variable image displacements $|\Delta \mathbf{X}|/d_I, N_p = 15, D_0 = 1.2$.

Visualization methods for fluid flow datasets

Lambertus Hesselink
James Helman
Paul Ning
Departments of Aeronautics/Astronautics,
Applied Physics
and Electrical Engineering
Room 359B Durand
Stanford University
Stanford, CA 94305-4035

May 21, 1991

Abstract

Recent advances in optical diagnostics and numerical simulations of fluid flows have generated large volumes of data that are difficult to interpret with conventional two-dimensional visualization techniques. It is the aim of this paper to review state-of-the-art techniques for extracting quantitative information from (large) experimentally and numerically generated datasets. Following our personal biases, a global viewpoint of digital image processing with application to fluid flow research is discussed. A comprehensive approach to extracting quantitative data from multivariate datasets is presented and examples of recent developments in this area are discussed. Attention is paid to issues in related fields that have a bearing on progress in analysis of fluid flow datasets.

1 Introduction

The characterization and understanding of fluid flows often involves the manipulation of large, 3-D, multivariate, time dependent datasets. These data may be obtained by experimental or computational methods. On the experimental side, optical diagnostics routinely provide 2-D images representing scalar or vectorial data, usually as a function of time. In certain

cases, as for tomography, these 2-D images may be processed to reveal truly three-dimensional flow representations. These representations are then displayed using graphics approaches, usually involving sophisticated hardware and software. Similarly, numerically generated flow data may be processed to reveal important flow features in multiple dimensions.

A schematic depiction of this process is shown in Figure 1. The chart represents classical experimental methods (shown in italic font) in conjunction with recent new approaches based on digital image processing such as gradient imaging, tomography and image synthesis. In this classification, flow visualization and analysis of numerically generated data are treated in the same way as visualization of experimental data. Regardless of the origin, once the data are available in digital format, distinction between the different branches disappears and processing proceeds down the path starting with enhancement and ultimately produces graphics representations or quantitative enumeration for comparison and evaluation purposes.

In the past, much work has been expended on improving the quality of the imagery, and on the extraction of important physical quantities such as velocity, density and temperature data. Classical image processing techniques - frequently developed for other applications such as pattern recognition in aerial images, Landsat scene understanding and improvement of digital imagery acquired by space probes - are readily adapted to fluid flow experiments. Several review articles have been devoted to these techniques, and much has been written about the merits of these methods compared with more conventional diagnostics involving hotwire and 1-D probes [7], [19], [1]. Most of these discussions limit themselves to specific problems in data acquisition and processing of flow visualization data. In this paper, we take a more global viewpoint and we put recent developments in image processing and graphics in perspective with the overall aim of understanding fluid flows. The approach advocated here views data acquisition, processing and understanding as closely related activities that ultimately lead to improved flow understanding and the generation of knowledge. In schematic form this process may be depicted as shown in Figure 1. This schematic representation provides the skeleton for the remainder of this paper.

The global viewpoint on flow visualization we advocate takes on the shape of a large puzzle. A substantial number of the individual pieces have been put in place, but significant segments are still missing. A framework of the visualization process has been developed and significant progress towards achieving the goal of closing the loop in Figure 1 in an automated fashion has been made. Yet much more can be done. We present here key elements

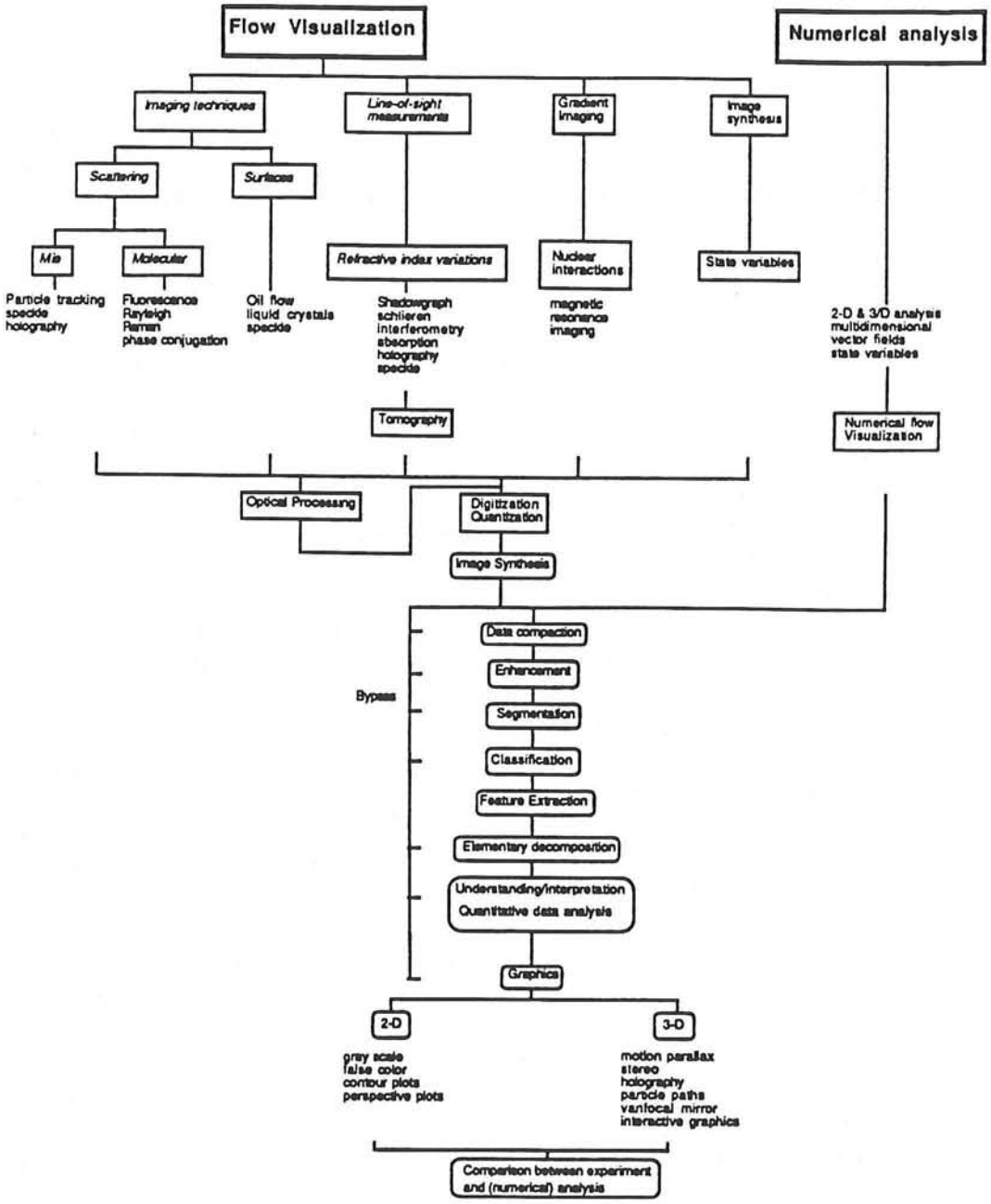

Figure 1: Classification of digital image processing and flow-visualization techniques

Demands on Resources

S = Storage Space

T_p = Processing Time

T_t = Transmission Time

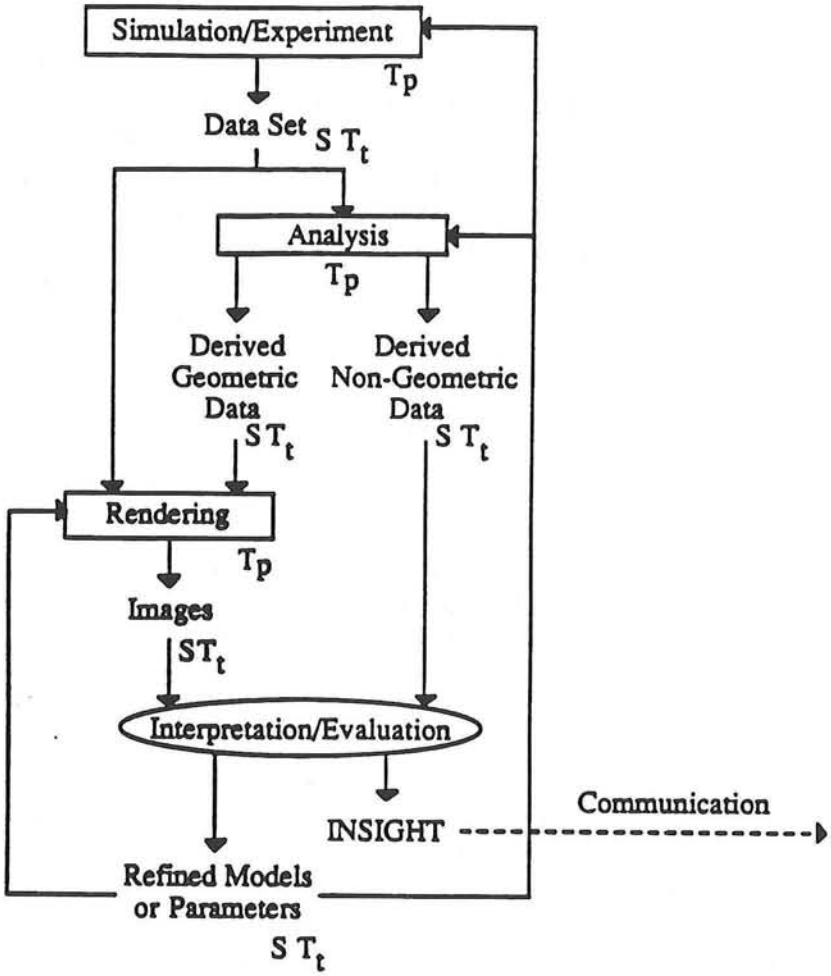

Figure 2: Flow visualization process. Activities are represented in boxes which are interconnected by flow lines. The cost function associated with each activity can be measured in terms of storage space, processing time and transmission time.

of the global flow visualization process and discuss relevant research issues.

1.1 Simulation/experiment

Numerical simulations are now capable of calculating very complex flows [11]. The results of these calculations are often 3-D time-varying datasets that represent pressure, temperature, velocity and other flow quantities. In some cases, e.g. the flow over a lifting body, only a few numbers are desired as the output of these calculations, such as the drag or lift coefficient as a function of angle of attack. In other instances, a complete three-dimensional representation of the flow over a body may be desired. In any event, the results of the calculation are a set of numbers on a mesh representing flow quantities. Recently, these sets have become increasingly large. For example, it is now possible to compute pressure, temperature, velocity and vorticity on a 3-D, time varying grid containing 10^6 grid points for hundreds of time steps. As a result, data storage and manipulation becomes a task that may equal the effort required for generation of the data in the first place. The cost of storing these data is expressed by S. Quite often, these data are generated at a remote site and must be transmitted over a network to the user's computer. The cost involved in this effort is denoted by T_t. For large datasets, involving billions of data points, transmission time can be enormous. For example, at a transmission rate of 50Kbits/sec (which may be a typical rate for long haul communication using Internet), it would take approximately 44 hrs to transmit a billion bytes to a remote site. To our knowledge, a full investigation of the cumulative costs involved in carrying out the functions of Figure 1 has not been carried out for fluid flow applications, but would be beneficial to the community at large. The example illustrates, nevertheless, that compression becomes an important aspect of handling these rich datasets. Conventional approaches are useful for this application, but generally (e.g., 2-D images of natural scenes) only a factor of ten compression can be achieved with good fidelity. Alternatively, it may be desirable to process the data on the supercomputer in a form suitable for later graphic representation or further data analysis on a workstation; these reduced datasets would be more amenable to post processing, because they would be substantially smaller in size. There are, however, instances in which the full dataset needs to be transmitted, for example when researchers at distant locations want to share the analysis effort. In that case, conventional data compression techniques alone may not be suitable and mass storage devices may have to be transported by other means

(plane) until the bandwidth of our electronic communication systems has sufficiently improved.

For large computations or extensive experiments, we are not only interested in analyzing the final result, but often it is highly desirable to be able to monitor intermediate results. Data compression and efficient analysis are then particularly important if we wish to close the loop in Figure 1 by providing feedback. The question is, "what information should be fed back to optimally modify the calculation (or experiment) ?" To answer this question, we need to consider how the data are analyzed.

1.2 Data processing

Data analysis often involves a number of steps that can be broken down into several categories, as described by Hesselink, 1988 [7]. In this paper we will not describe all the techniques denoted there, but refer to the original reference for further details. The analysis effort provides derived data that need to be stored or transmitted for further interpretation or evaluation. This step may involve various approaches. As an example, scalar data may be readily displayed as gray scale or color images using lookup tables. For more sophisticated graphics approaches, geometric data may be derived from the raw dataset for rendering. A popular algorithm called Marching Cubes [12], for example, allows rendering of 3-D imagery using polygonal surface tiles. The 3-D images can be manipulated, often under mouse control for further visual analysis and display.

1.2.1 Visualization

Sampled data may be visualized in two principal ways. The first is by generating geometric primitives (polygons) that correspond to isosurfaces at specific threshold values within the dataset [4], [17], [12]. The other method involves volume rendering by which the data are presented as a translucent image in three-dimensional space without generating primitives [10].

Polygonal surface representations may be used with common graphics rendering algorithms implemented in either software or hardware. Interaction with the data can be accomplished by allowing, for example, object rotation, scaling and surface peeling. Opaque surface representations provide strong depth cues, but obscure underlying detail. In these cases, interior structures may be visualized by peeling outer layers away, thereby opening a window into the object. In some cases, however, it may be desirable to

partially look into the object by making the outer layers semi transparent. Interior surfaces are discernible and can be viewed in relation to the outer layers to provide structural information about the object.

A general implementation of this approach is volume rendering, which superimposes color contributions from all the available voxels (volume elements). In one particular material model, each voxel acts as a source of radiation in proportion to its parameter value, and all the voxels between the observer and this source act as attenuators. By varying the degree of attenuation, the penetration depth of the viewer into the image can be altered. No attenuation implies complete transparency, and strong attenuation approaches the isosurface representation [8].

The two rendering techniques described here have been used for display of fluid flow data with varying degrees of success. In general, the isosurface approach is very useful for displaying interface surfaces between, for example, two mixing fluids. The outer surfaces of the structures are easily visualized, but finding a good way to visualize the interior structures still remains a difficult problem [18]. The volumetric approach is useful when dealing with, for example, water flows in which turbulent eddies are marked by dye. In that case the interfaces tend to be sharp, because diffusion is slow compared with the relevant measuring times, and the interfaces provide good depth cues. On the other hand, gas flows are difficult to visualize, because marker particles or dyes diffuse rapidly giving rise to fuzzy boundaries. Images tend to look like nebulous clouds [9].

1.3 Generation and dissemination of knowledge

Visualization alone can aid in understanding of the flow field by allowing global qualitative observations to be made concerning structures and features. It is somewhat more difficult, however, to extract quantitative information from volumetric datasets. With this as motivation, studies have been carried out resulting in semi automated 2-D and 3-D feature extraction algorithms (Helman & Hesselink [6], 1991). Scalar data are most readily examined, because display devices allow intensity or color mapping on a two-dimensional grid. Vectorial data, on the other hand, are very difficult to display and discern, because our human visual system is not well suited for this purpose. New approaches, therefore, need to be explored when dealing with such data. Here we describe several examples of how digital image processing can aid in understanding complicated flow datasets. This understanding ultimately should lead to improved insight into physical phe-

nomena, or provide refined models for data display, experiment or numerical calculation. We expect that this may be best achieved by closing the loop in an automated fashion, but at present this approach is still in the early stages of development. A question that still remains is how to best convey the results of such a study in a meaningful way to others.

Dissemination of knowledge about multivariate datasets is a topic that has received little attention, but is at the heart of the scientific enterprise. Without efficient means for communication of results, progress in our quest of understanding nature is severely hampered. New ideas in this area are surfacing, but it is not clear how the future will shape up.

2 Data processing

Traditionally, digital image processing has been used to improve image quality or extract data from 2-D images. In fluid mechanics this activity is still very important and has been studied in many papers and reviews. In this paper we refer to these studies and concentrate on less well known techniques that provide two and three dimensional data using signal processing approaches different from those used for direct imaging. For example, with an anamorphic optical processor planar velocity fields can be measured from double exposed speckle images in a fraction of the time normally required when using traditional 2-D Fourier transforming techniques. The velocity field can then be further analyzed in semi-automated fashion by using a topological decomposition comprised of critical points and dividing surfaces connecting them. The flow field is then quite amenable to further analysis by displaying the topological decomposition instead of the original vector field thereby avoiding the confusing vector field displays. An efficient algorithm for visualizing grayscale imagery is the Marching Cubes technique, which we have implemented using a variable resolution approach.

2.1 Traditional image processing

Many of the well known techniques such as laser induced fluorescence, particle tracking, laser scattering, speckle velocimetry, interferometry, and direct imaging methods are included in this class. Each method requires a specialized approach to extract the desired data from the images, but the preprocessing steps such as noise removal, edge enhancement, and radiometry correction are well documented [15] and suitable for a large number of fluid flow applications. Specific efforts to extract the desired quantities,

such as the velocity field from a multiple exposure particle image, require approaches that are largely ad-hoc in nature, but often provide good results. Quality assessment, however, is not always carried out leading to erroneous results. For example, it is often desired to compute vorticity fields from planar velocity fields. This requires numerical differentiation of the data, implying stringent accuracy requirements of the velocity field. Few studies have been carried out, unfortunately, characterizing all random and systematic errors. It is often straightforward to compute a velocity field from particle tracking data, but the derived vorticity field could be in error by as much as 10-40%. For certain applications this may be sufficient, but for comparison of data obtained with numerical and experimental techniques, this error is too large.

2.2 Separation of functions

To avoid some of these difficulties, we may pose the question: What diagnostic approaches lead to accurate results? Answers to this question will vary, and here a personal viewpoint will be presented. Our approaches have been based on the simple principle: **"Separation of Functions"**. In its broadest interpretation, a technique or device can be broken down into elementary parts, each of which performs a certain function. Each element is optimized for its own purpose, yet is an integral part of the whole device or approach. How can we translate this principle into flow visualization terms?

Flow visualization techniques usually involve data acquisition, data processing and interpretation. For example, if we want to measure vorticity, we should try to measure velocity gradients and not the velocity field itself. Numerical differentiation is a process prone to errors, but integration is usually not. How can we accomplish vorticity measurement directly? By separation of functions. Optics is well suited for taking images but not so useful for accurate computation. Electronic systems, on the other hand, are marvelous for carrying out complicated processing tasks. The final result of the data manipulation, however, is strongly determined by the quality of the input data. Therefore, we should be using optics to obtain accurate representations of the velocity gradients which can than be used to compute the vorticity field. From the vorticity field, the velocity can be obtained by integration, which tends to reduce noise by averaging, albeit perhaps at the expense of a slight reduction in resolution. This is not to say that particle tracking techniques are not useful, on the contrary. But the idea is to optimize each element of the data acquisition system so that the final result

may be optimized as well. In this spirit, optical processors can perform preprocessing operations that save a lot of computational time by acquiring the data in such a form that subsequent digital processing can provide accurate results at a reasonable cost. Thus there is an interplay between digital and optical processing that deserves further attention.

2.3 Hybrid processing

Optics describes the propagation and interaction of waves, made up of photons. Photons are Bosons and, therefore, do not interact easily. Electrons, on the other hand, are Fermions and like to interact with each other. This characteristic gives rise to profound differences between optical and digital processors. Photons can pass through each other with little or no interaction, and allow diagnostic systems to be built around multiple, noninteracting superimposed optical beams. Optical tomography is such an example, in which information about an object, e.g. the index of refraction, is averaged along the pathlength of multiple beams rotated about the center of the object. This information (referred to as projections) is acquired in the time it takes for the light beam to traverse the object size.

The accuracy of the projection data is strongly dependent on noise, and time averaging is almost always required, unless strong probe beams are used. The projections are subsequently digitized and analyzed by digital computer, because these calculations can be accurately carried out with electronics. Optical reconstructions have been investigated as well, but accuracy of optical processors is often limited to about 6 bits. On the other hand, the medium could not easily be probed with electrons, because overlapping particle beams would strongly interact making it difficult to extract information about the object from the projections.

This example also illustrates another point, namely that optical systems have enormous bandwidths. For example, a projection beam recorded on film may represent a space bandwidth product of 10^{10} or more based on a resolution of 1000 line pairs per millimeter and a size of 10x10 cm of film.

In summary, optics is well suited at parallel, extremely fast processing with low precision, whereas digital processors offer flexibility, lower bandwidth, but superior accuracy. Good diagnostic devices take advantage of these properties and may be considered hybrid processing systems.

In the past, flow visualization was limited almost exclusively to optical processing - namely, the taking of pictures - but recently digital processors have been added to extend the realm of flow visualization into quantitative

analysis. Digital image processing, however, is not a separate entity, uncoupled from the data acquisition system. In the spirit of the thesis of this paper, therefore, we will discuss digital image processing in close relationship to the probe radiation and its accompanying recording and processing system. In order not to duplicate previous efforts, we will restrict ourselves here to hybrid digital/optical processors that have significantly reduced the required digital processing task as compared with traditional approaches that produce the same kind of information. Hybrid systems that have significantly improved performance in terms of accuracy or spatial and temporal resolution are also of interest. Typical examples include: 1. vorticity measurement by optical processing [2], 2. speckle velocimetry using an anamorphic optical processor and digital computer [3], and 3. tomography using optical, acoustical or second sound probe radiation [16]. It is beyond the scope of this paper to discuss details about these processors, and the reader is referred to the original references.

2.4 Fluid flow vector field topology

Three-dimensional flow patterns over bodies often exhibit a complex structure that can be analyzed using topology concepts. In this approach, the flow field is divided into regions that are topologically equivalent to uniform flow. The regions are bounded by dividing surfaces (3D) or lines (2D) that meet at critical points [14]. Critical points are those points in the flow where the velocity vector vanishes.

In the past, the results of experimental flow studies or numerical calculations where often analyzed using hand drawings of the flow topology [20]. For complicated flow fields this method is difficult to carry out, and critical points may be overlooked. We have studied an automated approach that delivers the topology of the vector field, which can then be displayed using graphics techniques. In this way, the data analysis process can be automated, but more importantly, extended to allow accurate representation of complex datasets. These may then be used for making automated comparisons between multivariate datasets, for example, by using syntactic pattern recognition [7].

In this approach, critical points are located and characterized in a two-dimensional domain, which may be either a two-dimensional flow field or the tangential velocity field near a three-dimensional body. Tangent curves are then integrated out along the principal directions of certain classes of critical points. The points and curves are linked to form a skeleton representing the

two-dimensional vector field topology.

For two dimensional, time-dependent fields, these skeletons may be stacked to form three-dimensional surfaces representing the time evolution of the instantaneous topologies.

When generated from the tangential velocity field near a body in a three-dimensional flow, the skeleton includes the critical points and curves which provide a basis for analyzing the three-dimensional structure of the flow separation. The points along the separation curves in the skeleton are used to start tangent curve integrations to generate surfaces representing the topology of the associated flow separations.

2.4.1 Critical points

Critical points are those points at which the magnitude of the vector vanishes. These points may be characterized according to the behavior of nearby tangent curves. The set of tangent curves which end on critical points are of special interest because they define the behavior of the vector field in the neighborhood of the point. A particular set of these curves can be used to define a skeleton which characterizes the global behavior of all other tangent curves in the vector field.

To first order approximation in 2-D, a critical point can be classified according to the eigenvalues of the Jacobian matrix of the vector (u, v) with respect to position at the critical point $(x0, y0)$:

$$\left.\frac{\partial(u,v)}{\partial(x,y)}\right|_{x0,y0} = \left.\begin{bmatrix} \frac{\partial u}{\partial x} & \frac{\partial u}{\partial y} \\ \frac{\partial v}{\partial x} & \frac{\partial v}{\partial y} \end{bmatrix}\right|_{x0,y0} \tag{1}$$

Figure 3 shows how the eigenvalues classify a critical point as an *attracting node*, a *repelling node*, an *attracting focus*, a *repelling focus*, a *center* or a *saddle*. This can be understood by observing that a positive or negative real part of an eigenvalue indicates an attracting or repelling nature, respectively. The imaginary part denotes circulation about the point. Among these points, the saddle points are distinct in that there are only four tangent curves which actually end at the point itself. At the saddle point, these curves are tangent to the two eigenvectors of the Jacobian matrix, which are the separatrices of the saddle point. The outgoing and incoming separatrices are parallel to the eigenvectors with positive and negative eigenvalues, respectively. In addition to these 2-D critical points, certain points on the walls of objects or bodies in a fluid flow can be important. On walls where

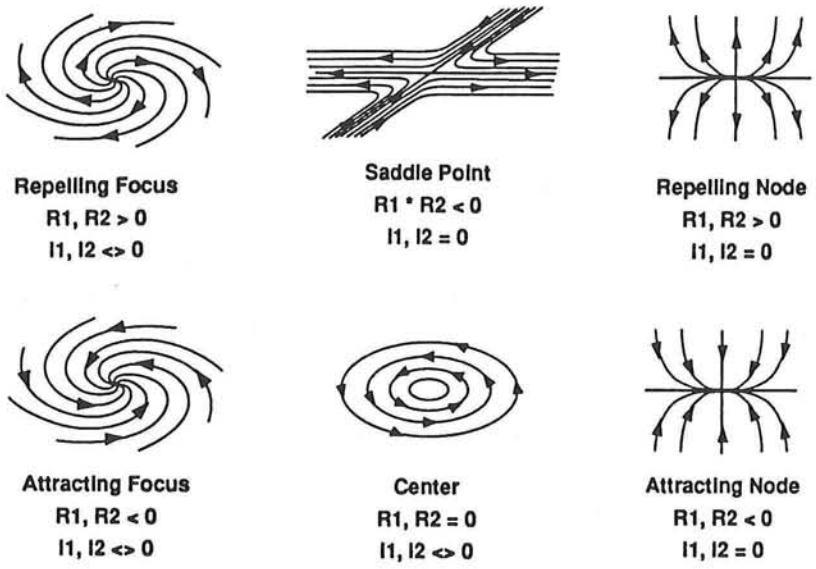

Figure 3: Classification criteria for critical points. R1 and R2 denote the real parts of the eigenvalues of the Jacobian, I1 and I2 the imaginary parts.

the velocity is constrained to be zero (no slip boundary in fluid dynamics), there may occur certain points, referred to as, *attachment nodes* or *detachment nodes* at which a tangent curve impinging on the surface terminates on the surface, rather than being deflected by the tangential velocity [5].

2.4.2 Topology in three dimensional separated flows

In these flows some stream surfaces near the surface of a body can abruptly move away and "separate" from the wall. The lines at which this occurs are known as "lines of separation." These lines are the three-dimensional extension of the *attachment nodes* and *detachment nodes* used in a two-dimensional analysis. Namely, these are curves on a body wall along which the tangent curves impinging on the body come very close to the surface and end on a critical point on the surface of the body rather than being deflected around it. Because separation surfaces are often associated with vortices and recirculation zones, determining separation topologies is important both for understanding fundamental fluid dynamics and practical applications in aircraft and jet nozzle design. But extracting topological information from numerical datasets using existing visualization tools is both difficult and time

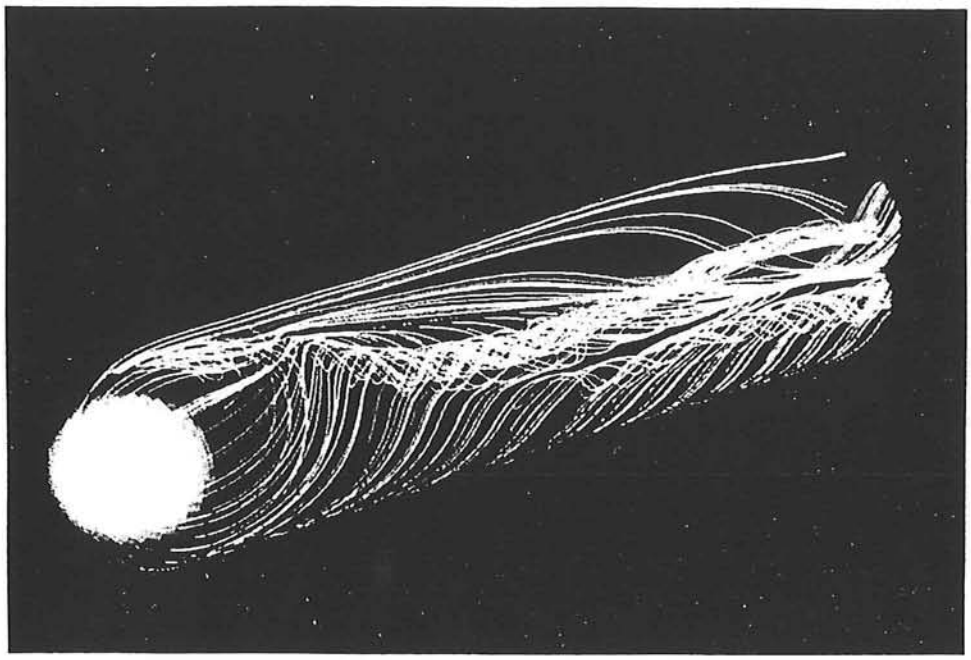

Figure 4: Streamlines in the computed flow past a hemisphere cylinder.

consuming. Typically, a researcher would try to determine the topology and the positions and shapes of the structures by looking at numerically integrated streamlines both in the volume (Figure 4) as well as integrations constrained to the surface. By manually selecting and refining integration starting points, structures and connections can be discerned. But since topological structures are complex and best portrayed graphically, those structures must then be hand drawn to capture the form of the structures, if not their exact shape, size, and position. Automatic methods of producing these schematic surfaces would not only simplify the work and eliminate manual errors, but most importantly, would accurately preserve and convey the quantitative aspects of the structures.

2.4.3 Surface topology

In general, when examining the topology of a flow, the surfaces of bodies in the flow are examined first. In experimental work, this is done by examining the streaks that form in an oil film on the surface of a body in a wind tunnel. In computer simulated flows, similar information can be derived by examining curves integrated along the surface [20] to produce topology skeletons.

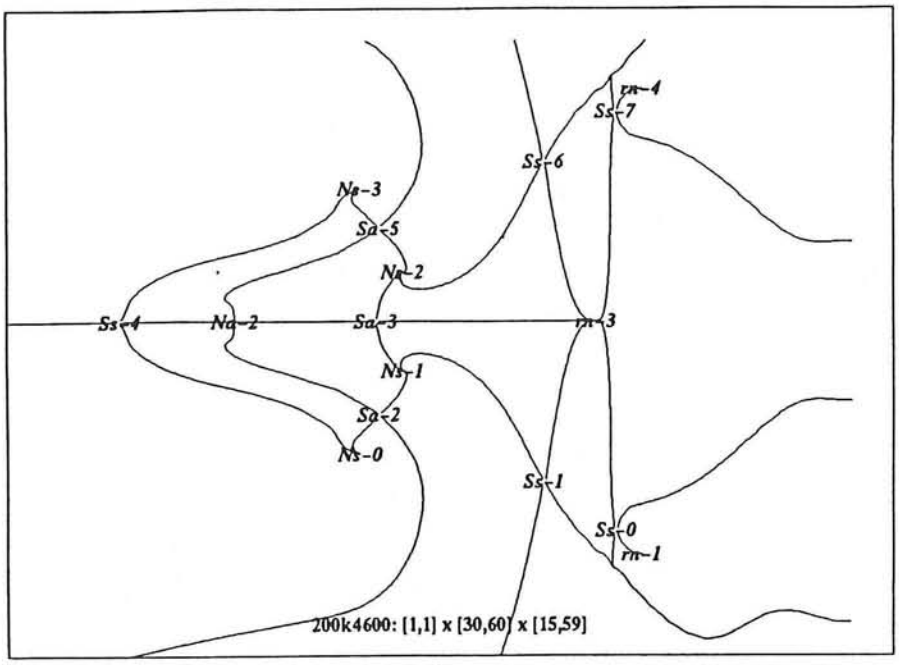

Figure 5: Computer generated skeleton of surface topology of flow over a hemispherical cylinder.

We can automatically generate the surface topology skeleton by applying the two-dimensional algorithm outlined above to the tangential velocity field near the body. Grids in these datasets conform to the shape of the body with one of the grid planes lying on the surface of the body. The velocity on this plane is zero. To analyze the surface topology we create the two-dimensional vector field which is the projection of the velocities in the grid plane one point away from the surface. If the body is defined by the $k = 0$ grid plane, the new two-dimensional field $(u'(i,j), v'(i,j))$ is computed as the projection of the three-dimensional velocity $(u(i,j,k), v(i,j,k), w(i,j,k))$ into the plane tangent to the body at $(i,j,0)$ Applying this approach to this field produces the surface topology skeleton in Figure 5. Here the critical points have been labeled according to the sign of the normal component. *Ss* denotes a saddle of separation (normal velocity positive), and *Sa* denotes a saddle of attachment (normal velocity negative).

The results of applying this analysis to the flow over a hemispherical cylinder are shown in Figures 6 and 7.

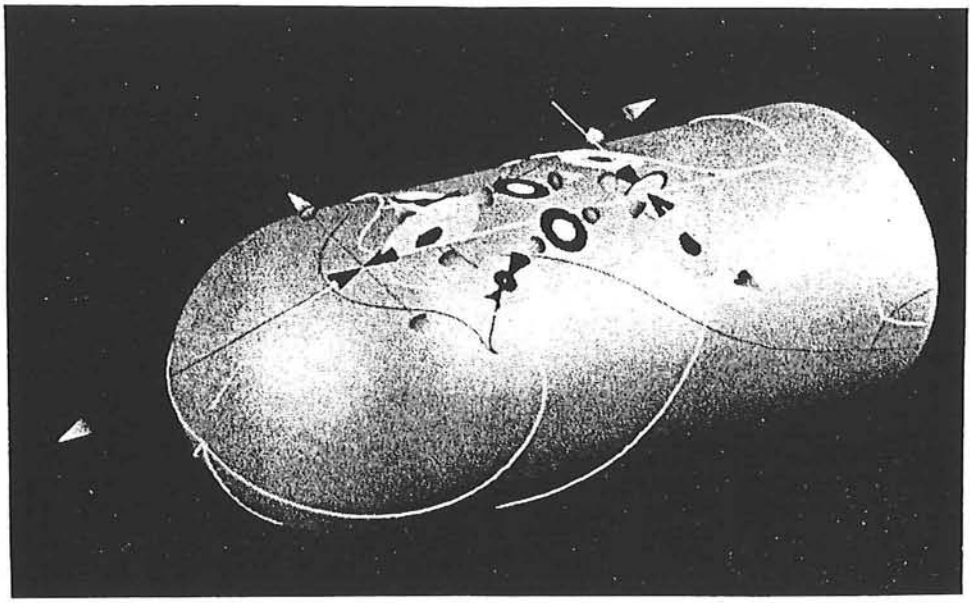

Figure 6: Surface topology skeleton shown on the body surface.

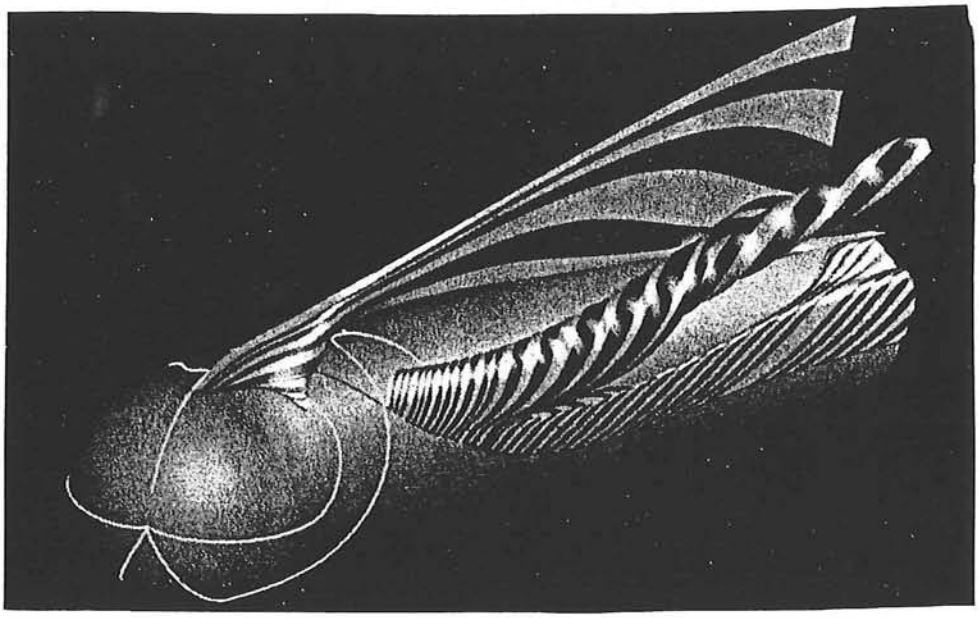

Figure 7: Computer generated surfaces depicting separation topology.

2.5 Isosurface analysis using Marching Cubes

Marching Cubes [12] is a popular algorithm for generating polygonal tilings of isosurfaces for sampled 3-D scalar fields. For the purpose of discussion we assume that the samples are defined on a rectilinear grid. Marching Cubes traverses the volume defined by the sample points, forms cubes (more generally, rectangular parallelepipeds) from clusters of eight neighboring samples, and for each cube, generates up to four triangles approximating the piece of the surface passing through that cube.

The triangles for each cube are generated by table lookup. First, an 8-bit index for that cube is computed based on the relative size of its sample points with respect to the isovalue. This index points to an entry in a table which identifies the orientation of the triangles for that cube. (Although there are 256 entries, there are only 15 basic types once symmetry is considered.) To determine the actual locations of the triangle vertices, linear interpolation along the cube edges is used. Normal vectors, needed for shading calculations, are estimated from the gradient of the scalar field. Gradient vectors are computed using central differences at the sample points and then linearly interpolated to the vertex positions.

After all the cubes are processed, the result is a list of triangles which may then be displayed with graphics hardware specifically designed for polygonal rendering.

We have implemented the Marching Cubes algorithm and applied it to the analysis and display of fluid flow datasets. The flows we have studied include the coflowing argon-helium jet that was measured using instantaneous optical tomography (Snyder & Hesselink [16], 1988) and the flow over a delta wing using a fast scanning laser sheet and Mie scattering to record a time sequence of cross sections (Yoda & Hesselink, [21], 1990). In both cases the data are interpolated onto a rectangular mesh, and surfaces of constant concentration are displayed; in the coflowing argon-helium jet case the contour surface represents constant argon-helium concentration and in the delta wing flow the surfaces denote constant smoke concentration.

Our software package consists of two parts : the surface generator and the interactive display program. The generator is written in C and can be ported to any Unix platform, while the display program is specifically written for the Silicon Graphics GL library. Some of the features of our software include interactive surface cutting, material property and light editing, and intuitive rotation/translation.

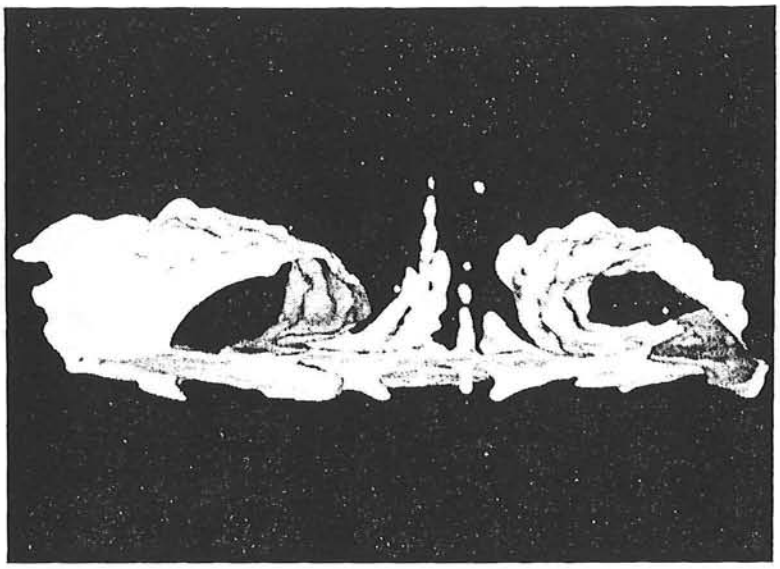

Figure 8: Isosurface of smoke concentration of the flow over a delta wing at 40 degree angle of attack.

2.5.1 Data compression

One problem with the basic algorithm is the number of triangles it generates. In one simulation, a modest 40x100x100 dataset generated about 100,000 polygons, which exceeds the animation ability of mid-performance graphics workstations. To address this problem we have investigated two approaches. The first approach is uniform subsampling, which reduces the global resolution of the image. This can be achieved by generating several lower resolution datasets by lowpass filtering and subsampling the original. When run on these new samples, Marching Cubes yields correspondingly smaller triangle counts. The display program then uses a low resolution surface for real-time manipulation. Higher resolution versions may be drawn with the same viewing parameters whenever desired.

Uniform subsampling is useful, but the accuracy of the low resolution surfaces leaves much to be desired. Our second approach improves low resolution accuracy using adaptive surface refinement. The basic idea is simple : use more polygons where the radius of curvature of the surface is small and fewer where the surface approaches that of a flat plate. The key to making this approach useful is defining an error measure that allows

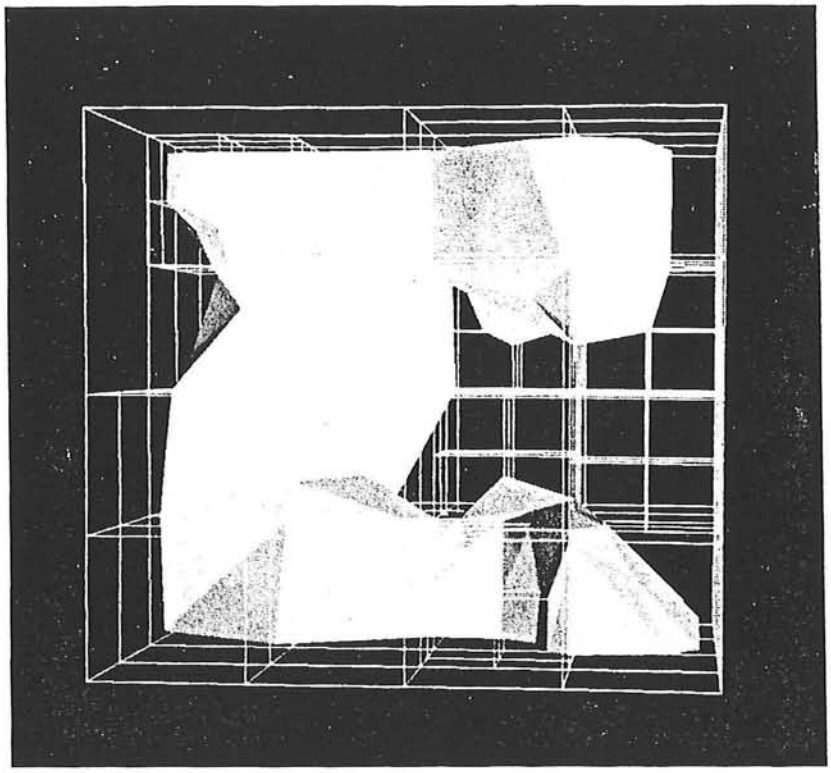

Figure 9: Adaptive polygonalization of constant concentration surface in argon-helium jet. Cube outlines indicate terminal octree nodes.

decisions to be made about the optimum distribution of the polygons in an automated fashion. The approach we have taken (Ning & Hesselink [13], 1991) is based on computing a global distortion measure, i.e. the difference between the true isovalue surface and the tiled surface. By quantifying the distortion in the surface approximation, and using the number of triangles as a rate measure, we can automate the process of determining good tilings at arbitrary resolutions.

Adaptive tiling is achieved by imposing an octree structure on the sample points, as shown in Figure 9. An octree is a hierarchical set of connected nodes which begins at a single root node. The root node is connected to eight child nodes, each of which, in turn, also has eight children, and so on.

For our application, the deepest nodes in the full octree correspond to the cubical cells in Marching Cubes. Eight of these nodes combine to form a node of the next larger size and the root encompasses the entire volume spanned by the samples.

Subtrees of the full octree yield surface models of different polygon counts. In our algorithm a good surface model is found at any resolution by minimizing the underlying approximation error.

In principle, two inverse methods can be used to vary resolution, namely

growing and pruning, although we have only implemented the pruning approach. Growing means starting with a small tree and selectively subdividing leaves with high curvature. Pruning entails building a deep uniform tree and trimming branches with low curvature. The pruning approach yields good results, but is rather slow in its present implementation. Growing appears to be an attractive alternative, and is currently being investigated.

Another way to improve rendering performance is to draw the surface as a triangular mesh instead of as independent polygons. The mesh primitive takes advantage of vertex sharing to avoid redundant transformation steps. As a byproduct, connectivity information can be used to perform surface-specific operations (like peeling).

There are several instances where the variable resolution model is helpful. First, to view datasets normally too large for real-time interaction due to hardware rendering speed. Second, in a distributed visualization environment where network bandwidth is the bottleneck, to enable progressive transmission of surface geometry between the compute server and the graphics terminal. Finally, for database browsing, where quick low resolution scanning is used to speed search times.

The data compression techniques described here are rather specific to the Marching Cubes algorithm. More general data compression techniques may be applied to the original scalar field as well. A logical extension of speech and image coding algorithms to 3-D can yield large compaction savings for archival purposes. Transform coders and vector quantizers, for example, both operate on arrays of N consecutive samples in speech and subblocks of NxN neighboring pixels in images. The same techniques are generalizable to clusters of NxNxN neighboring 3-D samples.

A significant feature of our efforts in data compression is the recognition that quantitative accuracy criteria should be applied to visualization. Computer graphics research is often preoccupied with qualitative rendering, which is perfectly acceptable for a large number of applications such as realistic rendering of solid objects or animation of natural scenes. For scientific applications, however, it is often desirable to extract quantitative information from the data, and for that purpose we need to carefully analyze and investigate the errors associated with the display system. Error bars, denoting bounds within which the rendered surfaces should fall, need to be provided for display of quantitative volumetric data in much the same way as has been the tradition in the scientific literature for decades when dealing with two-dimensional information. This topic has been largely neglected in the visualization literature.

3 Research issues

Improvement of current techniques is a complicated task that involves many issues. Here we will restrict ourselves to a subset of issues that appear particularly relevant to analysis and display of data with the objective of improving our knowledge of physical phenomena related to fluid flows.

3.1 Usage

Many of the flow visualization techniques have been developed by researchers for their own purposes. As a result there is little commonality in the various approaches, and transportability has suffered. Many software programs are now coupled to a graphical interface, but no standard has emerged. This is particularly significant, because many visualization approaches require interactive data analysis, and a standard interface is highly desirable. By adopting some standard, current approaches could be more easily extended to include user defined options particular to a specific need. For example, very few attempts have been made to include feedback loops that influence the course of calculation or an experiment. There have been several studies that provide flow control, but often only point measurements have been made. Visualization of intermediate computational results is important, however, and quite often one can only analyze the results of multi-dimensional data by graphical means. In that case data compaction and automated data extraction are highly desirable, if not absolutely necessary.

3.2 Representation

Visual data are often displayed as images on a graphics monitor. Much work has been carried out with regards to rendering these images, in particular when dealing with three-dimensional data. Sometimes a graphics display is sufficient to discern structures such as turbulent eddies, and their exact shape and size are not required. In other applications, such as in combusting flows, we may wish to compute certain global parameters, such as the surface-to-volume ratio. That requires accurate representation of the data, and error bounds are essential. The question then arises in what visualization space the data should be displayed. As vectors, or as contour plots, as multiple superimposed data, or as time varying animations? Answers to these questions are strongly application dependent, but, again, some sort of standard may be useful here, too. In related disciplines, such as com-

puter graphics, little attention is paid to analyzing the accuracy of certain graphics such as the Marching Cubes algorithm. For fluid flow diagnostics accuracy issues need to be addressed. Once that information is known, we can determine how good our estimates of the size and shape of structures really are.

3.3 The role of visualization in data generation and evaluation

Much information obtained by visualization tools is currently processed by intervention of humans. Yet, in many applications, the datasets are so large that we no longer are capable of analyzing and evaluating this information. In particular we need to find new ways for comparing multivariate datasets. As an example, decomposition of vector fields into topological representations is useful, because it provides a means for data compression, yet most significantly the important structural data are retained. Conventional data compression techniques must be applied to flow visualization problems, too. These reduced datasets may then be analyzed in a more automated fashion by using, for example, syntactic pattern recognition. The whole visualization environment must be integrated into the work environment, with easy access to the raw and reduced data by multiple users. We advocate the approach of first analyzing large datasets and then visualizing them.

3.4 Dissemination of results

In a shareable computational environment results must often be disseminated by electronic means. It would be desirable if papers could be published in a similar fashion, because the results of modern visualization tools are no longer compatible with two-dimensional paper media. As a compromise, we often derive global information from the volumetric data or reduce the dimensions to two. In the process much valuable data are lost. Holograms or stereo pairs are useful to discern three-dimensional structures [7] [2], because they convey a large amount of data, and even time can be incorporated into the display so that 3-D time varying sequences can be projected. But much work needs to be done to standardize some of these approaches so that the community at large can benefit from them, rather than only a few research groups suitably equipped with hardware and software. In particular, we need to address the question: Is the human interpreter needed in the analysis and presentation of the data? If the answer is affirmative, we need to

try to optimize our graphics representation to allow as rich a representation as is possible given current constraints on publishing. An effort should be expended to allow electronic publishing of multivariate datasets.

3.5 Education

Sophisticated visualization techniques require a considerable effort on the part of the user before they can be effectively used by someone other than the originator. This requires that better means must be found to introduce the results of a large number of different researchers into the community. In the past little attention has been paid to this technology transfer issue, but the current level of sophistication is so high that previous, simple, approaches are no longer satisfactory. For example, should researchers develop specific tools that are highly specialized for their work and should they be generalized by vendors of graphics workstations and software houses, or should they develop more general purpose tools that can be used by a large variety of users, but under sometimes less than optimal conditions? These issues are usually not discussed in scientific papers, but have a place in a review of the kind presented here. These secondary issues often are the most pressing when dealing with the introduction of new tools into the research community.

4 Summary

In this paper we have taken a viewpoint that considers optical and digital processing as closely related activities. One strongly influences the other. A simple but very powerful principle: "Separation of Functions", provides guidance to the development and analysis of flow visualization tools. But it is certainly not restricted to this application. It holds in general and is useful for instrument design and numerical analysis alike. From this perspective, it is highly desirable to use optics as a preprocessor in conjunction with digital processing systems. Optical approaches are extremely useful for obtaining image based data and often can perform preprocessing tasks such as taking spatial averages or derivatives of velocity with respect to spatial coordinates. This approach allows digital processors to further extract quantitative information from the optimized input data, which usually yields better accuracy and final results. In particular, novel approaches to diagnostics may be developed that are highly suitable for a specific task such as vorticity measurement in a conventional or liquid helium flow field. The raw data then need to be interpreted using computer based methods. Essential

information needs to be extracted for data evaluation and for comparison between multivariate datasets. In many instances this effort needs to be semi automated, involving only minimal intervention by humans, because the sheer size of these datasets is now beyond the capability of human interpretation alone. As an example, topological decomposition of vector fields allows a simple representation commensurate with graphics workstations, yet retains much of the original richness of the dataset.

5 Acknowledgements

This work is supported by NASA under contract NAG 2-489-S3, including support from the NASA Ames Numerical Aerodynamics Simulation Program and the NASA Ames Fluid Dynamics Division, and by the NSF under grant ECS 8815815.

References

[1] Ronald Adrian. Particle imaging techniques for experimental fluid mechanics. *Ann. Review of Fluid Mech.*, 23:261–301, 1991.

[2] Juan C. Agui and Lambertus Hesselink. Flow visualization and numerical analysis of a co-flowing jet: A three-dimensional approach. *J. Fluid Mech.*, 191:19 – 45, 1988.

[3] Steven Collicott and Lambertus Hesselink. Analysis and design of an anamorphic optical processor for speckle metrology and velocimetry. *Submitted to Appl. Opt.*, 1991.

[4] H. Fuchs, Z. M. Kedem, and S. P. Uselton. Optimal surface reconstructions from planar contours. *Communications of the ACM*, 20(10):693–702, October 1977.

[5] James L. Helman and Lambertus Hesselink. Representation and display of vector field topology in fluid flow data sets. *IEEE Computer*, pages 27–36, August 1989. Also appears in *Visualization in Scientific Computing*, G. M. Nielson & B. Shriver, eds. Companion videotape available from IEEE Computer Society Press.

[6] James L. Helman and Lambertus Hesselink. Visualization of vector field topology in fluid flows. *IEEE Computer Graphics and Applications*, May 1991.

[7] Lambertus Hesselink. Digital image processing in flow visualization. *Ann. Review of Fluid Mech.*, 20:421–485, 1988.

[8] Lambertus Hesselink, J. Pender, S. Jaffey, and K. Dutta. Quantitative three-dimensional flow visualization. In *Proceedings of the Third International Symposium of Flow Visualization*, 1984.

[9] S. Jaffey, K. Dutta, and L. Hesselink. Digital reconstruction methods for three-dimensional image visualization. In *Three-Dimensional Image Processing and Display.* SPIE. vol 507, 1984.

[10] Marc Levoy. Display of surfaces from volume data. *IEEE Computer Graphics and Applications*, 8(3):29–37, 1988.

[11] Y. Levy, D. Degani, and A. Seginer. Graphical visualization of vortical flows by means of helicity. *AIAA Journal*, 28(8):1347–1352, 1990.

[12] W. E. Lorensen and H. E. Cline. Marching cubes : a high resolution 3-D surface construction algorithm. *Computer Graphics*, 21(4):163–169, July 1987.

[13] Paul Ning and Lambertus Hesselink. Adaptive isosurface generation in a distortion-rate framework. In *Proceedings of the SPIE, vol 1459*, 1991.

[14] A.E. Perry and M.S. Chong. *Annual Review of Fluid Mechanics*, chapter A description of eddying motions and flow patterns using critical point concepts, pages 125–156. Annual Reviews Inc., 1987.

[15] William K. Pratt. *Digital Image Processing.* Wiley-Interscience, 1978.

[16] R. Snyder and L. Hesselink. High speed tomography for flow visualization. *Applied Optics*, 24:4046–4051, 1985.

[17] J. Wilhelms and A. Van Gelder. Topological considerations in isosurface generation. *Computer Graphics*, 24(5):79–86, November 1990.

[18] K. Wu and Lambertus Hesselink. Computer display of reconstructed scalar data. *Appl. Opt.*, 27(2), 1988.

[19] Wen-Jei Yang, editor. *Handbook of Flow Visualization.* Hemisphere Publishing, 1989.

[20] Susan X. Ying, Lewis B. Schiff, and Joseph L. Steger. A numerical study of three-dimensional separated flow past a hemisphere cylinder. In *Proceedings of the AIAA 19th Fluid Dynamics, Plasma Dynamics and Lasers Conference.* American Institute of Aeronautics and Astronautics, June 1987. Paper 87-1207.

[21] Minami Yoda and Lambertus Hesselink. A three-dimensional visualization technique applied to flow around a delta wing. *Experiments in Fluids*, 10:102–108, 1990.

CONTRIBUTION OF MICROHOLOGRAPHY TO 3-D FLOW MEASUREMENTS

H. ROYER
French-German Research Institute of Saint-Louis
68301 SAINT LOUIS CEDEX
FRANCE

I. INTRODUCTION

Microholography is a powerful means of visualizing and measuring three-dimensional clouds of small particles (droplets, bubbles, dusts, etc.). The particles are often used as tracers in fuids, thus allowing the study of some parameters of the fluid behavior. We describe here the main characteristics of the method, its advantages and limits, and the possible applications to flow measurements.

II. DESCRIPTION OF THE METHOD

Fourty-three years ago, D. GABOR proposed a technique for visualizing the atoms [1]. It consisted in recording the diffraction pattern produced by an X-ray beam travelling through a sample of matter. Then the recorded pattern was illuminated by a visible light beam in order to reconstruct a magnified image of the object. This very application has never been brought to light in this original form and it is now admitted that a three-step process will be necessary to achieve X-ray holography with a good image quality.

However, the expression "brought to light" is to be taken in a figurative sense as the original idea does work if the same wavelength (visible light) is used both for the recording and for the reconstruction. Of course, the image magnification is equal to one but this is sufficient for a large variety of uses.

The "in-line" or "Gabor" recording system is the most simple one can imagine. A parallel light beam travels through the object field (particles in a transparent medium) and goes directly to the photographic plate (figure 1). If the particles are not too concentrated, a small part of the light is diffused and the combination of the diffracted waves with the non-diffused ones produces the hologram. The spacing of the interference fringes roughly ranges from 1 to 10 μm, which explains why the photographic emulsion must have a fine grain.

By putting the processed plate back into the same laser beam, one may observe two symmetrical images, one of which is real and can be magnified by classical means (lens and TV system). This gives the possibility of measuring the shape, the size and the 3-D position of every particle present in the volume.

If two successive holograms are recorded on the same plate, two images are observed simultaneously. If the particles were moving, their displacements can be measured, which leads to their velocities. The latter are also three-dimensional but the radial component is obtained with a lower precision. More than two exposures can be superimposed for delivering more data (velocity sign, acceleration) but the image contrast decreases rapidly (figure 2).

Thus holography appears as the only non-intrusive method providing instantaneous 3-D maps of the particle behaviour and eventually of the fluid behaviour. The huge amount of information contained in a hologram is explained by the fact that a standard-size holographic plate includes about 10^{11} pixels.

III. IMAGE QUALITY

The practical limits of the method are imposed by the quality of the image, which depends on various experimental parameters.

- The diffraction blur is determined by the recording wavelength and by the object-to-hologram distance. In standard experimental conditions, the size limit of visualization is of the order of 5 μm though it is theoretically possible to go beyond this value.
- Every particle diffuses light toward the other particles. Speckle appears in the images and its effects increase with the number of particles and with their cross-sections. A practical criterion to evaluate the corresponding degradation is the obscuration ratio (o.R.) of the recording beam by the particles. If it is smaller than 1%, the images are very good; between 1% and 10% the quality remains acceptable; beyond 10% the method does not apply to the smaller particles, and it is obvious that at 100% the reference vanishes and there is no more hologram (figure 3a and b).
- The darkening of the holographic emulsion is an important parameter. The optimal density is of the order of 1.5. With a 10E75 plate, the corresponding image/background contrast is roughly equal to 8.
- The particle velocity also generates a blur corresponding to the laser pulse duration. Typically, with a duration of 20 ns, a velocity of 150 m/s leads to a blur of 3 μm, smaller than the diffraction limit.
- A change of wavelength (or of geometry) between the recording and the reconstruction gives rise to spherical aberration. It will be

negligible if the wavelength variation remains smaller than 10% (ruby→He-Ne or YAG→Ar).

- Every optical element is a source of spurious light: reflexions on the faces, diffusion by the edges, by the dusts or the scratches. The effects being much stronger than with incoherent light, it is important to use new, clean and anti-reflection coated optics and to avoid any redundant element (a single lens produces 1 second-order reflexion, a doublet 6 and a triplet 15).
- The quality of the emulsion substrate is also very important (figure 4). The degradation is not visible with large-size objects but it can be really disastrous with microimages.
- Let us finally mention the role of the reference-wave shape. It implies that the index gradients be strictly limited in the fluid surrounding the particles.

IV. OTHER RECORDING ARRANGEMENTS

In the classical off-axis system, the reference is distinct from the object waves. However, the image is subject to strong aberrations (especially astigmatism) if great attention is not paid to the geometry and to the wavelength used at the reconstruction. For this reason it is rather recommended for the study of phenomena including high index gradients (combustion) [2].

It is also possible to make use of two beams which meet in the object field. The weaker goes to the hologram (reference) while the other (much brighter) is only used to illuminate the particles which scatter the light toward the hologram. Here it is possible to adjust the beam ratio for various purposes [3] (subdiffraction particles or great number of exposures) but the images are not subject to field aberrations (figure 5). The information on the sizes is not available but this system offers interesting possibilities for velocimetry in gases.

V. APPLICATIONS

Since Welford suggested the use of microholography for bubble-chamber visualization [4], it has been applied in a large variety of domains: Meteorology (cloud droplets, fogs, snow flakes in flight) [5]; fuel injection (size, velocity, pulverization process and evaporation of droplets) [6]; aerodynamics [7] and hydrodynamics [8]; nuclear safety (sedimentation of radioactive dusts etc.); combustion [9]; turbine erosion by dusts or by hot water droplets [10]; chemistry (medical or chemical aerosols) [11]; cavitation [12] etc. Figures 6 to 9 show some images obtained in various domains.

VI. RECENT PROGRESS

The main problem for a routine use of microholography is the automatic data reduction from the reconstructed field. The works of STANISLAS and SCHON should lead to an operational system working on a PC in a very near future [13]. A comparison between automatic and manual exploration of the same volume in a bunch of particles has already shown a very good agreement between both methods.

The possibility of instantaneous edge-extraction on holographic images (figure 10) is expected to improve substantially the automatic process [14]: the number of pixels to be processed is much smaller, the size measurements do not rely on the TV adjustments and the depth measurements are more accurate - a good point for 3-D velocimetry.

It is now possible to image the object field near holographic plate with the help of a wide-field transfer optics whose aberrations are automatically corrected at the reconstruction. This technique reduces the influence of the glass-substrate defects and, in some cases, it provides a substantial gain of contrast.

VII. CONCLUSION

After years of basic research and applications, microholography is now studied in its practical aspects. It is likely that in the next few years a complete system including recording, reconstruction and data reduction will be commercialized for non-specialists.

This does not mean that basic research is to be abandoned. A rapid-development emulsion (similar to thermoplastics used is off-axis holography) would save a precious time for the use of the in-line system. The development of thick materials would open the way to colour holographic velocimetry. Pulse UV lasers with a wavelength of about $10^{-1}\ \mu m$ would allow the visualization of micrometric particles with the in-line system (the Rayleigh diffusion is proportional to λ^{-4}). From this point of view, microholography still appears as a technique with a future.

REFERENCES

[1] GABOR D.
Nature 161-777 (1948)

[2] BELZ R.A., MENZEL R.W.
Opt. Eng. 18-256 (1979)

[3] ROYER H.
Opt. Com. 20-73 (1977)

[4] WELFORD W.T.
Appl. Optics 5-872 (1966)

[5] BROWN P.
Jl. Atm. Ocean. Techn. 6-293 (1989)

[6] ARNDT S.
Holo-Graphics 90, Nurnberg, FRG (1990)

[7] STANISLAS M.
Sciences et Techniques de l'Armement, 61-149 (1987)

[8] WEINSTEIN L.M., BEELER G.B.
Symposium on Aerodynamics and Related Hydrodynamics Studies, Monterey/CA (1986)

[9] KARAGOUNIS S.G.
Thesis, Monterey/CA (1981)

[10] KLEITZ A.
La Houille Blanche, 8-677 (1973)

[11] SEGER G, SINSEL F.
Staub-Reinhalt. Luft, 30-741 (1970)

[12] EBELING K.J, LAUTERBORN W.
Opt. Com. 21-67 (1977)

[13] STANISLAS M. et al.
Euromech Colloquium n° 279, Delft, NL (1991)

[14] CHRISTNACHER F., ROYER H.
Colloque OPTO 91, Paris, France (1991)

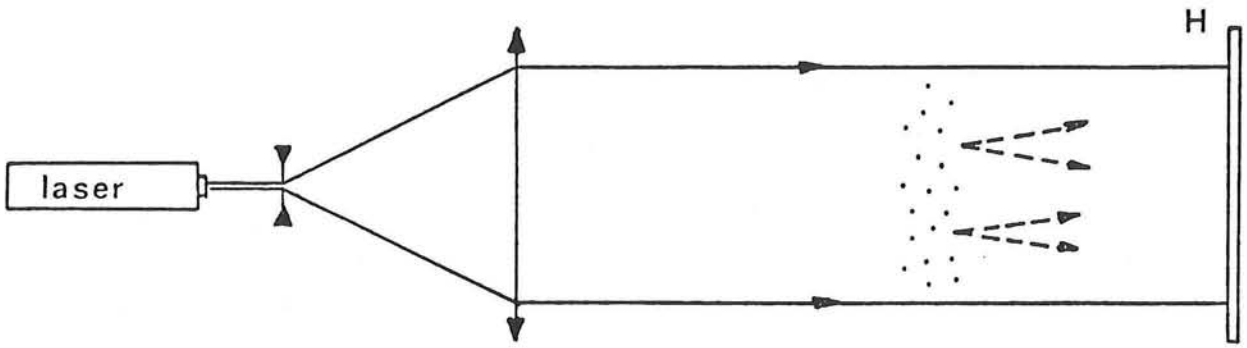

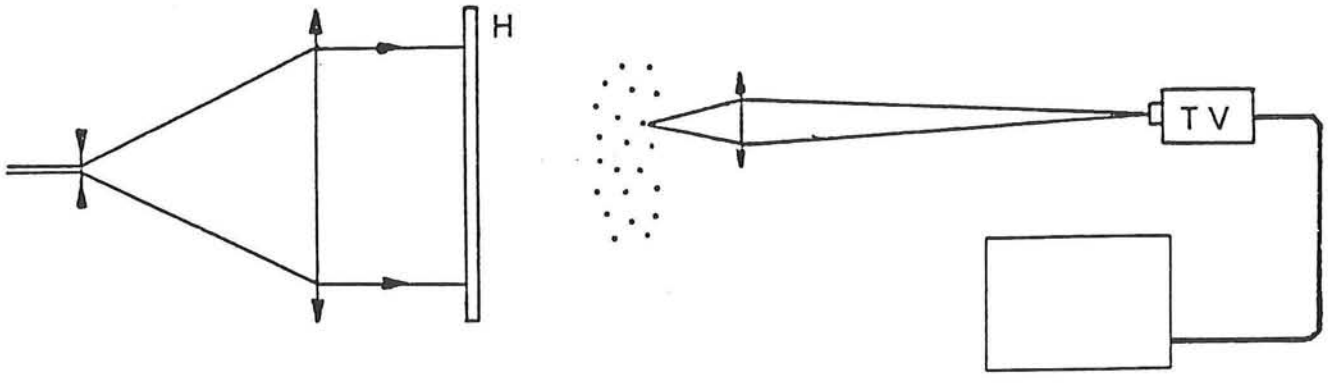

Fig. 1 : Recording and reconstruction arrangements

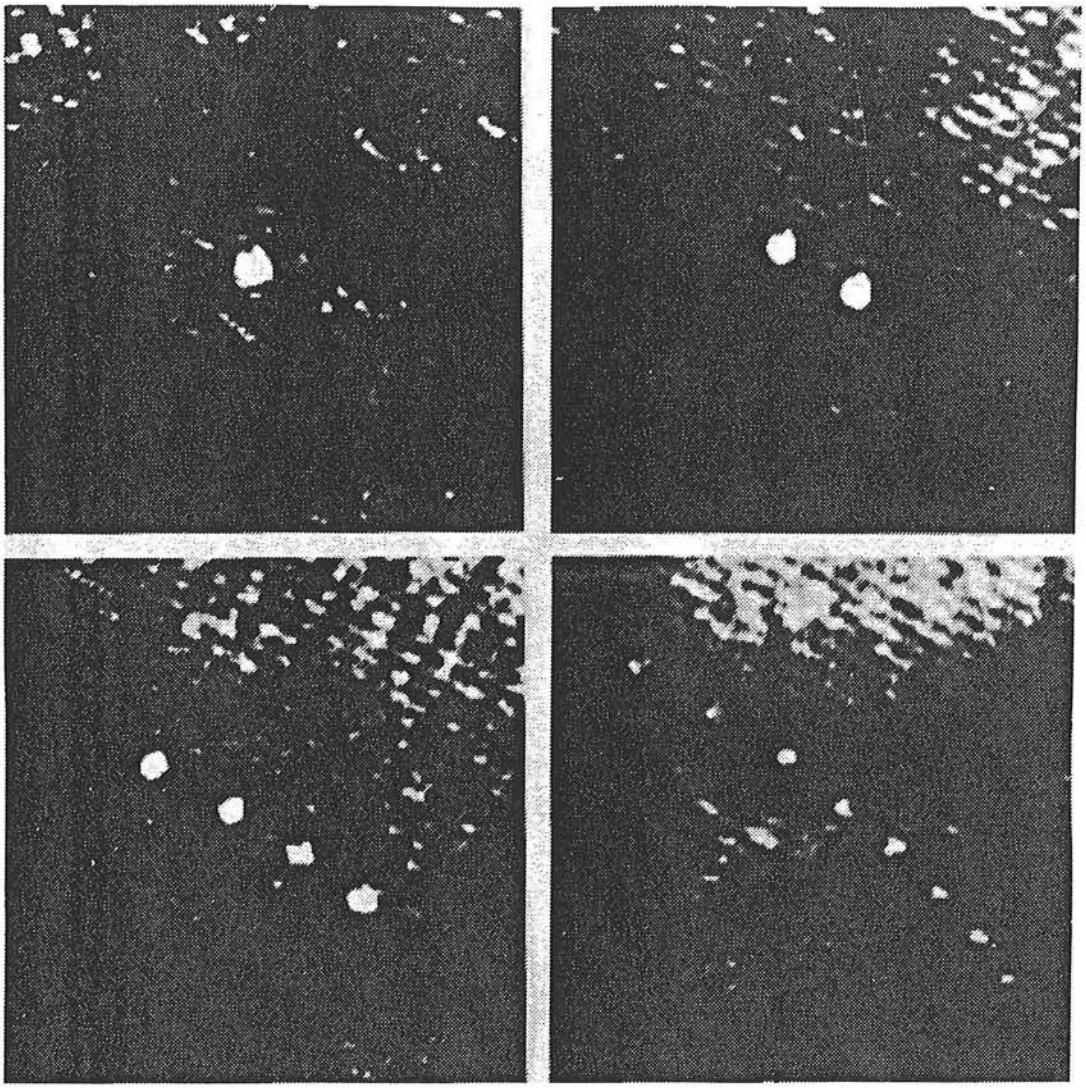

Fig. 2 : Contrast evolution as a function of the number of exposures

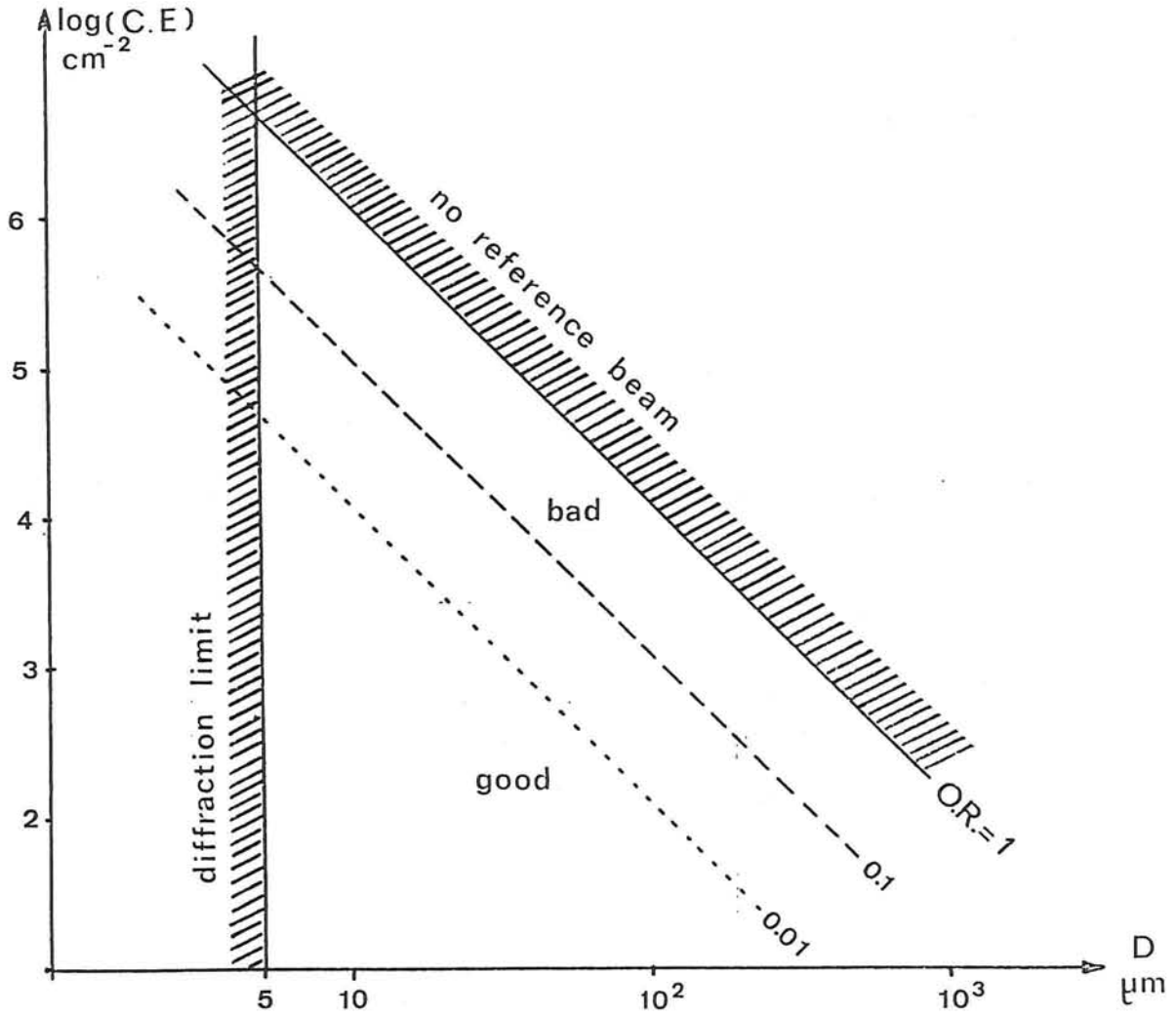

Fig. 3 : Influence of the particle concentration on the image quality. C = concentration (cm^{-3}), E = depth (cm), D = droplet size (μm), a) diagram, b) typical images

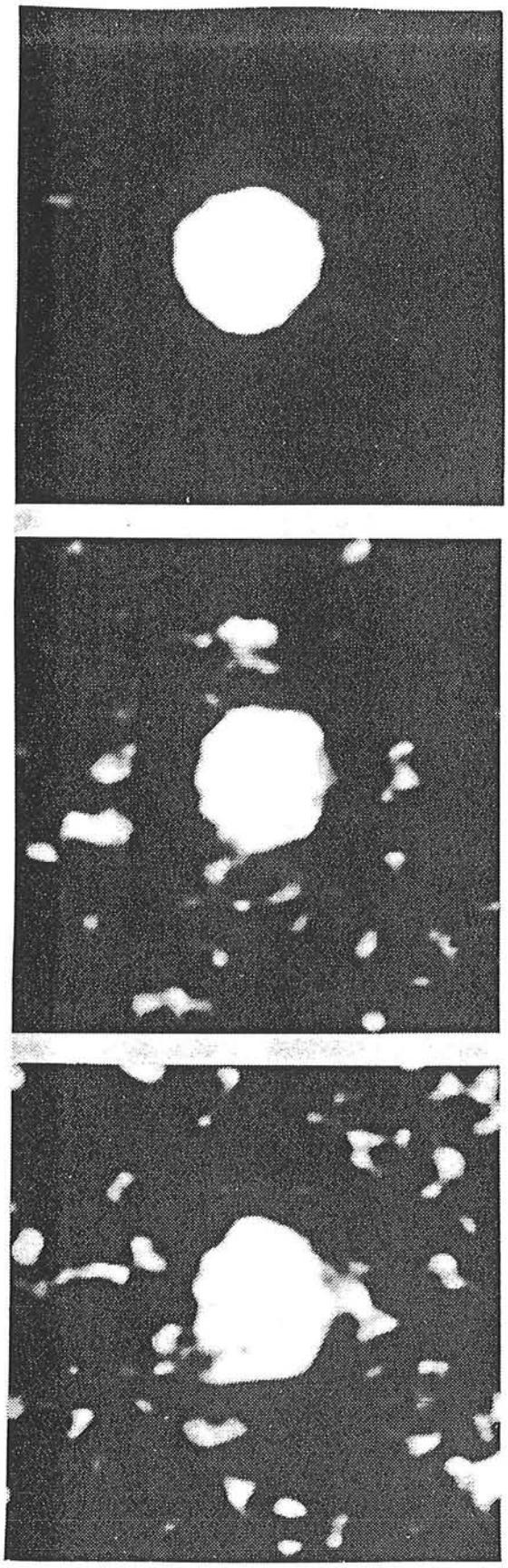

Fig. 3b .

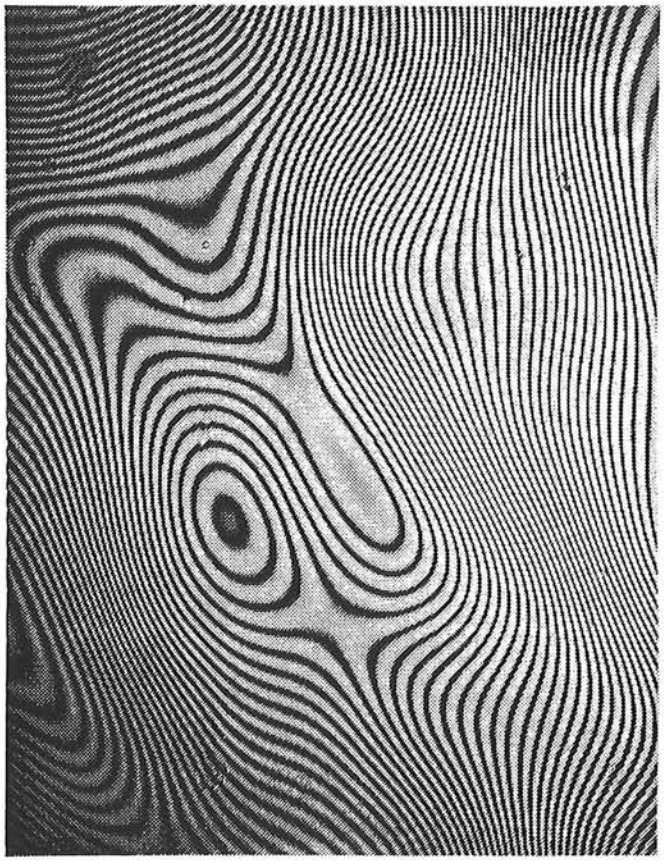

Fig. 4 : Interferogram of a holographic glass substrate

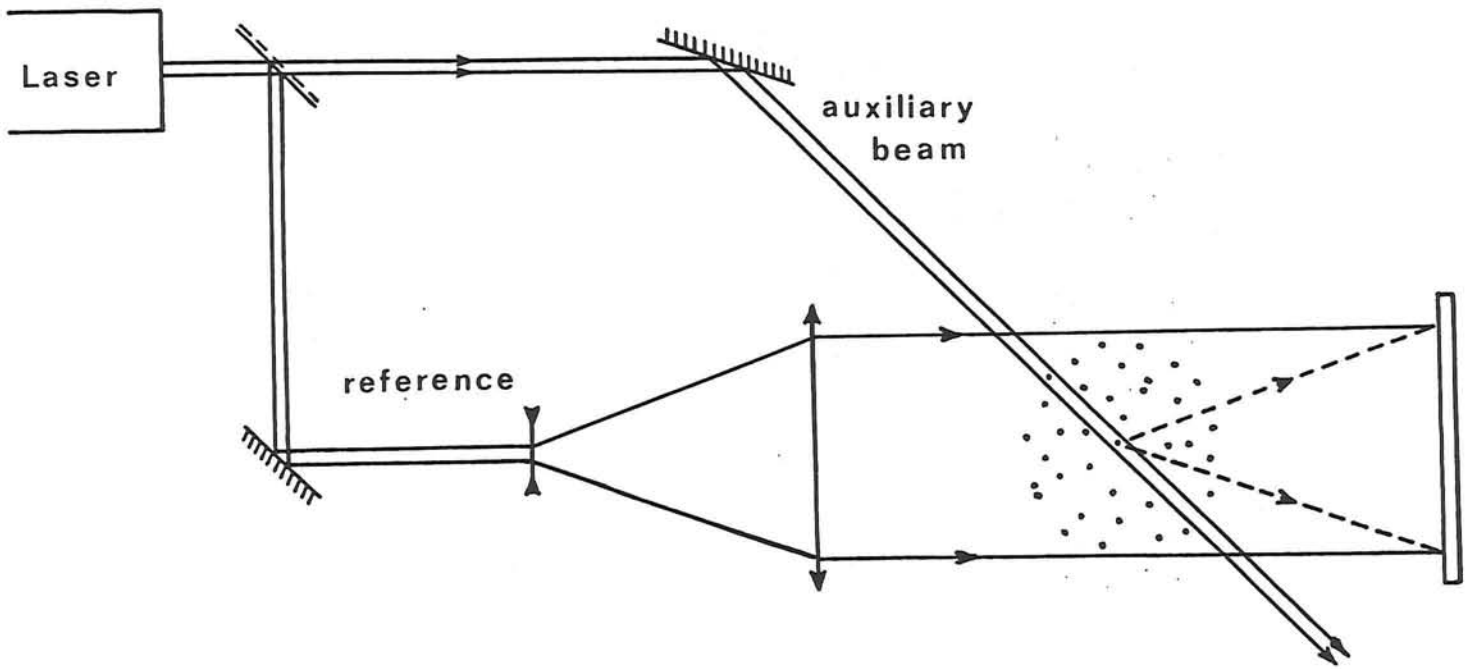

Fig. 5 : Recording arrangement for submicron particles

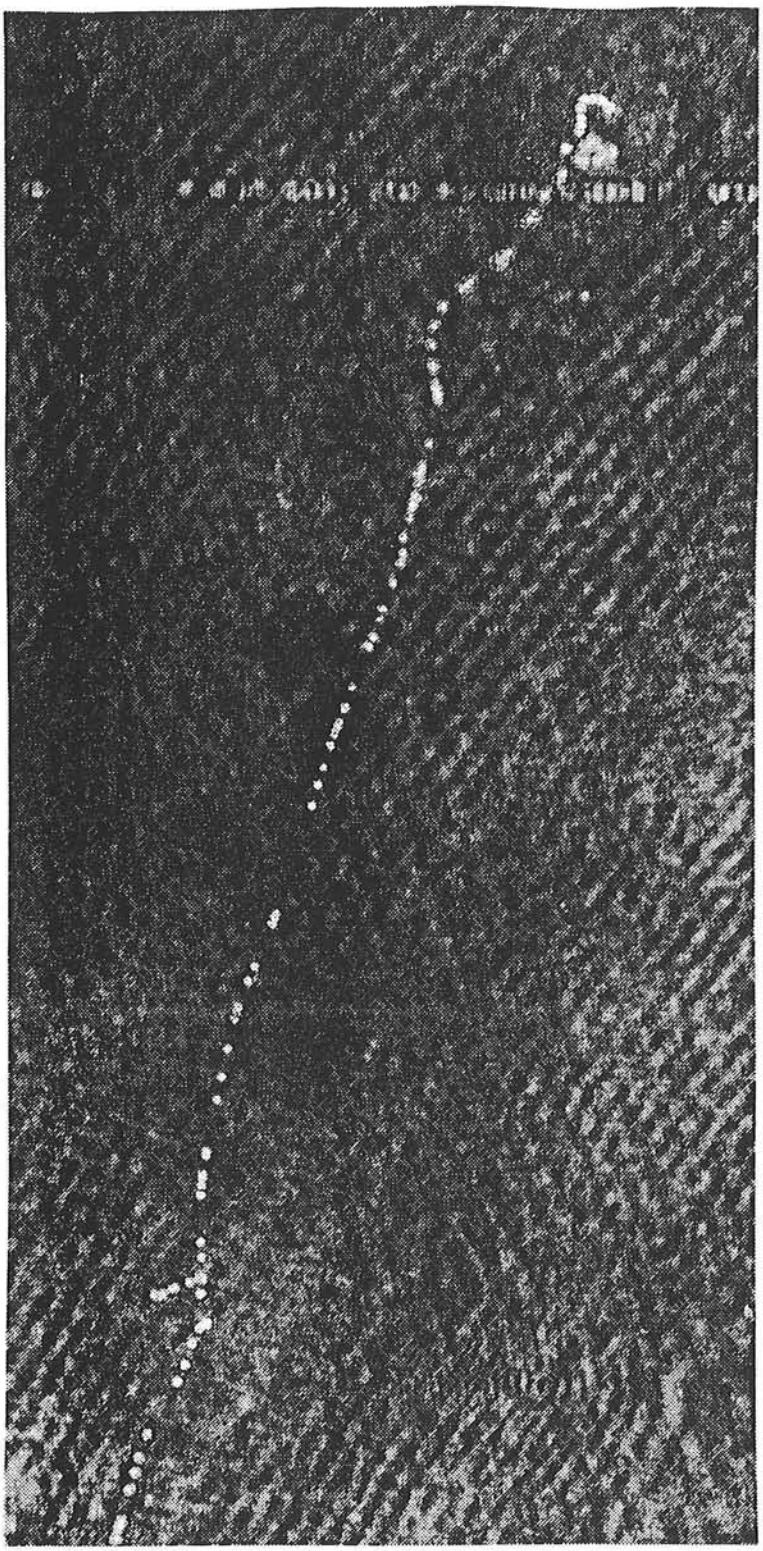

Fig. 6 : Image of a particle track in a bubble-chamber

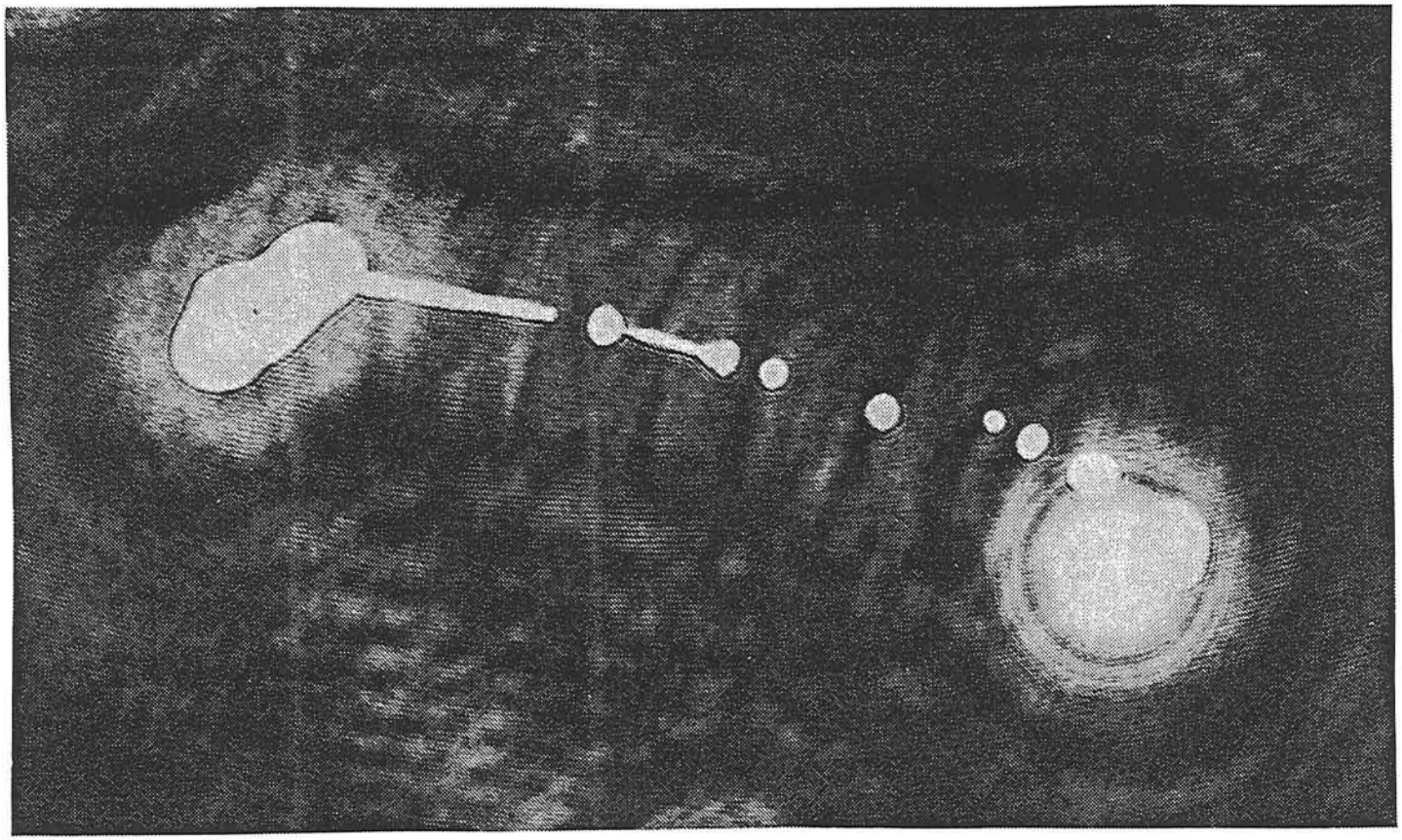

Fig. 7 : Pulverization of liquid fuel

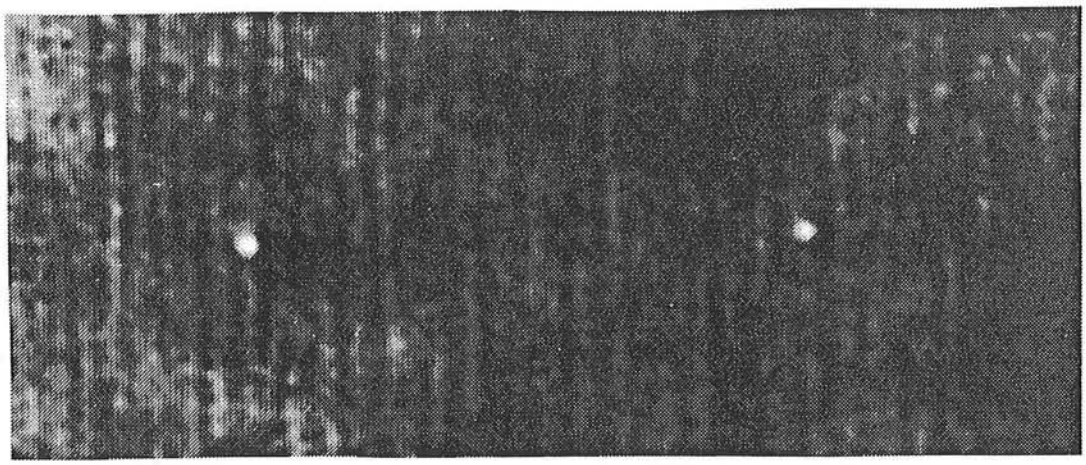

Fig. 8 : Double-exposure image of a 4 μm particle

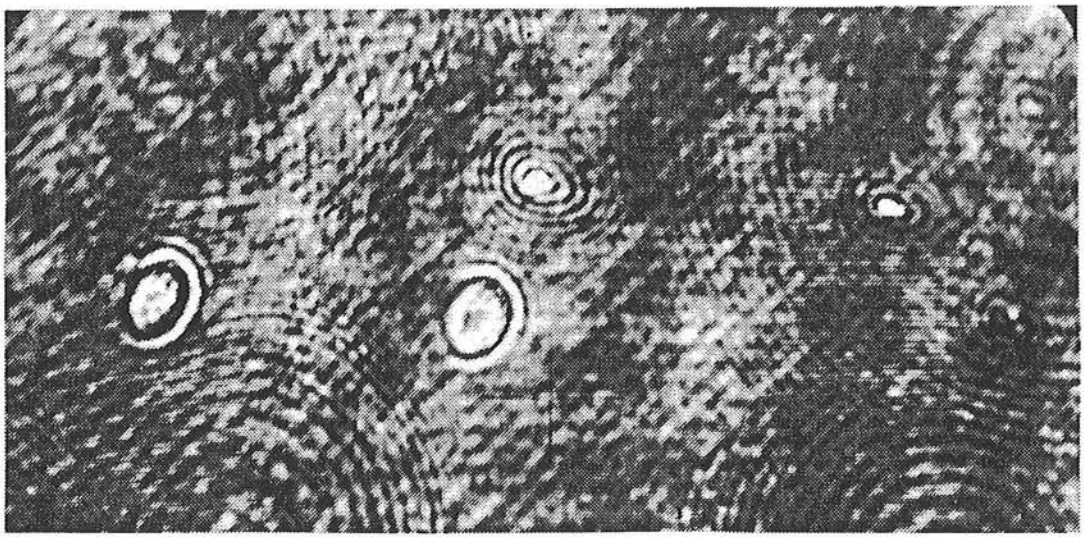

Fig. 9 : Double-exposure image of a micrometric particle

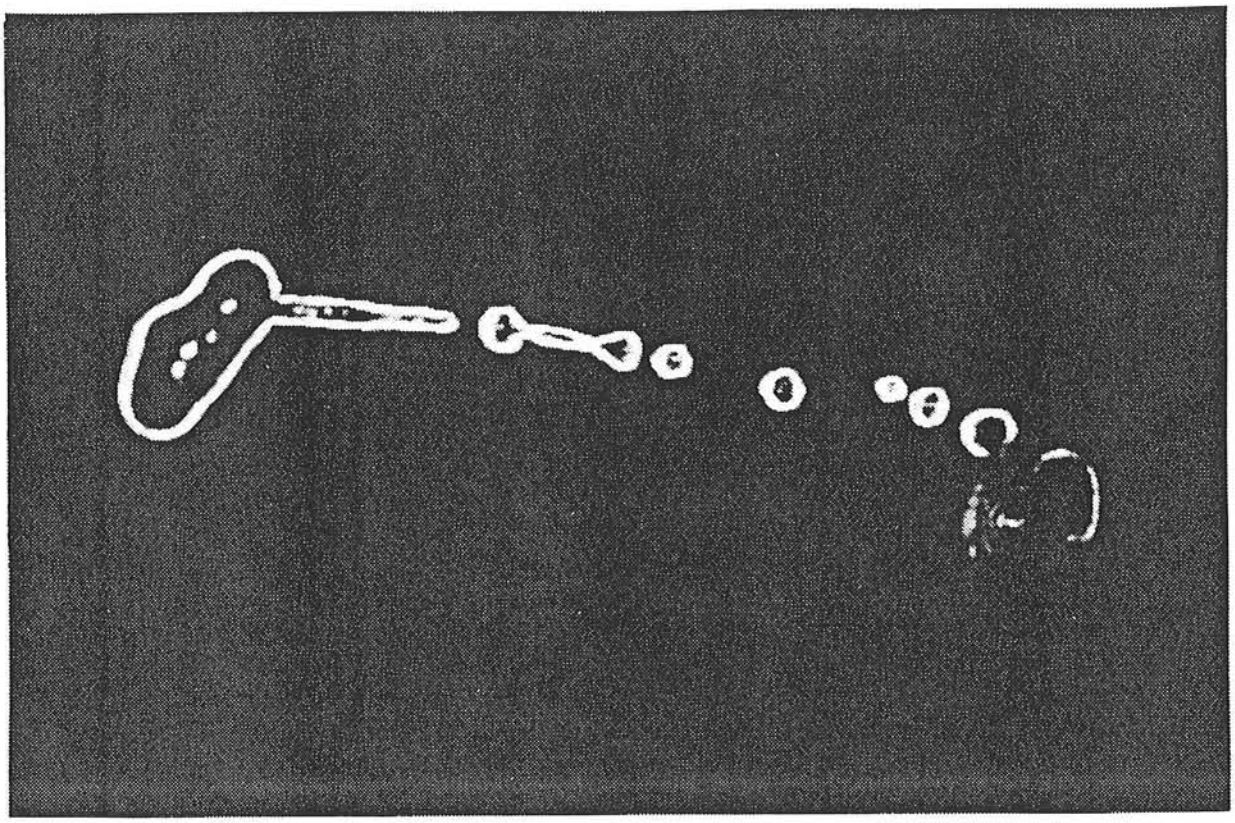

Fig. 10 : Optical edge extraction of the same droplet as in figure 7

PIV-methods:
techniques and applications

Tuesday 2 July.

STOCHASTIC OPTIMIZATION OF PROCESSING TECHNIQUES FOR PIV

C.S. Moraitis, M.L. Riethmuller
von Karman Institute for Fluid Dynamics
Chaussee de Waterloo, 72
1640, Rhode-Saint-Genèse,Belgium

ABSTRACT

An older study by these authors attempted a stochastic modelling of the parameters involved in a Particle Image Velocimetry (PIV) experiment, mainly photographic and seeding parameters, and the way they affect the quality of a fringe pattern. Today, the processing by analysis of a fringe pattern is no longer the dominant processing technique and a similar analysis has to be carried out for techniques relying on the image plane.

This study relies on a probabilistic estimation of the expected realization of a power spectrum or an autocorrelation pattern of a double exposure negative of a particle cloud in motion. Imposed requirements regarding the quality of these patterns result in the establishment of criteria to be satisfied, for an experiment to be successfull. It is also proven that processing techniques based on the power spectrum pattern of the input transparency (Young's fringes) are equally reliable independently of whether the power spectrum has been obtained optically or digitally. Quite contrary to this conclusion is the outcome that digital evaluation of autocorrelation functions proves to be superior to optical formation, in terms of manageability of the peak finding task.

The impact of the processing technique on the dynamic range is also rigorously studied and 2-D ACFs prove to be superior to Young's fringes formation in the sense that they allow a broader dynamic range, especially when they are obtained digitally. It is also proven that an optically formed ACF pattern is only comparable to a digitally obtained one when the quantization error at the camera-frame grabber level is kept very low. Furthermore, it is shown that when the flow velocity is not uniform in the probed region, the complete probability density function of the velocity within that region can be recovered in certain conditions. This allows, for instance, for resolving a velocity gradient.

Finally, an error analysis of various accompanying digital image processing techniques is attempted and it is demonstrated that the characteristics of usual image processing equipment by far outperform any reasonable accuracy requirements. This last point is of paramount importance because it suggests that digital processing load can be significantly reduced without sacrificing the accuracy of the measurements.

DEVELOPMENT OF PARTICLE IMAGE VELOCIMETRY:

A NEW COMPUTATION METHOD WITH DIRECTIONAL RESOLUTION

P. GUIBERT, M. MURAT, Q.C. DUAN, J. JULLIEN

Université PARIS VI - UA CNRS 879
Laboratoire de Thermodynamique Appliquée aux Machines et Thermique
2 Place de la gare de ceinture - 78210 Saint Cyr l'Ecole

This paper describes the results of different solutions to resolve PIV (Particle Image Velocimetry) photographs. The aim is to determine the module and the direction of the particle velocity vector. The directional ambiguity dilemma is eliminated by using an asymmetric laser light sheet exposure sequence. Two computation programs were applied to an artificial image:

- The first uses the locally periodic random image produced by a multiple exposure photograph. This periodicity can be determined by using spacial autocorrelation or Fourrier technics: computation of the power spectrum of the PIV image (it produces Young's fringe) followed by the computation of the power spectrum of Young's fringe (it produces correlation peaks).
- The second processing (called linear histogram) was developed. The centre of gravity of each point of image is located and used in the whole linear histogram processing. Its principle is based on the search of interval histogram on a band with a fixed width. This band is moved virtually with a fixed steepness θ over the whole image, θ varying in the range 0-180°. Three peaks with the distance interval corresponding respectively to d_{12}, d_{13} and d_{23} appear on the histogram, when the mean flow angle is reached (d_{13} is the distance covered by the particle between the first and the third laser pulse). A standard deviation criterion enables us to find the right angle. This criterion is necessary because the three peaks are no more visible when flow fluctuation is important. The next step is to determine the right direction (± 180°). Two masks with two dissymmetric patterns are used and moved at the flow inclinaison over the whole image.

This two methods were tested with a computed image. The image is the representation of a small region of the visualization field. A group of parameters are taken into account to create it. One can notice especially significant parameters as the module fluctuation and angle deviation. they are applied to each bipoint and tripoint to characterise the turbulence flow. A bipoint is a particle seen during the two first laser pulses or during the two last laser pulses. A tripoint is a particle seen during the three laser pulses. Some isolated points (monopoint) are added to present the particles seen during one of the three laser pulse. The location of each monopoint, bipoint and tripoint is determinated by a random calculation.

A systematic study of all the parameters has permitted to compare the two methods to solve PIV patterns. Similar results were obtained, but one can notice better performances of the linear histogram method for high fluctuations (20 to 30 % for the module fluctuation and ± 10° for angle deviation). The histogram treatment takes about the same time as the autocorrelation calculation which uses generally an array processor. The directional ambiguity is eliminated by the utilization of asymmetric coding. In the near future, this new technique will be applied to an air/air free jet and validated with a LDA (Laser Doppler Anenometry).

An automatic evaluation system for PIV records and specklegrams based on transputers

H. Wintrich and W. Merzkirch
Lehrstuhl für Strömungslehre
Universität Essen, D.43oo Essen, Germany

The application of particle image velocimetry (PIV) and speckle photography to the measurement of flow velocity or fluid density, respectively, requires the evaluation of patterns of Young's interference fringes. Fringe distance and fringe direction have to be determined for each pattern. A number of image processing systems have been proposed and, to some extent, realized for the automatic evaluation of specklegrams or PIV records. Two algorithms are available for determining the two quantities from each Young's pattern, fringe distance and direction: one-dimensional algorithms (e.g. 1D-Fourier transform, linear correlations), and two-dimensional algorithms (e.g. 2D-Fourier transform). The appropriateness of the algorithms depends mainly on the quality (signal-to-noise ratio) of the interference patterns.

Most of the automatic systems make use of an array processor that allows a relatively fast performance of the 2D-Fourier transform. As an alternative solution, a system is described here that is based on the use of four transputers of type Immos T 8oo . These transputers form a special type of processor. They are linked and able to mutually transmit data with a speed of 2o Mbit/s. Several processors of this type can be used in parallel to reach a high processing velocity. The two evaluation algorithms, one- and two-dimensional, are implemented by means of 3L-C, a version of the language "C", that allows a direct programming of the transputer system by means of additional constructions.

The processing and evaluation of Young's interference patterns is demonstrated with records obtained from both velocity (PIV) and density fields. The processing velocity is of the same order as that of systems using array processors. The major advantage of the present system is the lower price of the hardware.

A PIV System for Application in Transonic Wind Tunnels

J. Kompenhans and R. Höcker

Institut für Experimentelle Strömungsmechanik
Deutsche Forschungsanstalt für Luft- und Raumfahrt (DLR)
D-3400 Göttingen, Germany

Abstract

Particle Image Velocimetry (PIV) is increasingly used for investigations of the instantaneous velocity field in wind tunnels. Due to the short time required for the recording of a complete 2-d velocity vector field, PIV is of special interest for aerodynamic investigation of transonic flow fields.

At DLR an experimental set-up for PIV has been developed which can be operated under the rough environmental conditions of a large wind tunnel. This system has successfully been applied as well to low speed as to high speed flows ($U = 10 \ldots 400$m/s) in different flow facilities. The evaluation of the PIV recordings runs fully automatical on an image processing computer. In order to be able to apply the PIV technique in a high speed blow-down wind tunnel with a measuring time of less than 20 seconds some improvements of the PIV technique had to be carried out.

The paper will describe some special features of our instrumentation, analysis and post-processing techniques, which were specially developed for the application of PIV in wind tunnels, e.g:

- double oscillator Nd:YAG laser for illumination,
- fast focusing procedure for the recording camera by means of video technique,
- seeding equipment,
- on-line observation of seeding quality by means of a CCD camera,
- particle behaviour (velocity lag),
- computer controlled automatic measurement with simultaneous acquisition of pressure and temperature data during the wind tunnel run,
- evaluation of PIV recordings by means of digital image processing of the Young's fringes pattern with automatic brightness control,
- alternative techniques for processing of Young's fringes pattern by means of analog-optical methods utilizing spatial light modulators,
- calibration procedure for scale factor, image distortion and for accuracy of data,
- data validation during post-processing.

After having performed these improvements the PIV technique has successfully been utilized by us in a wind tunnel with transonic flow. The object of the investigation was the instantaneous flow field about a bluff cylinder at a Mach number $Ma_\infty = 0.98$. The spatial structure of shocks embedded in the transonic flow field could be revealed. By applying vector operators like **div** and **rot** to the velocity data it was possible to obtain the exact location of the shocks. Though further improvements of the PIV technique will be recommended in our paper, our investigations have already shown that the PIV technique is a useful tool for aerodynamic investigations of transonic flow fields.

ABSTRACT for EUROMECH 279, Delft University, 2-5 July, 1991

An experimental comparison between Optical and Digital Particle Velocimetry.

J.M. CORNELISSE, H.W.H.E. GODEFROY, F. KOOPMANS, R.E. UITTENBOGAARD, J. WESTERWEEL*

DELFT HYDRAULICS
P.O. Box 177
2600 MH Delft, The Netherlands

*) Delft University of Technology
Laboratory of Aero- and Hydrodynamics
Rotterdamseweg 145
2628 AL Delft, The Netherlands

Commissioned by the Dutch Ministry of Transport and Public Works DELFT HYDRAULICS performs long term research on turbulence and mud transport. Sedimentation and erosion of mud is influenced by shearing motions at scales of the order of magnitude larger than Kolmogoroff's length scale.

Particle Image Displacement Velocimetry (PIV) may provide detailed information on the intensity and time scales of the small scale shearing motions and on the accuracy of turbulence models to predict the relevant parameters.

For this purpose two methods of PIV, Optical PIV (OPIV) using Young's fringes and Digital PIV (DPIV) using 2-D FFT's on digitized exposures, are considered feasible. We compare DPIV and OPIV experimentally and discuss their accuracy and over-all efficiency for automatic read-out of many exposures to obtain reliable statistics.

At a mean flow velocity of about 150 mm/s in a small water channel (0.14*0.15*1.2 m) turbulence is generated using a grid. At several distances behind the grid turbulence levels and spectra are obtained with a one-component LDA. At these distances double and multiple exposures of particles illuminated in the channel's symmetry plane are recorded on black and white film and also colour diapositive film. The 60 mm wide light sheet is formed by the 0.8 mm beam of a 300 mW Argon-ion laser. A rotating mirror produces 200-400 sweeps/s. Using Bragg cells a system has been developed which switches between two sweeps the colour of the laser beam from blue to green and vice versa. In this manner two-colour exposures (one green and one blue) of particles are made on a diapositive film. For OPIV the read-out unit consists of a He-Ne laser with adjustable diameter (0.5-2.0 mm) that illuminates a circle of the film positioned with an x-y table; lenses produce Young's fringes. For DPIV the read-out unit consists of a high-pressure mercury lamp, colour filters, x-y table containing the colour slide and an optical imaging system. Both units project their images on a CCD-camera.
Illumination of the colour slides with blue, respectively green filtered light in the DPIV read-unit allows for the application of cross correlation in DPIV. This new technique gives the otherwise unknown sign of the velocity vector and is expected to reduce the noise level of DPIV. This experimental procedure facilitates a good comparison between the LDA-measurements, OPIV and DPIV either with auto-correlation (no optical fitering) or with cross-correlation.

Abstract:

Particle image velocimetry at T. U. Denmark

by Preben Buchhave and Michael Linde Jakobsen
Physics Lab. I,
Technical University of Denmark
DK 2800 Lyngby, Denmark

At T. U. Denmark we have since 1989 been setting up a particle image velocimetry (PIV) facility. Our aim is partly to establish a facility, which can be used by other institutes at the university, partly to work at improvements in the PIV technique.

Our work so far has been aimed at improving the speed of PIV image processing. We have established a numerical processing facility consisting of video equipment, frame grabber and a 386 PC with a floating point vector processor. This is our basis for comparisons with other methods. On this system we can scan a PIV image and perform numerical autocorrelation on the selected interrogation areas.

To improve processing speed we have implemented an optical correlation processor based on a photorefractive crystal (BSO). This processor is now operational and can be used to process PIV image at a speed, which is much higher than that of the numerical processor, and with a quality equal to or surpassing that of the numerical method.

However, we are still investigating the behaviour of this crystal as we have found interesting phenomena like asymmetric correlation peaks and complicated polarization properties. Understanding these properties may lead to further improvements in speed and performance.

We are further investigating the possibility of processing a large area of the PIV image in parallel to obtain fast statistics on the flow field.

Finally we are investigating holographic PIV recording with separate reference beams. This technique, in addition to holding out the promise of volume measurements of 3-D velocity vectors, also allow the use of cross correlation to remove the directional ambiguity inherent in the autocorrelation method.

We would like to report on the status of these investigations as well as on the results of practical PIV measurements now in progress at T. U., Denmark. These include the measurement of the secondary flow in a cylindrical Cuette flow and possibly the flow at the transition to chaos as well as measurements in a engine model and measurements in a free jet in water (as a reference measurement).

A 3D PIV System and its application to the measurement of acoustic streaming: Pilar Arroyo, Mechanical Engineering Dept. Stamford Univ.: Clive Greated and David Hann, Physics Dept. Edinburgh Univ.

A three-dimensional PIV system has been developed, based on the concept of stereo-photography. A pulsed laser beam is used to illuminate a plane of light in the usual manner and this is photographed by a camera, adapted to form stereoscopic images by the addition of four mirrors, two placed in front of the camera and the other two between the lens and the film plane. With this arrangement two images are formed simultaneously, side-by-side on the film. The centre of each image is shifted laterally, as though the camera had taken each picture from a different position, but with the film and illumination planes remaining parallel in each case. This optical arrangement is particularly convenient in application, since it is operated in essentially the same way as a conventional camera.

Both halves of the film are analysed as with standard 2D PIV, in our case using the Edinburgh automatic fringe analysis system. The resulting records are then combined to give the two in-plane velocity components and the component perpendicular to the illumination plane i.e the out-of-plane component.

The system described has been utilised in the study of acoustic streaming i.e. the mean flow patterns set up when a fluid is disturbed by an intense acoustic field. In this case it was the 3D cellular patterns within a rectangular tube that were measured. Typical results from these studies will be presented. An analysis of the optical system will also be given, which enables the three velocity components to be calculated at each point in the illumination plane. Figures 1-4 show typical records of the three velocity components. Results from these 3D PIV studies agree well with theoretical predictions developed from the Rayleigh theory.

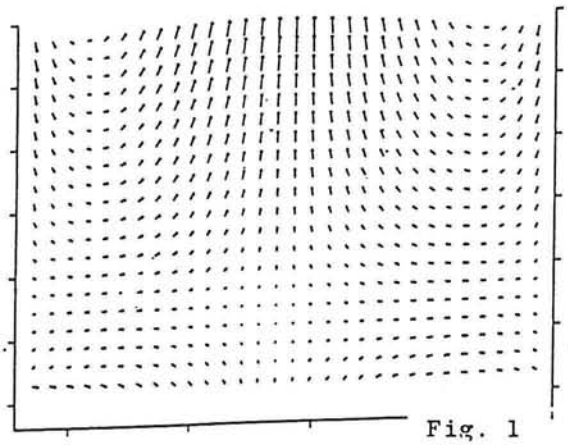

Fig. 1

Typical Velocity records for acoustic streaming in a tube measured with the 3D PIV system:

Fig. 1. In-plane velocity map
Fig. 2. Vertical in-plane component at different heights
Fig. 3. Horizontal in-plane component
Fig. 4. Out-of-plane component

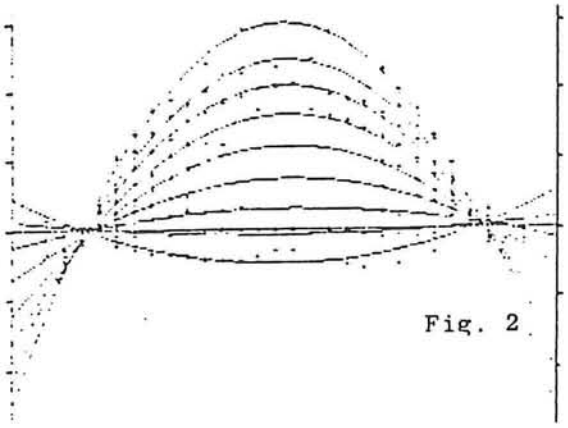

Fig. 2

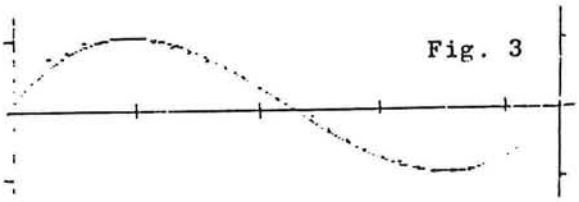

Fig. 3

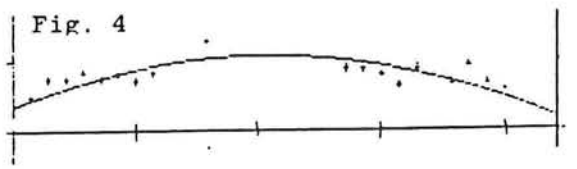

Fig. 4

INVESTIGATION OF TURBULENCE STRUCTURE USING IMAGING METHODS

by

Ronald J. Adrian
Peter W. Offutt
Theoretical and Applied Mechanics
University of Illinois at Urbana –Champaign

and

Candace E. Wark
Illinois Institute of Technology
Chicago, Illinois

ABSTRACT

Coherent turbulent motions in the wall layer region, $0 \leq y^+ < 100$, are responsible for over one-half of the mean velocity drop in a turbulent boundary layer and most of the net production and export turbulence. Various aspects of the structures have been described: low-speed streaks close to the wall (Kline et al., 1964), vortex rings forming Falco's "pockets" (1980), hairpin vortices, as originally suggested by Theodorsen (1952), bursts and sweeps (Kline et al., 1967), and ejections and outflows (Brodkey et al., 1974), VITA events (Blackwelder and Kaplan, 1971) and quadrant II and quadrant IV Reynolds stress events (Willmarth and Lu, 1972). There is not, however, a universally accepted model which unifies all of these aspects into a simple picture.

This presentation describes experimental studies of the instantaneous velocity vector fields in the streamwise-normal plane of high Reynolds number turbulent pipe flow performed using Particle Image Velocimetry. The PIV technique has 300 micron spatial resolution, and it is able to capture over 10,000 simultaneous two-dimensional vectors in each measurement. Statistics computed by ensemble averaging the individual field measurements agree well with other measurements and direct numerical simulations. The instantaneous vorticity fields confirm the existence of hairpin vortices, and reveal combinations of structures that are associated with linear growth of the length scale in the logarithmic layer. The experiments demonstrate the feasibility of performing PIV measurements in high Reynolds number flows with non-resolved scales of motion, and the limitations of said experiments.

Abstract submitted to Euromech Colloquium No. 279, July 2–5, 1991, Delft.

APPLICATION OF DIGITAL PARTICLE IMAGE VELOCIMETRY TO TURBULENT FLOWS

J. Westerweel, C. Elgaard* and F.T.M. Nieuwstadt

Delft University of Technology, Laboratory for Aero- & Hydrodynamics,
Rotterdamseweg 145, 2628 AL Delft, the Netherlands

*Edinburgh University, Fluid Dynamics Unit, Department of Physics,
The King's Buildings, Mayfield Road, Edinburgh EH9 3JZ, Scotland (U.K.)

Traditionally PIV images are analyzed with an optical/electronic interrogation technique (referred to as OPIV). Digital Particle Image Velocimetry (DPIV) is an alternative interrogation method in which a digital PIV image is analyzed by direct computation of the auto-correlation of small sub-images. The basic principles of OPIV and DPIV are equal; the main difference between these techniques is that DPIV provides high processing speed compared with OPIV; this gain in processing speed is paid by a decrease in resolution and accuracy. Up to now DPIV was applied to relatively simple flows in which the decrease in resolution and accuracy were acceptable. However, these limitations may not be acceptable in the application of DPIV to turbulent flows.

At the Fluid Dynamics Unit (FDU) of the Edinburgh University we took a few PIV photographs of a turbulent air flow behind a grid in a small windtunnel. The negatives were subsequently analyzed with the OPIV analysis system at the FDU and with the DPIV analysis program at the Delft University of Technology (DUT). In this way we could compare the results from the same PIV record obtained by both techniques.

We selected an area of 20×14 mm^2 on the film negative for analysis. With the OPIV system this area was analyzed in 41×41 interrogation positions, which took about 200 minutes (after the implementation of special hardware it is expected that the analysis time will be reduced to 15 minutes). We digitized the analysis area to a 512×512-pixel image, which yielded a data set of 31×31 data points after DPIV analysis. The digital analysis takes 36 seconds on our laboratory computer (HP9000/835S).

The resulting data sets contain about 5% spurious vectors. In a post-processing procedure these vectors were detected and removed successfully. The FDU and DUT data sets agree very well (the average correlation coefficient is equal to 0.90), and the differences mainly seem determined by the differences in spatial resolution.

More important is the performance of DPIV relative to OPIV with respect to the detection of coherent structures in the observed (turbulent) flow. We therefore computed the out-of-plane component of the vorticity and the second invariant of the two-dimensional deformation tensor, and subsequently applied certain criteria to these quantities to detect coherent structures[1]. We found that the majority of the larger structures detected in the FDU data sets were also detected in the DUT data sets. The differences in the observed areas of these structures are within the statistical accuracy for the estimation of the area of (small) objects.

From the present results we conclude that the differences between OPIV and DPIV mainly seem determined by differences in measurement resolution and accuracy (which are imposed by technological possibilities). Therefore DPIV can presently only be applied to turbulent flows with a relatively high turbulence level (more than 5%). Finally we would like to emphasize that the present results apply to PIV negatives of good quality, which is of main importance to obtain useful results with both OPIV and DPIV.

[1] J.C.R. Hunt, A.A. Wray, P. Moin *Eddies, Streams and Convergence Zones in Turbulent Flows* Proc. of the Summer Porgram 1988, Center for Turbulence Research, p. 193.

APPLICATION OF PARTICLE IMAGE DISPLACEMENT VELOCIMETRY TO INDUSTRIAL FLOWS

S. AREFI*, M. CHANCONIE*, B. BROUSSOULOUX*
Mlle M. MOINE**

* Centre Techique des Industries Aérauliques et Thermiques, Plateau du Moulon, 91400 ORSAY FRANCE

** Université de Saint-Etienne, 23, rue du Docteur Paul Michelon, 42023 SAINT-ETIENNE Cedex FRANCE

Abstract

A laser tomography system has been set up in order to study the possibilities offered by particle image velocimetry for low and high speed industrial flows (200 $m.s^{-1}$ V 20 $cm.s^{-1}$). The experimental set up contains a continuous Argon and a pulsed YAG laser associated with a fibre and a cylindrical lens, the video cameras with electronic gatings, the Umatic Video players and recorders and finaly an automatic processing based on autocorrelation. This processing permits to determine instantaneous, mean velocity field and standard deviation from the images obtained in industrial conditions (poor contrast, obstacle inside the visualisation field, highly turbulent Flows). Results of the investigation (Velocity field) of air flow inside a cooling system and an air intake system of a turbine are presented in the full paper.

We join to this abstract an example concerning the air flow at the outlet of an electric convector.

Image of the particles

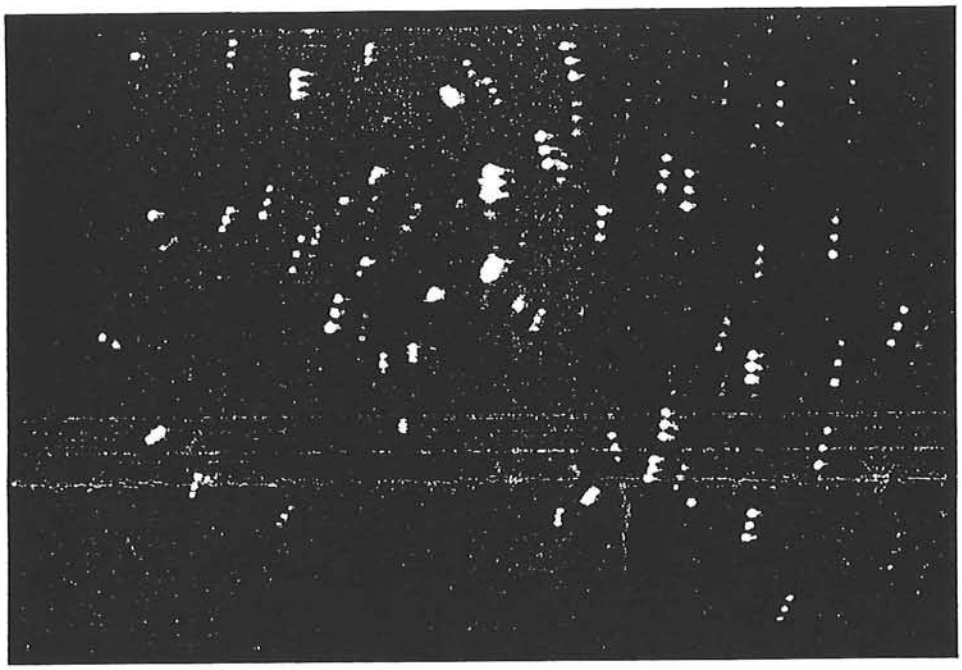

Figure N° 1

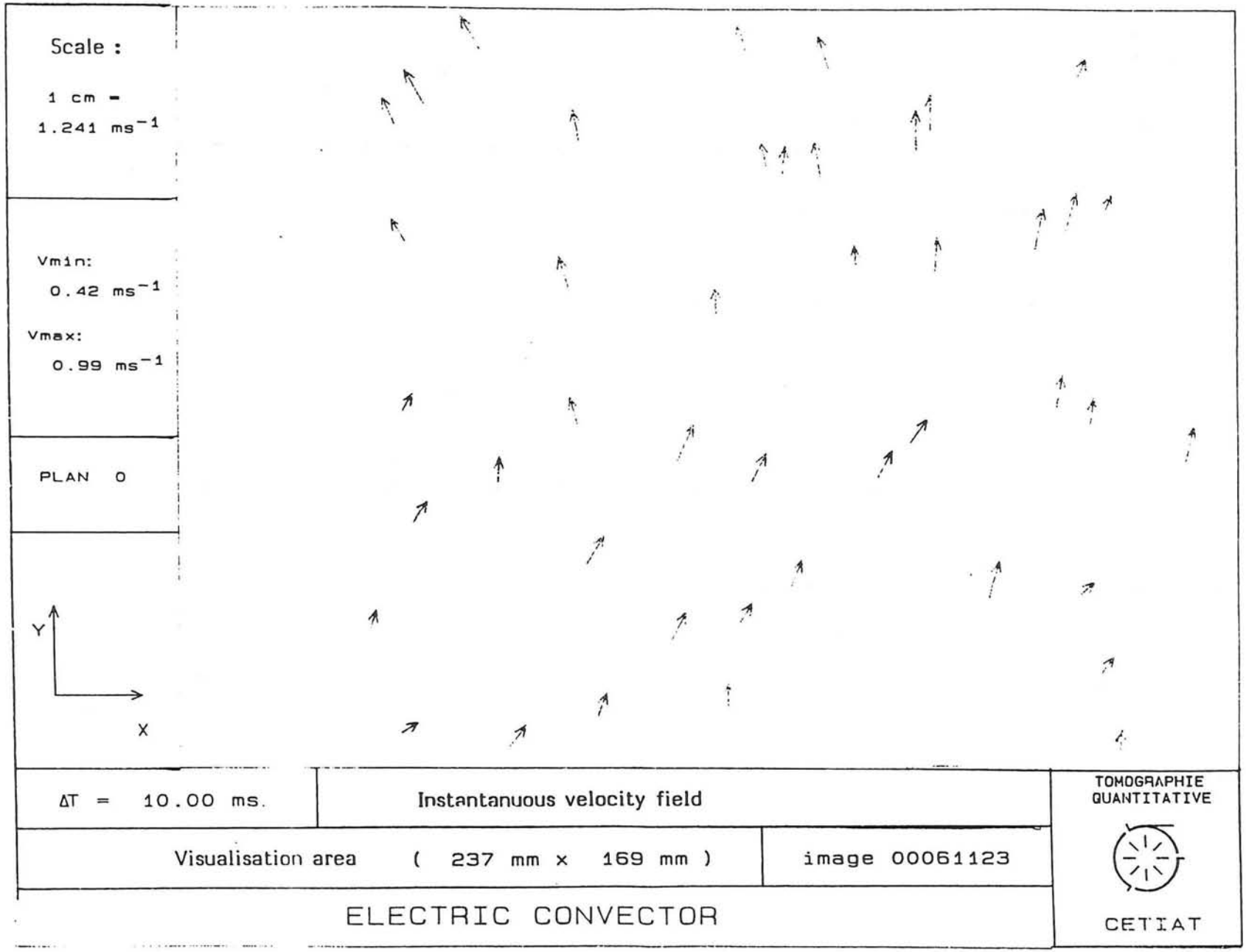
Scale :
1 cm =
1.241 ms-1
Vmin:
0.42 ms-1
Vmax:
0.99 ms-1
PLAN 0
Y
X
ΔT = 10.00 ms.
Instantanuous velocity field
TOMOGRAPHIE QUANTITATIVE
Visualisation area (237 mm x 169 mm)
image 00061123
ELECTRIC CONVECTOR
CETIAT

Figure N° 2

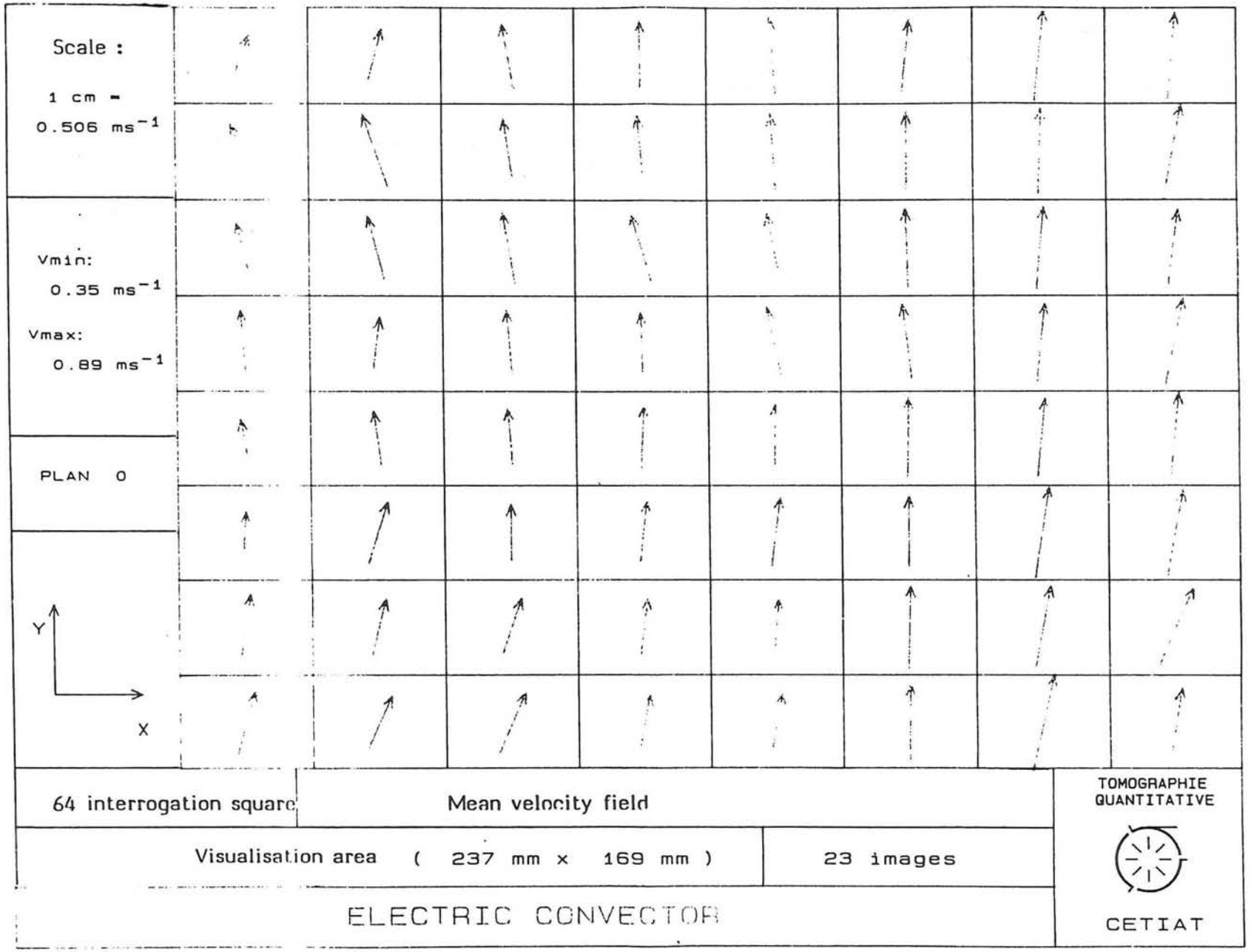
Scale :
1 cm =
0.506 ms-1
Vmin:
0.35 ms-1
Vmax:
0.89 ms-1
PLAN 0
Y
X
64 interrogation square
Mean velocity field
Visualisation area (237 mm x 169 mm)
23 images
ELECTRIC CONVECTOR
TOMOGRAPHIE
QUANTITATIVE
CETIAT

Figure N° 3

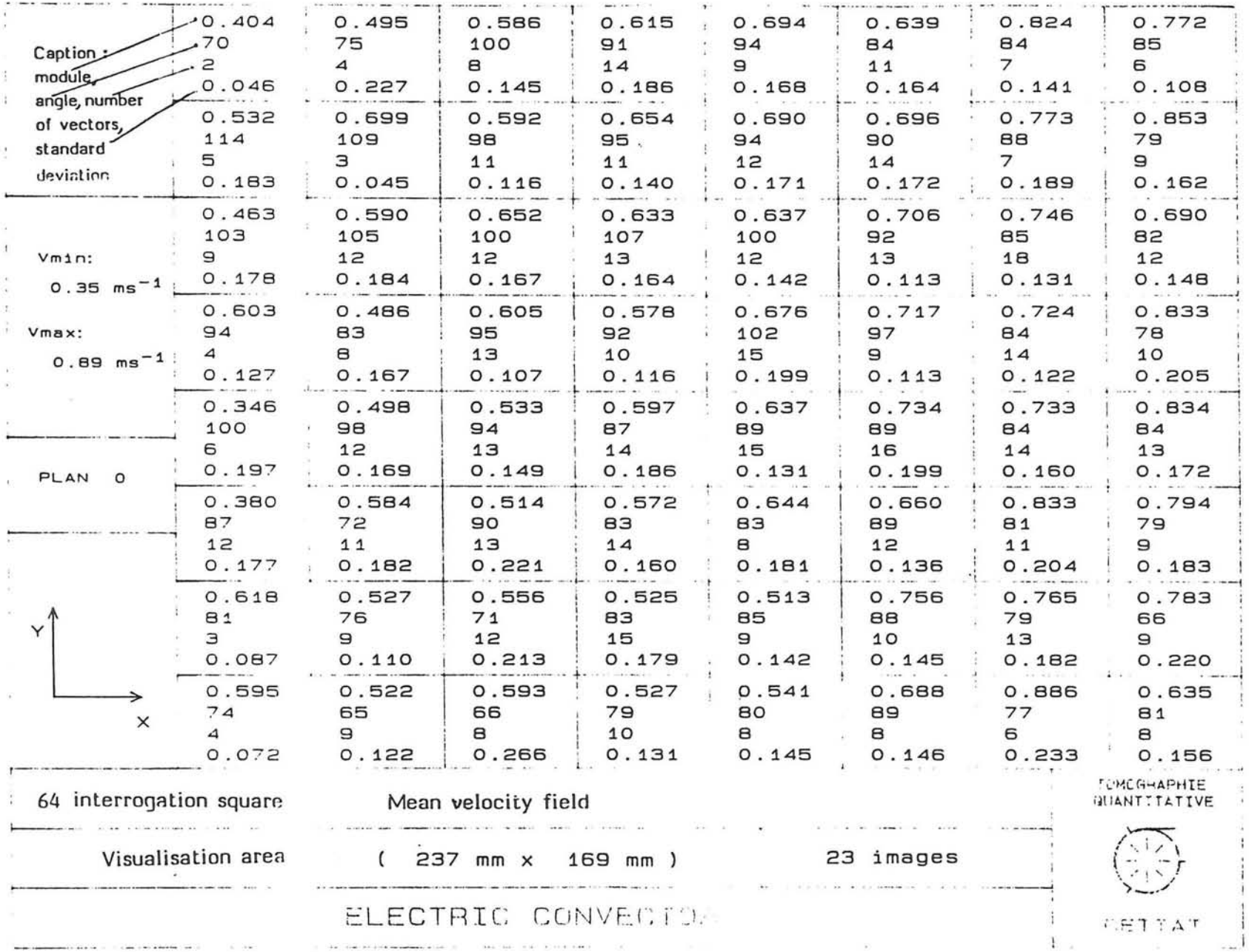
Caption : module, angle, number of vectors, standard deviation
0.404
70
2
0.046
0.495
75
4
0.227
0.586
100
8
0.145
0.615
91
14
0.186
0.694
94
9
0.168
0.639
84
11
0.164
0.824
84
7
0.141
0.772
85
6
0.108
0.532
114
5
0.183
0.699
109
3
0.045
0.592
98
11
0.116
0.654
95
11
0.140
0.690
94
12
0.171
0.696
90
14
0.172
0.773
88
7
0.189
0.853
79
9
0.162
0.463
103
9
0.178
0.590
105
12
0.184
0.652
100
12
0.167
0.633
107
13
0.164
0.637
100
12
0.142
0.706
92
13
0.113
0.746
85
18
0.131
0.690
82
12
0.148
Vmin:
0.35 ms-1
0.603
94
4
0.127
0.486
83
8
0.167
0.605
95
13
0.107
0.578
92
10
0.116
0.676
102
15
0.199
0.717
97
9
0.113
0.724
84
14
0.122
0.833
78
10
0.205
Vmax:
0.89 ms-1
0.346
100
6
0.197
0.498
98
12
0.169
0.533
94
13
0.149
0.597
87
14
0.186
0.637
89
15
0.131
0.734
89
16
0.199
0.733
84
14
0.160
0.834
84
13
0.172
PLAN 0
0.380
87
12
0.177
0.584
72
11
0.182
0.514
90
13
0.221
0.572
83
14
0.160
0.644
83
8
0.181
0.660
89
12
0.136
0.833
81
11
0.204
0.794
79
9
0.183
0.618
81
3
0.087
0.527
76
9
0.110
0.556
71
12
0.213
0.525
83
15
0.179
0.513
85
9
0.142
0.756
88
10
0.145
0.765
79
13
0.182
0.783
66
9
0.220
Y
X
0.595
74
4
0.072
0.522
65
9
0.122
0.593
66
8
0.266
0.527
79
10
0.131
0.541
80
8
0.145
0.688
89
8
0.146
0.886
77
6
0.233
0.635
81
8
0.156
64 interrogation square
Mean velocity field
Visualisation area
(237 mm x 169 mm)
23 images
ELECTRIC CONVECTO
TOMOGRAPHIE QUANTITATIVE
ETTAT

Figure N° 4

PIV and Particle Tracking: techniques and applications

Wednesday 3 July.

Development and Potential of a Photogrammetric 3-D Particle Tracking Velocimeter

H.-G. Maas and Th. Dracos
Swiss Federal Institute of Technology
ETH - Hoenggerberg
CH - 8093 Zurich

Abstract:

In cooperation of the Institute of Hydromechanics and Water Resources Management with the Institute of Geodesy and Photogrammetry at ETH Zurich a fully automatic 3-D Particle Tracking Velocimetry System based on digital multimedia photogrammetry has been developed, which offers high spatial resolution, accuracy and reliability. Issue of this paper will be the hardware configuration of our system, an overview on certain algorithmic problems and the presentation of some results showing the potential of the method.

Most of the hardware components of the presented system are off-the-shelf products and can be acquired at reasonable cost. Essential point of the configuration is the employment of three synchronized CCD-cameras imaging the flow, which proved to be crucial for a reliable determination of 3-D particle coordinates. For intermediate data storage videorecorders are being used which in combination with a PC suitably equipped for video image sequence digitization allows the examination of arbitrarily long image sequences with a temporal resolution of 25/sec. An exact calibration of the system and a strict mathematical modelling of the complex geometry given by three cameras in arbitrary orientation, different refractive indices on the lightpass from the particle to the sensor and non-negligible lens distortion is a fundamental presupposition to achieve high coordinate accuracy. From consecutive coordinate sets the velocity field is determined by a 3-D particle tracking in the object space.

The system has been applied to the determination of velocity fields in an open channel flow, in an agitated tank and in buoyant puffs. It allows the measurement of more than 1000 instantaneous velocity vectors and an accuracy of better than 0.1 mm for all three components of the displacement vectors in a volume of $200 \cdot 200 \cdot 40$ mm^3.

PIV Technique in the Turbulent Intensity and Space Derivatives Evaluation

A. Cenedese, G.P. Romano
Dipartimento di Meccanica e Aeronautica
Università degli Studi di Roma – "La Sapienza"

ABSTRACT

The Particle Image Velocimetry (PIV) allows to determine the two velocity components in a plane illuminated with a light sheet. With the PIV it is possible to obtain simultaneously information in several points (multipoints measurement), but with the analysis of one multiexposed image it is not possible to evaluate the turbulent quantities. These quantities are usually determined from time histories with a single point measurement method if the phenomenon is steady and the ergodicity hypothesis is assumed.

A new method, based on the particle image velocimetry, is proposed to measure the turbulent quantities. The method consists in the analysis of a large number of multiexposed images and in the determination of the velocity of each particle standing on the light plane.

The proposed method allows also the measurement of space derivatives which play a fundamental role in the evaluation of the dissipation term which appears in the balance equation of the turbulence energy. Restricting to the field of validity of Taylor's hypothesis, only the space derivatives in the mean flow direction can be calculated, and this is possible by means of the velocity-time history. The other terms of the tensor $(\partial u_i/\partial x_j)$ cannot be deduced in anyway from single-point velocity measurements. Particle Image Velocimetry (PIV) which gives detailed information in a plane by a light sheet, appears to be the only technique able to measure simultaneously velocity components in different points and hence the space derivatives.

A special attention, however, must be paid in the analysis of multi-exposed images in order to make this evaluation possible. The Young's fringe method

of analysis and the film utilization cannot be practically used anymore for this purpose.

If one uses the Young's fringe method or some other equivalent device, which integrates the information on a plane, space derivatives are calculated with a very low spatial resolution (of the same order of magnitude of the interrogation area). In order to increase this resolution, velocity of single particle must be known and this is possible through a direct image acquisition of the interrogation area and the use of a suitable software which permits to track the successive positions of each particle. Since a great number of images is necessary to store for a correct statistical evaluation of the mean value of space derivatives, the utilization of photographic film becomes very heavy from the economical and time-computing point of view.

To avoid this inconvenient, it has been made a direct acquisition via a video-camera equipped with a microscope of the interrogation area and subsequently digitized. An automatic procedure of acquisition and successive elaboration which gives the particles trajectories, is able to treat some hundreds of images per hour using a personal computer. The described methodology has been applied for the study of the turbulent boundary layer in proximity of a wall.

EUROMECH 279
Image Analysis as Measuring Technique in Flows

A COLORED METHOD FOR P.I.V TECHNIQUE

J.STEFANINI-G.COGNET-J.C.VILA-B.MERITE

Since the last decade,the P.I.V technique has received an increasing amount of attention.With the progress of the C.C.D and video camera,and the increase of the speed and the capacity of micro-computer,it is possible now to obtain correctly and more rapidly the velocity field of a laminar or turbulent flow.However,the time consumption to achieve the flow map is generally long,this is mainly due to the image processing and that prevents this technique from having a large development.

In this paper,we propose a new method based on a colored technique.Three pulses of differents colours (red,green and blue) are provided with an adjustable time delay.The first pulse is coming from a pulsed laser (rubis) and the other are given by a continous laser (multi-waves argon).The colours separation and modulation of the continuos laser beam are carried out by dichroic plate,filters and electro-optics shutters.Other dichroics plates allow to obtain the differents beams on the same axis.A cylindrical lens creates a laser sheet and a three exposure photograph records the displacement of the particles.

The main avantage of this technique is an easier method to analyse the images.The image of the particles is recorded with a video camera in the computer memory and an image processing software converts the information in three files containing respectively the red,green and blue particles.After a detection and a measure of the characteristics (centre of gravity , diameter,number of pixels) of the particles in each file,a programm developped at our laboratory gives us the velocities field and the flow direction.Nevertheless,we have had some difficulties to find a film wich has a sufficient reponse for the three wavelengths.

After discribing the experimental procedure,some results are presented on a water mock-up of an impinging jet upon a circular flat.

Finally,we compare these results with the same ones obtained by a laser doppler anemometry method.

CEA-CADARACHE DRN/DER/SERA/LTME
13108 ST PAUL LEZ DURANCE-FRANCE

EUROMECH 279: Image Analysis as Measuring Technique in Flows

A CAMERA FOR MEASURING DENSITY, SIZE AND VELOCITY OF RISING AIR BUBBLES AND WATER VELOCITY IN A BUBBLE PLUME

Andreas Mueller, Christoph Hugi
Institute of Hydromechanics and Water Resources Managment
Swiss Federal Institute of Technology
CH-8093 Zurich, Switzerland

ABSTRACT

A bubble camera was designed which can measure locally the density, the size and the rise velocity of small air bubbles. The flow velocity is measured by tracking of small particles. The instrument is immersed in a laboratory tank where bubble plumes are modelled. The size of the bubbles range between 0.1 and 1 mm and their slip velocity is between 40 and 250 mm/sec. Water velocities are of the order of 0.1 m/sec.

Good images of small spherical bubbles can be produced in parallel back light which is blocked by the bubble due to total reflection at the water-air interface. A microscope objective with a viewing area of 4x5 mm has its object plane about 50 mm in front of the lens in order to avoid a long light path in the water bubble mixture. The bubble motion is frozen by a strobe light which is triggered at twice the field rate of a CCD-camera. The image is recorded by a video tape recorder and later converted to digital images.

The diameter and the displacement of bubble images were evaluated. The resolution of the edges of the bubbles and of the bright spot of the central beam were used as a criterion to define the depth of view of the optics. It allowed to calculate the bulk density of the mixture based on the average volume of bubbles seen on one field of the video. Their velocity was determined from the displacement during the interval of 10 msec between strobes. The displacement of buoyant particles allowed simultaneously to calculate the flow velocity.

Decay of Rotating Turbulence: Some Particle Tracking Experiments

Stuart Dalziel
Department of Applied Mathematics and Theoretical Physics
University of Cambridge
Silver Street, Cambridge CB3 9EW, ENGLAND

The study of turbulence is one of the most difficult and important areas in fluid dynamics. It is an area where new experimental techniques, such as those made possible by digital image processing, are able to offer a quantitative insight into the underlying dynamics. This is particularly true in situations where the turbulent field is not statistically steady and the spatial structure of the flow is not readily accessible to traditional point measurements. The work described in this paper arises from an experimental studies of the decay of grid-generated turbulence in a rotating system.

The development of a flexible, fully automated particle tracking system has played a central role in this studies. The system utilises relatively inexpensive hardware and is based around a PC/AT compatible computer with a grey-scale frame grabber. Computer control of a Super VHS video recorder allows efficient, asynchronous sampling at frequencies up to the video field rate (50Hz). Discrete particles are tracked with subpixel accuracy using a modified version of the *Transportation Algorithm*. This approach enables ready incorporation of both particle properties and Lagrangian fluid dynamics into a linear framework. High computational efficiency allows the processing of between eight and twenty frame pairs per minute, the computation increasing only slightly more rapidly than the number of particles. Due to the memory limitations imposed by MS-DOS, the present implementation is limited to 511 particles with tracking in two dimensions. As spatial velocity correlation is not assumed, the system is not confined to *thin* light sheets and may be extended, using a number of methods, to include information on a third dimension.

Some of the experimental results are discussed to highlight those features of the flow which are not readily obtainable using more traditional measurement techniques. Eulerian and Lagrangian descriptions are utilised in conjunction with additional information derived from other measurement techniques (some of which are also image based) to provide further details of the dynamics.

STEREOMETRY IN STUDIES OF FRICTION WAKES

A.A. Borisov, B.G. Novikov, V.D. Fedosenko

Institute of Thermophysics, Siberian Branch of the USSR Academy of Sciences, Novosibirsk 630090, pr. Lavrentyev, 1, U S S R

Studies of H.Reichardt and H.Ermshaus (1962) had found strong action of the body form on characteristics of automodel wakes and raised doubts about universal representation of these flows. However, this action could be a result of small Reynolds numbers and distances. To do the evidence of the obtained data required investigations at large both Reynolds numbers and distances. However, possibilities of wind tunnels were practically settled for the matter of that.

Stereometry of tracing particles found · real possibilities of study of statictically non-stationary wake flows behind bodies, moving in medium at the rest. Therefore, it removed the restrictions on diametrical dimensions of a flow and time of their evolution, corresponding to the wake distance. It was shown, that the result of ensamble averaging of thousand instantaneous values of the tracing particle velocity in the limits of the averaging error doesn't depend on the flow realization and is in good agreement with the results, obtained in wind tunnels at small Reynolds numbers. It gave wide latitude to confirm the results of H.Reichardt and H. Ermshaus at Reynolds numbers, which are 300 times greater, than the early studied range.

Measurements were made in vertical pipe (7 m long and 0.525 m in diameter), filled by water and poor polymer solution. Bodies under study were autonomously immersed along vertical string. Essentially non-stationary pulse and free-pulse flows, generated by the pulse displacement along the axis of very long strings, were studied. A flow was lighted by three serieses of the pulse flushs with the time ratio between flushs in a series of 3:5:7:9. Stereocamera MK 10/13 x 18 and stereocomparator (Carl Zeiss, Jena, Germany) were used for stereometry. The analysis of the measuring results was made by the help of electronic computer.

Coherent structures in two-dimensional flow: Measurement and results.

J.B. Flór & C.W.M. Williams
Technical University of Eindhoven

Coherent structures, like monopolar, dipolar and tripolar vortices, can be observed in two-dimensional flows. Characteristic of two-dimensional flows is that for stationary structures the vorticity equation reduces to $J(\omega, \psi) = 0$, with J the Jacobian, ω the vorticity and ψ the streamfunction. As any analytical function $F(\psi) = \omega$ satifies this equation, this function has to be investigated experimentally. In the conducted laboratory experiments the two-dimensionality is enforced by either stratification or rotation of the fluid. The observed flow patterns are visualized by adding small tracer particles, and recorded by means of streak-line photography. By digitizing the streaklines, either by hand or using image processing techniques, the velocity field is obtained. This velocity field is interpolated using cubic splines to a regular 30 x 30 grid. Streamfunction and vorticity field of the observed structure are calculated from the interpolated velocity field. Plotting the value of streamfunction versus vorticity for each gridpoint in a so called scatterplot enables the experimental determination of the characteristic relationship.

The measurement technique to arrive at streamfunction and vorticity from streaklines will be presented, as well as some of the results that are obtained through the application of this technique to the study of dipolar and tripolar vortices.

Particle Image Velocimetry Measurements of the Aerodynamics of a Wind Turbine

by

I Grant[x], G H Smith[x], A Liu[x], D Infield[+], T Eich[Δ]

x Fluid Loading and Instrumentation Centre, Heriot-Watt University, Edinburgh.
+ Energy Centre, Rutherford Laboratory, Didcot.
Δ Universitat Gesamthoschule, Essen, Germany.

Abstract

The aerodynamics of rotating aerofoils is of interest to those concerned with helicopter and wind turbine design. In both cases the high rotation speeds of an aerofoil produce trailing tip vortices whose downstream characteristics can be related to the dynamics of the rotor. In particular the circulation around an aerofoil is the direct cause of lift and can be related to the performance and loading to the foil. In the case of a helicopter blade the interaction between blade and vortex is of primary interest. In the wind turbine case the interest is the interaction of the shed vorticity from the blades with the wake behind the rotor.

The present paper describes wind tunnel experiments, using Particle Image Velocity (PIV), carried out to examine flow over a small, commercial, wind turbine. The study describes how PIV was used to measure the circulation around a blade. The extension of the measurements to the examination of the distribution of circulation along the blade, (defining the radial variation in the lift characteristics) is discussed. A second series of measurements are presented which describe the characteristics of the vorticity shed from consecutive blades of the wind turbine.

The experimental apparatus is described which was used in the sampling of the periodic, but unsteady, flow found behind the rotor. The data processing techniques used to extract velocity, vorticity and circulation measurements from PIV images are also described.

Typical experimental results are shown in figures 1 and 2. Figure 1 shows velocity vectors obtained for flow close to the blade surface whilst figure 2 illustrates the effect of removing the local wind speed of the blade from the raw data. The circulation around the blade is clearly seen.

Further data, from the area behind the rotor disk will be described. In particular the strengths of the shed vortices will be presented.

Acknowledgement

The authors acknowledge the helpful and supportive advice of Dr. R Galbraith and Mr. M Horner of the Aeronautics Department, University of Glasgow, Scotland.

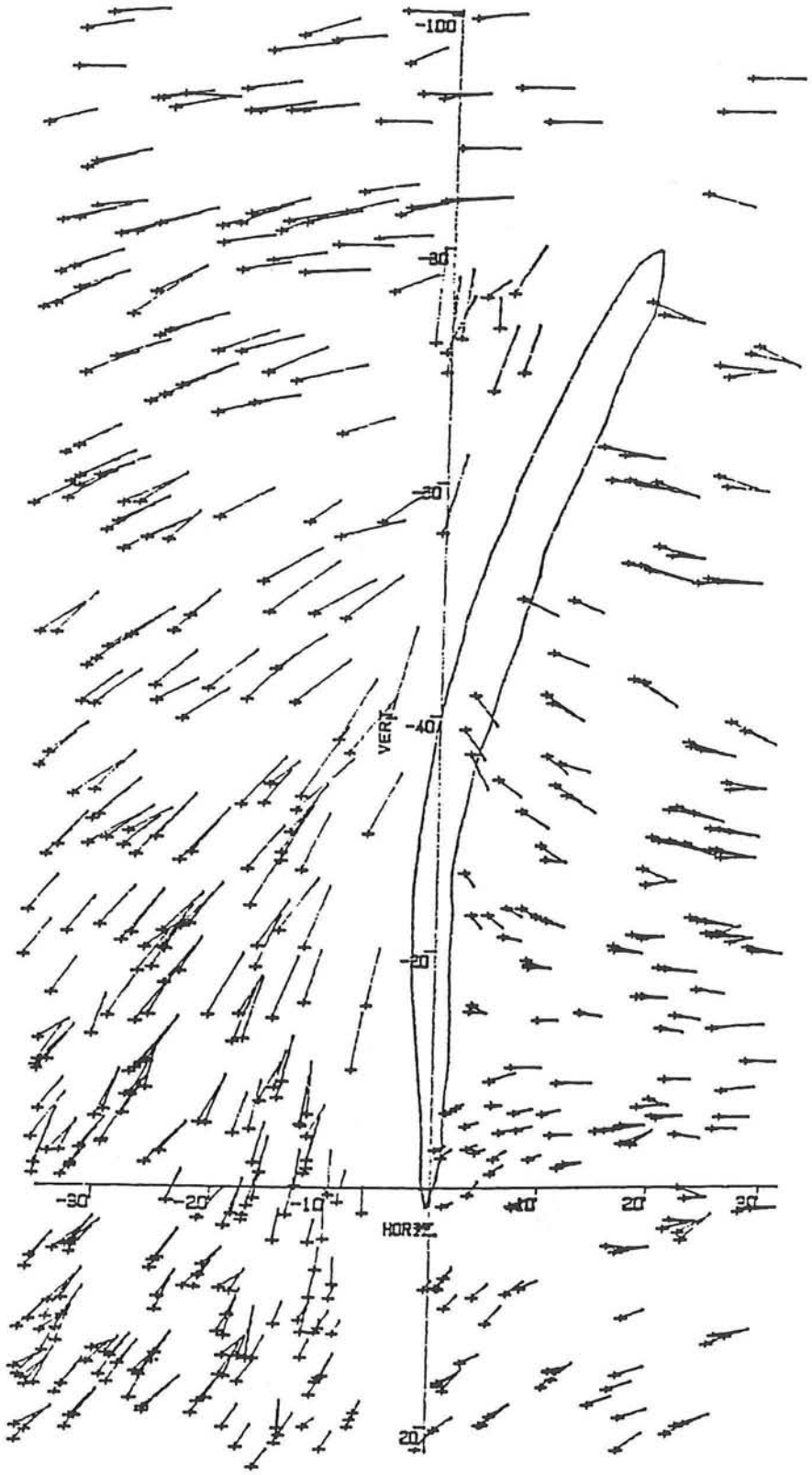

Fig. 1 The raw velocity vector field around the blade at 0.78R (15mm = 20m/s)

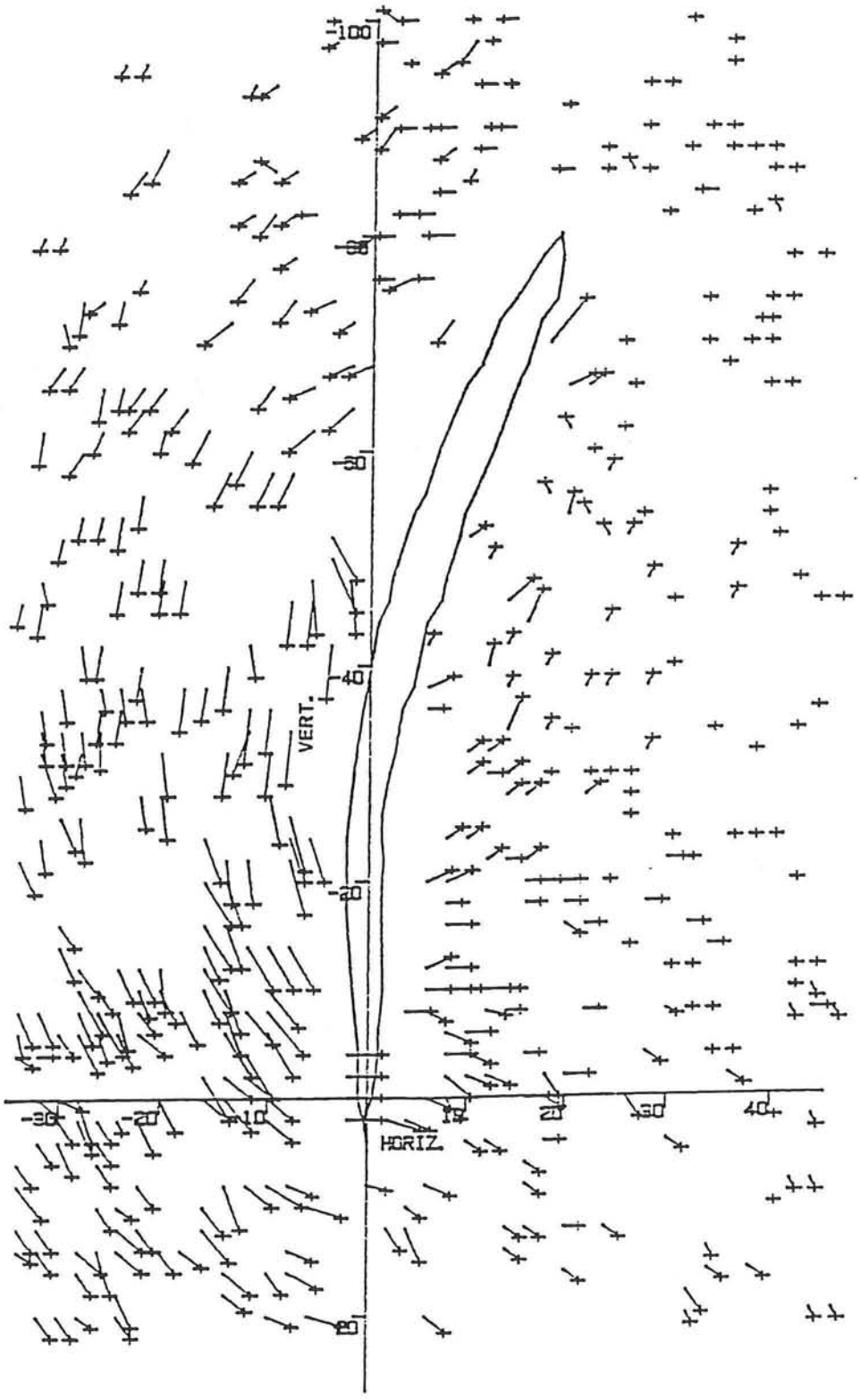

Fig.2 Circulation around a blade after subtracting local wind speed 7m/s (15mm = 20m/s)

A Critical Analysis of the Particle Image Velocimetry technique as applied to Waves on Beaches.

P. A. Quinn, C. Gray, D. J. Skyner,
C. A. Greated, W. J. Easson
Fluid Dynamics Unit, Edinburgh University.

Abstract

Quantitative measurements have been made of the inherent uncertainties, in the PIV technique. These errors can be divided up into three categories. The distortion in the optical recording of the flow field, due to limited lens quality and the effect of the glass tank walls are systematic and do not vary between experiments, and can consequently be accounted for. Random errors, such as distortion of the particle images due to grain noise, adjacency, shrinkage etc., are accounted for by a net estimate of their effect. The third category includes the errors arising from the measurement of the particle displacement from the developed negative. The main errors in this category are the influence of random correlation noise in determining the centroid of the signal peak and the effect of discrete and random sampling of an effectively continuous flow by the randomly distributed particles. Rigorous measurements of these uncertainties have been made experimentally with a plunging breaker on a flat bed, where a theoretical comparison with a non-linear time stepping model can be made. Figure 1 illustrates the horizontal components of velocity, on a line vertically down through the wave, from a position just behind the spout, together with a line indicating the results of the numerical model. The relative uncertainties associated with the velocities are shown to vary from approximately 7% in the lower regions of the wave, down to 1.4% near the crest region, as shown in Figure 2.

Having assessed the level of uncertainty in PIV, this process has been applied to measurements of breaking waves on beaches. The beach is made in two main parts, a supporting framework and an interlocking beach profile. The slope of the beach can be easily and accurately adjusted, the preliminary test slope was chosen to be 1:30 in line with other work under way in the EEC MAST Program. Tests are to be carried out on other slopes and complex beach forms. To allow access of the scanning laser beam from beneath the tank, a narrow, transparent strip is built in to the beach profile; this runs longitudinally down the middle of the beach. The scanning laser beam assembly is mounted on rails underneath the tank to facilitate optical access to any part of the 6m measurement zone. Figures 3, 4 and 5 show typical velocity fields at different positions on the beach.

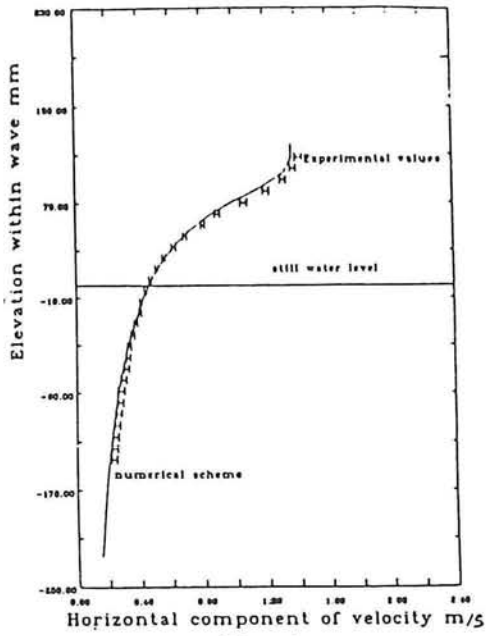

Fig. 1.

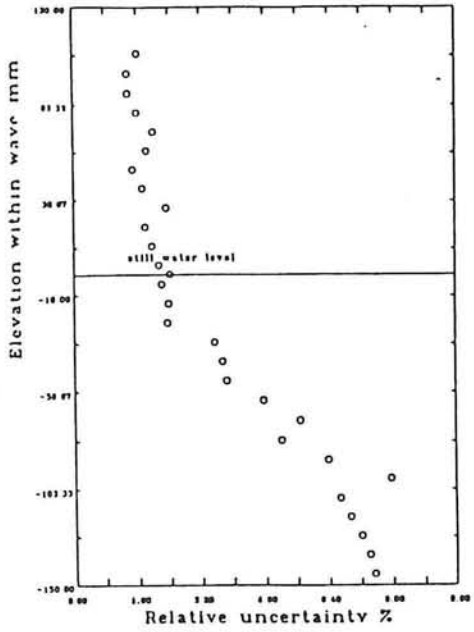

Fig. 2.

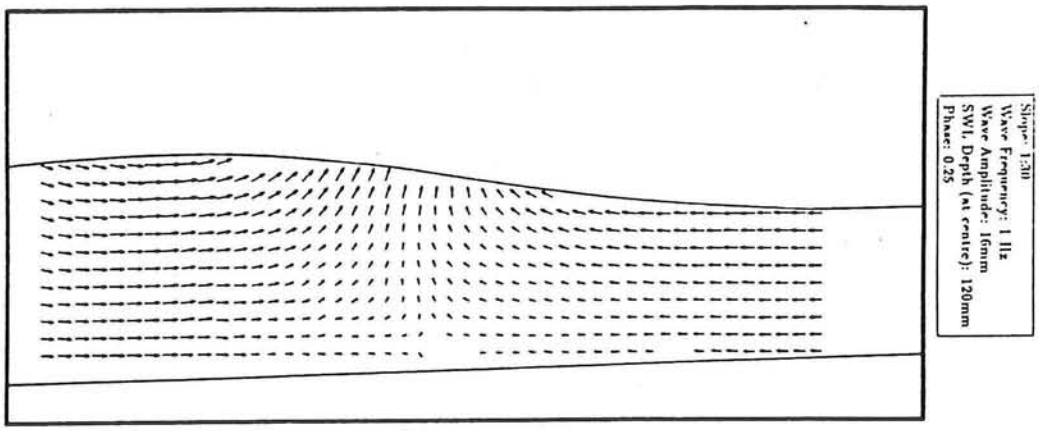

Fig. 3.

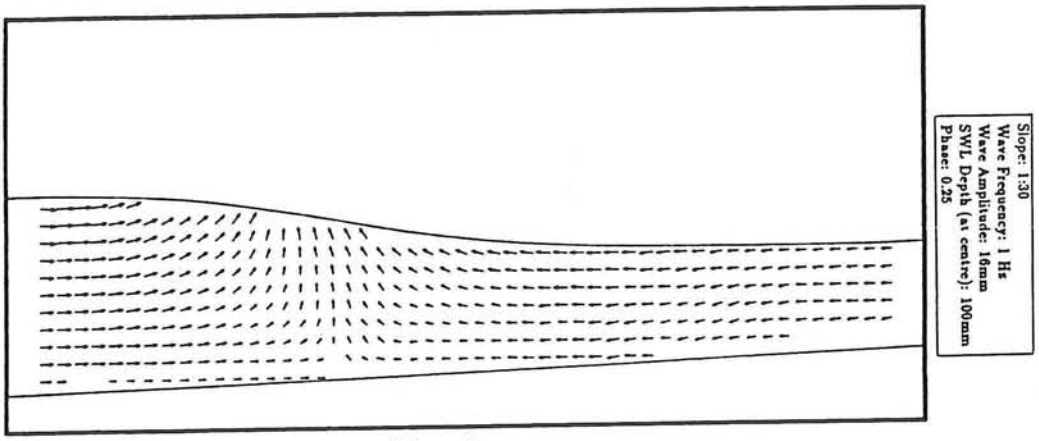

Fig. 4.

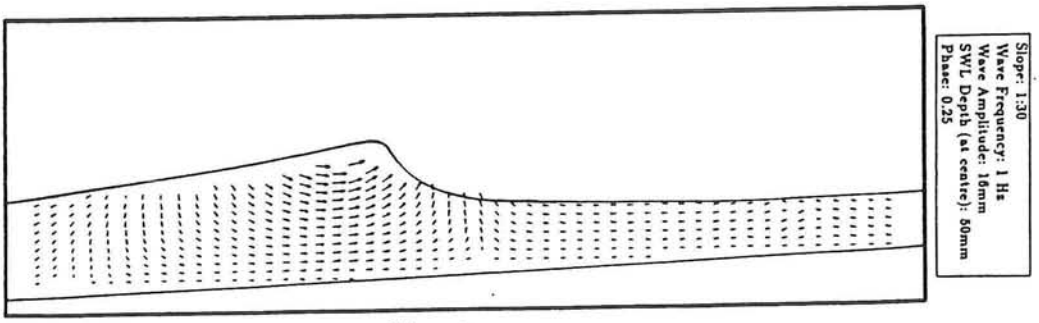

Fig. 5.

Scalar fields and data analysis

Thursday 4 July.

EUROMECH 279
Delft University of Technology, the Netherlands, July 2-5, 1991

DIGITAL IMAGE PROCESSING FOR SCHLIEREN OPTICS

Günter H. Schnerr, Rolf R. Huber, Hans-Arno Jantzen

Institut für Strömungslehre und Strömungsmaschinen
Universität (TH) Karlsruhe Kaiserstrasse 12
D-7500 Karlsruhe 1 Germany

Abstract

A new application of digital imaging processing technique for quantitative analysis of correlated schlieren pictures is presented. The method proposed here eliminates variable adjustments of the intensity of the light source, of the sensitivity of the system and optical imperfections. This procedure results in grey scale distributions representing the effects caused by the density variation in the flow.

In detail the method consists of the following steps:

1. Normalization of the correlated schlieren pictures:

   - correction of size (scale) and position of the pictures;
   - elimination of nonuniform brightness of the background;
   - reduction of spatial noise;
   - grey scale transformation based on physical conditions.

2. Quantitative detection of characteristic deviations (compression or expansion):

   - determination of the difference signal of the related pictures;
   - detection of the onset point (coordinates in pixels);
   - determination of Mach number, pressure etc. at the onset.

Comparing normalized pictures, the local variation of the density in the whole 2-D compressible flow, e.g. continuous or discontinuos by shocks, can be detected in a high accuracy. This is demonstrated for schlieren pictures of transonic flows with so called "Condensation Shocks" from homogeneous condensation of water vapor in carrier gas (moist air). With this new method the coordinates of the compression front can be found automatically and in a good agreement with other results. For the diabatic flow problem we finally determine the occurence and the onset Mach number of homogeneous condensation.

A Study of Pressurised Gas Releases by Laser-Induced-Fluorescence and Image Analysis Techniques

S.G. Bryce and R.E.J. Fryer-Taylor
Shell Research Ltd, Thornton Research Centre, Chester, U.K.

Very limited experimental data exists on the release of pressurised gas into confined or obstructed surroundings. In order to develop a predictive model for such releases it is necessary to characterise the effects of a restricted environment on the flow structure and the associated dispersion of the gas.

Three release configurations have been studied for a range of pressures: an unobstructed jet, a jet impinging on a flat plate, and a jet impinging on a circular cylinder. Flow visualisation tests were performed by the laser sheet illumination of smoke-seeded air releases (< 1.5 bar) and video recorded via a CCD camera. These recordings were subsequently enhanced and analysed using the system shown in Fig.1. These recordings highlighted the presence of large-scale vortical structures in the flow. Averaging of eight successive images removed all such detail, and reduced the jet to a smooth form. Therefore it was concluded that a time-averaged model is not a suitable representation for such flows where the jet core pressure is low (< 1.5 bar). However, the time-dependent images may be easily subjected to a fractal analysis in order to obtain more information on the turbulent structure.

Only qualitative concentration information can be obtained from the smoke tests, as the functional form of the relationship between pixel intensity and smoke/gas concentration cannot be determined. Quantitative information is obtained from laser-induced-fluorescence (L.I.F.) tests, which utilise the known relationship between the fluorescent intensity produced by the laser illumination of a fluorescing species, and the local concentration of the species. In this case the species is iodine, which fluoresces when excited by the 514.5 nm line of an Argon-ion laser. Optical expansion of the laser beam into a planar sheet permits the simultaneous determination of concentration over a two-dimensional section through the flow. The iodine is seeded into a pressurised nitrogen flow ($\lesssim$ 5 bar) and the release video recorded via a CCD camera/image intensifier configuration.

A range of image analysis techniques were applied to the L.I.F. images to extract maximum information on the geometric form of the flows and the varying concentration distributions. It was found that at release pressures in excess of 1.5 bar the formation of large scale structures close to the release point was suppressed. Therefore it was possible to perform some image-averaging in order to remove the noise inherent to image intensifier operation. Low-pass filtering was not successful in this respect.

Concentration distributions across the free jet were found to have a Gaussian form, whereas the centreline concentration decayed downstream in an exponential manner. For impingement scenarios, the jet form was found to be highly dependent on the ratio of the release point-to-obstacle distance to the size of the obstacle. At low values of the ratio there were major variations in jet behaviour, including pronounced Coanda and

asymmetric separation effects. At higher values, there was little effect on the jet behaviour. In these cases extraction of the jet boundaries showed that it would be possible to model the release by simple modification of a free jet representation.

The study has provided information on gas jet structure and dispersion for a range of release conditions and geometries. Through the combination of L.I.F. and image analysis techniques it is possible to obtain simultaneous measurements over a two-dimensional section through a flow in a non-intrusive manner. Further detailed analysis of the experimental data will enable a suitable modelling approach to be determined.

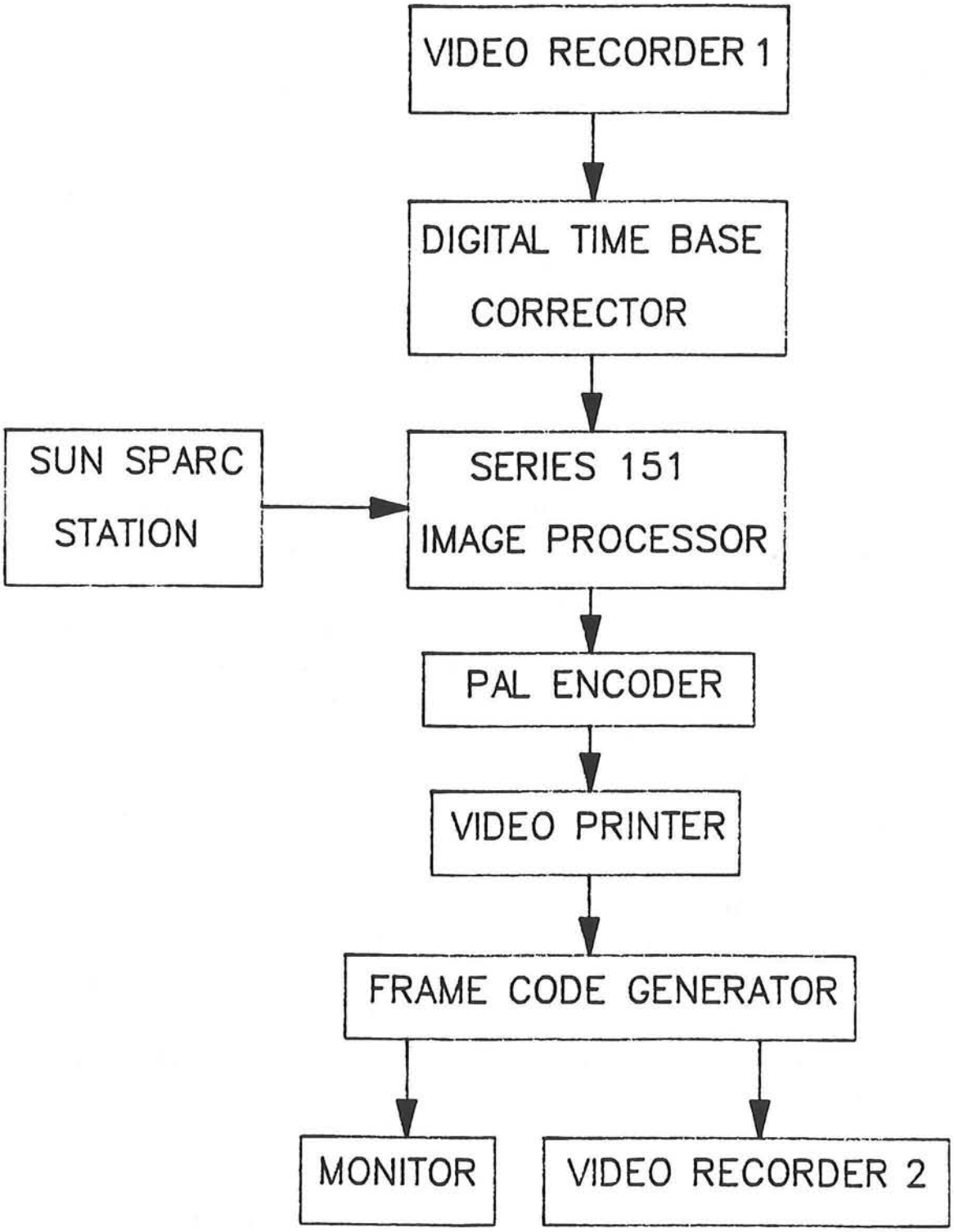

FIG. 1 REAL TIME IMAGE PROCESSING SYSTEM

Applications of an Automated PIV and Post-Processing System

T Bruce, C Elgaard & D R McCluskey

Fluid Dynamics Unit, University of Edinburgh,
Kings Buildings, Mayfield Road, Edinburgh, EH9 3JL,
Scotland, UK

Abstract

The Automated PIV Analysis System, developed at Edinburgh, has been upgraded in the speed of analysis and in the range of post-processing software. The improvements in speed enable the interrogation of a flow field at a rate of 2 points per second. Thus a 50 X 50 grid of velocity vectors is obtained in less than 25 minutes. Extension of the post-processing options allows further information, such as particle concentration, turbulence and vorticity, to be extracted from the PIV flow record. The application of this system to two-phase air-particle flows and homogeneous grid turbulence will be described.

PIV has proved useful in obtaining velocities of particles in airstreams. In addition, particle concentration distributions have been obtained from the visibility of the Young's fringes. This enabled the factors affecting the dispersion of particle jets to be characterised. A small wind tunnel was used to generate the uniform air flow into which particle jets of varying velocity were injected.

The system has also been employed to study turbulent flows. Grids are placed in the wind-tunnel referred to above, producing turbulence levels in the range 5% - 9%. The resulting homogeneous, isotropic turbulent flow fields have been investigated for a range of mean flow velocities. The resulting PIV records allow turbulent structures of length scales comparable to Taylor's microscale to be investigated.

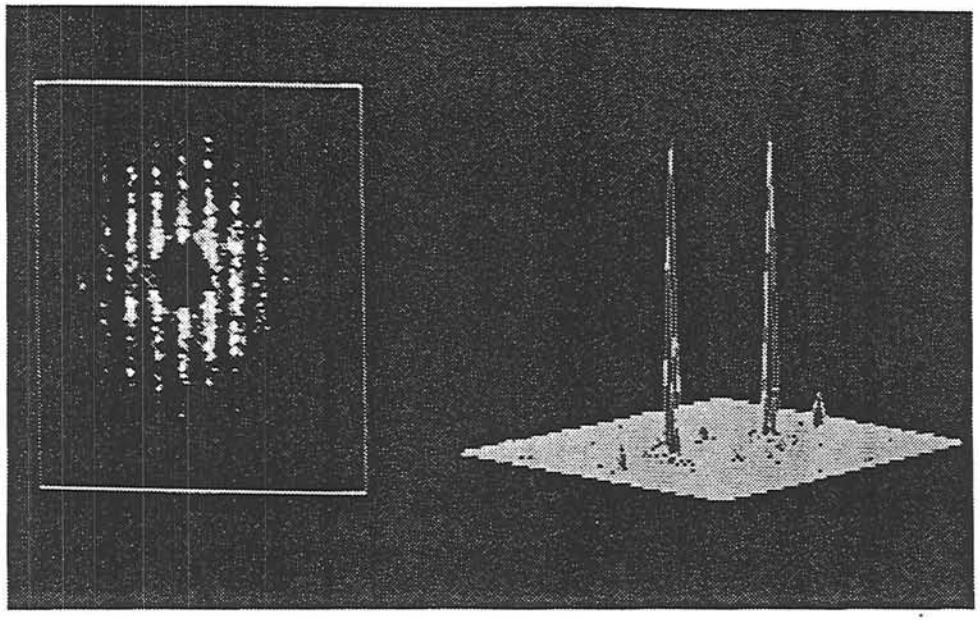

FIGURE 1

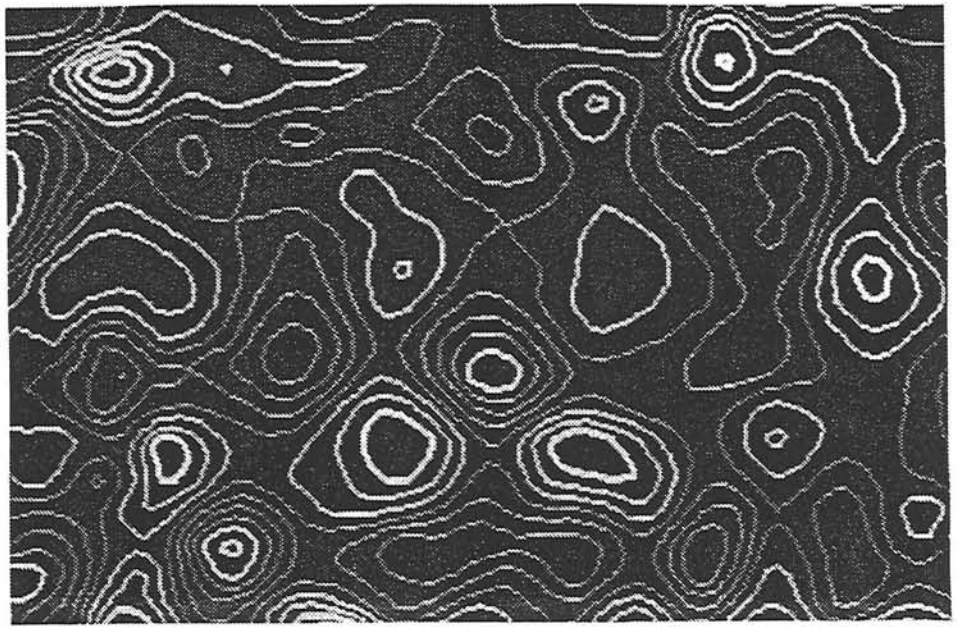

FIGURE 2

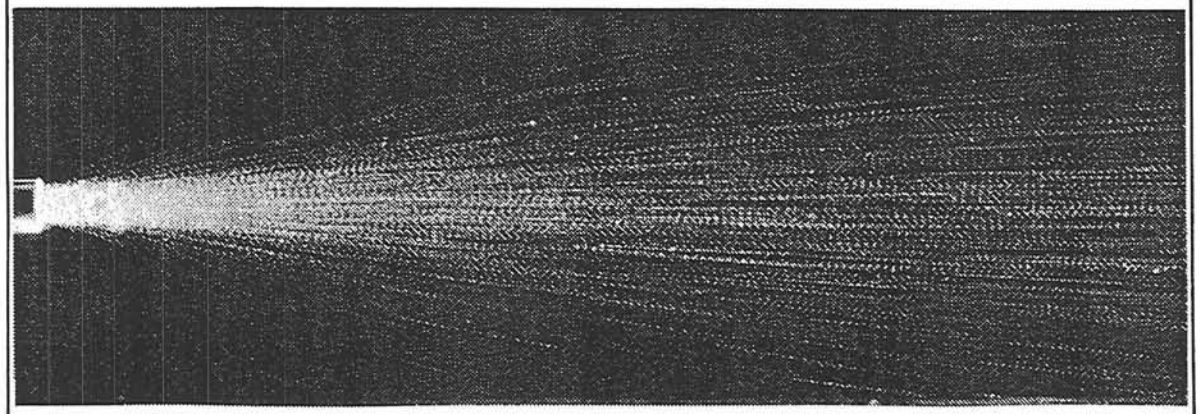

FIGURE 3

FIGURE 1: AUTOMATIC PIV ANALYSIS SYSTEM
The anaysis system at Edinburgh is based on the Youngs' fringe technique. . The spacing and orientation are determined in the Auto-correlation plane. .

FIGURE 2: VORTICITY MAP OF TURBULENT FLOW
This shows a vorticity map of homogeneous isotropic turbulent flow with the turbulence level decaying from 9%.

FIGURE 3: PARTICLE JET DISPERSAL
PIV can determine *both* velocity and concentration information concerning the behaviour of the particle jet.

Determination of velocity - concentration correlations by Particle Image Velocimetry and Laser Induced Fluorescence Imaging

Serge SIMOENS & Michel AYRAULT

Laboratoire de Mécanique des Fluides et d'Acoustique - Ecole Centrale de Lyon

B.P.163 - 36 Av Guy de Collongue - 69131 ECULLY Cedex (FRANCE)

An experimental technique allowing the determination of the velocity - concentration correlations has been developped in a bidimensional water jet submerged in an isotropic homogeneous turbulent channel. The velocities are measured using the Particle Image Velocimetry technique and the concentrations using the Laser Induced Fluorescence technique.

In order to measure the dispersion of a passive contaminant, the water jet is marked with fluorescein and seeded, for the velocities determination, with particles of iriodin. A 1mm thick sheet of Argon ion laser light, associated with a mechanical chopper, is used to illuminate the plane of interest with λ_i = 488 nm. The light sheet is recorded with two synchronized 35mm Nikon cameras and high sensitive B/W films.

For the concentration, a high pass filter Kodak Wratten n°12 is placed in front of the lens of one camera. Only the fluoresced light (λ_f = 515 nm) impress the film (single exposure) and the intensity of the fluoresced light is proportional to the concentration of fluorescein in water. We have to account for some non-linearities, in particular the response of a silver based emulsion (the H-D curve). After digitalization, a calibration is necessary so that the grey level of each pictures is proportional to the instantaneous concentration of fluorescein in the flow. Then, we can compute the turbulent characteristics of the concentration field (ensemble averages with 200 images or samples), in particular the mean concentration $\overline{C}$ and the fluctuations c'.

In front of the second camera, a low pass filter Kodak Wratten n°32 attenuates the fluoresced light and the light diffused by the particles is principally recorded on the film. The pictures, taken in triple exposure, once digitized, allow us to compute the instantaneous velocity and so, the mean velocity $\overline{U}$ and the fluctuations u' and v'. All the images are numerically analysed (image enhancement : histogram modification and smoothing, FFT of small areas, measurement of the spacing and the orientation of the fringes, velocities determination) and processed automatically.

As the images correspond to the same time, we can associate the instantaneous velocity and concentration fields and compute the correlations $\overline{u'c'}$ and $\overline{v'c'}$.

The results concerning the concentration ($\overline{C}$ and $\overline{c'^2}$) and the velocities ($\overline{U}$, $\overline{u'^2}$ and $\overline{v'^2}$) are compared with those obtained by means of classical methods (L.I.F. and L.D.A.) in several cross-sections and show a good agreement. We also present some transversal correlation profiles along the water jet axis.

An Application of Image Processing Methods to determine the Critical Shear Stress in Sewer Systems

W. Bechteler, V. Baier, S. Hartmann

Institute for Hydraulic Engineering
University of the Armed Forces Munich
Werner-Heisenberg-Weg 39, D-8014 Neubiberg, Germany

ABSTRACT

The knowledge of the critical erosion velocity or of the critical shear stress in a river or sewer is of importance for the calculation of the transported sediment by water. This value is mostly obtained from literature (e.g. Shields-Diagram). The knowledge of the incipient motion is also of interest in ecological viewpoints because the sediment depositions in rivers or sewers contain more or less pollutants (e.g. heavy metals).

The in situ-measurement of the critical erosion velocity yields an important basis for a realistic calculation of the transported sediments and for the consideration of the sedimentological peculiarities in a river or sewer.

Therefore in the laboratory of the Institute for Hydraulic Engineering (University of the Armed Forces Munich), a measuring device was constructed which was used to test 10 different types of soil (different sands, bentonite, and mixtures). An underwater video camera is mounted on the plexiglass-cover of the measuring channel to record the incipient motion of the tested sediment. The measured water discharge is the basis for the calculation of the critical erosion velocity and the critical shear stress with different methods.

The video images are digitalized and stored on a PC. The image processing system is half-automatic by a user-defined program. It takes a certain number of pictures with a time difference of 24 msec and stores them as a time-series.

In the first step of processing the image files (524 x 524 pixels, 256 gray steps) have to be enhanced. Because of disturbances within the whole image system there are signals of certain frequencies creating non-gaussian noises visible on the image files. With different filter operations and Fourier Analysis Methods these are eliminated as far as possible.

The second step contains the processing itself. Two following image files are substracted and the difference of the images is a certain value of pixels which represents the amount of transported material within the time step. The values of a complete series for a certain water discharge are combined to a mean value. The mean values for different water discharges against the water discharge itself lead to a curve (Fig.1).

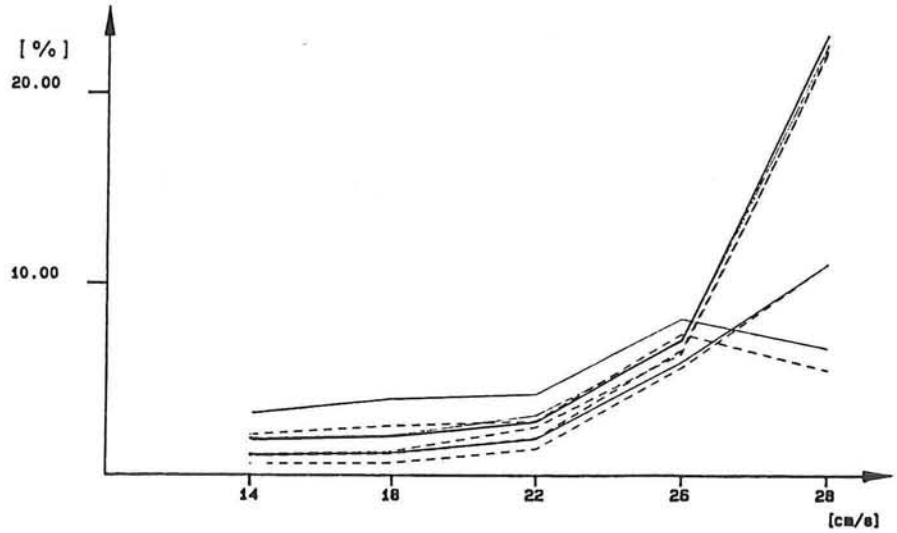

Fig. 1 : Percentage of transported material in a time step against flow velocity (sand 0.7-1.2 mm)

The graphical output allows the determination of an objective range for the critical erosion velocity. Fig. 1 shows the begin of transport at a velocity of 22 cm/s and a mass erosion in the range of more than 26 cm/s.

So the former determination of the critical shear stress by observation, dependant on the single experimentator, is now more objective and reproducable for the laboratory model. The results will be approved by measurements in sewer systems to get values of the critical shear stress more easy and without physical or chemical examinations.

STUDY OF VORTEX MULTIPOLES IN A STRATIFIED FLUID BY PARTICLES DISPLACEMENT ANALYSIS

S.I.Voropayev, Ya.D.Afanasyev
Institute of Oceanology, Acad.of Sci.USSR,Krasikova 23,
Moscow,117218, USSR

Vortex multipoles (dipoles, quadrupoles etc.) in a stratified fluid recently became the object of an essential interest. Vortex structures dynamics was studied by motion pictures analysis. A pH-indicator, aluminum powder, particles of neutral buoyancy and Schlieren technique were used for flow visualization and velocimetry.

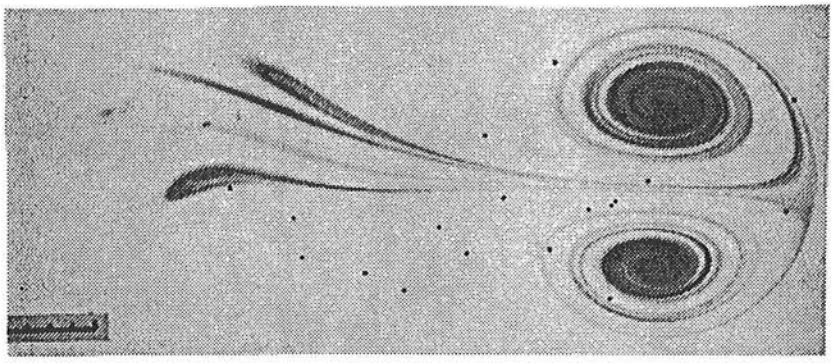

Neutrally buoyant particles in the dipolar flow. Thymol-blue visualization. Top view.

The results of laboratory experiments on the mechanism of vortex multipoles generation, their dynamics and dipoles interactions with one another and with a vertical barrier will be presented. Partly the results are published in [1,2,3].

REFERENCES

1.Afanasyev Ya.D., Voropayev S.I., Filippov I.A.1988. Transaction (Doklady) of the USSR Acad.of Sci.: Earth Science Sections.300(3): 217-220.

2.Barenblatt G.I., Voropayev S.I., Filippov I.A.1989. Transaction (Doklady) of the USSR Acad.of Sci.: Earth Science Sections.307(3): 720-724.

3.Afanasyev Ya.D., Voropayev S.I.1989.Izvestia USSR Acad. of Sci.:Atm. and Ocean Phys., 25(8): 843-852.

LASER TOMOGRAPHY OF A BUOYANT TURBULENT DIFFUSION FLAME

G. Wheater and K. N. C. Bray

Cambridge University Engineering Department,
Trumpington Street, Cambridge, England.

The structure of a 28kW buoyancy driven turbulent methane/air diffusion flame, of visible height 1m, has been investigated by means of a laser light scattering technique. A pulsed ruby laser has been employed to produce an intense light sheet of 15 cm in height, allowing the capture of both large scale coherent structures and small scale features with good resolution. Much phenomenological insight into the nature of buoyancy driven turbulent diffusion flames has been gleaned.

Scattered laser light from soot particles, embedded within the flow, has been recorded by means of a 35mm still camera, fitted with a narrow band interference filter. The soot structures within the luminous flame boundary are generally filamentary, and exhibit good connectivity. Non-luminous soot, emitted from the flame, is evident in pictures taken above the height $Z = 50$cm. At heights greater than $Z = 70$cm it is seen that non-luminous soot permeates the flow field in a quasi homogeneous fashion, co-existing with intermittently occurring luminous islands of combusting gas.

An Argon ion laser has been used to obtain high resolution 1-D scattered light images at four heights and nine radial locations in the flame. Images have been digitised for analysis with an IBM PC based system. Radial distributions and thicknesses of both luminous and non-luminous soot sheets have been measured. A software technique which can distinguish between luminous and non-luminous soot in the scattered light images is described; less than 3% of the soot at $Z = 77$cm (by scattering volume) is luminous.

Incorporation of soot length scale data into a simple model of soot radiation is described. It is estimated that at $Z = 77$cm over 90% of the emitted continuum radiation is from non-luminous soot. Estimates of soot sheet optical depth, mean absorption coefficient and volume fraction have been made at four heights in the flame. The results obtained are in rough agreement with theoretical predictions for the same flame.

MEASUREMENT OF PRODUCT CONCENTRATION FLUCTUATIONS OF TWO PARALLEL REACTIVE JETS USING DIGITAL IMAGE PROCESSING.

J.M. Bessem, F.T.M. Nieuwstadt, J. Westerweel
TU-Delft, Laboratory for Aero- and Hydrodynamics,
Rotterdamseweg 145, 2628 AL Delft, the Netherlands

H. Stapountzis
University of Thessaloniki, Dept. of Mech. Eng., Thessaloniki 540 06 Greece

ABSTRACT

Euromech Colloquium 279, Delft, July 1991

Chemically reactive flows are influenced by turbulence structure, fluid properties like the Schmidt number and flow conditions such as stoichiometry, geometry, mean shear, Damkohler number. As a consequence the distributions of reactant and product concentrations and the mean reaction rate are affected. The study of these distributions is important in many industrial and environmental flows.

In this work the Visible Reaction Product Technique, Breidenthal 1981, is employed to measure the reaction product distribution in a turbulent shear flow. The product is made visible by Laser Induced Fluorescence (LIF). Two round jets carrying 1N acqueous solutions of nitric acid and sodium hydroxide issue vertically downwards into a tank filled with water (nozzle exit Re numbers 9000 approx.). The stream carrying the nitric acid contains Fluorescein. Under normal lighting conditions neither the reactants nor the reaction product fluoresce. When the flow is exposed to an Argon-ion laser light sheet strong fluorescence of only the reaction product, which is now carrying some of the fluorescein, is observed. Video recordings of the flow in the plane of the jet axes are made and are digitally processed to yield the mean and root mean square product concentrations. The distance, l, between the nozzle axes is a geometrical parameter that is varied in the experiments.

A number M of frames from the video tape are sampled, digitized (512x512 pixels) and stored on disk. The digitized image is resampled again and is "condensed" in the direction normal to the jet axes (y) by discarding every other row of the two dimensional array. Problems related with bad interlacing are avoided this way. The resulting image has 512 columns and 256 rows, i.e. it is represented by 512x256 pixels of intensity 0 to 256. The mean and rms pixel intensity is computed by averaging over the digized frames, see example in Fig. 1a for M = 25. To account for possible displacement of the camera with respect to the nozzles all the frames are aligned relatively to a fixed light source included in the digitized screen. The displacement vector is found by computing the cross correlation function of each picture. Background noise, which is very low in the present experiments can also be subtracted.

Fig. 1b shows the variation of mean and mean square concentration of the product in the direction y, normal to nozzle axes and at column 256. Concentrations are expressed in pixel value. Conversion into absolute product concentration is made possible from calibration runs with uniform known product distribution. The maximum mean concentrations occur midway between the jets, while there is indication that the max rms concentrations occur off the center line. With increasing distance between the jets, l/d, the mean maximum product concentrations (Fig. 2) and maximum rms product concentrations decrease. The streamwise positions x/l where these maxima occur appear to be related by power laws with the geometrical parameter l/d, see Figs 3 and 4.

References.

Breidenthal R. 1981 J. Fluid Mech. vol 109 pp. 1-24

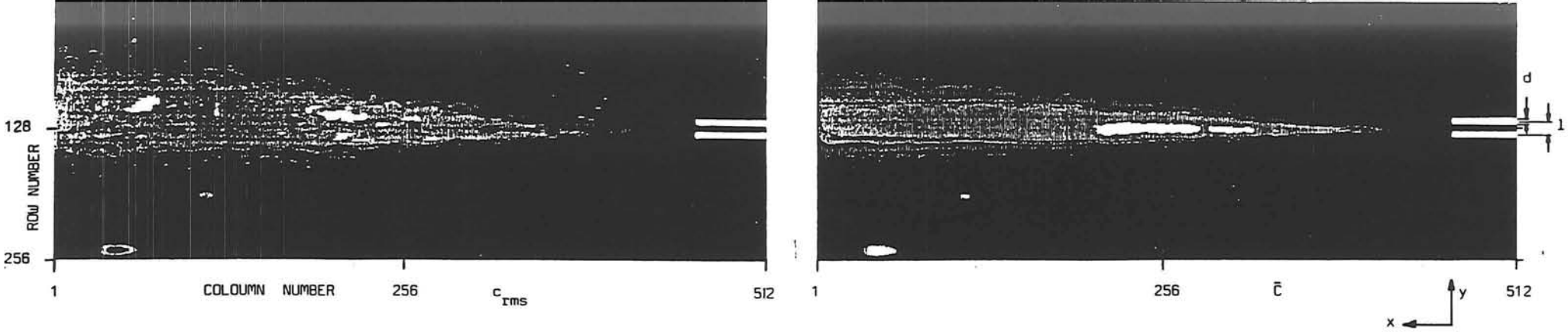

Fig. 1a Grey level representation of the mean and rms product concentration fluctuations for two parallel reactive jets.

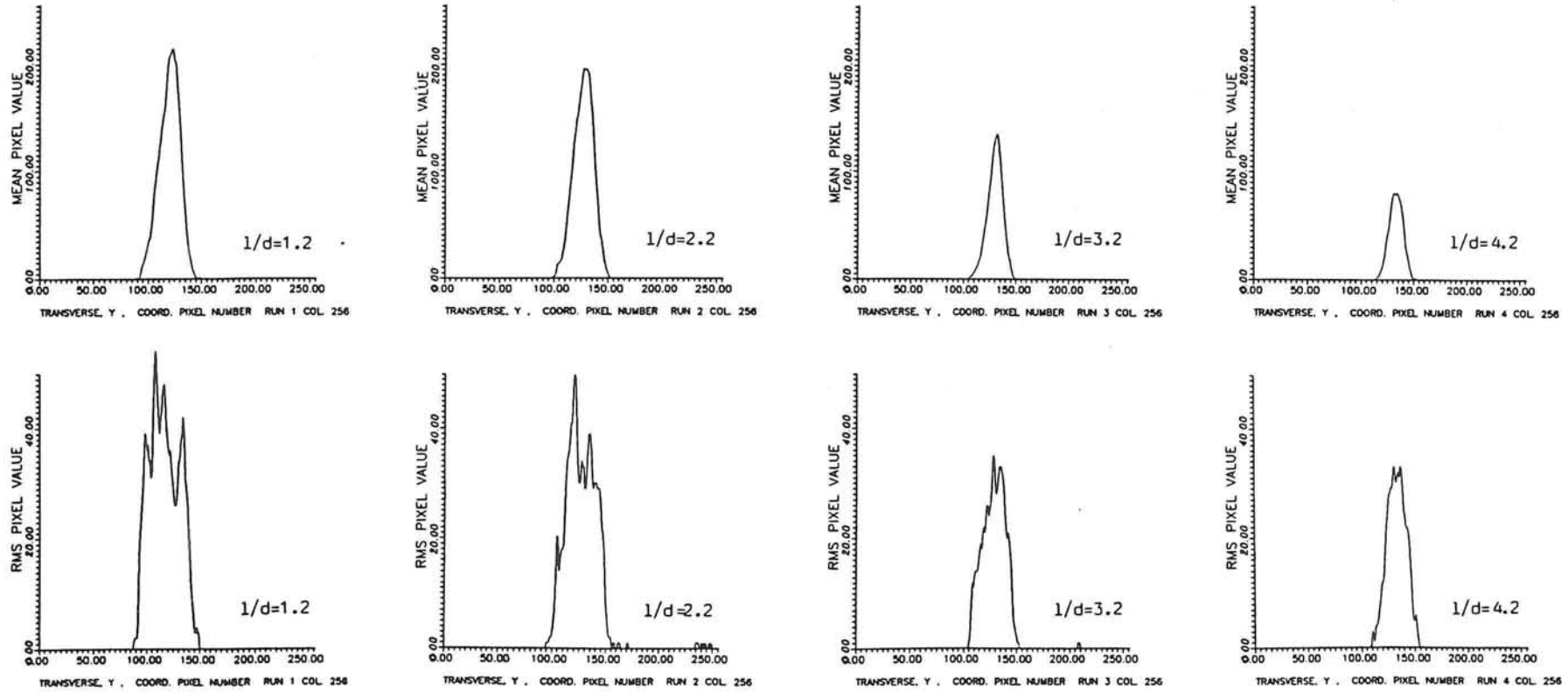

Fig. 1 b Variation of $\bar{C}$ and c_{rms} normal to jet axis

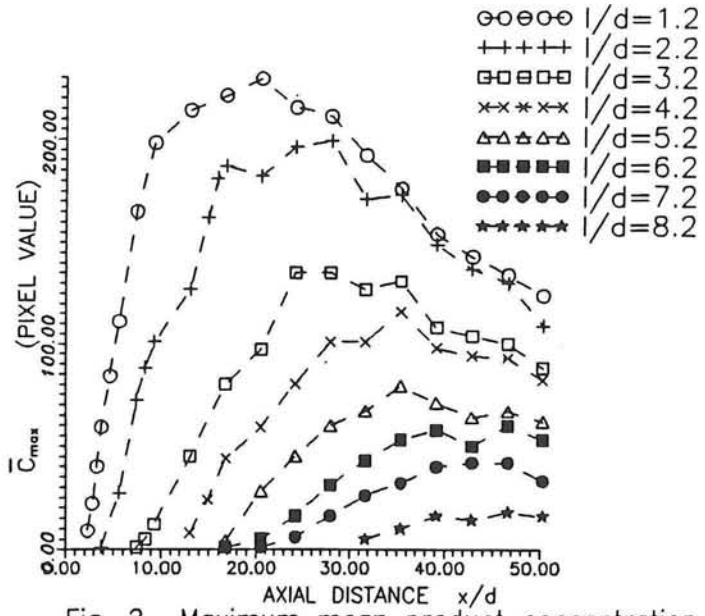

Fig. 2 Maximum mean product concentration

Fig. 3 Streamwise position of max. concentration

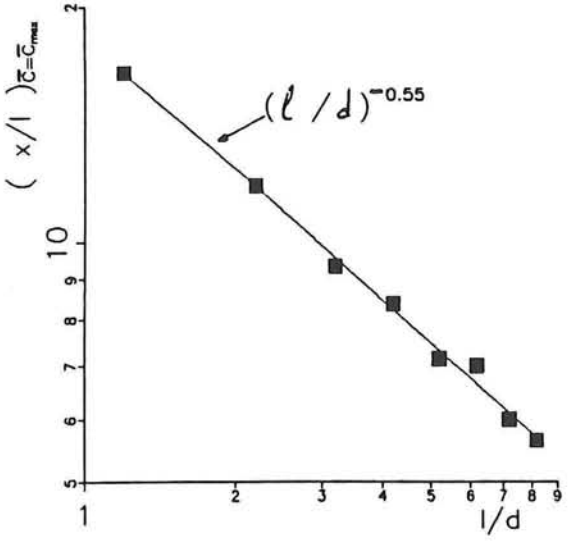

Fig. 4 Streamwise position of $c_{rms_{max}}$

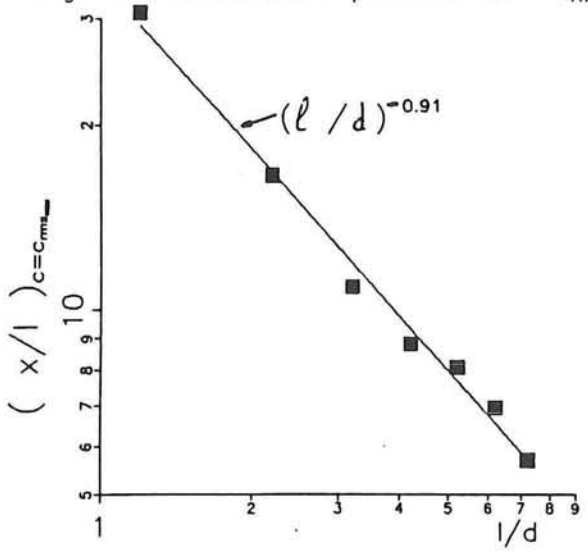

EUROMECH 279

NEW PROCESSING TECHNIQUES FOR FLUID VELOCITY MEASUREMENTS BY LASER TOMOGRAPHY.

Thierry FOURNEL *, Marie José LABOURE *, Marie-Claire HOYEZ **, Jean-Claude MONNIER **, Jacques PIGEON *, Jean-Paul SCHON *.

* Laboratoire T.S.I. et I.U.T. Université de St Etienne rue Paul Michelon 42023 St Etienne cedex France.

** Institut de Mécanique des Fluides de Lille 5 Bd Painlevé 59000 Lille.France

New processing techniques for Fluid velocity measurements by laser tomography are described and compared to more classical methods .

The first technique described consists in detecting particle displacements by echo methods used in radar techniques (Cepstrum). This technique gives in general results equivalent to those obtained by the autocorrelation method. The differences in the two methods can be in favour of the new one, but not systematically. The reasons of theses deviations are discussed.

The second method is devoted to visualisations where the individual particles cannot be distinguished,but where the flow structures can be determined. The evolution of these structures can be derived by a close description of the boarder of these structures by " dominant points ". These dominant points characterize the local concavity or convexity. The association of these points on two successive images allows the determination of their velocities and of the local characteristics of the dispersion.

Holographic Techniques

Friday 5 July.

OPTICAL PROCESSING OF IN-LINE AND OFF-LINE HOLOGRAMS FOR 3D INSTANTANEOUS VELOCITY MEASUREMENTS

C.S. Moraitis, M.L. Riethmuller
von Karman Institute for Fluid Dynamics
Chaussee de Waterloo, 72
1640, Rhode-Saint-Genèse,Belgium

ABSTRACT

Double exposure holographic recording of particle images for 3D velocity measurements is not a new idea. However, the processing of holographically recorded data is not straightforward and most of the approaches proposed in the literature are tedious and time consuming. Most techniques rely on the focusing of a video camera on particle images within the reconstructed optical wave and the subsequent identification of doublets and the evaluation of their position on a video monitor manually, by the operator. Among the more intelligent techiques which incorporate some kind of elementary optical processing, the most promising sems to be the one by Shofner et al., according to which a thin slice of the flow field can be holographically reconstructed, instead of the whole field, using appropriate matched filtering. This results in a selective reconstruction in depth, while lateral coordinate selection of the area to be reconstructed is provided by mechanical scanning (thus restricting the applicability of the technique to on-line holography). However, as the matched filter cannot be produced in real time, this technique, apart from being quite inaccurate, is also time consuming. Among the automatic techniques, the one proposed by Iwata and Nagata relies on the mechanical movement of an aperture for the selection of the area to be interrogated and hence is limited to 2D measurements. By virtue of this fact, this technique is conceptually similar to conventional PIV, except that the holographic multiple exposure recording makes the technique insensitive to focusing errors. Another technique that merits mentioning is that of Ewans, which provides 1D spatial statistics only and has been used successfully in axisymmetric jets. Its main advantage is the use of very low cost optical equipment but, apart from being limited to one dimension, it requires digital image processing algorithms which are not straightforward to implement.

Unlike these approaches, we propose a novel technique for the optical processing of holographic velocimetry data, consisting of:

(i) selective reconstruction of an axisymmetric volume within the reconstructed image (x-y selection)

(ii) selective reconstruction of a slice within the said axisymmetric volume (z selection)

(iii) fringe formation by double images of particles within the reconstructed volume and subsequent digital image processing of fringe images to yield the corresponding velocity vector.

With intrinsically three-dimensional flows in mind, mainly from turbomachinery related applications, we have worked out two variants of the technique: one of them requires big particles, but can be used even when optical access to the flow is available from one side only. This variant, the principle of which has been presented elsewhere, is very powerful but requires expensive optical hardware. Recently, we have worked out a simplification of this technique, which uses in-line holography, thus requiring a "see-through" access to the flow field, but can be used with particles of diameter as small as 0.1 micron. Details of this technique, which relies entirely on linear optical processing, as well as results of thorough computer simulations will be given in the paper.

The first stage of the processing (x-y selection) is accomplished by the formation of a real time hologram in an electrooptic crystal (Bismouth Silicon Oxide) of the reconstructed flow field. During this real time hologram recording, the reference wave, which is spherical, is selected in such a way that particles in the region of interest result in linear terms of the intensity in the hologram plane. Particles in areas other than the selected one, result in rapidly varying quadratic terms, which are eliminated by spatial filtering.

The second stage of the processing (z selection) relies on a novel concept of image plane filtering: only those particles are finally visible, which are perfectly focused on a real time positive film, using appropriate image formation optics. This real time positive film is a novel device proposed by the authors, relying on a combination of the electrooptic phenomenon and photoconduction in Bismuth Silicon Oxide.

A schematic view of the device providing for x-y and z selection is given in Fig. 1, while a typical fringe image, corresponding to a single velocity vector, is given in Fig. 2 (this last image has been produced by computer simulation of the complete optical processing). A detail of the central part of the fringe pattern is shown in Fig. 3. This part exhibits almost circular fringes which can be easily analyzed by rather simple image processing algorithms.

Up to now, a comprehensive theoretical modelling of the optical processing involved by the proposed technique has been accomplished, as well as appropriate computer simulations. Moreover, software originally written for conventional PIV has successfully been adapted to the requirements of this technique. An experimental demonstration is planned for the near future. The theoretical model, simulation results and eventually experimental results will be given in detail in the final paper.

A simplification of the technique, appropriate to on-line (Gabor) holography, was also worked out. In this case, x-y selection can be reduced to simple mechanical scanning.

Z selection is accomplished by appropriate matched filtering. A thorough mathematical analysis of the depth selection process demonstrates that it can be performed using a filter of well known form (in fact a phase grating) the spatial frequency of which depends on the depth to be selected. Instead of changing the filter for every depth, a variable size Fourier transform is produced, using appropriate optics. Hence, the same matched filter is used for the processing of the entire hologram. Extensive computer simulations of the entire processing chain, including systematic variations of particle size, hologram recording configuration and velocity magnitude, performed recently, have given very encouraging results. This variant of the technique presents practically no size limitations. Furthermore, the fringe formation is accomplished on a shift invariant plane, resulting in circular fringes. An example of such a fringe pattern is given in Fig. 4, where the fringes, altough circular, appear elliptical because the aspect ratio of the image monitor is greater than one.

The proposed technique, conceptually close to PIV, can be used with optical configurations considerably simpler than the ones used for 2-D measurements, yet allow for 3-D instantaneous velocity measurements. Although intrinsically relying on light interference, it is as simple to realize as other interferometric techniques, without suffering from limitations such as requirements for unidimensionality or reduced dynamic range. Compared to its best known rival, the so called "3-D particle tracking velocimetry", it proves superior, not only due to the absence of depth of field limitations but also because it is much less sensitive to high seeding concentrations. Furthermore, it is expected to require processing times comparable to video rate, for obtaining a single velocity vector, while the 3-D particle tracking would not achieve such performances, even with the fastest microcomputers nowadays available. However, there is a price to pay for these performances and this is the requirement for using accurately designed optical components (mainly lenses and diffraction gratings).

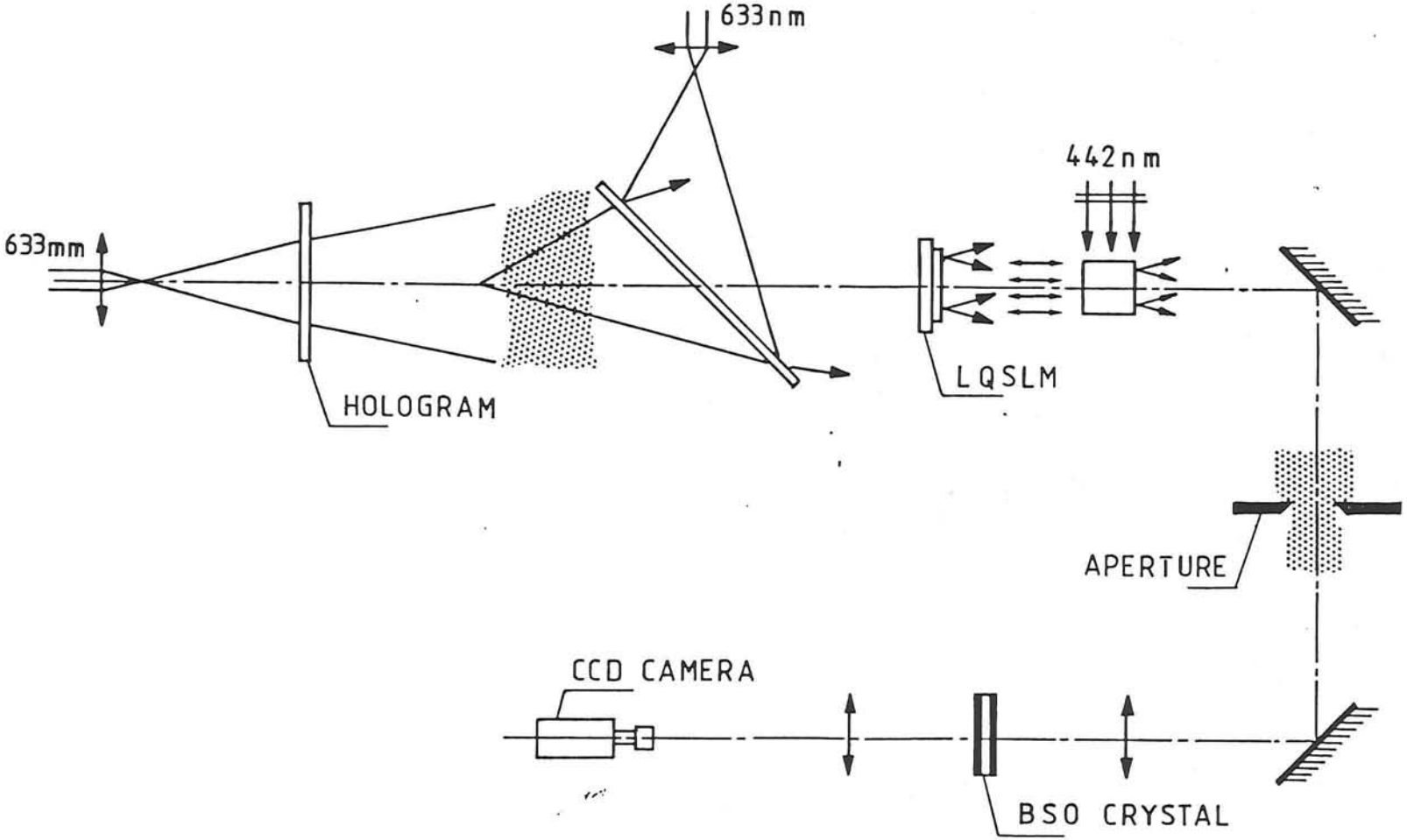
633nm
442nm
633mm
HOLOGRAM
LQSLM
APERTURE
CCD CAMERA
BSO CRYSTAL

FIG.1

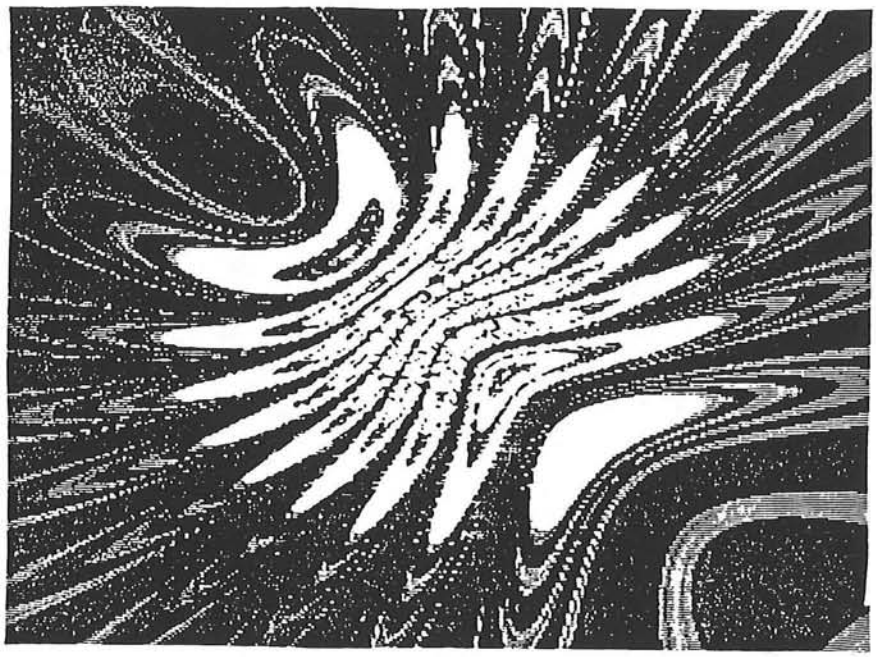

FIG. 2

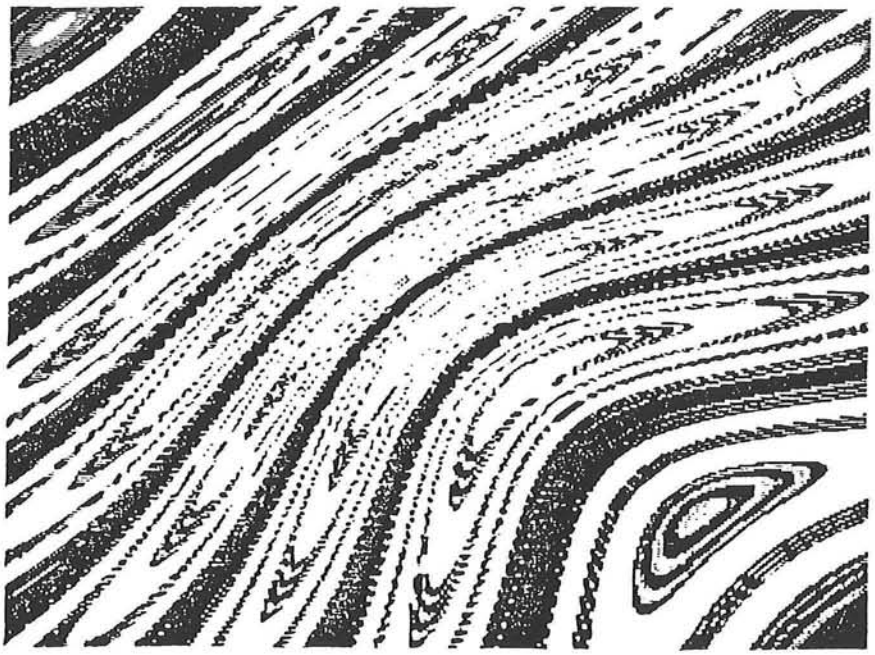

FIG. 3

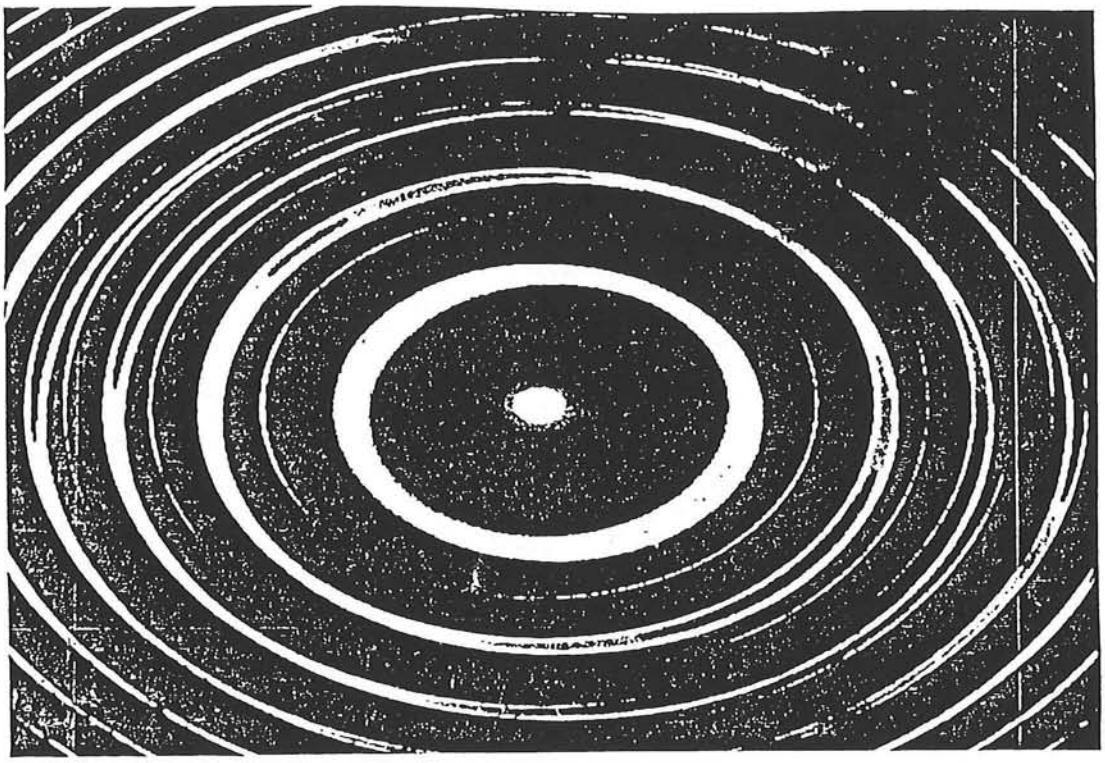

Fig. 4 - Circular interference fringes in in-line particle image interferometry

DIGITAL PROCESSING OF MULTIPLASS HOLOGRAMS

par R. Deron

Office National d'Etudes et de Recherches Aérospatiales
BP 72 - 92322 Châtillon Cedex - France

Summary

A procedure for digitized holographic interferogram evaluation based on an image processing system connected to a microcomputer has been implemented.

A semi-automatic code enables to obtain measurements such as density variations from pictures of disturbed finite fringe patterns caused by steady hypersonic flows around profiles such as a cone or a sphere. Software converts pictures of fringe patterns into maps of 512x512 pixels with 8 bits in intensity. Image enhancement and digital spatial filtering are applied to reduce high frequency noise, such as speckle noise introduced by the optical technique. Fringe patterns are subjected to thinning by using kirsch filters and particular routines implemented within the framework of the digital image processing capabilities available. Some information has to be input interactively. This includes the position of the profile, the decision as to whether subsections of the fringe pattern should be analysed. Value of the interfringe is computed in region of the inviscid flow fringes. Then the procedure is fully automatic to number and to give a coordinate to each fringe, to interpolate or extrapolate fringe functions for regions where refraction or noise have destroyed the fringes, to converse fringe data into aerodynamic flows and to reconstruct variations of density field around a profile.

Examples of data extraction from pictures of finite fringe patterns obtained in an experiment of multipass holographic interferometry for low density gas flow will be presented at the conference.

Extension of Particle Image Velocimetry (PIV) to a 3-D Measuring Method

H. Hinrichs, K. Hinsch, G.Kuhfahl, P. Meinlschmidt

Fachbereich 8-Physik, Carl-von-Ossietzky Universität
D-2900 Oldenburg, Germany

Introduction

Particle Image Velocimetry (PIV) has become a powerful tool in flow diagnostics since it provides simultaneous velocity data from a large field of view. In its most common applications, a thin sheet of laser light illuminates a portion of the flow. A double-exposure photograph is taken, recording small light scattering particles seeding the flow. Thus the information recorded is restricted to the velocity components transverse to the direction of observation and to velocity data in the plane selected by the illuminating light. PIV would greatly gain could it be extended in both cases:
1. simultaneous recording over a certain region in depth
2. registration of the out-of-plane component of the velocity vectors.
The paper presents independent solutions to each of these problems which could be combined to provide the complete velocity information on a flow field.

1. Covering a deep flow field by illuminating with a batch of light sheets

The main objective of the proposed recording scheme is to avoid noise produced by out-of-focus particles when focusing on a selected plane in depth. To cover the space of interest a suitable configuration of reflection prisms and cylindrical lenses is used to produce a batch of light sheets arranged in depth. A holographic recording is made of the flow field thus illuminated. The optical paths are arranged such that light from one sheet each is recorded with a specific reference beam direction. Upon reconstruction the double-exposure images of the different sheets can thus be separated. In adjusting the path lengths advantage is taken of the limited coherence of the laser.

2. 3-D velocity registration by stereoscopic recording

To provide the third component of the velocity vector a light sheet is shaped in such a way that the majority of particles will not leave the illuminated field due to their depth velocity component. A stereoscopic pair of double exposures is recorded. Contact copies of the images are projected back simultaneously through the same optical system used for recording. This provides a superimposed image of two slightly different double exposures. Thus distortions by the imaging system are reduced to a minimum. Interrogation is done by the well established technique: A small area of the final record is illuminated by a focused laser beam. The resulting fringe system is recorded and Fourier transformed to produce the autocorrelation function of the particle arrangement. In extension of the results obtained by ordinary 2-D PIV applications this output contains additional peaks that are separated by a distance directly proportional to the depth component of the displacement.

The paper presents first applications of both these extentions to a real flow field and discusses the main restricting quantities.

PARTICLE DETECTION CRITERIA FOR AUTOMATIC DATA REDUCTION FROM MICRO-HOLOGRAMS.

M. Stanislas, C. Geiler, H. Royer,
M. Courbon, J. Azema, J Danieres.

High speed holography is a powerful tool to study the behaviour of particles. This technique, which is fully three-dimensionnal, gives access to the position in space, the size, the shape and even the velocity of particles beeing in suspension in a transparent medium (solid, liquid or gaz, the particle beeing also solid, liquid or gazeous). The method can be used to study the particle itself or, using it as a tracer, to study the velocity field of the carriing medium. This could be called Holgraphic Particle Image Velocimetry (HPIV).

The main actual limitation of the method is due to the time necessary to analyse the hologram. To observe the particles images, which are generally small, a magnification system consisting of a lens and a video camera has to be used. Thus, the analysis of a large field, which is necessarry in HPIV, is very time consuming.

To overcome this limitation, IMFL-ONERA, in collaboration with Université de St Etienne and ISL, has developped an automatic analysis system. This system is based on a PC computer including a digital image analysis card. The objective is to be able to analyse fully automatically the holographic image and obtain the size, position and velocity of the particles present in the image. The main difficulty in such a system is to detect that the particle is present and that it is in the focus plane of the observing lense. For this purpose, various criteria which are presented, has been tested. The most simple and efficient one has been retained and applied to a reference hologram realized by H. Royer at ISL. A comparison between the automatic analysis results and those obtained manually by H. Royer is presented and discussed.

ALGORITHMS FOR AUTOMATIC MEASUREMENT OF SIZE AND VELOCITY OF SPRAY DROPLETS FROM HOLOGRAPHIC RECONSTRUCTIONS

A. Chávez, F. Mayinger

Lehrstuhl A für Thermodynamik, Technische Universität München
Arcisstr. 21, 8000 München 2, W. Germany
Fax: 49 89 - 21 05 34 51

ABSTRACT

This work presents some substantial improvements in the evaluation of "off-axis" pulsed laser holograms of particle fields using digital image processing. More efficient focussing (based on the idea of Haussmann, 1980) and classifying criteria could be applied throughout the whole evaluation process. The processing system for automatic hologram evaluation was implemented on a personal computer which makes the work suitable for applications in small optical laboratories.

Software procedures based on spacial Fourier transformations were developed to evaluate the velocity of spray droplets from double pulsed holographic reconstructions. The build up of these procedures and their application for automated particle identification and measurement are described in detail. They complete a series of algorithms, presented earlier, developed to measure drop size distributions from single pulsed holograms.

The application of both groups of algorithms allows for direct measurement of size and velocity distributions of spray droplets. Recent results of the evaluation of a series of 120 holograms of sprays used to calculate direct-contact condensation rates are presented as an example of application. The holograms contain information about the situation in which liquid refrigerant R113 is injected through a hollow cone atomizer (Ø 0.6 mm) into a pure R113 saturated vapor environment. The liquid mass flow rate and the vapor pressure were varied between 0.5 and 5 g/s and 0.1 and 1 Mpa respectively. The resulting dropsizes ranged in between 30 and 300 μm.

Keywords: droplet sizing, evaluation of pulsed holograms, spray characterization, image processing of holographic reconstructions.

DIGITAL HOLOGRAPHIC INTERFEROMETRY IN THE INVESTIGATION OF UNSTEADY COMPRESSIBLE FLOWS

T.A.W.M. Lanen

Delft University of Technology, Dept. of Aerospace Engineering
Kluyverweg 1, P.O. Box 5058, 2629 HS Delft, The Netherlands

Abstract. The quantitative experimental investigation of unsteady compressible flows generated in a wind tunnel by means of digital holographic interferometry is presented. To investigate unsteady flow fields by this technique, the instantaneous realization of the flow field at a certain moment is frozen on a holographic plate for subsequent analysis by a 30 ns laser puls. By piezo-electrically translating a mirror in the path of the reconstruction beam (i.e., the beam which reconstructs the flow field from the holographic plate) 4 phase-stepped interferograms are generated which, after being digitized, are stored in the computer memory. These data serve as input to the automatic computation of the projected density distribution in the flow field by means of digital image-processing.

The experiments are carried out in a blow-down wind tunnel. In particular, the flow phenomenon indicated by "shock wave - turbulent boundary layer interaction" attracts the attention. This flow phenomenon can hardly be investigated by conventional measurement techniques because of the disturbing effects resulting from the physical presence of a probe (e.g., a pressure tube) in such flow fields. Therefore a mobile holographic interferometer was build which is placed over the wind tunnel at the position of the test section area. This part of the wind tunnel is bounded by windows to allow the non-intrusive optical measurements.

POSTERS

CHARACTERIZATION OF SAVONIUS ROTOR WAKE USING IMAGE PROCESSING TECHNIQUES

J.Massons, Jna.Gavaldà, J.Escoda, X.Ruiz and F.Díaz

Lab. Física Aplicada. Dept. Química. Univ. Barcelona. P. Imperial Tarraco, 1, 43005 Tarragona. Spain

INTRODUCTION.- The consciousness about the limited character of the fossil supply has led to considerable attention being focused on the utilization of renewable energy sources, one of which is wind energy. The characterization of the Savonius wind machine has been a subject of main interest [1], [2]. However, little experimental information exists on the flow field generated by the Savonius rotor. In the present study, image processing techniques have been applied to the visualizations of the Savonius wake generation. This characterization is carried out by determining the evolution of the geometric parameters governing the wake, together with the velocity, streamfunction and vorticity distributions.

EXPERIMENTAL DETAILS AND IMAGE PROCESSING TECHNIQUES.- Figure 1 presents a sample of the chronophotographic visualizations of the Savonius wake [3]. The pictures were digitalized using a PANASONIC video camera and analyzed on VIDAS/IPS equipment. The first step in processing involved the uniformization of lighting and the increasing of the contrast between traces and background. Once optimum image quality was achieved, binarization was carried out selecting a suitable threshold of grey level to discriminate traces from the background. This value was obtained from the analysis of the grey level histogram using Otsu's method [4]. The noise existing in this resulting binary image was reduced according the procedure described in a previous paper [5], which involves the boolean operation of two different binary images. When the image has been stated in right binary form, each of the particle paths was assimilated to an object. A measurement program carried out a screen scan, locating each of these objects, identifying them and quantifying the previously selected geometrical characteristics. Finally, these data were processed on IBM 3090/200 computer in order to determine the bidimensional velocity field, streamfunction and vorticity distribution.

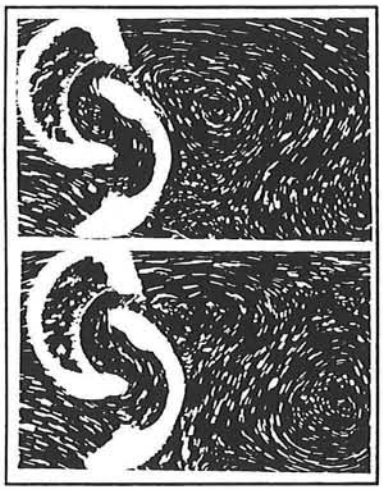

Figure 2.- Flow visualizations

RESULTS AND DISCUSSION.- The visualizations show that initially a pair of vortices are formed, later, the setting up of the stablished wake takes place and a double Kármán vortex street characterizes the structure of the flow. The streamfunction and vorticity distributions obtained by means of image processing techniques allow to determine the temporal evolution of the geometric parameters of the vortices (downstream wake length, maximum wake width, vortex center position, and axial and lateral displacement between vortex centers). The analysis of these evolutions show that the steady flow is stablished after a brief transient phase ($t^* = 4$) and existing also a difference in the vorticity values of the two alternate vortices, which produces an aerodynamic torque upon the rotor.

References.-

[1] **Modi,V.J., Roth.,N.J. and Pittalwala,A.,** *"Blade configurations and performance of the Savonius rotor with applications to an irrigation system in Indonesia".* **Journal of Solar Engineering,** 105, 295, (1983).

[2] **Khan,M.,** *"Model and prototype performance of a Savonius rotor windmill".* **Wind Engineering,** 2, (2), (1978).

[3] **Massons,J., Gavaldà,Jna., Ruiz,X. and Díaz,F.,** *"Image analysis of the wake generated by a Savonius rotor".* **Wind Engineering,** 12, (6), 341, (1988).

[4] **Otsu, N.,** *"A threshold selection method for grey-level histograms".* **IEEE Trans. Syst. Man and Cybern.,** SMC-9, 62, (1979).

[5] **Massons,J., Gavaldà,Jna., Díaz,F. and Solé,Ll.,** *"Image processing of cylinder wake generation".* **Physics of Fluids, A,** 1, (8), 1415, (1989).

FLOW EXPERIMENTS AND VISUALIZATION IN A HYDROSTATIC JOURNAL BEARING

M.J.BRAUN
Dept. of Mechanical Engineering
Univ. of Akron
Akron, OH 44325

R.C. HENDRICKS
NASA Lewis Research Center
MS 5-11
Cleveland, OH 44135

Even though the hydrostatic journal bearing has had a long and successful technical life there are still unanswered questions regarding flow characteristics in the pockets, pressure drop fluctuations as a function of the bearing pockets feeding characteristics, and pressure profiles in the region of the pocket. The research to be presented here will endeavor to clarify some of these issues.

The flow visualization method developed by the authors(FFFT) uses tracing particles in conjunction with a laser planar sheet of light to determine flow patterns and measure non-intrusively its velocities and accelerations. The research will connect the flow patterns, that resemble those of a driven cavity, to the pressure profiles that will be measured in the pockets. Pocket depth and footprint as well as shaft angular velocities will be the parameters of the experiment.

Particular attention will be paid to visualization of the fluid inertia effects in the region where the pockets meet the bearing sill. The inertia effects in the hydrostatic bearing are extremely influential on both the pocket mass flow, the final pressure distribution and the load carrying capacity.

The flow in the bearing clearance will be also visualized and streamlines, velocity and particularly flow acceleration patterns will be quantified at the juncture between the pocket and the sill.

A computer algorithm that allows semiautomatic flow tracking and quantizatio will be presented.

****
For further correspondence please adress:
Prof. Dr. Minel J. Braun
Dept. of Mechanical Engineering
University of Akron
Akron, OH 44325
USA
****

LSV Applied to the Flow in a Rotating Channel

St. Uellner K.G. Roesner

Institut für Mechanik

TH Darmstadt, D-6100 Darmstadt, Germany

The object of the investigation is the laminar flow through a rotating channel.

The three dominant parameters are the aspect ratio, the Ekman and the Rossby numbers. The Rossby number is the ratio of convective inertial force to Coriolis force and the Ekman number is the ratio of viscous force to Coriolis force.

In the case of no rotation the velocity field has the analytically well-known quasi-parabolic shape with a component parallel to the direction of the channel axis.

A rotation of the channel leads to the additional action of centrifugal and Coriolis forces. The quasi-parabolic ground state of the flow field is disturbed and a secondary motion with components perpendicular to the main flow appears. According to the aspect ratios, the Rossby and the Ekman number, the secondary flow can be classified.

This flow field is optically registered and the transient character of the motion is analyzed by postprocessing. For this the multiple exposed Specklegram is scanned pointwise and the velocity in each point is retrieved by a twodimensional Fast Fourier Transformation of the diffraction picture in the Fourier plane of a lens. The FFT is carried out on an array processing board to gain high evaluation rates. It takes about eight hours to determine 10 000 velocities.

The velocity field which is obtained by the postprocessing of the pictures is compared with the numerical results which are gained by a spectral element method due to Patera.

The Title : An Automatic Image Analysis Method for Determining Each Sense of Velocity Vectors Using A Path-Line Picture

ABSTRACT :

Image analysis methods have been used to quantitatively analyze flow visualization pictures for measurements in velocities, concentrations and densities. Path-line pictures obtained in flow visualizations have come to be used actively, especially in velocity measurements. In such particle image displacement velocimetries, the judgement of senses of velocity vectors is also of important problem. As the means of solving, several methods in which a pair of cameras are used synchronously have been proposed before.

From the point of view of simplifying the both experimental instruments and procedure, a simple method for determining senses of velocity vectors was then investigated in this study. It is an automatic image analysis method for determining the senses using a path-line picture taken by an only camera. : Each sense of path-lines is determined one after another on the basis of angles of inclination between each of path-lines. In this processing program made by FORTRAN language, a series of the working procesis, inclusive of digitalizing a path-line picture and computing each vector of path-lines, is automated using an image processing system on the market which is consisted of an image processor and a personal computer with 16 bit processing unit.

This simple method was applied to determine each sense of velocity vectors in both the flows around a plate and those around a cylinder. Almost all of senses of velocity vectors observed in the both flows were determined correctly using the processing program. Because a series of the procesis has been automated completely, whole working hours, inclusive of drawing a vector diagram, were shortened fairly.

This method developed in this study is also considered to be effective for different processing systems because this program is almost consisted of standardized functions in image processing systems on the market.

EUROMECH 279

"Image Analysis as Measuring Technique in Flows"
Delft University of Technology, the Netherlands, 2-5 July 1991

'Unsteady flows velocity field restoration by a specific digital image processing'

P.de Ramefort - A. Texier - M.Coutanceau
Laboratoire de Mécanique des Fluides
Composante du LEA - URA CNRS 191
Université de Poitiers - France

Introduction

The visualization technique using solid tracer particles allows, at a given time, a qualitative as well quantitative, two-dimensional flow investigation. Profiting both by the experience of the Laboratoire de Mécanique des Fluides de Poitiers in flow visualization experience and the increasing availability of computer techniques, an automatic analysis system for unsteady flows (hydrodynamic wakes), based on the digital image processing technique, has been developed, and is still being improved, to provide, more particularly, accurate and reliable experimental data about the velocity field.

The automatic analysis system

Taking into account our resolution requirements, our photographs are digitalized either with a scanning photo-cell, or, for improving the acquisition speed, with a CCD camera linked to an image processor. The hardware system, controling the image acquisition, storage and various processing tasks, is built around 32 bit industrial VME bus micro-computers. In order to obtain the velocity field with a sufficient precision, original algorithms of data extraction (location, shape and length of the particle path elements) as well as a specific graphics software, wich permits us to control each of the processing steps, have been developed.

Results

Considering our analysis system precision, one can regard our results as very satisfactory (the mean relative error between manual and automatic measures has been estimated at around 2%). However, a problem due to a lack of information in some interesting flow regions still persists, but this difficulty is being partially solved by the superposition of results coming from several images obtained in analogous experimental conditions.

Use of Fractal Analysis in Turbulent Flows

José M. Redondo

Departament de Física Aplicada
Universitat Politécnica de Catalunya, Jordi Girona 31, Barcelona, España,
& Department of Applied Mathematics and Theoretical Physics
University of Cambridge, Silver Street, Cambridge CB3 9EW, UK.

In this work the way in which fractal analysis (looking at different aspects of self-similarity) may be used in order to extract geometrical information from turbulent flows is studied. A microcomputer controled video digitizer analyses images of the turbulece with various box counting algorithms.

The effect of multiple interacting scales on density interfaces is investigated, with particular reference to the fractal and multifractal structure of the turbulence and the increased area available for transport across isoscalar surfaces. Both stable and unstable density interfaces in a turbulent fluid are considered as examples of the effect of body forces on turbulent flows.

Several visual techniques (laser induced fluorescence, shadowgraph, digitization of the light attenuation across the tank, and colour change produced by chemical reactions) are used in order to investigate experimentally turbulent flows. A series of colour coded photographs of the light intensity change produced by a pH indicator in mixing turbulent flows indicates the fractal behaviour of the dissipation field (as high dissipation is associated with high molecular mixing, which is indicated by a phenolphthalein colour change at a preset volume fraction). The effects of body forces in a turbulent flow produce both changes in the range of self-similarity exhibited by the flow and in its fractal dimension.

INVESTIGATION OF THE FREE EDGE OF AN UNSTEADY AXISYMMETRIC TURBULENT JET

F.Z. LAHBABI, J. BOREE, H.J. NUGLISCH and G. CHARNAY
INSTITUT DE MECANIQUE DES FLUIDES DE TOULOUSE
E.N.S.E.E.I.H.T., I.N.P.T., C.N.R.S.- U.R.A. 005
Avenue du Professeur Camille Soula
31400 Toulouse FRANCE

Abstract:

The jet flow configuration is one of the basic flows in fluid mechanics which is of practical and theoretical interest. Precise observations and predictions of its mean and fluctuating properties have led to an accurate understanding of its characteristic turbulent structures and mixing properties.

Various types of artificial jet excitations have already been applied in previous works such as modulation of the nozzle mass flow on external accoustic excitation. Nevertheless, these perturbations were usually periodic and of small amplitude in order to study the frequency behaviour of organised structures in turbulence.

We study here the response of the jet flow submitted to a sudden important decrease of ejection velocity. This situation can be of practical interest in injector applications.

A non stationary integral modelisation based on mass and momentum conservation equations has already enabled us to predict transition phase between the two jet flows of different velocities [1]. Its propagation due to inertial waves is quantitatively predicted by the model. Experimentation and particularly image analysis techniques should give us a picture of this propagation and of its impact on the turbulent structure , the mixing properties and the spatial distribution of the flow.`

The jet is discharging from a 5 mm diameter nozzle in a cavity having a cross section of 200 x 300 mm^2 and a lenght of 650 mm (fig. 1). The initial velocity is varying as a step function realised by an electric by-pass valve. A manual throttle-valve is mounted in the main branch adjusted for delivering the half flow rate when the by-pass is closed. The flow is visualized by dye injection (black indian ink, fluorescein) and laser sheet technique (fig. 2) .

The image processing system is composed of a H.P. Vectra computer equiped with the 386 series processor and two Matrox's cards allowing digitizing and processing with the associated software. Acquisition of pictures is realised with a C.C.D. camera (512 x 512 pixels quantified on 8 bits).

To treate binary pictures the Otsu's method of automatic threshold selection was chosen and implemented [2]. In order to isolate the jet a morphological transform of opening was applied followed by a Sobel's contour. A procedure of skeleton was been developed using C language to obtain a jet contour of one pixel width.

The overall velocity of the jet front will be determined at differents times and the evolution of the jet entrainment will be compared with theoretical results [3]. The deformation of turbulent structures and the convection time of the perturbation's displacement will be discussed.

References:

[1] J. Borée, H.J. Nuglisch, A.K. Chesters and G. Charnay
"Theorical and experimental investigation of compressed jet flow"
Euromech 272, 14-17 Janvier 1991, Aussois

[2] N. Otsu
"A threshold selection method from grey level histogram"
Trans. on Syst. man. and Cyb., Vol. SMC-9, N°: 1, p: 62-66, 1979

[3] M. Shirakashi, H. Kawase and S. Wakiya
"Analysis of turbulent structure of an impulsively started jet by applying image processing"
Bulletin of JSME, Vol.29, N°: 257, Novembre 1986

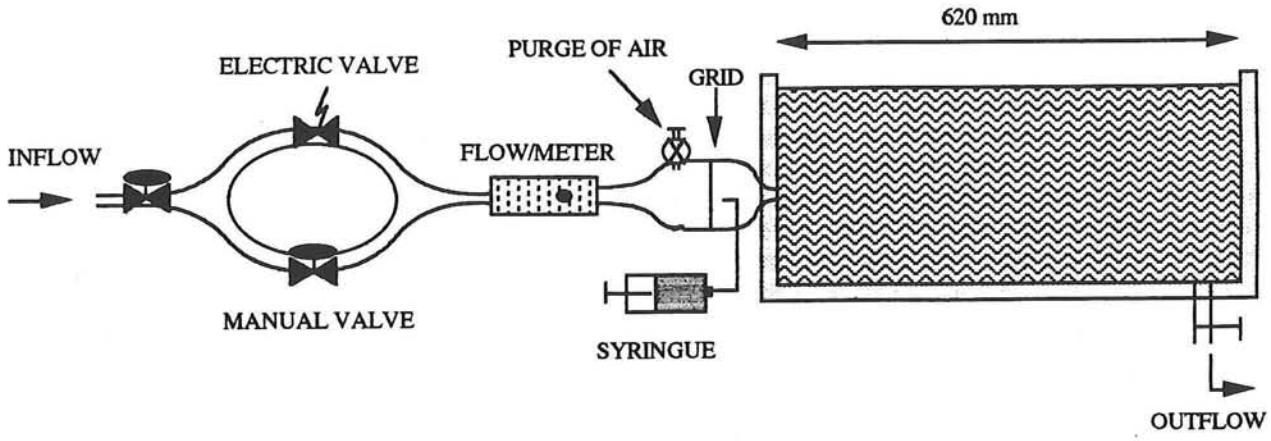

FIGURE. 1: EXPERIMENTAL SETUP

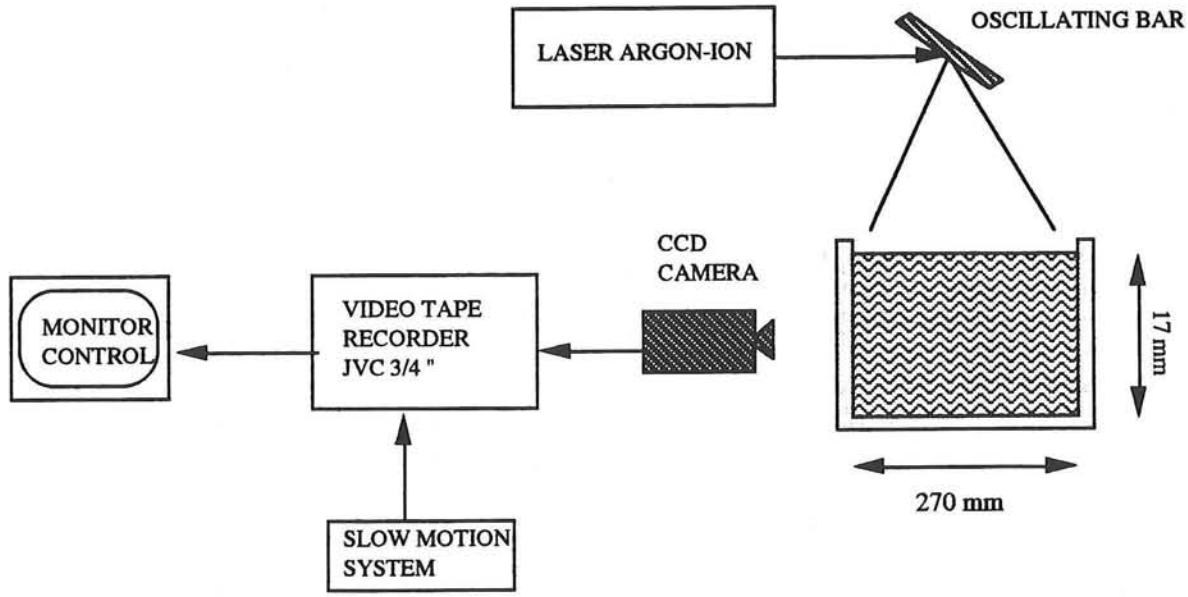

FIGURE. 2: VISUALIZATION AND ACQUISITION SYSTEM

STUDY OF HORIZONTAL JET IN A STRATIFIED FLUID USING THYMOL BLUE VELOCIMETRY AND "WEAK" DISTURBANCE PROPAGATION METHOD

S.I.Voropayev, Ya.D.Afanasyev
Institute of Oceanology, Acad.of Sci.USSR,Krasikova 23,
Moscow,117218, USSR

Classical Schlichting's solution for steady round jet in a homogeneous fluid was verified experimentally by many authors and is used now for different calibration purposes. We studied similar problem for horizontal round jet in a density stratified fluid. It appears that hydrogen bubbles, aluminium powder and Laser-Doppler velocimetry are not suitable here. Thus we chose a method of "weak" disturbance propagation [1] and Baker's thymol blue velocimetry [2].

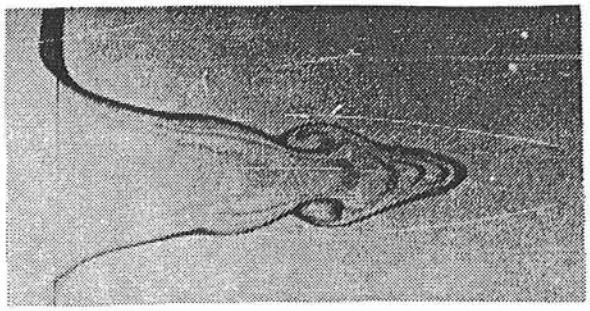

Starting jet in a linearly stratified fluid. Thymol blue velocimetry. Side view.

A cross of two fine platinum wires (diameter 2 10^{-3}cm) was used for thymol blue velocimetry. Velocity profiles in horizontal and vertical planes were measured simultaneously for different values of governing parameters (Re and Ri). The results obtained are in good agreement with the proposed theory and numerical simulation. Some data on a density field was obtained. Partly the results are published in [3,4].

REFERENCES

1.Stern M.E., Voropayev S.I. 1984. Phys. Fluids, 27(4):848-855.
2.Baker D.T.1966. J. Fluid Mech., 26(3):573-575.
3.Voropayev S.I.1989.In Proc. 20th Intern. Liege Coll. on Ocean Hydrod. Elsevier: 671-689.
4.Afanasyev Ya.D., Voropayev S.I., Filippov I.A.1989. Izvestia USSR Acad. of Sci.: Atm and Ocen Phys.,25(7):741-749.

A COMPARATIVE STUDY OF OPTICAL AUTOCORRELATORS FOR PIV

C.S. Moraitis, M.L. Riethmuller
von Karman Institute for Fluid Dynamics
Chaussee de Waterloo, 72
1640, Rhode-Saint-Genèse,Belgium

ABSTRACT

Processing techniques for Particle Image Velocimetry (PIV), except from the one relying on the digital image processing of Young's fringes, usually consist of forming the 2-D autocorrelation function (ACF) of the probed region of the transparency and subsequently locating the coordinates of the peaks present in the ACF pattern. This is usually accomplished digitally, using a fast array processing board for performing the heavy part of the computing involved. The disadvantage of digital processing is that it is particularly time consuming and its accuracy is intrinsically redundant: 32 bits floating point arithmetic is usually employed for getting a pattern which simply constitutes the input to a rather trivial peak-finding algorithm.

The optical formation of ACFs has been considered by different authors (including ourselves) as an alternative to digital processing. Different attitudes regarding compromizing between simplicity, speed and cost have led to three main groups of designs: holographic autocorrelators, autocorrelators using electrooptic spatial light modulators and autocorrelators using liquid crystal light valves.

In this paper, we attempt a comparative study, on a theoretical basis, of the performances of these three classes of optical devices. The main results of this study have as follows:

(i) Devices based on liquid crystal light valves involve electronic digitization of an optically produced power spectrum. This digitization intinsically affects throughput rate. Typically, two video frame cycles are required for processing one point with this kind of devices. On the other hand, the resolution of these devices in terms of spatial frequency is comparable to that obtained by fully digital processing (which is, in any case, higher than necessary, as we demonstrate rigorously).

(ii) Devices based on electrooptic spatial light modulators (SLMs) have performances which vary drastically with wavelength and the use of a suitable laser can dramatically increase the cost of a system. Their spatial resolution is rather limited (still adequate in most cases) but the throughput rate can be as high as 100 velocity vectors per second, for carefully designed systems, if adequate laser power is available.

(iii) Holographic autocorrelators, involving erasable hologram recording in photorefractive crystals, combine the advantages of both the previous classes of devices in terms of spatial resolution and speed. This is due to the fact that they use a transverse bias electric field, resulting in high resolution without affecting sensitivity. However, they involve holographic setups, implying severe alignment and component quality requirements and suffer from the same power and wavelength restrictions as the second class of devices.

Finally, an overall comparison of optical devices to digital processing is attempted, which highlights a serious (and probably the unique) drawback of optical devices: the quantization resolution is that of a frame grabber (typically 8 bits) while digital techniques use the full resolution of floating point operations. This has to be cured either be increasing the amplitude resolution of the frame grabber or by applying sophisticated image reduction algorithms. Both approaches, as we demonstrate in this paper, increase dramatically the procesing time, and can result in bottlenecks which compromize the efficiency of the optical device.

Detection of low speed streaks over a drag reducing surface.
by

A. D. Schwarz – van Manen, H. P. Sparidans and K. Krishna Prasad
Eindhoven University of Technology, The Netherlands.

F. T. M. Nieuwstadt
Delft University of Technology, The Netherlands.

The work described in this presentation is part of a collaborative project on drag reduction with microgrooves between Eindhoven University of Technology and Delft University of Technology. It concerns the results obtained from flow visualization studies carried out in a low speed water channel with the help of hydrogen bubbles generated by a platinum wire of 20μm diameter placed parallel to the wall and normal to the flow. The hydrogen bubble lines generated by the wire was illuminated by a light sheet from a mercury vapour lamp and recorded by a 512 × 512 pixels CCD camera for a period of 15 minutes. The records were digitized and analyzed by a picture processing system comprising of a DT 2861 arithmetic frame grabber and a DT 2858 auxiliary frame processor coupled to an Ampton AT computer.

Over 5000 pictures per experiment were analyzed using a fairly simple but fast algorithm. The interval between two pictures is 80 or 120 msec depending on the dimensionless time scale. The purpose of the work is to provide a detailed characterization of the low speed streaks over smooth and grooved surfaces. Results will be presented indicating the total duration of a low speed streak along with the frequency and amplitude of meandering of these streaks over smooth and grooved surfaces. Since previous studies have indicated very little differences in the velocity in streamwise and vertical directions over the two types of surfaces, it is believed that there would be significant differences in the spanwise directions. It is further expected that the meandering of the streaks are caused by these spanwise motions. The purpose of the work is to quantify the differences in these motions between smooth and grooved surfaces. In addition the average values of the distances between two streaks, their width and their duration will be reported.

Digital image processing for the analysis of hydrogen-bubble time-line visualizations in a turbulent boundary layer

A.J. Brand[1] and F.T.M. Nieuwstadt

Lab Aero & Hydrodynamics TU-Delft, Rotterdamseweg 145, 2628 AL Delft, Netherlands

Introduction

The use of hydrogen-bubble time-lines is a well established method to obtain quantitative data out of flow visualization. Here we report on the digital image processing that was involved in investigations on the spanwise structure of the flow in a turbulent boundary layer.

Image recording

The hydrogen-bubble time-lines were illuminated with light from a 5 W Ar-ion laser (Spectra Physics Model 2020). A fiber-optic cable transported the light to an optical system that produced a thin light sheet. The light scattered by the bubbles was recorded with a CCD video camera (High Technology Holland MX). An electro-optical shutter (Displaytech Model PV-050C) appropriately synchronized the light for the camera. The recordings were stored on video tape. The angle between the camera axis and the axis of the light sheet was about 40^o. The time lapse between two time-line generations was set such that only one time line was present in each recording. Usually 6 recordings of a time line could be obtained.

Image processing

A frame grabber (Data Translation DT 2851) mounted in a personal computer (Hewlett Packard Vectra RS/20) was used to digitize the time-line pictures that were stored on video tape. The pictures were then available in a format of 512x512 non-square pixels and 256 grey levels. Standard and customized commands in an image processing software package (PC Semper) were used to process the digitized pictures.

The pictures were re-sampled in order to reduce storage requirements and computation times. This had as an additional (and not un-welcome) side effect the disappearance of image flicker due to the interlaced and non-ideal video signal. The contrast was improved by subtracting a recording of the background from the pictures. Uneven illumination was taken care of by applying a minmax filter to the pictures, and control grid matching was used to obtain a value for the angle over which the image field must be rotated in order to rectify the images.

Next, the binary versions of the pictures were created. An opening of size 1, followed by a closing of size 1 (in the case of 128x128 pictures) was used to remove 'salt-and-pepper noise', and to smooth the boundaries of the time line. The thickness of the line was then reduced to the size of one pixel with the rim function. By taking the 'inclusive or' of the thinned time-line pictures the picture was created which contained the positions of the time line at intervals of 40 ms. To avoid the merging of time lines due to small displacements this operation was performed with a preshift which added a multiple of 16 grid units to the position of each picture.

The distance between the time lines and the bubble-generating wire was measured at each scan line. This distance was compensated for the preshift, and used to compute the corresponding $u(z)$ velocity profile. This yielded a profile pattern, in which each profile contained an estimate of the velocity of the time line at a specific time instant. Due to the intrinsic uncertainty of the hydrogen-bubble technique and the errors introduced at the preceding stages, the uncertainty in the spanwise velocity profiles was about 10% for u, and about 1 grid unit for z.

[1]Present address: Netherlands Energy Research Foundation ECN, P.O. Box 1, 1755 ZG Petten, Netherlands

Analysis of a bubbling 2D-gas-fluidized bed using Image Processing

H.B.M Schulte, R.F Mudde, H.E.A. van den Akker
Kramers Laboratorium voor F.T., TUD

Abstract

The bubble behaviour of a 2-dimensional bed (2m*0.5m*0.03m) containing polystyrene powder (mean particle diameter $\overline{d_p}$ = 0.56mm) fluidized with air at ambient conditions is investigated with the use of image processing of a video movie recorded with standard video equipment. After the usual operations necessary to segment the bubbles from the background in a video frame (using the minimal entropy method) several properties of the bubbles are obtained. The bubble area, frontal diameter (Feret diameter) as well as the area occupied by the bubbles in a slab (at given height above the gas distributor) are measured. These properties are averaged by processing more than 100 independent video frames for a given height and gas throughput.

Furthermore we calculated the "instantaneous" velocity of an individual bubble by measuring the displacement of the center of gravity (obtained with the Freeman-Ehrlich method) of a bubble from eight consecutive video frames. The time between to frames was as less as 40ms.

The averaged velocity of several bubbles is obtained as function of the height above the gas distributor and as function of the bubble size, the latter showing good agreement with results reported in literature (usually obtained with intruding measuring techniques).

Finally using the Freeman code the contour of a bubble is cut in two parts. To these parts circles are fitted and in this way the bubble wake radius and wake angle are obtained.

The entire analysis is performed with the Tcl Image software package.

Oil Film Interferometry

An optical method of measuring wall shear stress

H.A. Siller [1] R.J. Perkins [1] G. Janke [2]

Abstract:

A thin oil film flowing on a flat plate under the influence of an external shear stress will change its height h according to

$$\frac{\partial h}{\partial t} = -\frac{\partial}{\partial x}\left(\tau \frac{h^2}{2\eta}\right) \tag{1}$$

where τ is the shear stress and η the dynamic viscosity of the oil. In principle, an unknown shear stress can be calculated by measuring the surface height $h(x,t)$, but the height of the film is of the order of microns and cannot be measured directly.

If the oilfilm is applied to a flat, horizontal glass plate with a black underside and is illuminated with monochromatic light, a fringe pattern is visible. These fringes result from interference between light reflected off the surface of the film and light reflected off the oil-glass interface; lines of equal intensity correspond to lines of equal height, and the difference in height between two neighbouring lines of equal intensity is about $0.21\,\mu m$ in a typical implementation. When the oil film is moving under the influence of an external flow, changes in the fringe pattern indicate changes in the film height.

Tanner [76] and Monson [81] made shear stress measurements by observing the changes in intensity at fixed points using laser beams. With the advent of inexpensive image processing equipment, it is now possible to extend this approach to measure shear stress that varies parallel to the flow only. In principle, it is even possible to develop a method for measurements of two-dimensional shear stress fields.

To measure shear stress that changes in one-dimension only, the evolution of the fringe pattern in an external flow is filmed using a video camera. In an image processing system, lines parallel to the mean flow are extracted from the pictures at regular time intervals and placed next to each other to form an x-t-diagram, representing the evolution of the fringe pattern in space and time.

The height of the oilfilm can be calculated from these diagrams, using either line-following algorithms or a surface-fitting-approach. Both methods break down when surface gradients become too large, as the spacing of the fringes becomes too narrow to be resolved.

The x-t-diagrams from the experiments require some preliminary processing before they can be used as input into an algorithm for shear stress calculation. The effects of varying background illumination have to be cancelled out, the noise level has to be reduced, and the contrast has to be improved.

The advantages of oil film interferometry are, that it is a direct method that requires no calibration, and that the experiments involved are relatively simple.

We present some shear stress measurements on a flat plate in front of a two-dimensional obstacle, to illustrate the method and analysis techniques. The results are compared with conventional measurements.

Tanner, L. H. & Blows, L. G. 1976 A study of the motion of oil films on surfaces in air flow, with application to the measurement of skin friction. *J. Phys. E: Sci. Instrum.* **9**, 194-202.

Monson, D. J. & Higuchi, H. 1981 Skin friction measurements by a dual-laser-beam interferometer technique. *AIAA Journal Vol.19* **6**, 739,744.

[1] Department of Applied Mathematics and Theoretical Physics, University of Cambridge

[2] Hermann-Föttinger-Institut, Technische Universität Berlin